PoliTO Springer Series

Marco Petrolo *Editor*

Advances in Predictive Models and Methodologies for Numerically Efficient Linear and Nonlinear Analysis of Composites

POLITECNICO
DI TORINO

Springer

PoliTO Springer Series

Springer, in cooperation with Politecnico di Torino, publishes the PoliTO Springer Series. This co-branded series of publications includes works by authors and volume editors mainly affiliated with Politecnico di Torino and covers academic and professional topics in the following areas: Mathematics and Statistics, Chemistry and Physical Sciences, Computer Science, All fields of Engineering. Interdisciplinary contributions combining the above areas are also welcome. The series will consist of lecture notes, research monographs, and briefs. Lectures notes are meant to provide quick information on research advances and may be based e.g. on summer schools or intensive courses on topics of current research, while SpringerBriefs are intended as concise summaries of cutting-edge research and its practical applications. The PoliTO Springer Series will promote international authorship, and addresses a global readership of scholars, students, researchers, professionals and policymakers.

More information about this series at http://www.springer.com/series/13890

Marco Petrolo
Editor

Advances in Predictive Models and Methodologies for Numerically Efficient Linear and Nonlinear Analysis of Composites

POLITECNICO
DI TORINO

Springer

Editor
Marco Petrolo
MUL2 Group, Department of Mechanical
and Aerospace Engineering
Politecnico di Torino
Turin, Italy

ISSN 2509-6796 ISSN 2509-7024 (electronic)
PoliTO Springer Series
ISBN 978-3-030-11968-3 ISBN 978-3-030-11969-0 (eBook)
https://doi.org/10.1007/978-3-030-11969-0

Library of Congress Control Number: 2019930977

This Springer imprint is published by the registered company Springer Nature Switzerland AG
The registered company address is: Gewerbestrasse 11, 6330 Cham, Switzerland

Foreword

The following comments stemmed from a meeting held in Sestri Levante, Italy, on June 2018, in which each first author of this book presented the chapter content extensively to a scientific panel. The chairman was Prof. Erasmo Carrera (Politecnico di Torino, FULLCOMP Coordinator), and the other members of the panel were the FULLCOMP project supervisors and three external experts, namely Prof. Olivier Allix (École normale supérieure de Cachan), Prof. J. N. Reddy (Texas A&M University), and Doctor Evan Pineda (NASA).

Prof. Olivier Allix, École normale supérieure de Cachan

The meeting took place at the beginning of the last year of the Ph.D. projects. This choice proved to be relevant to the students being able to deliver a significant amount of results during their presentations. They lasted about one hour, and the friendly atmosphere allowed the external participants to address their questions or remarks straightforwardly. Moreover, the presence of most of the student supervisors was also beneficial for very fruitful interactions.

The first striking aspect was the outstanding level of the students. It appears that the different partners managed to attract, thanks to the Marie Sklodowska-Curie fellowships, extremely talented students from all over the world. Moreover, the level of cooperation between the students and the strong cohort spirit that emerged from the meeting was noticeable and particularly pleasant; such an outcome is not that common. Finally, presentations proved the flexibility of Carrera Unified Formulation (CUF) to address a variety of complex physical problems at various scales efficiently. Moreover, as can be seen from the following chapters, the subjects selected both cover a wide range of topics and are at the same time coherent and complementary, challenging and constitute essential topics regarding the design of composite materials and structures.

The first part focused on high-fidelity and computationally efficient models for multiphysics and design and presented the extension of the CUF via the introduction of new and significant features. First set of new features concern the

coupling of CUF with the asymptotic numerical method for very fast buckling and post-buckling analyses of structural parts including the investigation of bi-stable structures, a hot topic today, and the analysis of sensitivity to imperfections. The second set is the derivation of a multiscale version of CUF to model regular microstructures concurrently with the macro- or mesostructures in the case of composites.

The second part focused on failure analysis, impact, and health monitoring. Outcomes deal with the analysis of the nonlinear response of composites at various scales. For example, the use of CUF for the efficient 3D nonlinear analysis of beam-like structures or the global-local nonlinear analysis. Such a global-local strategy may use legacy codes at all scales or a legacy code at the global scale and CUF at the local one, leading to a very precise determination of stresses. The results presented during the meeting were encouraging. Some results concerning the global–local analysis of the buckling and post-buckling response of complex composite parts, including delamination, were particularly impressive. Several challenging aspects remain unexplored for the CUF, i.e., discontinuities.

The third part focused on virtual characterization, manufacturing effects, and uncertainty quantification. The results show extended insights on the sensitivity in the post-buckling behavior of composite panels opening the door to robust design. Moreover, several important and new aspects regarding the FULLCOMP project are the multiscale identification in an inverse setting and uncertainty quantification in the response of complex composite materials.

Dr. Evan Pineda, NASA

The use of composite materials in modern structural applications is already prevalent. However, the full potential of these materials has yet to be achieved. Composites function more as "microstructures" than as "traditional" materials. As such, there exists a great potential not only to design with the material but to design the material itself, so that it is tailored specifically for enhanced and optimized performances. Moreover, advanced composite materials can be used in multifunctional applications which significantly expands the design space for next-generation structures. The realization of such tremendous capabilities requires synergistic approaches including multiscale and multiphysics modeling, characterization, and validation testing. These methods must be employed at all stages of the composite's life cycle: from processing to performance. Only by integrating these stages, in an optimized and coupled fashion, can the maximum ability of composites be exploited. To facilitate such a transition in design, analysis, manufacturing, and experimentation, there must be a paradigm shift in the research projects on composite materials, and the projects themselves must be integrated and multidisciplinary.

The primary goals of the FULLCOMP project have been to conduct unified, multidisciplinary, cutting-edge research on composite structures at all phases included in the entire composite life cycle. Specifically, collaborative research topics have targeted the areas of optimization, manufacturing, structural analysis, health

monitoring, uncertainty quantification, failure prediction, multiscale and multiphysics modeling, testing, prognosis, and prognostic. Not only is the research itself versatile, but so are the academic and industrial research partners which consist of an international team from throughout Europe, Australia, and the USA. Finally, the project served to educate and train a number of students who will enter the workforce with expertise in a wide range of disciplines related to advanced composite materials and structures, further promoting this technology and its possibilities.

I was honored and excited to be invited by Prof. Erasmo Carrera to attend a research retreat for FULLCOMP in Sestri Levante, Italy. Throughout the day and one-half of meetings, I was exposed to the breadth and quality of research that was conducted under FULLCOMP. I was equally impressed with the relevance and synergy of the program—although the research may have been conducted at various locations throughout the world, the research was not conducted in isolation. Each piece of research fits together to form part of a bigger puzzle. It is through the multidisciplinary and integrated structure and management that FULLCOMP should serve as a precedent for future research projects in composites, as well as many other fields.

I am extremely pleased that the outcome of the FULLCOMP project has been consolidated into a single, comprehensive manuscript. Within this volume are several articles summarizing work aimed at filling technology gaps present within the life cycle of composite structures. The book is broken up into three parts. In the first part, high-fidelity, multiscale models are used to solve a variety of multiphysics problems related to composites including piezoelectric composites, thermomechanical coupling, post-buckling, and multistability. The second portion covers failure, impact, and health monitoring through the benchmarking of higher-order, one-dimensional models to provide solutions for problems involving local plasticity and progressive damage, computational modeling of coupling between panel post-buckling and delamination, hyperelastic modeling of textile yarns under impulse loading, and simulation of lamb waves with higher-order numerical models. Papers on virtual characterization, manufacturing effects, and uncertainty quantification are compiled in the third and final section of the manuscript. Specifically the effects of gradation in material properties on post-buckling, an inverse approach to multiscale characterization in-situ, anisotropic material properties, and uncertainty quantification utilizing metamodels.

Prof. J. N. Reddy, Texas A&M University

In general, the research being carried out by the FULLCOMP graduate students is excellent. The presentations were, overall, very good and inspired many comments and advice. The works presented are all excellent and have high scientific value, and each early stage researcher must be the main ambassador of such a value. Although contributions by most researchers around the world, for the most part, are infinitesimal, one should take pride in what you do, however small it is, because collectively we make an impact on the humanity. In doing so, a researcher must

always have the big picture about what is doing and derive motivations from the potential usefulness and impact of what does. Moreover, in a project like FULLCOMP, it is essential to know the mathematical models the assumptions made in deriving it, and the computational approach must include all of the significant features of the mathematical model.

Preface

The use of composite materials in engineering grows continuously together with a multibillion market in which automotive, aerospace, and wind energy sectors are the main players. Composites' success stems from their superior specific properties and the possibility of creating fit-for-purpose materials and structures. However, lack of knowledge still undermines the cost-effectiveness of composites and overweight. This book presents contributions tackling some of the current issues related to the analysis of composite structures. For a given problem, each chapter offers detailed theoretical descriptions and significant numerical examples.

The contributions of this volume are outcomes from the research project FULLCOMP, FULLy integrated analysis, design, manufacturing, and health monitoring of COMPosite structures. FULLCOMP is a Marie Sklodowska-Curie project dedicated to the training of twelve Ph.D. students in the field of advanced models for composite structures. The most relevant common thread of the contributions is the augmented numerical efficiency with superior accuracy for given computational costs than existing methods and methodologies.

FULLCOMP started in 2015 as an European Training Network composed by Politecnico di Torino, University of Bristol, Leibniz Universität Hannover, Ecole Nationale Superieure d'Arts et Metiers of Bordeaux, Luxembourg Institute of Science and Technology, ELAN-AUSY GmbH, Universidade do Porto, University of Washington, and RMIT. The training through research of the Ph.D. students followed five main work packages, namely analysis and computational methods, design and optimization, damage and failure analysis, multiscale methods, and experimental approaches. Other forms of training included three courses on entrepreneurship and project management, four workshops on composite materials and structures, one spring school, and some ten seminars or courses. Also, each student spent two secondment periods of several weeks in academic and non-academic institutions to increase the multidisciplinarity, facilitate cross-fertilization, and the transfer of knowledge toward industry.

The first authors of the following chapters are the FULLCOMP Ph.D. students who, coherently with the meaning of a Marie Sklodowska-Curie project, are the main actors of the entire network. Students and supervisors established individual

career development plans at the beginning of the project, and this book aims to show the scientific results of such plans. As anticipated in the foreword, the contents of each chapter were subjects of extensive presentations held in Sestri Levante, Italy, on June 2018, in which each Ph.D. student presented before a scientific panel chaired by Prof. Erasmo Carrera (Politecnico di Torino, FULLCOMP Coordinator) and composed by the FULLCOMP project supervisors and three external experts, namely Prof. Olivier Allix (École normale supérieure de Cachan), Prof. J. N. Reddy (Texas A&M University), and Dr. Evan Pineda (NASA).

This book intends to provide insights on some of the latest developments in the virtual modeling of composite structures. The intended audience ranges from graduate students to professionals from aerospace and mechanical engineering. The theoretical parts are the most extensive in each chapter to furnish more details related to the implementation aspects. The most significant numerical results close each chapter to underline the capabilities of the developed models.

The European Union's Horizon 2020 Research and Innovation program is acknowledged for the funding of Marie Sklodowska-Curie grant agreement No. 642121.

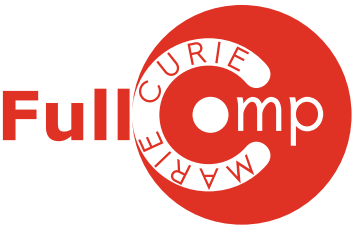

Turin, Italy Marco Petrolo

Contents

Chapter 1
Introduction

M. Petrolo

Abstract This chapter provides an overview of the book contents and the most significant works from the literature on related topics. Each section of this chapter deals with one of the main parts of the book, namely, advanced structural theories, failure and damage analyses, virtual characterization and manufacturing. The first part of this volume presents structural theories to deal with the anisotropy of composites and to embed multifield and nonlinear effects to widen design capabilities. The aim is to provide methods to augment the fidelity of structural theories and lower computational costs with attention paid to the finite element method. The second part handles the damage analysis. The multiscale and multicomponent nature of composites leads to extremely complex failure mechanisms and predictive tools require physics-based models to lower the need for fitting and tuning from costly and lengthy experimental campaigns, and lower computational costs. Furthermore, the proper monitoring of in-service damage is decisive in a damage tolerant perspective. The third part presents recent advances to embed characterization and manufacturing effects in virtual testing. Higher cost-effectiveness claims the reduction of physical characterization campaigns as well as higher fidelity for multiscale identification. Variations of properties due to defects stemming from manufacturing can propagate through scales and dramatically alter performances. The characterization of the material requires proper uncertainty quantification tools based on stochastic models and should embed metadata handling for informed virtual testing.

1.1 Advanced Structural Models

The first part of this book presents advanced one-dimensional (1D) and two-dimensional (2D) models, commonly referred to as beams and shells, respectively. The use of such theories enables the accurate prediction of 3D displacement

M. Petrolo (✉)
MUL2 Group, Department of Mechanical and Aerospace Engineering, Politecnico di Torino, Torino, Italy
e-mail: marco.petrolo@polito.it

M. Petrolo (ed.), *Advances in Predictive Models and Methodologies for Numerically Efficient Linear and Nonlinear Analysis of Composites*, PoliTO Springer Series,
https://doi.org/10.1007/978-3-030-11969-0_1

and stress fields and the reduction of computational costs if compared to classical 3D finite elements. The structural theories of this part stemmed from the use of the Carrera Unified Formulation (CUF) [11] and employed for multifield analyses, bistable structures and multiscale frameworks.

Traditional shell theories include Classical Lamination Theory (CLT) based on the Kirchhoff–Love hypotheses, First-Order Shear Deformation Theory (FSDT) using the Mindlin–Reissner assumptions, and Higher-Order Theories (HOT) [65]. The CUF [10, 11] is a general framework to develop continuum-based reduced models in either an Equivalent Single-Layer (ESL) or Layer-Wise (LW) approach. Through the *fundamental nuclei* (FNs), the finite element formulation has a compact form facilitating the implementation of diverse theories of structures. CUF can deal with various and miscellaneous theories and construct finite element models with variable nodal kinematic capabilities through the Node-Dependent Kinematics (NDK) technique for adaptable refinements. These features allow the improvement of the numerical efficiency and accuracy and optimize the finite element mesh grids [44]. Advanced models are particularly relevant for multilayered shells of doubly curved shells [42] and hygro-thermo-electro-mechanical couplings [5, 69].

In this book, one of the applications of advanced structural models deals with bistable pre-buckled beam-like structures. Due to the release of energy and motion provided by the snap-instability, bistable beam structures are of interest for energy harvesting applications [78], actuators [62] and shape-adaptive structures [6]. Past works used classical modeling approaches based on the Euler-Bernoulli or Timoshenko kinematics [9, 17, 75]. More recently, developments of CUF led to a class of refined one-dimensional models based on a Maclaurin expansion of the displacement field through the beam thickness in the framework of an ESL approach [12, 23, 32]. Such developments account for the geometrical nonlinearities to address post-buckling and snap-through behaviors in a total Lagrangian formulation.

The use of advanced structural models is beneficial in a multiscale nonlinear framework. Advances in this book fall within the FE^2 method, see Feyel and Chaboche [28] and Nezamabadi et al. [55] in which the analysis has a macroscopic/structural problem and a microscopic/material one. Concerning the geometrically nonlinear problem, a promising tool is the Asymptotic Numerical Method (ANM), see Damil and Potier-Ferry [21] and Cochelin et al. [18], that is more reliable and less time consuming when compared to classical iterative methods.

1.2 Damage and Failure

The second part of this book presents advances in the development of modeling tools for damage and failure analysis of composites and a closing chapter on structural health monitoring (SHM). The modeling strategies act at the theory of structures level - e.g., by using CUF - to have highly accurate 3D stress fields with lower costs, and coupling tools - such as global-local methods - to limit highly expensive analysis into local areas and, therefore, extend the predictive tools to large and com-

plex structures. The inclusion of material nonlinearities into 1D structural models is desirable to lower the computational costs and mandatory to deal with damage and failure. Among the others, papers particularly significant on this topic are by Timoshenko and Gere for inelastic beams [73], Abambres et al. for the elastoplasticity and post-buckling analyses of thin-walled beam structures [1] via the Generalized Beam Theory (GBT), Pollayi et al. to model the matrix cracking in helicopter rotors or wind turbine blades via the Variational Asymptotic Beam Section Analysis (VABS) [64], Jiang and Yu for hyperelastic beams and damage analyses of composites [36, 37], Škec et al [68] for mixed-mode delamination analyses, Eijo et al. to model delamination in composite laminated beams via Zig-Zag theories [26], and Pagani and Kaleel for the extension of CUF to geometrical and material nonlinearities [13, 38, 59].

A class of strategies to deal with progressive failure analyses exploits global-local methods to accurately model the damage onset and propagation in localized areas at reasonable computational effort. The submodeling technique, or so-called zooming technique, was successful for having a detailed investigation at the local level of modeling while using a relatively coarse global model. Examples are in the works of Mote [53], Noor [57], Mao and Sun [48], and Whitcomb [76]. In contrast, in a two-way coupling, the information exchange is in both directions to account for interactions of global and local effects. Recent global-local approaches are, for instance, the multiscale projection method by Löhnert and Belytischko [46], the adaptive progressive damage modeling technique by Labeas et al. [39], the homogenization-based iterative two-way multiscale approach by Chrupalla et al. [16], the non-intrusive global-local technique by Gendre et al.[31], and the two-way loose coupling method for intralaminar damage by Hühne et al. [35]. The efficient homogenization technique for the matrix and fiber failure in the latter work [35] had a further enhancement in Akterskaia et al. [4] for large structures such as a curved multi-stringer composite panel. In the context of interlaminar damage analysis, for the modeling of skin-stringer debonding in stiffened panels, presently, mainly one-way coupling methods are in use, such as the approaches of Reinoso et al. [66] based on cohesive elements, and Orifici et al. [58] based on user-defined multi-point constraint elements in the framework of the Virtual Crack Closure Technique. Akterskaia et al. [3] introduced a novel two-way coupling method, in the spirit of [4], for modeling skin-stringer debonding that ensures an appropriate exchange of information between the global and local analysis levels.

One class of composites investigated in this project makes use of dry fabric layers. The modeling approach deals with hyperelastic constitutive laws for the yarn structure and full characterization via experimental or numerical approaches avoiding the numerical calibration. Various numerical models exist for dry fabric layers in bibliography [70]. Among them, the so-called mesoscopic models resulted in being the most successful since they offer a good compromise regarding accuracy and computational costs. Since their introduction by Duan [24, 25], this type of models remains substantially unvaried while adopted for different studies [15, 34, 56]. The constitutive law universally adopted in mesoscopic models of dry fabrics is due to Gasser [30] and consists of an anisotropic linear elastic law. The ability of the Gasser

model in representing the yarn longitudinal behavior is the subject of various studies [15, 25] while the modeling of the yarn transverse behavior remains an unsolved problem. Unfortunately, this last aspect assumes a fundamental role in determining ballistic performance of multilayer textiles [19, 56].

One of the tools to handle damage and defects is SHM as proved by the recent gain of interest in the engineering community. SHM may serve as a tool for the on-line monitoring of the structure, ensuring structural integrity during service, and reducing substantially the operating costs. In this framework, the guided ultrasonic waves (GUW) are a suitable candidate to detect, localize and characterize the structural defects using a network of actuators, sensors and on-board computers that elaborate information [33]. Lamb waves, first described by Lamb [40], are a class of GUW that propagate in plates with free surfaces. They are highly dispersive and exhibit very short wavelengths, which makes them appropriate for the detection of small defects in large areas. In laminated structures, the physical phenomena involved in the propagation of Lamb waves are highly complex [41]. The anisotropy of the material causes distorted wavefronts, and the heterogeneities of the multiphase materials might result in mode couplings and continuous conversions. Numerical models are essential to obtain the dispersion curves of Lamb waves in different media [22, 47]. Moreover, the simulation of the transient response in reinforced structures requires the use of advanced finite element models to capture the scattering of the time signals due to material discontinuities and structural defects [77]. In this matter, higher-order multi-layered theories based on the CUF [11] present many advantages for the wave propagation analysis in composite laminates.

1.3 Virtual Characterization and Manufacturing Effects

Real structures are imperfect, despite advances in production processes and quality control, manufactured structures deviate from the ideal geometry and properties. This is due to variations in the manufacturing process throughout the production line [45, 80]. The corresponding variations of the structure may lead to conservative design procedures, such as using safety factors.

One of the contributions in this book presents advances towards a better understanding of the effects that spatial variations of structural properties can have on the mechanical response of the structure. This can lead to more robust structures, and potentially improve the performance of structures. Stochastic analyses are typical in this field and most of them try to analyze the response of structures with given stochastic parameters as input [60, 61, 67]. This approach relies on the availability of accurate statistical parameters of the variations of the structure, which are usually not available [43, 71]. Without accurate inputs, quantifying the variability of the outputs is not possible. The method discussed in this book deals with the sensitivity of the structural behavior concerning the spatial variations. Analyzing the correlation of spatial variations of a material property with another measure - e.g., a structural performance parameter such as the buckling load - may lead to map a type of non-

dimensional sensitivity topology of the structure. These sensitivity topology maps help with identifying areas in which variations have the most effect, areas for product inspection, and improve the performance of a structure. By redistributing material properties using a scaled version of the sensitivity topology map, it is possible to improve the performance of the structure without increasing the mean value of the property.

As shown in the last chapter of this book, the multiphase and heterogeneous nature of composite materials make uncertainties related to constituents and various scales significant for the overall response. Examples are the aleatory uncertainties related to the matrix or fiber properties, but also the geometrical variability in lower scales. Early efforts focused on the simulation of random fiber distributions for micromechanics [50], propagation of uncertainties though the scales and the response variability [14], and the introduction of probabilistic models for the fiber strength [20]. A classic review paper on uncertainty quantification [71] established the stochastic perspective of composites by classifying sources of uncertainty, modeling approaches and reliability methods for structural components. Recently, more and more studies have been dealing with the geometrical randomness such as random voids at lower scales [72] or waviness of the fiber reinforcement in textiles [74]. However, the major topic in stochastic analysis is the quantification of the random input. To avoid non-physical assumptions, the current trend of this research field is focusing on the statistical information of the input random parameters [8].

The multiscale nature of composites makes the characterization of the full set of the material properties at each pertinent scale, e.g., the mesoscopic scale of the constitutive lamina and microscopic scale of constituent phases, mandatory for the design and optimization of parts. From an industrial point of view, the cost reduction of experimental characterization tests is of paramount importance. Usually, destructive procedures are necessary for a significant number of samples and reliable results [2]. Concerning the mesoscopic scale, the most common tests are the ASTM tests - e.g., tension test for flat specimens, three/four points bending test - which cannot provide the full set of 3D elastic properties but only the in-plane material properties together with an approximated value of the out-of-plane shear moduli. Conversely, only a few standard tests are available for the microscopic scale, i.e., the single fiber test to obtain the Young modulus along the fiber longitudinal direction - ASTM D3379 - and the matrix tensile test - ASTM D638. To characterize the rest of the constitutive phase properties, only non-standard tests are available in literature, e.g., the pull-out [54], micro-indentation [49], fragmentation tests [27]. It is important to observe that unconventional destructive tests present some major shortcomings, such as the experimental set-up is quite complex, and the obtained results show a significant dispersion [49, 79]. In this book, to overcome the main restrictions imposed by destructive tests, the approach presented focuses on the development of a multiscale identification strategy (MSIS). The MSIS aims at identifying the full set of elastic properties at both lamina-level and constitutive phases-level starting from the analysis of the macroscopic dynamic response of a multilayer plate. In particular, the macroscopic dynamic behavior stems from the non-destructive modal tests and the information restrained in the harmonic spectrum response of the specimen leads to the multi-

scale characterization process. This kind of approach is in the literature [29, 81] for characterizing the elastic properties of the constitutive lamina. An assessment of these approaches is available in [63]. Most of these techniques, e.g., [52], make use of an optimization tool to minimize the difference between the measured dynamic response - typically a given set of natural frequencies - and the numerical one calculated via a finite element model of the structure. However, this approach lacks generalization to characterize the material and geometrical features of the microstructure of composite materials. In the framework of the MSIS, the multi-scale identification problem derives from two optimization problems stated at different scales. The MSIS has several original features. On the one hand, it relies on a special hybrid optimization tool to perform the solution search [51]. On the other hand, a general numerical homogenization scheme ensures the scale transition [7].

References

1. Abambres M, Camotim D, Silvestre N (2014) GBT-based elastic-plastic post-buckling analysis of stainless steel thin-walled members. Thin-Walled Struct 83:85–102
2. Adams FD, Carlsson AL, Pipes RB (2003) Experimental characterization of advanced composite materials, 3rd edn. CRC Press LLC, New York
3. Akterskaia M, Jansen E, Hallett SR, Weaver R, Raimund R (2018) Analysis of skin-stringer debonding in composite panels through a two-way global-local method. Compos Struct 202:1280–1294
4. Akterskaia M, Jansen E, Hühne S, Rolfes R (2018) Efficient progressive failure analysis of multi-stringer stiffened composite panels through a two-way loose coupling global-local approach. Compos Struct 183:137–145
5. Altay G, Dökmeci MC (2008) Certain hygrothermopiezoelectric multi-field variational principles for smart elastic laminae. Mech Adv Mater Struct 15(1):21–32
6. Arena G, Groh RMJ, Brinkmeyer A, Theunissen R, Weaver PM, Pirrera A (2017) Adaptive compliant structures for flow regulation. Proc R Soc A 473 (2204)
7. Barbero E (2007) Finite element analysis of composite materials. CRC Press, Taylor and Francis Group, New York
8. Bessa MA, Bostanabad RB, Liu Z, Hu A, Apley DW, Brinson C, Chen W, Liu WK (2017) A framework for data-driven analysis of materials under uncertainty: countering the curse of dimensionality. Comput Method Appl M 320(15):633–667
9. Camescasse B, Fernandes A, Pouget J (2013) Bistable buckled beam: Elastica modeling and analysis of static actuation. Int J Solids Struct 50(19):2881–2893
10. Carrera E (2002) Theories and finite elements for multilayered, anisotropic, composite plates and shells. Arch Comput Methods Eng 9(2):87–140
11. Carrera E, Cinefra M, Zappino E, Petrolo M (2014) Finite element analysis of structures through unified formulation. Wiley Ltd, United Kingdom
12. Carrera E, Giunta G, Petrolo M (2011) Beam structures: classical and advanced theories. Wiley, Chichester
13. Carrera E, Kaleel I, Petrolo M (2017) Elastoplastic analysis of compact and thin-walled structures using classical and refined beam finite element models. Mechanics of advanced materials and structures. In Press
14. Chamis CC (2004) Probabilistic simulation of multi-scale composite behavior. Theor Appl Fract Mec 41(1–3):51–61
15. Chocron S, Figueroa E, King N, Kirchdoerfer T, Nicholls A, Sagebiel E, Weiss C, Freitas CJ (2010) Modeling and validation of full fabric targets under ballistic impact. Compos Sci Technol 70(13):2012–2022

16. Chrupalla D, Berg S, Kärger L, Doreille M, Ludwig T, Jansen E, Rolfes R, Kling A (2011) A homogenization-based two-way multiscale approach for composite structures. In: Rolfes R, Jansen EL (eds) Proceedings of the 3rd ECCOMAS thematic conference on the mechanical response of composites. Hannover, Germany, pp 263–270
17. Cleary J, Su HJ (2015) Modeling and experimental validation of actuating a bistable buckled beam via moment input. J Appl Mech 82(5):051005
18. Cochelin B, Damil N, Potier-Ferry M (1994) Asymptotic-numerical methods and pade approximants for non-linear elastic structures. Int J Number Meth Eng 37(7):1187–1213
19. Cunniff P (1999) Decoupled response of textile body armor. Decoupled response of textile body armor. Proceedings of the 18th international symposium on ballistics
20. Curtin WA (1998) Stochastic damage evolution and failure in fiber-reinforced composites. Adv Appl Mech 36:163–253
21. Damil N, Potier-Ferry M (1990) A new method to compute perturbed bifurcations: application to the buckling of imperfect elastic structures. Int J Eng Sci 28(9):943–957
22. Datta SK, Shah AH, Bratton RL, Chakraborty T (1988) Wave propagation in laminated composite plates. J Acoust Soc Am 83(6):2020–2026
23. De Pietro G, Giunta G, Belouettar S, Carrera E (2017) A static analysis of three-dimensional sandwich beam structures by hierarchical finite elements modelling. J Sandw Struct Mater https://doi.org/10.1177/1099636217732907
24. Duan Y, Keefe M, Bogetti TA, Cheeseman BA, Powers B (2006) A numerical investigation of the influence of friction on energy absorption by a high-strength fabric subjected to ballistic impact. Int J Impact Eng 32(8):1299–1312
25. Duan Y, Keefe M, Bogetti TA, Powers B (2006) Finite element modeling of transverse impact on a ballistic fabric. Int J Mech Sci 48(1):33–43
26. Eijo A, Oñate E, Oller S (2013) A numerical model of delamination in composite laminated beams using the LRZ beam element based on the refined zigzag theory. Comp Struct 104:270–280
27. Feih S, Wonsyld K, Minzari D, Westermann P, Lilholt H (2004) Testing procedure for the single fiber fragmentation test. Denmark. Forskningscenter Risoe. Risoe-R No. 1483(EN)
28. Feyel F, Chaboche JL (2000) FE^2 multiscale approach for modelling the elastoviscoplastic behaviour of long fibre sic/ti composite materials. Comput Methods Appl Mech Eng 183(3):309–330
29. Furtado SCR, Araujo A, Silva A (2018) Inverse characterization of vegetable fibre-reinforced composites exposed to environmental degradation. Compos Struct 189:529–544
30. Gasser A, Boisse P, Hanklar S (2000) Mechanical behaviour of dry fabric reinforcements. 3D simulations versus biaxial tests. Comput Mater Sci 17(1):7–20
31. Gendre L, Allix O, Gosselet P, Comte F (2009) Non-intrusive and exact global/local techniques for structural problems with local plasticity. Comput Mech 44:233–245
32. Giunta G, De Pietro G, Nasser H, Belouettar S, Carrera E, Petrolo M (2016) A thermal stress finite element analysis of beam structures by hierarchical modelling. Compos Part B: Eng 95:179–195
33. Giurgiutiu V (2014) Structural health monitoring with piezoelectric wafer active sensors, 2nd edn. Academic, Oxford
34. Ha-Minh C, Imad A, Kanit T, Boussu F (2013) Numerical analysis of a ballistic impact on textile fabric. Int J Mech Sci 69:32–39
35. Hühne S, Reinoso J, Jansen E, Rolfes R (2016) A two-way loose coupling procedure for investigating the buckling and damage behaviour of stiffened composite panels. Compos Struct 136:513–525
36. Jiang F, Yu W (2016) Nonlinear variational asymptotic sectional analysis of hyperelastic beams. AIAA J 54(2):679–690
37. Jiang F, Yu W (2017) Damage analysis by physically nonlinear composite beam theory. Compos Struct 182:652–665
38. Kaleel I, Petrolo M, Waas AM, Carrera E (2018) Micromechanical progressive failure analysis of fiber-reinforced composite using refined beam models. J Appl Mech 85(2)

39. Labeas GN, Belesis SD, Diamantakos I, Tserpes KI (2012) Adaptative progressive damage modeling for large-scale composite structures. Int J Damage Mech 21(3):441–462
40. Lamb H (1917) On waves in an elastic plate. Roy Soc Lond Proc Ser A 93:114–128
41. Lammering R, Gabbert U, Sinapius M, Schuster T, Wierach P (eds) (2018) Lamb-wave based structural health monitoring in polymer composites. Springer, Cham
42. Leissa AW (1973) Vibration of shells, vol 288. Scientific and Technical Information Office, National Aeronautics and Space Administration Washington
43. Lekou DJ, Philippidis TP (2008) Mechanical property variability in FRP laminates and its effect on failure prediction. Compos Part B: Eng 39(7–8):1247–1256
44. Li G, Carrera E, Cinefra M, de Miguel A, Pagani A, Zappino E (2018) An adaptable refinement approach for shell finite element models based on node-dependent kinematics. Composite structures, vol 210, 15 February 2019, pp 1–19
45. Liu L, Zhang BM, Wang DF, Wu ZJ (2006) Effects of cure cycles on void content and mechanical properties of composite laminates. Compos Struct 73(3):303–309
46. Loehnert S, Belytschko T (2007) A multiscale projection method for macro/microcrack simulations. Int J Numer Methods Eng 71:1466–1482
47. Lowe MJS (1995) Matrix techniques for modeling ultrasonic waves in multilayered media. IEEE Trans Ultrason, Ferroelectr, Freq Control 42(4):525–542
48. Mao KM, Sun CT (1991) A refined global-local finite element analysis method. Int J Numer Methods Eng 32:29–43
49. Maurin R, Davies P, Baral N, Baley C (2018) Transverse properties of carbon fibres by nano-indentation and micro-mechanics. Appl Compos Mater 15:61
50. Melro AR, Camanho PP, Pinho ST (2008) Generation of random distribution of fibres in long-fibre reinforced composites. Compos Sci Technol 68(9):2092–2102
51. Montemurro M (2012) Optimal design of advanced engineering modular systems through a new genetic approach. PhD thesis, UPMC, Paris VI, France. http://tel.archives-ouvertes.fr/tel-00955533
52. Mota Soares CM, Moreira de Freitas M, Arújo AL, Pedersen P (1993) Identification of material properties of composite plate specimens. Compos Struct 25(1–4):277–285
53. Mote CD (1971) Global-local finite element. Int J Numer Methods Eng 3:565–574
54. Nairn JA (2000) Analytical fracture mechanics analysis of the pull-out test including the effects of friction and thermal stresses. Adv Compos Lett 9(6):373–383
55. Nezamabadi S, Yvonnet J, Zahrouni H et al (2009) A multilevel computational strategy for handling microscopic and macroscopic instabilities. Comput Methods Appl Mech Eng 198(27):2099–2110
56. Nilakantan G (2018) Experimentally validated predictive finite element modeling of the V0-V100 probabilistic penetration response of a Kevlar fabric against a spherical projectile. Int J Prot Struct. In Press
57. Noor AK (1986) Global-local methodologies and their application to nonlinear analysis. Finite ElemTs Anal Des 2:333–346
58. Orifici AC, Ortiz I, Alberdi DZ, Thomson RS, Bayandor J (2008) Compression and post-buckling damage growth and collapse analysis of flat composite stiffened panels. Compos Sci Technol 68(15–16):3150–3160
59. Pagani A, Carrera E (2017) Large-deflection and post-buckling analyses of laminated composite beams by Carrera unified formulation. Compos Struct 170:40–52
60. Papadopoulos V, Papadrakakis M (2005) The effect of material and thickness variability on the buckling load of shells with random initial imperfections. Comput Methods Appl Mech Eng 194(12–16):1405–1426
61. Papadopoulos V, Soimiris G, Papadrakakis M (2013) Buckling analysis of I-section portal frames with stochastic imperfections. Eng Struct 47:54–66
62. Park S, Hah D (2008) Pre-shaped buckled-beam actuators: theory and experiments. Sens Actuators A: Phys 148(1):186–192
63. Pedersen P, Frederiksen PS (1992) Identification of orthotropic material modul by a combined experimental/numerical method. Measurement 10(3):113–118

64. Pollayi H, Yu W (2014) Modeling matrix cracking in composite rotor blades within VABS framework. Compos Struct 110:62–76
65. Reddy J (2004) Mechanics of laminated composite plates and shells: theory and analysis. CRC Press, Boca Raton
66. Reinoso J, Blázquez A, Estefani A, París F, Cañas J, Arévalo E, Cruz F (2012) Experimental and three-dimensional global-local finite element analysis of a composite component including degradation process at the interfaces. Compos Part B 43(4):1929–1942
67. Shang S, Yun GJ (2013) Stochastic finite element with material uncertainties: Implementation in a general purpose simulation program. Finite Elem Anal Des 64:65–78
68. Škec L, Jelenić G, Lustig N (2015) Mixed-mode delamination in 2D layered beam finite elements. Int J Numer Meth Eng 104:767–788
69. Smittakorn W, Heyliger PR (2000) A discrete-layer model of laminated hygrothermopiezoelectric plates. Mech Compos Mater Struct 7(1):79–104
70. Sockalingam S, Chowdhury SC, Gillespie JW, Keefe M (2017) Recent advances in modeling and experiments of Kevlar ballistic fibrils, fibers, yarns and flexible woven textile fabrics - a review. Text Res J 87(8):984–1010
71. Sriramula S, Chryssanthopoulos MK (2009) Quantification of uncertainty modelling in stochastic analysis of FRP composites. Compos Part A: Appl Sci Manuf 40(11):1673–1684
72. Stefanou G, Savvas D, Papadrakakis M (2015) Stochastic finite element analysis of composite structures based on material microstructure. Compos Struct 132:384–392
73. Timoshenko SP, Gere JM (1991) Mechanics of materials. Springer-Science+Business Media, Berlin
74. Vanaerschot A, Cox BN, Lomov SV, Vandepitte D (2016) Multi-scale modelling strategy for textile composites based on stochastic reinforcement geometry. Comput Method Appl M 310:906–934
75. Vangbo M (1998) An analytical analysis of a compressed bistable buckled beam. Sens Actuators A: Phys 69(3):212–216
76. Whitcomb JD (1991) Iterative global/local finite element analysis. Comput Struct 40(4):1027–1031
77. Willberg C, Duczek S, Vivar Perez JM, Schmicker D, Gabbert U (2012) Comparison of different higher order finite element schemes for the simulation of Lamb waves. Comput Methods Appl Mech Eng 241–244:246–261
78. Xu C, Liang Z, Ren B, Di W, Luo H, Wang D, Wang K, Chen Z (2013) Bi-stable energy harvesting based on a simply supported piezoelectric buckled beam. J Appl Phys 114(11):114507
79. Young TJ (2012) Characterisation of interfaces in micro- and nano-composites. PhD thesis, University of Surrey
80. Yurgartis SW (1987) Measurement of small angle fiber misalignments in continuous fiber composites. Compos Sci Technol 30(4):279–293
81. Zhou XY, Gosling PD, Ullah Z, Kaczmarczyk L, Pearce C (2016) Exploiting the benefits of multi-scale analysis in reliability analysis for composite structures. Compos Struct 155:197–212

Part I
High-Fidelity and Computationally Efficient Models for Multiphysics and Design

Chapter 2
Variable Kinematic Shell Formulations Accounting for Multi-field Effects for the Analysis of Multi-layered Structures

G. Li, E. Carrera, M. Cinefra, E. Zappino and E. Jansen

Abstract This chapter presents refined shell finite element models with variable kinematics for the analysis of multi-layered structures involved in four physical fields: mechanical, electric, thermal, and hygroscopic. Variable kinematic models in the framework of Carrera Unified Formulation (CUF) with various kinematic assumptions are discussed. An efficient tool to realize adaptable refinement in finite element models, Node-Dependent Kinematics approach, is introduced. Refined doubly curved shell finite element formulations derived from the principle of virtual displacements accounting for multi-field coupling effects are presented.

2.1 Introduction

Laminated shells are extensively utilized in modern engineering due to their high capabilities in holding loads. Meanwhile, smart structures containing piezoelectric sensing and actuating components have been widely applied in structural health monitoring, damage detection, shape control, and energy harvesting. Temperature and moisture are important environmental factors for structures during their service life that need to be investigated. The consideration of hygro-thermo-electro-mechanical coupling effects will lead to more rigorous modeling of such problems.

A series of shell theories have been suggested and broadly adopted in structural analyses. Traditional models include Classical Lamination Theory (CLT) based on Kirchhoff–Love hypothesis [15], First-Order Shear Deformation Theory (FSDT) built on the Mindlin–Reissner assumption [19, 22], and Higher-Order Theories (HOT) [21]. Carrera [3] suggested the Unified Formulation (CUF) as a general framework to develop continuum-based degenerated 2D models through either

G. Li (✉) · E. Carrera · M. Cinefra · E. Zappino
MUL2 Group, Department of Mechanical and Aerospace Engineering,
Politecnico di Torino, Torino, Italy
e-mail: guohong.li@polito.it

E. Jansen
Institute of Structural Analysis, Leibniz Universität Hannover, Hannover, Germany

M. Petrolo (ed.), *Advances in Predictive Models and Methodologies for Numerically Efficient Linear and Nonlinear Analysis of Composites*, PoliTO Springer Series,
https://doi.org/10.1007/978-3-030-11969-0_2

Equivalent Single-Layer (ESL) or Layer-Wise (LW) approach. CUF allows the governing equations of refined finite elements (FE) to be expressed compactly through *fundamental nuclei* (FNs), core units of the stiffness matrix and load vector. The forms of the FNs are independent of the selected kinematic assumptions [7] and can facilitate the implementation of various theories of structures.

CUF provides convenience to carry out two levels of mathematical refinement, namely the enhancement of structural theories and the enrichment of shape functions. In the CUF framework, one can incorporate various and miscellaneous approximation theories into the plate/shell FE models [5, 6]. FE models with variable nodal kinematic capabilities can be constructed through Node-Dependent Kinematics (NDK), and adaptable refinement can be realized. These features allow the numerical accuracy to be improved conveniently and fully exploit the potential of FE meshes [17, 30].

The consistent multi-field constitutive equations can be derived from thermodynamics as demonstrated by Ikeda [14] and Sih et al. [23]. Variational principles for a series of multi-field couplings were discussed by Sung and Thompson [24], Dökmeci [11], and Altay and Dökmeci [1], as well as other researchers. Regarding the FE formulations, most 2D models are based on CLT or FSDT, besides the getting popular HOT. 2D electromechanical models based on CUF were developed by Carrera and Fagiano [8] and Carrera and Robaldo [9]. Cinefra et al. [10] reported refined hygrothermal models. The main advantages of CUF-based models are their high accuracy, high numerical efficiency, and adaptable refinement capability. In the CUF framework, this chapter presents shell FE formulations with variable kinematics accounting for hygro-thermo-electro-mechanical interactions.

2.2 Basic Equations of Multi-field Problems

This section consists of the fundamental equations of the steady-state hygro-thermo-electro-mechanical problems. The considered primary variables include displacements u_i, electric potential ϕ, temperature increment θ, and change of moisture concentration c. Strain tensor ε_{ij}, electrical field E_i, temperature gradients ϑ_i, and moisture gradients Υ_i are given by the following gradient equations:

$$\varepsilon_{ij} = \frac{1}{2}(u_{i,j} + u_{j,i}) \tag{2.1}$$

$$E_i = -\phi_{,i} \tag{2.2}$$

$$\vartheta_i = -\theta_{,i} \tag{2.3}$$

$$\Upsilon_i = -c_{,i} \tag{2.4}$$

where $i, j = 1, 2, 3$. The linear constitutive relations take the following form [1, 28]:

$$\sigma_{ij} = C_{ijkl}\varepsilon_{kl} - e_{kij}E_k - \lambda_{ij}\theta - \psi_{ij}c \tag{2.5}$$

$$D_i = e_{ikl}\varepsilon_{kl} + \chi_{ik}E_k + r_i\theta + \iota_i c \tag{2.6}$$

$$q_i = \kappa_{ik}\vartheta_k + \varphi_{ik}\Upsilon_k \tag{2.7}$$

$$h_i = \gamma_{ik}\vartheta_k + \xi_{ik}\Upsilon_k \tag{2.8}$$

wherein σ_{ij} indicates the stress tensor, D_i the electric displacement vector, q_i the heat flux vector, and h_i the moisture flux vector. The related material coefficients include: elastic material coefficients C_{ijkl}, dielectric permittivity coefficients χ_{ij}, thermal stress coefficients λ_{ij}, hygroscopic stress coefficients ψ_{ij}, piezoelectric coefficients e_{ikl}, pyroelectric coefficients r_i, hygroscopic-electric coupling coefficients ι_i, thermal-hygroscopic coupling coefficient ζ, thermal conductivity κ_{ik}, moisture diffusivity ξ_{ik}, moisture flux due to the thermal field γ_{ik} (Soret effect), and heat flux caused by the moisture field φ_{ik} (Dufour effect). Note that λ_{ij} and ψ_{ij} can be considered as:

$$\lambda_{ij} = C_{ijkl}\alpha_{kl} \tag{2.9}$$

$$\psi_{ij} = C_{ijkl}\beta_{kl} \tag{2.10}$$

where α_{kl} and β_{kl} are the thermal and hygroscopic expansion coefficients, respectively. In the above equations, $i, j, k, l = 1, 2, 3$.

The boundary conditions on the external sub-surfaces of the elastic body are:

$$\begin{aligned} u_i &= \overline{u}_i \quad \text{on } \Gamma_u, \qquad \phi = \overline{\phi} \quad \text{on } \Gamma_\phi, \\ \theta &= \overline{\theta} \quad \text{on } \Gamma_\theta, \qquad c = \overline{c} \quad \text{on } \Gamma_c. \end{aligned} \tag{2.11}$$

$$\begin{aligned} \sigma_{ij}\, n_j &= \overline{p}_i \quad \text{on } \Gamma_p, \qquad -D_i\, n_i = \overline{D}_n \quad \text{on } \Gamma_D, \\ -q_i\, n_i &= \overline{q}_n \quad \text{on } \Gamma_q, \qquad -h_i\, n_i = \overline{h}_n \quad \text{on } \Gamma_h. \end{aligned} \tag{2.12}$$

in which n_i are the outward unit normal vector of the bounding external surfaces, $\overline{u}_i$, $\overline{\phi}$, $\overline{\theta}$, and $\overline{c}$ the essential boundary conditions, and $\overline{p}_i$, $\overline{D}_n$, $\overline{q}_n$, and $\overline{h}_n$ the natural boundary conditions. The overbar symbol ($\bar{}$) denotes prescribed values.

In the absence of body forces, free charge, internal heat source, and moisture source, the equilibrium equations, conservation of charge (Gauss's law), heat conduction equation (Fourier's law), and moisture diffusion equation (Fick's law) read:

$$\sigma_{ij,j} = 0 \tag{2.13}$$

$$D_{i,i} = 0 \tag{2.14}$$

$$q_{i,i} = 0 \tag{2.15}$$

$$h_{i,i} = 0 \tag{2.16}$$

2.3 Laminated Shell Models Considering Multi-field Effects

As illustrated in Fig. 2.1, the geometry of a typical shell structure with uniform thickness can be described through the orthogonal curvilinear coordinates (α, β, z), in which α and β indicate the lines of curvature on the middle surface and z the thickness direction. The infinitesimal area dS parallel to the middle surface at z is:

$$dS = H_\alpha \, H_\beta \, d\alpha \, d\beta \, = H_\alpha \, H_\beta \, d\Omega \tag{2.17}$$

An elemental volume dV is given by:

$$dV = H_\alpha \, H_\beta \, H_z \, d\alpha \, d\beta \, dz \, . \tag{2.18}$$

in which $d\Omega$ is the infinitesimal area on the middle surface of the shell. For shells with constant radii of curvature, the metric coefficients H_α, H_β, and H_z read:

$$H_\alpha = (1 + z/R_\alpha), \quad H_\beta = (1 + z/R_\beta), \quad H_z = 1 \, . \tag{2.19}$$

where R_α and R_β are the principal radii of curvature of the middle surface. For more details about shell theories, the reader is referred to [16, 21].

The displacement vector in the kth layer is $\boldsymbol{u}^k = \{u, v, w\}^{k\top}$. The differential operator matrix $\mathbf{b}$ and gradient operator ∇ can be introduced:

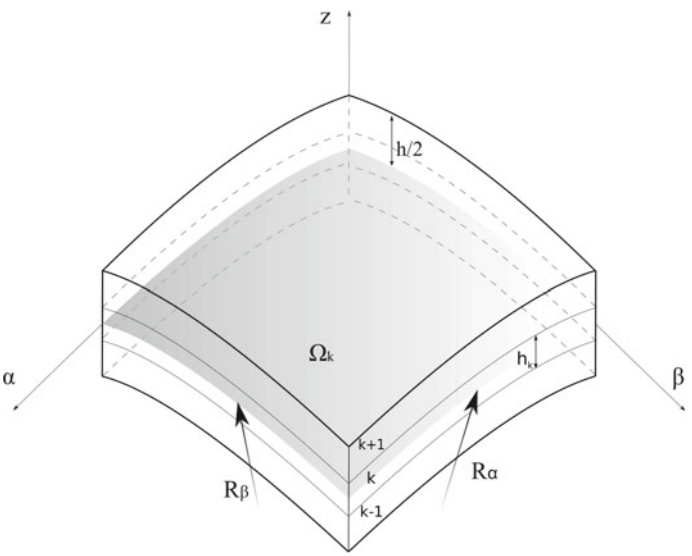

Fig. 2.1 Models for doubly-curved laminated shells

$$\mathbf{b} = \begin{bmatrix} \frac{\partial_\alpha}{H_\alpha} & 0 & \frac{1}{H_\alpha R_\alpha} \\ 0 & \frac{\partial_\beta}{H_\beta} & \frac{1}{H_\beta R_\beta} \\ 0 & 0 & \partial_z \\ \partial_z - \frac{1}{H_\alpha R_\alpha} & 0 & \frac{\partial_\alpha}{H_\alpha} \\ 0 & \partial_z - \frac{1}{H_\beta R_\beta} & \frac{\partial_\beta}{H_\beta} \\ \frac{\partial_\beta}{H_\beta} & \frac{\partial_\alpha}{H_\alpha} & 0 \end{bmatrix} \tag{2.20}$$

$$\nabla = \left[\frac{\partial_\alpha}{H_\alpha}, \frac{\partial_\beta}{H_\beta}, \partial_z \right]^\top \tag{2.21}$$

thus, engineering strain vector $\boldsymbol{\varepsilon}^k = \{\varepsilon_{\alpha\alpha}, \varepsilon_{\beta\beta}, \varepsilon_{zz}, \varepsilon_{\alpha z}, \varepsilon_{\beta z}, \varepsilon_{\alpha\beta}\}^{k\top}$, electric field vector $\boldsymbol{E}^k = \{E_\alpha, E_\beta, E_z\}^{k\top}$, temperature gradient vector $\boldsymbol{\vartheta}^k = \{\vartheta_\alpha, \vartheta_\beta, \vartheta_z\}^{k\top}$, and moisture gradient vector $\boldsymbol{\Upsilon}^k = \{\Upsilon_\alpha, \Upsilon_\beta, \Upsilon_z\}^{k\top}$ can be obtained through:

$$\boldsymbol{\varepsilon}^k = \mathbf{b}\boldsymbol{u}^k \tag{2.22}$$

$$\boldsymbol{E}^k = -\nabla\phi^k \tag{2.23}$$

$$\boldsymbol{\vartheta}^k = -\nabla\theta^k \tag{2.24}$$

$$\boldsymbol{\Upsilon}^k = -\nabla c^k \tag{2.25}$$

It is assumed that the laminae are homogeneous and orthotropic, and the stress vector $\boldsymbol{\sigma}^k = \{\sigma_{\alpha\alpha}, \sigma_{\beta\beta}, \sigma_{zz}, \sigma_{\alpha z}, \sigma_{\beta z}, \sigma_{\alpha\varepsilon_z}\}^{k\top}$, electric displacements vector $\boldsymbol{D}^k = \{D_\alpha, D_\beta, D_z\}^{k\top}$, heat flux vector $\boldsymbol{q}^k = \{q_\alpha, q_\beta, q_z\}^{k\top}$, and moisture flux vector $\boldsymbol{h}^k = \{h_\alpha, h_\beta, h_z\}^{k\top}$ can be expressed through the constitutive relations in matrix form:

$$\boldsymbol{\sigma}^k = \boldsymbol{C}^k\boldsymbol{\varepsilon}^k - \boldsymbol{e}^{k\top}\boldsymbol{E}^k - \boldsymbol{\lambda}^{k\top}\theta^k - \boldsymbol{\psi}^{k\top}c^k \tag{2.26}$$

$$\boldsymbol{D}^k = \boldsymbol{e}^k\boldsymbol{\varepsilon}^k + \boldsymbol{\chi}^k\boldsymbol{E}^k + \boldsymbol{r}^{k\top}\theta^k + \boldsymbol{\iota}^{k\top}c^k \tag{2.27}$$

$$\boldsymbol{q}^k = \boldsymbol{\kappa}^k\boldsymbol{\vartheta}^k + \boldsymbol{\varphi}^k\boldsymbol{\Upsilon}^k \tag{2.28}$$

$$\boldsymbol{h}^k = \boldsymbol{\gamma}^k\boldsymbol{\vartheta}^k + \boldsymbol{\xi}^k\boldsymbol{\Upsilon}^k \tag{2.29}$$

in which the material coefficients matrices used in the problem coordinate system (α, β, z) are obtained by transforming their original forms in the material coordinate system $(1, 2, 3)$ according to the orientation of the kth layer.

2.4 Variable Kinematic Shell Finite Elements

In the framework of CUF, the displacement field in a shell can be assumed to be:

$$\boldsymbol{u}(\alpha, \beta, z) = F_\tau(z)\boldsymbol{u}_\tau(\alpha, \beta) \tag{2.30}$$

in which $\boldsymbol{u}_\tau(\alpha, \beta)$ represents the mid-surface displacement vector, and $F_\tau(z)$ are determined by the theory of shell structures. The repeated index τ implies the application of Einstein's summation convention. When FE discretization is introduced, shape functions $N_i(\alpha, \beta)$ are used to approximate $\boldsymbol{u}_\tau(\alpha, \beta)$, and one gets:

$$\boldsymbol{u}(\alpha, \beta, z) = N_i(\alpha, \beta)F_\tau(z)\boldsymbol{u}_{i\tau} \tag{2.31}$$

where $\boldsymbol{u}_{i\tau}$ are the unknowns to be calculated.

In the CUF framework, both the refinement of shell theories and the enhancement of shape functions can be carried out conveniently. This feature leads to a broad spectrum of variable kinematic FE models.

2.4.1 Refined Theories of Shell Structures

Since $F_\tau(z)$ depends only on the thickness coordinate, they are also referred to as the thickness functions. The highest order of $F_\tau(z)$ can be increased gradually till the expected numerical convergence is reached. The thickness functions for laminated shells can be formulated in two major frameworks, namely the Equivalent-Single Layer (ESL) model and the Layer-Wise (LW) model, as shown in Fig. 2.2.

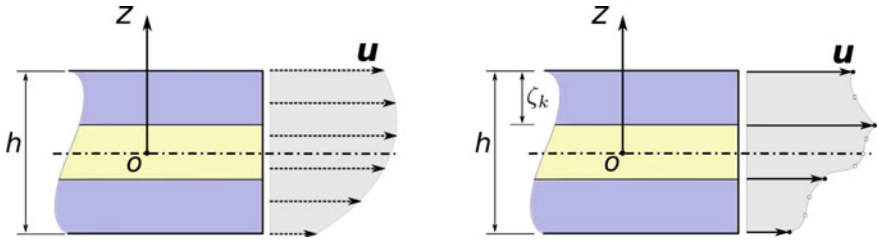

(a) Equivalent Single-Layer (ESL) (b) Layer-Wise (LW)

Fig. 2.2 Two types of models for multi-layered structures

2.4.1.1 ESL Models Based on Various Series Expansions

When generating ESL models, $F_\tau(z)$ is expressed throughout the whole thickness domain of multi-layered shells ($z \in [-\frac{h}{2}, \frac{h}{2}]$, h being the shell thickness), as illustrated in Fig. 2.2a. Taylor expansions (TE) can be utilized to formulate ESL models by taking:

$$F_0 = 1, \quad F_1 = z^1, \quad \ldots, \quad F_\tau = z^\tau, \quad \ldots \tag{2.32}$$

FSDT can be treated as a particular case of the complete linear TE model. TE theories are most commonly used due to their inherent simplicity. Exponential series can be employed by taking $F_\tau = e^{(z\tau/h)}$. Other theories such as trigonometric and hyperbolic series can be implemented accordingly [5, 6, 10].

ESL models cannot guarantee the interfacial continuity of transverse shear stresses. Murakami [20] suggested a zig-zag function as a remedy which reads:

$$F_Z^k(z) = (-1)^k \zeta_k \tag{2.33}$$

This zig-zag term can be appended to the expansions of refined ESL theories to improve the approximation of interfacial connectivity of transverse stresses.

2.4.1.2 LW Models Adopting Polynomial Interpolation Theories

For LW models, the displacements can be assumed to be:

$$\boldsymbol{u}^k(\alpha, \beta, \zeta_k) = F_\tau^k(\zeta_k)\boldsymbol{u}_\tau{}^k(\alpha, \beta) \tag{2.34}$$

where $-1 \leq \zeta_k \leq 1$ is the adimensional thickness coordinate within layer k, as in Fig. 2.2b. When Lagrange polynomial expansions (LE) are used, one has:

$$F_\tau^k(\zeta_k) = \prod_{i=0, i\neq s}^{N} \frac{\zeta_k - \zeta_{k_i}}{\zeta_{k_\tau} - \zeta_{k_i}} \tag{2.35}$$

where ζ_{k_τ} are located at prescribed interpolation points, which are usually equally distributed through the thickness of a layer. $\zeta_{k_0} = -1$ and 1 represent the bottom and the top surfaces of the kth layer, respectively. Legendre and Chebyshev polynomials can also be utilized to construct LW theories, as discussed in [5, 6].

In LW models, to enforce the displacement continuity at layer interfaces, the following constraints should be introduced:

$$\boldsymbol{u}_t{}^k = \boldsymbol{u}_b{}^{k+1}, \qquad k = 1, \ldots, N_l - 1. \tag{2.36}$$

in which N_l is the number of layers. The interfacial continuity of transverse shear stresses is not ensured but can be approximately achieved by refining F_τ^k [6].

2.4.2 Various Finite Element Shape Functions

There are a great variety of shape functions for 2D FEs. The most commonly used elements are quadrilateral Lagrangian elements Q4 (four-node) and Q9 (nine-node). Some researchers also assessed higher-order Lagrangian elements such as Q25, Q49, and Q81. Other 2D shape functions include Hermitian, serendipity, and hierarchical elements, among others.

The p-version hierarchical shape functions [26] have drawn significant attention due to their hierarchical characteristics and high numerical efficiency. When polynomial degree p increases to $p + 1$, only the newly added shape functions and the resulting matrices need to be introduced, and mathematical enrichment can be conveniently performed on the same meshes to improve the solution accuracy. Such shape functions also provide the convenience of geometric mapping through blending functions [26]. Moreover, the shear and membrane locking phenomena can be mitigated through the p-version refinement [25, 26]. An evaluation of hierarchical shell elements in the analysis of laminated structures was reported by Li et al. [18].

2.4.3 Node-Dependent Kinematics

The dependency of thickness functions on the shape functions can be introduced through:

$$\boldsymbol{u}(\alpha, \beta, z) = N_i(\alpha, \beta) F_\tau^i(z) \boldsymbol{u}_{i\tau} \tag{2.37}$$

The difference between Eqs. (2.37) and (2.31) is the additional superscript i, which is the index of the "anchoring node". Equation (2.37) leads to FE models with Node-Dependent Kinematics (NDK). With NDK, shell FE models can be refined locally on specific nodes, and adaptable local kinematic refinement can be performed conveniently. Different nodal kinematics will be blended naturally by the shape functions within the element domain.

A typical application of NDK is the construction of global-local models. In the example shown on the left-hand side of Fig. 2.3, the four-node element possesses different theories on its four nodes. A series of such elements form a kinematic transition zone Ω_r, which bridges the locally refined region Ω_β to the less refined outlying area Ω_α. Global-local models can be constructed conveniently without modifying the mesh grid, and the same FE meshes can be re-used to build a family of models for concurrent global-local analyses, as discussed in [17, 29].

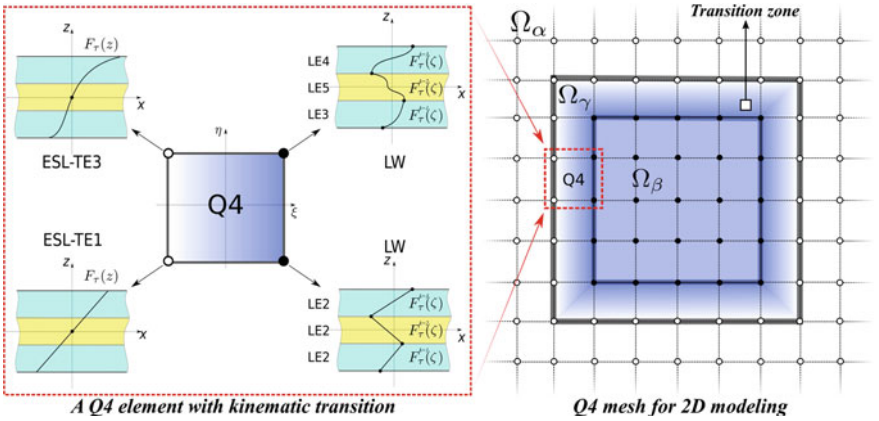

Fig. 2.3 Four-node Lagrangian finite element (Q4) model with Node-Dependent Kinematics

2.5 Weak-Form Governing Equations

For a unit volume in the kth layer in a shell element, by applying the principle of virtual displacements one has:

$$\delta E_p = \delta W \tag{2.38}$$

in which

$$\delta E_p = \int_V (\boldsymbol{\sigma}^{k\top} \delta \boldsymbol{\varepsilon}^k - \boldsymbol{D}^{k\top} \delta \boldsymbol{E}^k - \boldsymbol{q}^{k\top} \delta \boldsymbol{\vartheta}^k - \boldsymbol{h}^{k\top} \delta \boldsymbol{\Upsilon}^k) dV \tag{2.39}$$

$$\delta W = \int_\Gamma (\delta \boldsymbol{u}^{k\top} \bar{\boldsymbol{p}} + \delta \phi^k \, \bar{D}_n + \delta \theta^k \, \bar{q}_n + \delta c^k \, \bar{h}_n) \, d\Gamma \tag{2.40}$$

In the above equations, E_p represents the potential energy, W the external work, $\boldsymbol{p}$ the surface traction vector, D_n the surface charge per unit area, q_n the normal heat flux, and h_n the normal moisture flux. In static cases, the inertial work is discarded.

The approximations of the primary variables are:

$$\boldsymbol{u}^k = N_i \, F_\tau^{ik} \boldsymbol{u}_{i\tau}^{(k)}, \qquad \delta \boldsymbol{u}^k = N_j \, F_s^{jk} \delta \boldsymbol{u}_{js}^{(k)}. \tag{2.41}$$

$$\phi^k = N_i \, F_\tau^{ik} \phi_{i\tau}^{(k)}, \qquad \delta \phi^k = N_j \, F_s^{jk} \delta \phi_{js}^{(k)}. \tag{2.42}$$

$$\theta^k = N_i \, F_\tau^{ik} \theta_{i\tau}^{(k)}, \qquad \delta \theta^k = N_j \, F_s^{jk} \delta \theta_{js}^{(k)}. \tag{2.43}$$

$$c^k = N_i \, F_\tau^{ik} c_{i\tau}^{(k)}, \qquad \delta c^k = N_j \, F_s^{jk} \delta c_{js}^{(k)}. \tag{2.44}$$

in which for ESL models $\boldsymbol{u}_{i\tau}^{(k)} = \boldsymbol{u}_{i\tau}$, and for LW models $\boldsymbol{u}_{i\tau}^{(k)} = \boldsymbol{u}_{i\tau}^{k}$. The same rule also applies to the other variables. The essential boundary conditions are considered through:

$$\begin{aligned} N_i\, F_\tau^{i\,k}\, \bar{\boldsymbol{u}}_{i\tau}^{(k)} &= \overline{\boldsymbol{u}} \quad \text{on } \Gamma_{\boldsymbol{u}}, & N_i\, F_\tau^{i\,k}\, \bar{\phi}_{i\tau}^{(k)} &= \overline{\phi} \quad \text{on } \Gamma_{\phi}, \\ N_i\, F_\tau^{i\,k}\, \bar{\theta}_{i\tau}^{(k)} &= \overline{\theta} \quad \text{on } \Gamma_{\theta}, & N_i\, F_\tau^{i\,k}\, \bar{c}_{i\tau}^{(k)} &= \overline{c} \quad \text{on } \Gamma_{c}. \end{aligned} \tag{2.45}$$

By considering the above approximations, the gradient equations Eqs. (2.22)–(2.25) and the constitutive relations Eqs. (2.26)–(2.29), Eq. (2.38) can be written into:

$$\begin{aligned} \delta \boldsymbol{u}_{js}^{(k)\top}: \quad & \boldsymbol{K}_{ij\tau s}^{\boldsymbol{uu}\;k}\boldsymbol{u}_{i\tau}^{(k)} + \boldsymbol{K}_{ij\tau s}^{\boldsymbol{u}\phi\;k}\phi_{i\tau}^{(k)} + \boldsymbol{K}_{ij\tau s}^{\boldsymbol{u}\theta\;k}\theta_{i\tau}^{(k)} + \boldsymbol{K}_{ij\tau s}^{\boldsymbol{u}c\;k}c_{i\tau}^{(k)} = \boldsymbol{P}_{js}^{\boldsymbol{u}\;k} \\ \delta \phi_{js}^{(k)}: \quad & \boldsymbol{K}_{ij\tau s}^{\phi\boldsymbol{u}\;k}\boldsymbol{u}_{i\tau}^{(k)} + K_{ij\tau s}^{\phi\phi\;k}\phi_{i\tau}^{(k)} + K_{ij\tau s}^{\phi\theta\;k}\theta_{i\tau}^{(k)} + K_{ij\tau s}^{\phi c\;k}c_{i\tau}^{(k)} = P_{js}^{\phi\;k} \\ \delta \theta_{js}^{(k)}: \quad & K_{ij\tau s}^{\theta\theta\;k}\theta_{i\tau}^{(k)} + K_{ij\tau s}^{\theta c\;k}c_{i\tau}^{(k)} = P_{js}^{\theta\;k} \\ \delta c_{js}^{(k)}: \quad & K_{ij\tau s}^{c\theta\;k}\theta_{i\tau}^{(k)} + K_{ij\tau s}^{cc\;k}c_{i\tau}^{(k)} = P_{js}^{c\;k} \end{aligned} \tag{2.46}$$

where the *fundamental nuclei* (FNs) of the generalized stiffness matrices are:

$$\boldsymbol{K}_{ij\tau s}^{\boldsymbol{uu}\;k} = \int_{\Omega}\int_{A^k} (\mathbf{b}N_j F_s^{j\,k})^{\top} \boldsymbol{C}^k (\mathbf{b}N_i F_\tau^{i\,k}) H_\alpha H_\beta dz^k d\Omega \tag{2.47}$$

$$\boldsymbol{K}_{ij\tau s}^{\boldsymbol{u}\phi\;k} = \int_{\Omega}\int_{A^k} (\mathbf{b}N_j F_s^{j\,k})^{\top} \boldsymbol{e}^{k\top} (\nabla N_i F_\tau^{i\,k}) H_\alpha H_\beta dz^k d\Omega \tag{2.48}$$

$$\boldsymbol{K}_{ij\tau s}^{\phi\boldsymbol{u}\;k} = \int_{\Omega}\int_{A^k} (\nabla N_j F_s^{j\,k})^{\top} \boldsymbol{e}^{k} (\mathbf{b}N_i F_\tau^{i\,k}) H_\alpha H_\beta dz^k d\Omega \tag{2.49}$$

$$K_{ij\tau s}^{\phi\phi\;k} = -\int_{\Omega}\int_{A^k} (\nabla N_j F_s^{j\,k})^{\top} \boldsymbol{\chi}^k (\nabla N_i F_\tau^{i\,k}) H_\alpha H_\beta dz^k d\Omega \tag{2.50}$$

$$\boldsymbol{K}_{ij\tau s}^{\boldsymbol{u}\theta\;k} = -\int_{\Omega}\int_{A^k} (\mathbf{b}N_j F_s^{j\,k})^{\top} \boldsymbol{\lambda}^{k\top} (N_i F_\tau^{i\,k}) H_\alpha H_\beta dz^k d\Omega \tag{2.51}$$

$$\boldsymbol{K}_{ij\tau s}^{\boldsymbol{u}c\;k} = -\int_{\Omega}\int_{A^k} (\mathbf{b}N_j F_s^{j\,k})^{\top} \boldsymbol{\Psi}^{k\top} (N_i F_\tau^{i\,k}) H_\alpha H_\beta dz^k d\Omega \tag{2.52}$$

$$K_{ij\tau s}^{\phi\theta\;k} = \int_{\Omega}\int_{A^k} (\nabla N_j F_s^{j\,k})^{\top} \boldsymbol{r}^{k\top} (N_i F_\tau^{i\,k}) H_\alpha H_\beta dz^k d\Omega \tag{2.53}$$

$$K_{ij\tau s}^{\phi c\;k} = \int_{\Omega}\int_{A^k} (\nabla N_j F_s^{j\,k})^{\top} \boldsymbol{\iota}^{k\top} (N_i F_\tau^{i\,k}) H_\alpha H_\beta dz^k d\Omega \tag{2.54}$$

$$K_{ij\tau s}^{\theta\theta\;k} = -\int_{\Omega}\int_{A^k} (\nabla N_j F_s^{j\,k})^{\top} \boldsymbol{\kappa}^k (\nabla N_i F_\tau^{i\,k}) H_\alpha H_\beta dz^k d\Omega \tag{2.55}$$

$$K_{ij\tau s}^{\theta c\ k} = -\int_{\Omega}\int_{A^k} (\nabla N_j F_s^{j\,k})^{\top} \boldsymbol{\varphi}^k (\nabla N_i F_\tau^{i\,k}) H_\alpha H_\beta dz^k d\Omega \tag{2.56}$$

$$K_{ij\tau s}^{c\theta\ k} = -\int_{\Omega}\int_{A^k} (\nabla N_j F_s^{j\,k})^{\top} \boldsymbol{\gamma}^k (\nabla N_i F_\tau^{i\,k}) H_\alpha H_\beta dz^k d\Omega \tag{2.57}$$

$$K_{ij\tau s}^{cc\ k} = -\int_{\Omega}\int_{A^k} (\nabla N_j F_s^{j\,k})^{\top} \boldsymbol{\xi}^k (\nabla N_i F_\tau^{i\,k}) H_\alpha H_\beta dz^k d\Omega \tag{2.58}$$

The explicit expressions of $\boldsymbol{K}_{ij\tau s}^{\boldsymbol{uu}}$ can be found in [17].

FNs of loads accounting for both natural and essential boundary conditions read:

$$\boldsymbol{P}_{js}^{\boldsymbol{u}\,k} = \int_{\Gamma_p} N_j F_s \bar{\boldsymbol{p}} d\Gamma - \boldsymbol{K}_{ij\tau s}^{\boldsymbol{uu}\ k} \bar{\boldsymbol{u}}_{i\tau}^{(k)} - \boldsymbol{K}_{ij\tau s}^{\boldsymbol{u}\phi\ k} \bar{\phi}_{i\tau}^{(k)} - \boldsymbol{K}_{ij\tau s}^{\boldsymbol{u}\theta\ k} \bar{\theta}_{i\tau}^{(k)} - \boldsymbol{K}_{ij\tau s}^{\boldsymbol{u}c\ k} \bar{c}_{i\tau}^{(k)} \tag{2.59}$$

$$P_{js}^{\phi\,k} = \int_{\Gamma_D} N_j F_s \bar{D}_n d\Gamma - \boldsymbol{K}_{ij\tau s}^{\boldsymbol{\phi u}\ k} \bar{\boldsymbol{u}}_{i\tau}^{(k)} - K_{ij\tau s}^{\phi\phi\ k} \bar{\phi}_{i\tau}^{(k)} - K_{ij\tau s}^{\phi\theta\ k} \bar{\theta}_{i\tau}^{(k)} - K_{ij\tau s}^{\phi c\ k} \bar{c}_{i\tau}^{(k)} \tag{2.60}$$

$$P_{js}^{\theta\,k} = \int_{\Gamma_q} N_j F_s \bar{q}_n d\Gamma - K_{ij\tau s}^{\theta\theta\ k} \bar{\theta}_{i\tau}^{(k)} - K_{ij\tau s}^{\theta c\ k} \bar{c}_{i\tau}^{(k)} \tag{2.61}$$

$$P_{js}^{c\,k} = \int_{\Gamma_h} N_j F_s \bar{h}_n d\Gamma - K_{ij\tau s}^{c\theta\ k} \bar{\theta}_{i\tau}^{(k)} - K_{ij\tau s}^{cc\ k} \bar{c}_{i\tau}^{(k)} \tag{2.62}$$

Note that the above boundary conditions should be considered at their corresponding external sub-surfaces.

FNs are core units of the stiffness matrix and load vector. By looping on the subscripts of FNs, the full stiffness matrix and load vector can be assembled step by step. For a detailed description of the assembly technique, one is referred to the works of Carrera et al. [7] and Zappino et al. [29].

In displacement-based FE models, the equilibrium equations (see Eq. 2.13), stress-free boundary conditions, and interfacial continuity of stresses are not satisfied rigorously but approximately. Better satisfaction of these requirements can be approached through the enrichment of FE models. The use of FNs facilitate the mathematical refinements on both shape functions and thickness functions in shell FE models.

Besides the piezoelectric effects, the steady-state thermal conduction and moisture diffusion are accounted for in the presented formulations. Some particular cases include partially coupled thermo-mechanical, hygro-mechanical, and fully coupled electro-mechanical models.

2.6 Selected Numerical Examples

This section includes two examples demonstrating hygro-mechanical and electro-mechanical simulations, respectively.

2.6.1 Hygro-Mechanical Modeling

Two-layered composite cylindrical panels with lamination sequence (0°/90°) (from bottom to top) under hygroscopic load are studied. The cylindrical panels have arch length $a = 0.1\,\text{m}$, axial length $b = 0.1\,\text{m}$, and mid-surface radii $R_\alpha = 0.1\,\text{m}$ and $R_\beta = \infty$. Radius-to-thickness ratios $R_\alpha/h = 2$ and 500 are considered. The mechanical properties of the lamina are listed in Table 2.1, moisture expansion and diffusivity coefficients in Table 2.2. The panels are simply supported on their four edges. The moisture concentration on the external surfaces reads:

$$\bar{c}(\alpha, \beta, z) = \bar{c}_A(z) \sin(\frac{\pi\alpha}{a}) \sin(\frac{\pi\beta}{b}) \tag{2.63}$$

where $\bar{c}_A(\frac{h}{2}) = 1.0\%$, $\bar{c}_A(-\frac{h}{2}) = 0\%$. Note that the moisture concentration is measured regarding percent weight of moisture absorption over the dry material.

The adopted elements are MITC9 (nine-node Lagrangian element with Mixed Interpolation of Tensorial Components, Bathe et al. [2]). 10×10 rectangular shell elements are used to model 1/4 of the shell with the help of symmetric boundary conditions. The reference results are obtained through Navier-type closed-form analytical solution with fourth-order LE theory in LW approach. Two types of refined ESL models are assessed, namely the nth-order kinematics TEn, and miscellaneous assumptions combining a first-order model with trigonometric series that read:

$$\begin{aligned} \boldsymbol{u} = \boldsymbol{u}_0 + z\boldsymbol{u}_1 + \sin\left(\frac{\pi z}{h}\right)\boldsymbol{u}_2 + \cos\left(\frac{\pi z}{h}\right)\boldsymbol{u}_3 + \sin\left(\frac{2\pi z}{h}\right)\boldsymbol{u}_4 \\ + \cos\left(\frac{2\pi z}{h}\right)\boldsymbol{u}_5 + \cdots + (-1)\zeta_k \boldsymbol{u}_N^k \end{aligned} \tag{2.64}$$

Table 2.1 Mechanical properties of T300/5208 lamina

E_1(GPa)	E_2, E_3(GPa)	G_{12}, G_{13}(GPa)	G_{23}(GPa)	ν_{12}, ν_{13}	ν_{23}
181	10.3	7.17	2.39	0.28	0.43

Table 2.2 Hygroscopic properties of T300/5208 lamina [27]

β_{11} (wt.%H_2O)$^{-1}$	β_{22}, β_{33} (wt.%H_2O)$^{-1}$	ξ_{11} (mm^2/s)	ξ_{22}, ξ_{33} (mm^2/s)
0	0.006	2.87×10^{-8}	1.63×10^{-8}

Table 2.3 Displacement and stress evaluation of the cylindrical panels under hygroscopic load

R_α/h	Kinematics	$w/10^{-3}$mm $(\frac{a}{2}, \frac{b}{2}, \frac{h}{2})$	$\sigma_{\alpha\alpha}$/MPa $(\frac{a}{2}, \frac{b}{2}, \frac{h}{2})$	$\sigma_{\alpha\beta}$/MPa $(a, b, \frac{h}{2})$	$\sigma_{\alpha z}$/MPa $(a, \frac{b}{2}, \frac{h}{4})$
2	FSDT	34.14	−75.38	−15.74	1.215
	T11Z	113.9	−30.96	−20.40	2.214
	T1S5C5Z	113.9	−30.94	−20.40	2.251
	Analytical	113.21	−31.009	−20.209	2.4303
500	FSDT	76.64	−90.10	0.1480	0.05690
	T7Z	43.36	−58.80	0.09777	0.08071
	T1S3C3Z	43.36	−58.93	0.09777	0.08036
	Analytical	43.359	−58.808	0.097332	0.080387

and such models are denoted by T1SnCnZ, wherein n is the number of sinusoidal/co-sinusoidal terms, and Z indicates the use of Murakami's zig-zag term. In the numerical analysis, the number of expansions is increased until the relative difference between ESL models with n and $n-1$ is less than 5%. FSDT is also tested. The obtained results are summarized in Table 2.3. It can be observed that FSDT fails to provide an accurate estimation, while the refined ESL assumptions lead to results in high agreement with the analytical solutions.

2.6.2 Electro-Mechanical Modeling

A two-layered cross-ply square laminated plate with PZT-4 piezoelectric layers bonded to the top and bottom surfaces is considered. Both actuator and sensor cases are studied. The length, width, and total thickness of the plate are a, b, and h, separately. The material properties of the laminae and piezoelectric layers, and analytical solutions can be found in [13].

In the current work, the structure is modeled with a single-element model employing eighth-order p-version shape functions and fourth-order LE thickness functions in each layer. Specially, in the actuator case, to obtain the weighting coefficients $\bar{\phi}^k_{i\tau}$ (see Eq. 2.45) that satisfy the bi-sinusoidal electric potential boundary condition on the top surface ($k=4$, $z=\frac{h}{2}$), linear least squares fitting is adopted.

The obtained solutions are summarized in Table 2.4 and Fig. 2.4. For both actuation and sensing mechanisms, most of the results agree well with the reference solutions. Exceptionally, the obtained ϕ in the sensor case is close to that given by D'Ottavio and Kröplin [12] and Carrera et al. [4] but is about one-tenth of the solution provided by Heyliger [13]. This might be caused by the dimensionalization factors as commented by D'Ottavio and Kröplin [12].

Table 2.4 Numerical evaluation of the laminated plate with two piezoelectric layers

Mesh	N_i	F_τ	Actuator			Sensor		
			$u \times 10^{12}$ $(0, \frac{b}{2}, \frac{h}{2})$	ϕ $(\frac{a}{2}, \frac{b}{2}, 0)$	$\sigma_{zz} \times 10^3$ $(\frac{a}{2}, \frac{b}{2}, 0)$	$u \times 10^{12}$ $(0, \frac{b}{2}, \frac{h}{2})$	$\phi \times 10$ $(\frac{a}{2}, \frac{b}{2}, 0)$	$D_z \times 10^{13}$ $(\frac{a}{2}, \frac{b}{2}, \frac{h}{2})$
1×1	$p = 8$	LE4	−32.704	0.4477	−14.782	−47.620	0.0601	161.66
Heyliger [13]			−32.764	0.4476	−14.612	−47.549	0.611	160.58
D'Ottavio and Kröplin [12]			–	–	–	–	0.0611	160.67
Carrera et al. [4]			–	0.4473	−14.612	–	0.0611	160.58

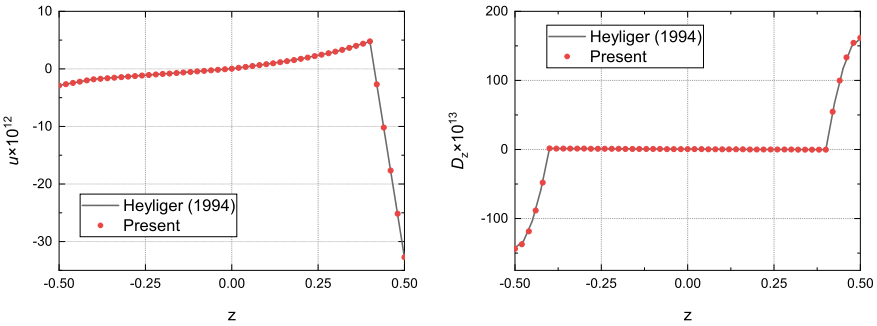

(a) Actuator case, $u(0, \frac{b}{2}, z) \times 10^{12}$ (b) Sensor case, $D_z(\frac{a}{2}, \frac{b}{2}, z) \times 10^{13}$

Fig. 2.4 Through-the-thickness variation of in-plane displacement (actuator case) and transverse electric displacement (sensor case) of the laminated plate with piezoelectric layers

References

1. Altay G, Dökmeci MC (2008) Certain hygrothermopiezoelectric multi-field variational principles for smart elastic laminae. Mech Adv Mater Struct 15(1):21–32
2. Bucalem ML, Bathe KJ (1993) Higher-order MITC general shell elements. Int J Numer Methods Eng 36(21):3729–3754
3. Carrera E (2002) Theories and finite elements for multilayered, anisotropic, composite plates and shells. Arch Comput Methods Eng 9(2):87–140
4. Carrera E, Büttner A, Nali P (2010) Mixed elements for the analysis of anisotropic multilayered piezoelectric plates. J Intell Mater Syst Struct 21(7):701–717
5. Carrera E, Cinefra M, Li G (2018) Refined finite element solutions for anisotropic laminated plates. Compos Struct 183:63–76
6. Carrera E, Cinefra M, Li G, Kulikov GM (2016) MITC9 shell finite elements with miscellaneous through-the-thickness functions for the analysis of laminated structures. Compos Struct 154:360–373
7. Carrera E, Cinefra M, Petrolo M, Zappino E (2014) Finite element analysis of structures through Unified Formulation. Wiley, New Jersey
8. Carrera E, Fagiano C (2007) Mixed piezoelectric plate elements with continuous transverse electric displacements. J Mech Mater Struct 2(3):421–438
9. Carrera E, Robaldo A (2010) Hierarchic finite elements based on a unified formulation for the static analysis of shear actuated multilayered piezoelectric plates. Multidiscip Model Mater Struct 6(1):45–77

10. Cinefra M, Petrolo M, Li G, Carrera E (2017) Variable kinematic shell elements for composite laminates accounting for hygrothermal effects. J Therm Stress 40(12):1523–1544
11. Dökmeci M (1973) Variational principles in piezoelectricity. Lettere al Nuovo Cimento (1971–1985) 7(11):449–454
12. D'Ottavio M, Kröplin B (2006) An extension of Reissner mixed variational theorem to piezoelectric laminates. Mech Adv Mater Struct 13(2):139–150
13. Heyliger P (1994) Static behavior of laminated elastic/piezoelectric plates. AIAA J 32(12):2481–2484
14. Ikeda T (1996) Fundamentals of piezoelectricity. Oxford University Press, Oxford
15. Koiter W (1970) On the foundations of the linear theory of thin elastic shell. Proc Kon Nederl Akad Wetensch 73(3):169–195
16. Leissa AW (1973) Vibration of shells, vol 288. Scientific and Technical Information Office, National Aeronautics and Space Administration Washington
17. Li G, Carrera E, Cinefra M, de Miguel A, Pagani A, Zappino E (2019) An adaptable refinement approach for shell finite element models based on node-dependent kinematics. Compos Struct 210:1–19
18. Li G, Carrera E, Cinefra M, de Miguel A, Kulikov GM, Pagani A, Zappino E (2019) Evaluation of locking in refined hierarchical shell finite elements for laminated structures. Advanced modeling and simulation in engineering sciences. Accepted manuscript
19. Mindlin RD (1951) Influence of rotatory inertia and shear on flexural motions of isotropic, elastic plates. J Appl Mech 18:31–38
20. Murakami H (1986) Laminated composite plate theory with improved in-plane responses. J Appl Mech 53(3):661–666
21. Reddy J (2004) Mechanics of laminated composite plates and shells: theory and analysis. CRC Press, Boca Raton
22. Reissner E (1945) The effect of transverse shear deformation on the bending of elastic plates. J Appl Mech A69–A77
23. Sih GC, Michopoulos J, Chou SC (2012) Hygrothermoelasticity. Springer Science & Business Media, Berlin
24. Sung C, Thompson B (1987) A variational principle for the hygrothermoelastodynamic analysis of mechanism systems. J Mech, Transm, Autom Des 109(3):294–300
25. Suri M (1996) Analytical and computational assessment of locking in the hp finite element method. Comput Methods Appl Mech Eng 133(3–4):347–371
26. Szabó B, Düster A, Rank E (2004) The p-version of the finite element method. Wiley Online Library, New Jersey
27. Tsai SW (1988) Composites design, vol 5. Think composites, Dayton
28. Smittakorn W, Heyliger PR (2000) A discrete-layer model of laminated hygrothermopiezoelectric plates. Mech Compos Mater Struct 7(1):79–104
29. Zappino E, Li G, Pagani A, Carrera E (2017) Global-local analysis of laminated plates by node-dependent kinematic finite elements with variable ESL/LW capabilities. Compos Struct 172:1–14
30. Zappino E, Li G, Pagani A, Carrera E, de Miguel AG (2018) Use of higher-order Legendre polynomials for multilayered plate elements with node-dependent kinematics. Compos Struct 202:222–232

Chapter 3
Bistable Buckled Beam-Like Structures by One-Dimensional Hierarchical Modeling

G. De Pietro, G. Giunta, S. Belouettar and E. Carrera

Abstract In the last few years, great interest has been shown in harnessing bistability, or more generally multistability, as a source of energy and motion in engineering applications, both at micro-scale (such as switches, relays, valves or pumps) and macro-scale (shape-changing aerodynamic panels, variable geometry engine exhausts and reconfigurable airplane wings). Bistability is a highly non-linear phenomenon relying on the snap-through buckling, an elastic instability in which a structure passes from one equilibrium configuration to another nonadjacent equilibrium state by means of a sudden displacement jump. The theoretical understanding of such phenomenon plays a key role in the structural design optimization for practical applications. To this aim, the development of accurate yet efficient computational models for the analysis of bistable composite structures represents an important and up-to-date research topic. This chapter addresses the development of a hierarchical framework based on the Carrera Unified Formulation that allows the derivation of several kinematic models by arbitrarily setting the polynomial order approximation of the displacement field. The proposed approach is assessed towards reference and commercial software finite elements solutions for the analysis of bistable buckled beam-like structures, showing the capability of accurately yet efficiently predicting stable configurations, snap-through load, force-displacement curves and stress evolution in the geometrically non-linear regime.

G. De Pietro · G. Giunta (✉) · S. Belouettar
Luxembourg Institute of Science and Technology, Esch-sur-Alzette, Luxembourg
e-mail: gaetano.giunta@list.lu

E. Carrera
MUL2 Group, Department of Mechanical and Aerospace Engineering, Politecnico di Torino, Torino, Italy

M. Petrolo (ed.), *Advances in Predictive Models and Methodologies for Numerically Efficient Linear and Nonlinear Analysis of Composites*, PoliTO Springer Series,
https://doi.org/10.1007/978-3-030-11969-0_3

3.1 Introduction

In this chapter, a computationally efficient hierarchical framework for the modeling of mechanically bistable beam-like structures is presented. Such particular kind of structures can be obtained by properly designing the geometry, material, boundary and loading conditions of a precompressed buckled beam. From the buckled configuration, a snap-instability phenomenon can be triggered by means of an appropriate transverse load, allowing the beam structure to switch from one structural stable configuration to another. A number of engineering applications harnessing the bistable beam structures has been recently proposed in the literature, including energy harvesters [21], actuators [15] and shape-adaptive structures [1]. Especially in the design of lightweight morphing applications, the use of composite materials is particularly beneficial, due to their optimal stiffness-to-weight and strength-to-weight ratios as well as their property tailoring capability. On the other hand, such advantages in terms of structural performance and design flexibility come with a greater modeling complexity. Therefore, in order to fully exploit the capabilities of such structures in industrial applications, reliable and computationally efficient models able to describe the complex kinematics of composites and deal with strong geometrical non-linearities such as those involved in post-buckling and snap-through behaviors are needed. In this respect, majority of prior research either adopted modeling approaches based on classical structural theories (the Euler–Bernoulli or Timoshenko kinematics) and mode superposition method or resorted to the use of computationally expensive 2D and 3D commercial software finite elements. Vangbo [20] investigated the influence of bending and compression energy in the snap-through of a doubly-clamped beam as well as the influence of an additional central constraint along the beam axis to prevent twisting during the snap. Based on [20], the influence of the ratio of initial deflection to beam thickness for the force-displacement relation in a stress-free bistable compliant micromechanism was studied by Qiu et al. [17]. The mechanism was fabricated using deep-reactive ion etching and predictions provided by the analytical solution showed a good agreement with the experimental tests. Beharic et al. [5] studied the bistability of a buckled beam for different supporting angles of the clamped edges, using MEMS for flexible and stretchable supports. A compressed doubly-clamped bistable buckled beam actuated by a pure moment load was studied in Cleary and Su [9]. In the analytical solution, the deformed shape of the buckled beam was considered to be a combination of only the first two Euler–Bernoulli's buckling modes, since, for the analyzed cases, they could provide a fairly accurate prediction of the actuation load. Camescasse et al. [6] proposed an elastica model for a simply supported bistable buckled beam subject to a transverse force, where large displacements and finite strains were accounted for. Governing equations were derived from the principle of virtual work and they were solved via a shooting numerical method in combination with a predictor-corrector scheme. The actuation force required for snapping, its optimal location, as well as the influence of the initial compression and beam extensibility parameter were investigated. An analytical

model based on Euler–Bernoulli's theory and first mode shape was adopted in Xu et al. [21] for the design of bistable buckled simply supported piezoelectric beams for broadband energy harvesting in the framework of self-power MEMS. Pontecorvo et al. [16] proposed a novel application concept of bistable arch elements embedded in honeycomb cellular structures for the morphing of a rotor blade. The authors studied the effects of slenderness ratio, initial deflection and spring stiffness on the bistability of cosine-shaped clamped arch restrained by a spring at one end. Classical beam and shell finite elements solution were compared with experimental tests.

In the next section, a family of advanced one-dimensional models based on the Carrera Unified Formulation (CUF) in the framework of an equivalent single layer approach is proposed for studying bistable beam structures. The CUF approach allows the derivation of several kinematic models, since the variation of the displacement field along the beam thickness is approximated by some general through-the-thickness functions which, in this work, are Maclaurin's polynomials of an arbitrary order N, which represents an input parameter of the analysis [7, 12, 13]. Locking phenomena are tackled by Mixed Interpolation of the Tensorial Components (MITC). Geometrical non-linearities in the Green–Lagrange sense are accounted for, since large displacements capabilities are essential for the prediction of the post-buckling behavior as well as for the snap-through analysis in bistable structures. A path-following technique based on the Asymptotic Numerical Method (ANM) is adopted as non-linear solver. In Sect. 3.3, the numerical results provided via the proposed formulation for the prediction of load-displacement curves, snap-through load, stable geometries and stress evolution in bistability analysis of prebuckled beam structures are presented, showing that a higher-order cross-sectional kinematics is required for an accurate prediction when dealing with moderately thick structures as well as for an accurate stress prediction in composite materials. For these reasons, CUF-based one-dimensional advanced models could represent an efficient alternative to state of the art solutions as implemented within commercial software finite elements for the analysis and design of multi-stable composite structures.

3.2 Geometrically Non-linear Hierarchical Models

3.2.1 Geometrical and Constitutive Equations

The initial geometry of the beam is defined by the length of its axis L, thickness h and width b. A two dimensional approach with a fixed Cartesian reference system is adopted, being the x coordinate coincident with the axis of the beam structure and bounded such that $0 \leq x \leq L$, whereas the z coordinate is the through-the-thickness transverse direction, ranging from $-h/2$ to $h/2$. The generic two-dimensional displacement field is:

$$\mathbf{u}^T(x,z) = \left\{ u(x,z)\ w(x,z) \right\} \tag{3.1}$$

u and w are the displacement components along the x- and z-axis, respectively, whereas the superscript 'T' represents the transposition operator. Let us introduce, for the sake of convenience, the displacements gradient vector $\boldsymbol{\theta}$:

$$\boldsymbol{\theta} = \left\{ u_{,x}\ u_{,z}\ w_{,x}\ w_{,z} \right\} \tag{3.2}$$

where the subscripts 'x' and 'z' preceded by comma represent the derivative versus that coordinate.

In order to account for large displacements and rotations, a full geometrical non-linearity based on Green–Lagrange strain-displacement relations is considered. The strain vector $\mathbf{E}$ is given by:

$$\mathbf{E}^T = \left\{ E_{xx}\ E_{zz}\ E_{xz} \right\} \tag{3.3}$$

where:

$$\begin{aligned} E_{xx} &= u_{,x} + \frac{1}{2}\left(u_{,x}^2 + w_{,x}^2\right) \\ E_{zz} &= w_{,z} + \frac{1}{2}\left(u_{,z}^2 + w_{,z}^2\right) \\ E_{xz} &= u_{,z} + w_{,x} + u_{,x}u_{,z} + w_{,x}w_{,z} \end{aligned} \tag{3.4}$$

The matrix form of Eq. (3.4) is:

$$\mathbf{E} = \left[\mathbf{H} + \frac{1}{2}\mathbf{A}(\boldsymbol{\theta})\right]\boldsymbol{\theta} \tag{3.5}$$

being:

$$\mathbf{H} = \begin{bmatrix} 1 & 0 & 0 & 0 \\ 0 & 0 & 0 & 1 \\ 0 & 1 & 1 & 0 \end{bmatrix} \tag{3.6}$$

$$\mathbf{A}(\boldsymbol{\theta}) = \begin{bmatrix} u_{,x} & 0 & w_{,x} & 0 \\ 0 & u_{,z} & 0 & w_{,z} \\ u_{,z} & u_{,x} & w_{,z} & w_{,x} \end{bmatrix} \tag{3.7}$$

By applying the virtual variation operator δ to Eq. (3.5), it can be shown that the virtual variation of the strain vector becomes, see Crisfield [11]:

$$\delta\mathbf{E} = \delta\left\{\left[\mathbf{H} + \frac{1}{2}\mathbf{A}(\boldsymbol{\theta})\right]\boldsymbol{\theta}\right\} = \left[\mathbf{H} + \mathbf{A}(\boldsymbol{\theta})\right]\delta\boldsymbol{\theta} \tag{3.8}$$

A linear elastic stress-strain relation is considered, therefore, the small strains hypothesis is assumed:

$$\mathbf{S} = \mathbf{Q}\mathbf{E} \tag{3.9}$$

being $\mathbf{S}$ the vectorial form of second Piola–Kirchhoff's stresses:

$$\mathbf{S}^T = \left\{ S_{xx} \;\; S_{zz} \;\; S_{xz} \right\} \tag{3.10}$$

In the framework of a plane stress analysis, the reduced material stiffness matrix $\mathbf{Q}$, in the generic case of an anisotropic material, reads:

$$\mathbf{Q} = \begin{bmatrix} Q_{11} & Q_{13} & Q_{15} \\ Q_{13} & Q_{33} & Q_{35} \\ Q_{15} & Q_{35} & Q_{55} \end{bmatrix} \tag{3.11}$$

For the sake of brevity, coefficients Q_{ij} are not reported here and can be found in Reddy [18]. By means of the Principle of Virtual Displacement, the governing equations can be obtained:

$$\delta\mathscr{L} = \delta\mathscr{L}_{int} - \delta\mathscr{L}_{ext} = 0 \tag{3.12}$$

where $\mathscr{L}$ is the total work, $\mathscr{L}_{int}$ the internal work and $\mathscr{L}_{ext}$ is the work done by the external forces. In the framework of a total Lagrangian formulation, the internal work can be written as the following integral over the volume of the reference undeformed configuration V_0:

$$\delta\mathscr{L}_{int} = \int_{V_0} \delta\mathbf{E}^T \mathbf{S} dV \tag{3.13}$$

An infinitesimal variation of the virtual internal work reads:

$$d\left(\delta\mathscr{L}_{int}\right) = \int_{V_0} \left[\delta\mathbf{E}^T d\mathbf{S} + d\left(\delta\mathbf{E}^T\right)\mathbf{S}\right] dV \tag{3.14}$$

which can be rearranged after few manipulations, see Crisfield [11], in the following manner:

$$d\left(\delta\mathscr{L}_{int}\right) = \int_{V_0} \left[\delta\mathbf{E}^T \mathbf{Q} d\mathbf{E} + \delta\boldsymbol{\theta}^T \hat{\mathbf{S}} d\boldsymbol{\theta}\right] dV \tag{3.15}$$

being $\hat{\mathbf{S}} \in \mathbb{R}^{4\times4}$:

$$\hat{\mathbf{S}} = \begin{bmatrix} S_{xx} & S_{xz} & 0 & 0 \\ S_{xz} & S_{zz} & 0 & 0 \\ 0 & 0 & S_{xx} & S_{xz} \\ 0 & 0 & S_{xz} & S_{zz} \end{bmatrix} \tag{3.16}$$

Finally, the virtual variation of the internal work is written in terms of the actual and virtual variation of the gradient vector:

$$d\left(\delta \mathscr{L}_{int}\right) = \int_{V_0} \delta \boldsymbol{\theta}^T \left\{ \left[\mathbf{H}^T + \mathbf{A}^T\left(\boldsymbol{\theta}\right) \right] \mathbf{Q} \left[\mathbf{H} + \mathbf{A}\left(\boldsymbol{\theta}\right) \right] + \hat{\mathbf{S}} \right\} d\boldsymbol{\theta} dV \tag{3.17}$$

3.2.2 CUF-Based Displacement Field

In the framework of the Carrera Unified Formulation, the through-the-thickness variation of the displacement field is approximated via the base functions $F_\tau\left(z\right)$, whereas classical one-dimensional finite elements shape functions $N_i\left(x\right)$ approximate the displacements along the beam axis:

$$\begin{array}{l} u\left(x,z\right) = F_\tau\left(z\right) N_i\left(x\right) q^u_{\tau i} \\ w\left(x,z\right) = F_\tau\left(z\right) N_i\left(x\right) q^w_{\tau i} \end{array} \text{ with } \tau = 1,\ 2,\ \ldots,\ N_u, i = 1,\ 2,\ \ldots,\ N^e_n \tag{3.18}$$

being $q^n_{\tau i} : n = \{u, w\}$ the nodal unknowns. In Eq. (3.18), Einstein's compact notation is used, i.e. a repeated index implicitly implies summation over its variation range. Index τ varies over the number of terms N_u accounted in the expansion, whereas the index i varies over the element number of nodes N^e_n. Both N_u and N^e_n are free parameters of the formulation. Therefore, by CUF approach, a family of higher-order displacement-based theories can be straightforwardly derived. The class of expansion functions $F_\tau\left(z\right)$ adopted in this work are Maclaurin polynomials, therefore the generic explicit form of the displacement field is:

$$\begin{array}{l} u_x = u_{x1} + u_{x2} z + u_{x3} z^2 + \cdots + u_{x(N+1)} z^N \\ u_z = u_{z1} + u_{z2} z + u_{z3} z^2 + \cdots + u_{z(N+1)} z^N \end{array} \tag{3.19}$$

An equivalent single layer approach is adopted. The displacements gradient vector in terms of the expansion functions F_τ and shape functions N_i is obtained by replacing Eq. (3.18) within Eq. (3.2):

$$\boldsymbol{\theta} = \left\{ F_\tau N_{i,x} q^u_{\tau i} \ F_{\tau,z} N_i q^u_{\tau i} \ F_\tau N_{i,x} q^w_{\tau i} \ F_{\tau,z} N_i q^w_{\tau i} \right\} = \mathbf{G}_{\tau i} \mathbf{q}_{\tau i} \tag{3.20}$$

being:

$$\mathbf{G}_{\tau i} = \begin{bmatrix} F_\tau N_{i,x} & 0 \\ F_{\tau,z} N_i & 0 \\ 0 & F_\tau N_{i,x} \\ 0 & F_{\tau,z} N_i \end{bmatrix} \tag{3.21}$$

and:

$$\mathbf{q}^T_{\tau i} = \left\{ q^u_{\tau i} \ q^w_{\tau i} \right\} \tag{3.22}$$

3.2.3 Fundamental Nuclei of the Tangent Stiffness Matrix

By replacing Eq. (3.20) within Eq. (3.17), the variation of the virtual internal work reads:

$$d\left(\delta \mathscr{L}_{int}^{e}\right) = \delta \mathbf{q}_{\tau i}^{T} \int_{V_0^e} \mathbf{G}_{\tau i}^{T} \left\{ \left[\mathbf{H}^{T} + \mathbf{A}^{T}(\boldsymbol{\theta})\right] \mathbf{Q} \left[\mathbf{H} + \mathbf{A}(\boldsymbol{\theta})\right] + \hat{\mathbf{S}} \right\} \mathbf{G}_{\sigma j} dV d\mathbf{q}_{\sigma j} = \delta \mathbf{q}_{\tau i}^{T} \left(\mathbf{K}_{\tau\sigma ij}^{el} + \mathbf{K}_{\tau\sigma ij}^{et1} + \mathbf{K}_{\tau\sigma ij}^{et2} \right) d\mathbf{q}_{\sigma j} \tag{3.23}$$

Superscript 'e' refers to a generic element, whereas $\mathbf{K}_{\tau\sigma ij}^{el}$ $\mathbf{K}_{\tau\sigma ij}^{et1}$ $\mathbf{K}_{\tau\sigma ij}^{et2} \in \mathbb{R}^{2\times 2}$ are the "fundamental nuclei" of the linear, initial-displacement and initial-stress contribution to the tangent stiffness matrix:

$$\begin{aligned} \mathbf{K}_{\tau\sigma ij}^{el} &= \int_{V_0^e} \mathbf{G}_{\tau i}^{T} \mathbf{H}^{T} \mathbf{Q} \mathbf{H} \mathbf{G}_{\sigma j} dV \\ \mathbf{K}_{\tau\sigma ij}^{et1} &= \int_{V_0^e} \mathbf{G}_{\tau i}^{T} \left[\mathbf{H}^{T} \mathbf{Q} \mathbf{A} + \mathbf{A}^{T} \mathbf{Q} (\mathbf{H} + \mathbf{A})\right] \mathbf{G}_{\sigma j} dV \\ \mathbf{K}_{\tau\sigma ij}^{et2} &= \int_{V_0^e} \mathbf{G}_{\tau i}^{T} \hat{\mathbf{S}} \mathbf{G}_{\sigma j} dV \end{aligned} \tag{3.24}$$

It should be noted that the expression of the nuclei is general and does not depend on the CUF expansion order N, the class of approximating functions F_τ or the number of nodes per element N_n^e. The explicit expressions of each fundamental nucleus are provided below. The components of the linear stiffness matrix $\mathbf{K}_{\tau\sigma ij}^{el}$ are:

$$\begin{aligned} K_{\tau\sigma ij}^{elxx} &= J_{\tau\sigma}^{11} I_{i,x\,j,x} + J_{\tau_{,z}\sigma_{,z}}^{55} I_{ij} + J_{\tau_{,z}\sigma}^{15} I_{ij,x} + J_{\tau\sigma_{,z}}^{15} I_{i,x\,j} \\ K_{\tau\sigma ij}^{elxz} &= J_{\tau\sigma_{,z}}^{13} I_{i,x\,j} + J_{\tau\sigma}^{15} I_{i,x\,j,x} + J_{\tau_{,z}\sigma_{,z}}^{35} I_{ij} + J_{\tau_{,z}\sigma}^{55} I_{ij,x} \\ K_{\tau\sigma ij}^{elzx} &= J_{\tau_{,z}\sigma}^{13} I_{ij,x} + J_{\tau\sigma}^{15} I_{i,x\,j,x} + J_{\tau_{,z}\sigma_{,z}}^{35} I_{ij} + J_{\tau\sigma_{,z}}^{55} I_{i,x\,j} \\ K_{\tau\sigma ij}^{elzz} &= J_{\tau_{,z}\sigma_{,z}}^{33} I_{ij} + J_{\tau\sigma}^{55} I_{i,x\,j,x} + J_{\tau\sigma_{,z}}^{35} I_{i,x\,j} + J_{\tau_{,z}\sigma}^{35} I_{ij,x} \end{aligned} \tag{3.25}$$

where the term $J_{\tau_{(,z)}\sigma_{(,z)}}^{gh}$ is the following integral over the beam element cross-section Ω^e:

$$J_{\tau_{(,z)}\sigma_{(,z)}}^{gh} = \int_{\Omega^e} Q_{gh} F_{\tau_{(,z)}} F_{\sigma_{(,z)}} \, d\Omega \tag{3.26}$$

$I_{i_{(,x)}j_{(,x)}}$ is the integral along the element axis length l^e of the product of the shape functions and/or their derivatives:

$$I_{i_{(,x)}j_{(,x)}} = \int_{l^e} N_{i_{(,x)}} N_{j_{(,x)}} \, dx \tag{3.27}$$

The components of the initial displacement contribution $\mathbf{K}^{et1}_{\tau\sigma ij}$ are:

$$
\begin{aligned}
K^{et1xx}_{\tau\sigma ij} = {} & q^u_{tl}\Big(2J^{11}_{\tau\sigma t} I_{i,x\,j,x\,l,x} + J^{13}_{\tau\sigma,z t,z} I_{i,x\,jl} + J^{13}_{\tau,z\sigma t,z} I_{ij,x\,l} + 2J^{15}_{\tau\sigma t,z} I_{i,x\,j,x\,l} + \\
& 2J^{15}_{\tau\sigma,z t} I_{i,x\,jl,x} + 2J^{15}_{\tau,z\sigma t} I_{ij,x\,l,x} + 2J^{35}_{\tau,z\sigma,z t,z} I_{ijl} + 2J^{55}_{\tau,z\sigma,z t} I_{ijl,x}\Big) + \\
& J^{55}_{\tau,z\sigma t,z} I_{ij,x\,l} + J^{55}_{\tau\sigma,z t,z} I_{i,x\,jl}\Big) + \\
& q^u_{tl} q^u_{sm}\Big(J^{11}_{\tau\sigma ts} I_{i,x\,j,x\,l,x\,m,x} + J^{13}_{\tau\sigma,z ts,z} I_{i,x\,jl,x\,m} + J^{13}_{\tau,z\sigma t,z s} I_{ij,x\,lm,x} + \\
& J^{15}_{\tau\sigma ts,z} I_{i,x\,j,x\,l,x\,m} + J^{15}_{\tau\sigma,z ts} I_{i,x\,jl,x\,m,x} + J^{15}_{\tau\sigma t,z s} I_{i,x\,j,x\,lm,x} + J^{15}_{\tau,z\sigma ts} I_{ij,x\,l,x\,m,x} + \\
& J^{35}_{\tau\sigma,z t,z s,z} I_{i,x\,jlm} + J^{35}_{\tau,z\sigma t,z s} I_{ij,x\,lm} + J^{35}_{\tau,z\sigma,z t,z s} I_{ijlm,x} + J^{35}_{\tau,z\sigma,z ts,z} I_{ijl,x\,m} + \\
& J^{33}_{\tau,z\sigma,z t,z s,z} I_{ijlm} + J^{55}_{\tau\sigma t,z s,z} I_{i,x\,j,x\,lm} + J^{55}_{\tau\sigma,z t,z s} I_{i,x\,jlm,x} + J^{55}_{\tau,z\sigma ts,z} I_{ij,x\,l,x\,m} + \\
& J^{55}_{\tau,z\sigma,z ts} I_{ijl,x\,m,x}\Big) \\
\\
K^{et1xz}_{\tau\sigma ij} = {} & q^u_{tl}\Big(J^{13}_{\tau\sigma,z t} I_{i,x\,jl,x} + J^{15}_{\tau\sigma t} I_{i,x\,j,x\,l,x} + J^{35}_{\tau\sigma,z t,z} I_{i,x\,jl} + J^{55}_{\tau\sigma t,z} I_{i,x\,j,x\,l} + \\
& J^{33}_{\tau,z\sigma,z t,z} I_{ijl} + J^{35}_{\tau,z\sigma t,z} I_{ij,x\,l} + J^{35}_{\tau,z\sigma,z t} I_{ijl,x} + J^{55}_{\tau,z\sigma t} I_{ij,x\,l,x}\Big) + \\
& q^w_{tl}\Big(J^{11}_{\tau\sigma t} I_{i,x\,j,x\,l,x} + J^{13}_{\tau\sigma,z t,z} I_{i,x\,jl} + J^{15}_{\tau\sigma t,z} I_{i,x\,j,x\,l} + J^{15}_{\tau\sigma,z t} I_{i,x\,jl,x} + \\
& J^{15}_{\tau,z\sigma t} I_{ij,x\,l,x} + J^{35}_{\tau,z\sigma,z t,z} I_{ijl} + J^{55}_{\tau,z\sigma t,z} I_{ij,x\,l} + J^{55}_{\tau,z\sigma,z t} I_{ijl,x}\Big) + \\
& q^u_{tl} q^w_{sm}\Big(J^{11}_{\tau\sigma ts} I_{i,x\,j,x\,l,x\,m,x} + J^{13}_{\tau\sigma,z ts,z} I_{i,x\,jl,x\,m} + J^{15}_{\tau\sigma ts,z} I_{i,x\,j,x\,l,x\,m} + \\
& J^{15}_{\tau\sigma,z ts} I_{i,x\,jl,x\,m,x} + J^{15}_{\tau\sigma t,z s} I_{i,x\,j,x\,lm,x} + J^{35}_{\tau\sigma,z t,z s,z} I_{i,x\,jlm} + J^{55}_{\tau\sigma t,z s,z} I_{i,x\,j,x\,lm} + \\
& J^{55}_{\tau\sigma,z t,z s} I_{i,x\,jlm,x} + J^{13}_{\tau,z\sigma t,z s} I_{ij,x\,lm,x} + J^{33}_{\tau,z\sigma,z t,z s,z} I_{ijlm} + J^{35}_{\tau,z\sigma t,z s,z} I_{ij,x\,lm} + \\
& J^{35}_{\tau,z\sigma,z t,z s} I_{ijlm,x} + J^{15}_{\tau,z\sigma ts} I_{ij,x\,l,x\,m,x} + J^{35}_{\tau,z\sigma,z ts,z} I_{ijl,x\,m} + J^{55}_{\tau,z\sigma ts,z} I_{ij,x\,l,x\,m} + \\
& J^{55}_{\tau,z\sigma,z ts} I_{ijl,x\,m,x}\Big) \\
\\
K^{et1zx}_{\tau\sigma ij} = {} & q^u_{tl}\Big(J^{15}_{\tau\sigma t} I_{i,x\,j,x\,l,x} + J^{35}_{\tau\sigma,z t,z} I_{i,x\,jl} + J^{55}_{\tau\sigma t,z} I_{i,x\,j,x\,l} + J^{55}_{\tau\sigma,z t} I_{i,x\,jl,x} + \\
& J^{13}_{\tau,z\sigma t} I_{ij,x\,l,x} + J^{33}_{\tau,z\sigma,z t,z} I_{ijl} + J^{35}_{\tau,z\sigma t,z} I_{ij,x\,l} + J^{35}_{\tau,z\sigma,z t} I_{ijl,x}\Big) + \\
& q^w_{tl}\Big(J^{11}_{\tau\sigma t} I_{i,x\,j,x\,l,x} + J^{15}_{\tau\sigma,z t} I_{i,x\,jl,x} + J^{15}_{\tau\sigma t,z} I_{i,x\,j,x\,l} + J^{55}_{\tau\sigma,z t,z} I_{i,x\,jl} + \\
& J^{13}_{\tau,z\sigma t,z} I_{ij,x\,l} + J^{35}_{\tau,z\sigma,z t,z} I_{ijl} + J^{15}_{\tau,z\sigma t} I_{ij,x\,l,x} + J^{55}_{\tau,z\sigma,z t} I_{ijl,x}\Big) + \\
& q^w_{tl} q^u_{sm}\Big(J^{11}_{\tau\sigma ts} I_{i,x\,j,x\,l,x\,m,x} + J^{13}_{\tau\sigma,z ts,z} I_{i,x\,jl,x\,m} + J^{15}_{\tau\sigma ts,z} I_{i,x\,j,x\,l,x\,m} + \\
& J^{15}_{\tau\sigma,z ts} I_{i,x\,jl,x\,m,x} + J^{15}_{\tau\sigma t,z s} I_{i,x\,j,x\,lm,x} + J^{35}_{\tau\sigma,z t,z s,z} I_{i,x\,jlm} + J^{55}_{\tau\sigma t,z s,z} I_{i,x\,j,x\,lm} + \\
& J^{55}_{\tau\sigma,z t,z s} I_{i,x\,jlm,x} + J^{13}_{\tau,z\sigma t,z s} I_{ij,x\,lm,x} + J^{33}_{\tau,z\sigma,z t,z s,z} I_{ijlm} + J^{35}_{\tau,z\sigma t,z s,z} I_{ij,x\,lm} + \\
& J^{35}_{\tau,z\sigma,z t,z s} I_{ijlm,x} + J^{15}_{\tau,z\sigma ts} I_{ij,x\,l,x\,m,x} + J^{35}_{\tau,z\sigma,z ts,z} I_{ijl,x\,m} + J^{55}_{\tau,z\sigma ts,z} I_{ij,x\,l,x\,m} + \\
& J^{55}_{\tau,z\sigma,z ts} I_{ijl,x\,m,x}\Big)
\end{aligned}
\tag{3.28}
$$

$$
\begin{aligned}
K^{et1zz}_{\tau\sigma ij} = {} & q^{w}_{tl}\Big(J^{13}_{\tau\sigma_{,z}t}I_{i_{,x}jl_{,x}} + J^{13}_{\tau_{,z}\sigma t}I_{ij_{,x}l_{,x}} + 2J^{15}_{\tau\sigma t}I_{i_{,x}j_{,x}l_{,x}} + 2J^{35}_{\tau\sigma_{,z}t_{,z}}I_{i_{,x}jl} + \\
& 2J^{35}_{\tau_{,z}\sigma t_{,z}}I_{i_{,x}jl} + 2J^{35}_{\tau_{,z}\sigma_{,z}t}I_{ijl_{,x}} + 2J^{55}_{\tau\sigma t_{,z}}I_{i_{,x}j_{,x}l} + J^{55}_{\tau\sigma_{,z}t}I_{i_{,x}jl_{,x}}\Big) + \\
& J^{55}_{\tau_{,z}\sigma t}I_{ij_{,x}l_{,x}} + 2J^{33}_{\tau_{,z}\sigma_{,z}t_{,z}}I_{ijl}\Big) + \\
& q^{w}_{tl}q^{w}_{sm}\Big(J^{11}_{\tau\sigma ts}I_{i_{,x}j_{,x}l_{,x}m_{,x}} + J^{33}_{\tau_{,z}\sigma_{,z}t_{,z}s_{,z}}I_{ijlm} + J^{55}_{\tau\sigma t_{,z}s_{,z}}I_{i_{,x}j_{,x}lm} + \\
& J^{55}_{\tau\sigma_{,z}t_{,z}s}I_{i_{,x}jlm_{,x}} + J^{55}_{\tau_{,z}\sigma ts_{,z}}I_{ij_{,x}l_{,x}m} + J^{55}_{\tau_{,z}\sigma_{,z}ts}I_{ijl_{,x}m_{,x}} + J^{13}_{\tau\sigma_{,z}ts_{,z}}I_{i_{,x}jl_{,x}m} + \\
& J^{13}_{\tau_{,z}\sigma t_{,z}s}I_{ij_{,x}lm_{,x}} + J^{15}_{\tau\sigma ts_{,z}}I_{i_{,x}j_{,x}l_{,x}m} + J^{15}_{\tau\sigma_{,z}ts}I_{i_{,x}jl_{,x}m_{,x}} + J^{15}_{\tau\sigma t_{,z}s}I_{i_{,x}j_{,x}lm_{,x}} + \\
& J^{15}_{\tau_{,z}\sigma ts}I_{ij_{,x}l_{,x}m_{,x}} + J^{35}_{\tau\sigma_{,z}t_{,z}s_{,z}}I_{i_{,x}jlm} + J^{35}_{\tau_{,z}\sigma t_{,z}s_{,z}}I_{ij_{,x}lm} + J^{35}_{\tau_{,z}\sigma_{,z}t_{,z}s}I_{ijlm_{,x}} + \\
& J^{35}_{\tau_{,z}\sigma_{,z}ts_{,z}}I_{ijl_{,x}m}\Big)
\end{aligned}
$$

Finally, the non-zero components of the initial-stress contribution $\mathbf{K}^{et2}_{\tau\sigma ij}$ are:

$$
\begin{aligned}
K^{et2xx}_{\tau\sigma ij} = K^{et2zz}_{\tau\sigma ij} = {} & q^{u}_{tl}\Big(J^{11}_{\tau\sigma t}I_{i_{,x}j_{,x}l_{,x}} + J^{15}_{\tau\sigma t_{,z}}I_{i_{,x}j_{,x}l} + J^{15}_{\tau\sigma_{,z}t}I_{i_{,x}jl_{,x}} + J^{55}_{\tau\sigma_{,z}t_{,z}}I_{i_{,x}jl} + \\
& J^{15}_{\tau_{,z}\sigma t}I_{ij_{,x}l_{,x}} + J^{55}_{\tau_{,z}\sigma t_{,z}}I_{ij_{,x}l} + J^{13}_{\tau_{,z}\sigma_{,z}t}I_{ijl_{,x}} + J^{35}_{\tau_{,z}\sigma_{,z}t_{,z}}I_{ijl}\Big) \\
& q^{w}_{tl}\Big(J^{13}_{\tau\sigma t_{,z}}I_{i_{,x}j_{,x}l} + J^{15}_{\tau\sigma t}I_{i_{,x}j_{,x}l_{,x}} + J^{35}_{\tau\sigma_{,z}t_{,z}}I_{i_{,x}jl} + J^{55}_{\tau\sigma_{,z}t}I_{i_{,x}jl_{,x}} + \\
& J^{35}_{\tau_{,z}\sigma t_{,z}}I_{ij_{,x}l} + J^{55}_{\tau_{,z}\sigma t}I_{ij_{,x}l_{,x}} + J^{33}_{\tau_{,z}\sigma_{,z}t_{,z}}I_{ijl} + J^{35}_{\tau_{,z}\sigma_{,z}t}I_{ijl_{,x}}\Big) \\
& \frac{1}{2}\left(q^{u}_{tl}q^{u}_{sm} + q^{w}_{tl}q^{w}_{sm}\right)\Big(J^{11}_{\tau\sigma ts}I_{i_{,x}j_{,x}l_{,x}m_{,x}} + J^{13}_{\tau\sigma t_{,z}s_{,z}}I_{i_{,x}j_{,x}lm} + J^{15}_{\tau\sigma t_{,z}s}I_{i_{,x}j_{,x}lm_{,x}} + \\
& J^{15}_{\tau\sigma ts_{,z}}I_{i_{,x}j_{,x}l_{,x}m} + J^{15}_{\tau\sigma_{,z}ts}I_{i_{,x}jl_{,x}m_{,x}} + J^{35}_{\tau\sigma_{,z}t_{,z}s_{,z}}I_{i_{,x}jlm} + J^{55}_{\tau\sigma_{,z}t_{,z}s}I_{i_{,x}jlm_{,x}} + \\
& J^{55}_{\tau\sigma_{,z}ts_{,z}}I_{i_{,x}jl_{,x}m} + J^{15}_{\tau_{,z}\sigma ts}I_{ij_{,x}l_{,x}m_{,x}} + J^{35}_{\tau_{,z}\sigma t_{,z}s_{,z}}I_{ij_{,x}lm} + J^{55}_{\tau_{,z}\sigma_{,z}t_{,z}s}I_{ijlm_{,x}} + \\
& J^{55}_{\tau_{,z}\sigma ts_{,z}}I_{ij_{,x}l_{,x}m} + J^{13}_{\tau_{,z}\sigma_{,z}ts}I_{ijl_{,x}m_{,x}} + J^{33}_{\tau_{,z}\sigma_{,z}t_{,z}s_{,z}}I_{ijlm} + J^{35}_{\tau_{,z}\sigma_{,z}t_{,z}s}I_{ijlm_{,x}} + \\
& J^{35}_{\tau_{,z}\sigma_{,z}ts_{,z}}I_{ijl_{,x}m}\Big)
\end{aligned}
\tag{3.29}
$$

The expressions of the integrals $J^{gh}_{\tau_{(,z)}\sigma_{(,z)}t_{(,z)}}$, $I_{i_{(,x)}j_{(,x)}l_{(,x)}}$, $J^{gh}_{\tau_{(,z)}\sigma_{(,z)}t_{(,z)}s_{(,z)}}$ and $I_{i_{(,x)}j_{(,x)}l_{(,x)}m_{(,x)}}$ in Eqs. (3.28) and (3.29) are:

$$
J^{gh}_{\tau_{(,z)}\sigma_{(,z)}t_{(,z)}} = \int_{\Omega^e} Q_{gh}F_{\tau_{(,z)}}F_{\sigma_{(,z)}}F_{t_{(,z)}}\,d\Omega \tag{3.30}
$$

$$
I_{i_{(,x)}j_{(,x)}l_{(,x)}} = \int_{l^e} N_{i_{(,x)}}N_{j_{(,x)}}N_{l_{(,x)}}\,dx \tag{3.31}
$$

$$
J^{gh}_{\tau_{(,z)}\sigma_{(,z)}t_{(,z)}s_{(,z)}} = \int_{\Omega^e} Q_{gh}F_{\tau_{(,z)}}F_{\sigma_{(,z)}}F_{t_{(,z)}}F_{s_{(,z)}}\,d\Omega \tag{3.32}
$$

$$
I_{i_{(,x)}j_{(,x)}l_{(,x)}m_{(,x)}} = \int_{l^e} N_{i_{(,x)}}N_{j_{(,x)}}N_{l_{(,x)}}N_{m_{(,x)}}\,dx \tag{3.33}
$$

The integrals are all numerically evaluated through Gaussian quadrature. Due to the total Lagrangian approach, the integrals are computed over the undeformed geometry, therefore they can be computed once and for all at the beginning of the solution process. Once the CUF expansion order N is fixed, the element tangent stiffness matrix $\mathbf{K}^e$ is obtained straightforwardly by assembling the previous fundamental nuclei, in a similar manner to classical finite elements, as described in Carrera et al. [7].

3.2.3.1 MITC-Based Locking Correction

Due to the coupling of the displacement components arising from the quadratic terms in the geometrically non-linear strain-displacement relations, see Eq. (3.4), membrane as well as shear locking need to be tackled. Especially when dealing with slender structures and low-order shape functions, such phenomena will degrade the performance of the finite element, see Reddy [19]. In order to mitigate the locking phenomena, MITC method is introduced, consisting in the following interpolation along the beam element axis of all the strain components, see Bathe et al. [3, 4]:

$$\begin{aligned} \overline{E}_{xx} &= \overline{N}_p E^p_{xx} \\ \overline{E}_{zz} &= \overline{N}_p E^p_{zz} \\ \overline{E}_{xz} &= \overline{N}_p E^p_{xz} \end{aligned} \tag{3.34}$$

where the subscript p implicitly stands for a summation from 1 to $N^e_n - 1$. E^p_{xx}, E^p_{zz} and E^p_{xz} are the strains computed at the pth tying point r_{Tp} expressed in natural coordinates and $\overline{N}_p$ are the assumed interpolating functions. The explicit expressions of tying points and assumed interpolating functions for linear, quadratic and cubic elements can be also found in Carrera et al. [8]. Finally, for beam elements with MITC-based locking correction, the I-integrals previously introduced in Eqs. (3.27), (3.31), (3.33) should be replaced, respectively, by the following integrals:

$$\overline{I}_{i_{(,x)}j_{(,x)}} = \int_{l_e} \overline{N}_p N^p_{i_{(,x)}} \overline{N}_q N^q_{j_{(,x)}} \, dx \tag{3.35}$$

$$\overline{I}_{i_{(,x)}j_{(,x)}l_{(,x)}} = \int_{l_e} \overline{N}_p N^p_{i_{(,x)}} \overline{N}_q N^q_{j_{(,x)}} N^q_{l_{(,x)}} \, dx \tag{3.36}$$

$$\overline{I}_{i_{(,x)}j_{(,x)}l_{(,x)}m_{(,x)}} = \int_{l_e} \overline{N}_p N^p_{i_{(,x)}} N^p_{j_{(,x)}} \overline{N}_q N^q_{l_{(,x)}} N^q_{m_{(,x)}} \, dx \tag{3.37}$$

3.2.3.2 ANM-Based Non-linear Solver

A path-following technique based on the Asymptotic Numerical Method (ANM) is used, see Cochelin [10], in order to solve the resulting non-linear problem:

$$\mathbf{K}(\boldsymbol{\theta})\mathbf{q} = \lambda\mathbf{F} \tag{3.38}$$

being $\mathbf{K}$ the global tangent stiffness matrix, $\mathbf{q}$ the global unknown vector and $\lambda\mathbf{F}$ the vector of the external forces. ANM is a perturbation technique in which, starting from the known solution at the step j, the displacement vector $\mathbf{u}$, the stress vector $\mathbf{S}$ and the load factor λ are approximated as a n-order power series with respect to a path parameter a:

$$\begin{aligned}
\mathbf{u} &= \mathbf{u}^j + a^p\mathbf{u}_p = \mathbf{u}^j + a\mathbf{u}_1 + a^2\mathbf{u}_2 + \cdots + a^n\mathbf{u}_n \\
\mathbf{S} &= \mathbf{S}^j + a^p\mathbf{S}_p = \mathbf{S}^j + a\mathbf{S}_1 + a^2\mathbf{S}_2 + \cdots + a^n\mathbf{S}_n \\
\lambda &= \lambda^j + a^p\lambda_p = \lambda^j + a\lambda_1 + a^2\lambda_2 + \cdots + a^n\lambda_n
\end{aligned} \tag{3.39}$$

with p ranging from 1 to n. The path parameter a is defined as a quasi-arc-length parameter as follows:

$$a = \mathbf{u}_1(\mathbf{u} - \mathbf{u}^j) + \lambda_1(\lambda - \lambda^j) \tag{3.40}$$

being $(\mathbf{u}_1, \lambda_1)$ the tangent vector. The sign of the path parameter a sets the path direction of the solution, therefore in snap-through analyses, a is taken positive when the tangent stiffness matrix is positive definite and it is taken negative otherwise. By taking into account Eqs. (3.9) and (3.18) and by replacing Eqs. (3.39) in Eq. (3.38) and by equating the terms with the same powers of a, a set of $3n + 1$ linear systems in $3n + 1$ unknown vectors can be derived. A convergence criterion based on the ratio between first order and n-order solutions is adopted in order to compute a posteriori the step length a_{max}:

$$a_{max} = \left(\varepsilon \frac{||\mathbf{u}_1||}{||\mathbf{u}_n||}\right)^{\frac{1}{n-1}} \tag{3.41}$$

being ε a tolerance parameter. The detailed complete formulation can be found in Cochelin et al. [10]. ANM has been proven to conveniently handle post-buckling and snap-through of elastic structures, since through the higher-order analytical representation given in Eq. (3.39), a larger non-linear branch with only one stiffness matrix inversion can be obtained. This leads to a more efficient solution procedure, compared to classical predictor-corrector schemes, in which the non-linear path is linearly approximated and iteratively corrected at each step. Moreover, since the length of each step is automatically chosen a posteriori according to the displacement criterion in Eq. (3.41), no choice of the step length or first increment (as in those algorithms with auto-stepping) is required, therefore avoiding time-consuming and case-dependent trial and error before a computationally efficient solution can be performed. Finally, this method proofs to be robust in the case of branch-switching as discussed in Baguet and Cochelin [2].

3.3 Numerical Results

In the first study case, a clamped-simply supported beam (u_x and $u_z = 0$ at $x = 0$ and $u_z = 0$ at $x = L$) initially buckled due to an axial compressive load F_x applied at the beam end ($x = L, z = 0$) is considered and starting from the deformed shape and full pre-stress field generated by the buckling step, the structure is snapped downwards into a reversed curvature configuration by means of a transverse load F_z applied at ($x = L/2, z = 0$). In order to demonstrate the influence of higher-order theories on the mechanics of bistable beams, a moderately thick beam is considered, being the slenderness ratio $S = L/h = 20$ smaller than typical values found in literature. A homogeneous material (aluminum with $E = 75$ GPa and $\nu = 0.33$) is considered and the cross-section is square ($h = b = 1$ m). Both the buckling and the snap-through phases are investigated via geometrically non-linear analyses. The following dimensionless parameters have been used for displacements, stresses and external loads: $\tilde{u} = u/L$, $\tilde{\sigma} = \frac{\sigma 2I}{F_x Lh}$, $\lambda_x = -\frac{F_x L^2}{\pi^2 EI}$ and $\lambda_z = -F_z/F_x$, being I the moment of inertia of the beam cross-section. Stress results are given in terms of Cauchy's stresses $\boldsymbol{\sigma}$ expressed in the local reference system that are equivalent to the Piola–Kirchoff's stresses in the global reference system **S**, under the assumption of small deformations. Results provided by the proposed family of one-dimensional finite elements under the hypothesis of plane stress, large displacements, large rotations and small strains are assessed towards two-dimensional eight-nodes finite elements ("FEM 2D") based on small strains assumption and developed using a total Lagrangian formulation, see Hu et al. [14]. 121 nodes and cubic beam elements with MITC-based locking correction are used for the one-dimensional models, whereas a 120×12 mesh is used for an accurate stress prediction via two-dimensional finite element solution. For the proposed advanced one-dimensional models, the number of degrees of freedom (N_{DOFs}) as function of the CUF expansion order N and number of nodes along the beam axis N_n is given by the following relation:

$$N_{DOFs} = 2 \cdot (N + 1) \cdot N_n \tag{3.42}$$

Table 3.1 provides the following displacements, axial and shear stresses at the end of the non-linear buckling step: $\tilde{u}_x(L, h/2)$, $\tilde{u}_z(L/2, -h/2)$, $\tilde{\sigma}_{xx}(L/2, -h/2)$ and

Table 3.1 Displacements and stresses for a moderately thick ($L/h = 20$) clamped-roller beam. Non-linear buckling step. $\lambda_x = 2.6347$

Structural model	$\tilde{u}_z \times 10$	$-\tilde{u}_x \times 10^2$	$-\tilde{\sigma}_{xx} \times 10^2$	$\tilde{\sigma}_{xz} \times 10^3$
FEM 2D	1.1951	3.6025	7.4363	4.6339
$N = 5$	1.2071	3.6956	7.5044	4.6517
$N = 4$	1.2015	3.6653	7.4731	4.6313
$N = 3$	1.1755	3.4891	7.3307	4.5319
$N = 2$	1.1356	3.2647	7.1131	3.1055

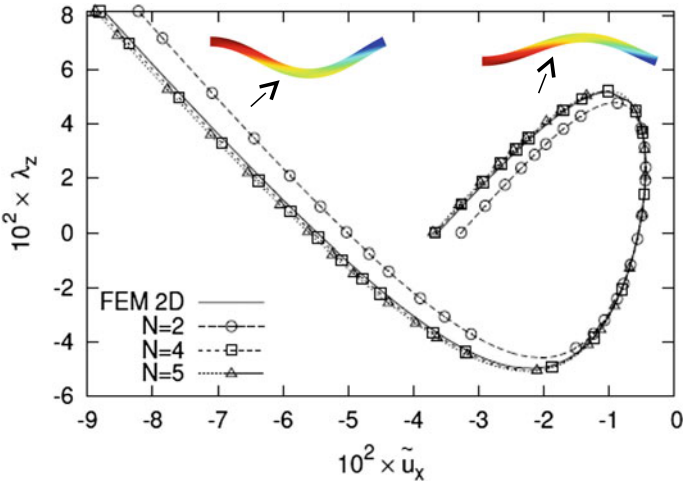

Fig. 3.1 Transverse load λ_z versus axial displacement $\tilde{u}_x$ in the snap-through analysis of a pre-buckled clamped-simply supported beam. Slenderness ratio $L/h = 20$

$\tilde{\sigma}_{xz}(L/4, 0)$. A lower-order theory such as N = 2 leads to some inaccuracies in the mechanical prediction, being the relative difference with respect to the two-dimensional finite elements solution as high as 9.4% for the displacements, 4.4% for the axial stress and 33.0% for the shear stress. On the other hand, by enriching the through-the-thickness kinematics of the model via a 4th order or 5th-order theory, errors on the displacement prediction as high as 2.6% can be obtained and being 0.9%, at worse, on the axial and shear stresses. Figures 3.1 and 3.2 show the force-displacement curves for the snap-through step carried out starting from the buckled configuration.

The evaluation points for the displacements in Figs. 3.1 and 3.2 are the same as those used for Table 3.1. A qualitative color plot distribution of the respective displacement component is also provided in Figs. 3.1 and 3.2. Markers in the line plots do not correspond to the steps of the non-linear solution, since the accumulation of steps in the proximity of the limit points provided by the ANM-based non-linear solver is not shown, for the sake of clarity. The highly non-linear snap-through buckling is well-described by higher-order theories such as N = 4 and N = 5. Starting from the initial state ($\lambda_z = 0$), the overall phenomenon consists in the transition from a first stable force-displacement region (increasing external force) to a second stable region passing through an instability region (decreasing external force) by means of a sudden displacement jump. From a mathematical point of view, the stability of such regions is assessed by checking the positive definiteness of the tangent stiffness matrix, whereas instability regions are characterized by the existence of at least one negative eigenvalue of the tangent stiffness matrix. Finally, the two stable configurations of the bistable structure are those states of equilibrium for which the external load is zero. Table 3.2 shows that a refinement of the one-dimensional

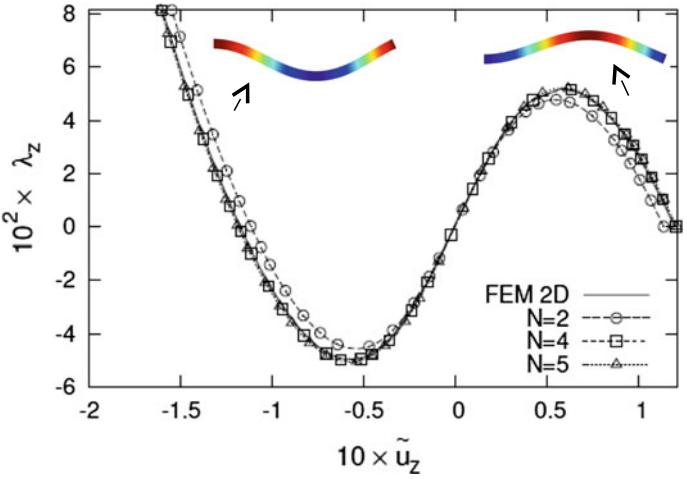

Fig. 3.2 Transverse load λ_z versus transverse displacement $\tilde{u}_z$ in the snap-through analysis of a pre-buckled clamped-simply supported beam. Slenderness ratio $L/h = 20$

Table 3.2 Snap-through load for a prebuckled clamped-roller beam, $\lambda_x = 2.6347$

Structural model	Snap-through load $10^2 \times \lambda_z$	Degrees of freedom (N_{DOFs})
FEM 2D	5.1738	9.2×10^3
$N = 5$	5.2111	1.5×10^3
$N = 4$	5.1915	1.2×10^3
$N = 3$	4.9553	9.7×10^2
$N = 2$	4.7726	7.3×10^2

model kinematics is recommended also for an accurate prediction of the snap-through load, which is the maximum load that the structure can carry before snapping into the second configuration and that represents one of the structural performance parameters for application design. The error provided by a 2nd order theory with respect to the reference solution, in fact, can be reduced from to 7.8 to 4.2% for N = 3 and being as high as 0.7% for N = 4 and N = 5. The stiffer structural behavior (i.e. higher snap-through load) provided by the refined CUF-based models with respect to the lower-order models (such as N = 2) is influenced by the prediction of the non-linear buckling step, which provides a more shallow initial geometry for less refined models and, therefore, lower actuation values λ_z. Table 3.2 also provides a summary concerning the computational costs in terms of number of degrees of freedom (N_{DOFs}) for all the structural models used in the presented numerical results.

A final assessment is presented for the stress prediction of a prebuckled pinned-roller composite beam ($u_x = u_z = 0$ at (0, 0) and $u_z = 0$ at (L,0)). ANSYS plane stress two-dimensional finite elements ("Plane183") with a 120 × 12 mesh are used for comparison. The structure is made of glass fibre epoxy resin composite (E-Glass/913) with the following elastic properties: $E_L = 43.7\,\text{GPa}$, $E_T = 7.5\,\text{GPa}$,

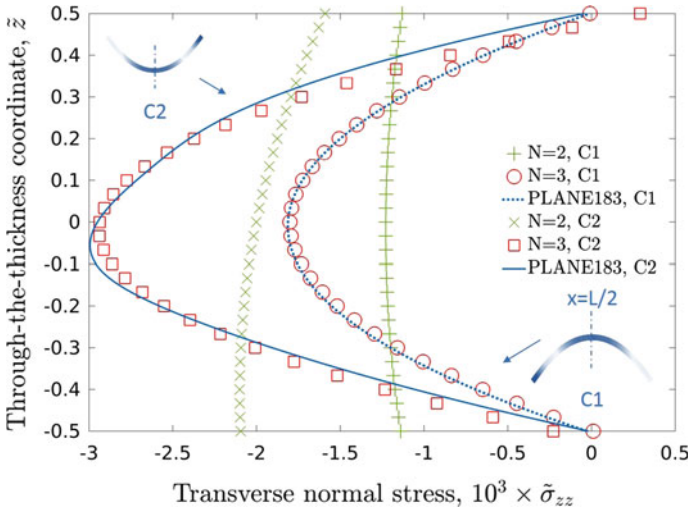

Fig. 3.3 Through-the-thickness distribution of the transverse normal stress $\tilde{\sigma}_{zz}$ at the mid-span of the beam ($x = L/2$) in the prebuckled configuration (C1) and in the snapped configuration (C2). Unidirectional [0] lay-up

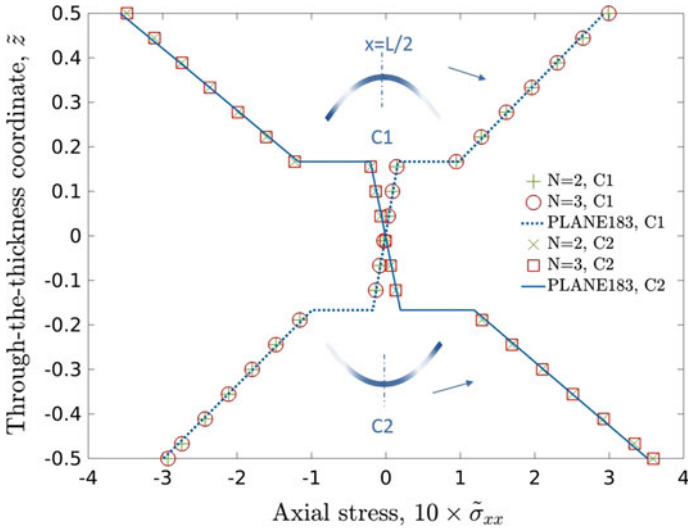

Fig. 3.4 Through-the-thickness distribution of the axial stress $\tilde{\sigma}_{xx}$ at the mid-span of the beam ($x = L/2$) in the pre-buckled configuration (C1) and in the snapped configuration (C2). Cross-ply [0/90/0] lay-up

$G_{LT} = 4.3\,\text{GPa}$ and $\nu_{LT} = 0.3$. A beam with slenderness ratio $L/h = 100$ is considered, being the cross-sectional dimensions $h = b = 1\,\text{m}$. The axial precompression load is equal to $F_x = \lambda_x \pi^2 E_L I/L^2$, with $\lambda_x = 1.1$. A transverse actuation load λ_z is applied at $(L/2, 0)$ and the through-the-thickness transverse normal stress distribution at the beginning of the snap-through analysis (prebuckled configuration, $\lambda_z = 0$) and at the end (snapped configuration, $\lambda_z = 0.1265$) is provided in Fig. 3.3 for a unidirectional lay-up. The through-the-thickness axial stress distribution in the prebuckled configuration ($\lambda_z = 0$) and in the snapped configuration ($\lambda_z = 0.1265$) for a three-layer cross-ply beam with stacking sequence [0/90/0] is shown in Fig. 3.4. As shown in the plots, a second-order theory is able to provide a fairly accurate estimation of the axial stress profile before and after the snap-through instability of the beam structure, whereas at least a third-order theory should be adopted to predict the distribution of the transverse normal stress.

3.4 Concluding Remarks

The development of a hierarchical modeling framework based on the Carrera Unified Formulation for the analysis of bistable beam-like structures has been presented. Geometrical non-linearities in a Green–Lagrange sense are accounted for in order to address the post-buckling and snap-through behavior. Through the CUF-based modeling approach, the significance of assuming higher-order terms in the cross-sectional kinematics of pre-buckled bistable beams has been demonstrated for an accurate prediction of the load-displacement curves, from which snap-through load and stable geometries can be derived. The enrichment of the kinematics from a second-order theory to a fifth-order theory leads to improvements of about 6.8% in the estimation of the axial displacement and about 32.1% on the shear stress prediction in the non-linear buckling phase, whereas a 7.1% improvement on the maximum load prediction can be obtained in the snap-through phase. As far as computational costs are concerned, the number of degrees of freedom for the reference two-dimensional eight-nodes finite elements solution are about 83.7% higher than in a fifth-order one-dimensional model, which is the most refined CUF-based theory used in this study. Through higher-order theories, an accurate stress field evolution (including axial, shear and transverse normal stresses) in strongly non-linear snap-through phenomena can be also obtained. For these reasons, the proposed hierarchical framework represents a reliable yet efficient modeling approach for the analysis of bistable composite structures.

References

1. Arena G, Groh RMJ, Brinkmeyer A, Theunissen R, Weaver PM, Pirrera A (2017) Adaptive compliant structures for flow regulation. Proc R Soc A 473(2204). https://doi.org/10.1098/rspa.2017.0334

2. Baguet S, Cochelin B (2003) On the behaviour of the ANM continuation in the presence of bifurcations. Commun Numer Methods Eng 19(6):459–471
3. Bathe KJ, Iosilevich A, Chapelle D (2000) An evaluation of the MITC shell elements. Comput Struct 75(1):1–30
4. Bathe KJ, Lee PS, Hiller JF (2003) Towards improving the MITC9 shell element. Comput Struct 81(8):477–489
5. Beharic J, Lucas TM, Harnett CK (2014) Analysis of a compressed bistable buckled beam on a flexible support. J Appl Mech 81(8):081011. https://doi.org/10.1115/1.4027463
6. Camescasse B, Fernandes A, Pouget J (2013) Bistable buckled beam: elastica modeling and analysis of static actuation. Int J Solids Struct 50(19):2881–2893
7. Carrera E, Giunta G, Petrolo M (2011) Beam structures: classical and advanced theories. Wiley, Chichester
8. Carrera E, de Miguel AG, Pagani A (2017) Extension of MITC to higher-order beam models and shear locking analysis for compact, thin-walled, and composite structures. Int J Numer Methods Eng 112(13):1889–1908
9. Cleary J, Su HJ (2015) Modeling and experimental validation of actuating a bistable buckled beam via moment input. J Appl Mech 82(5):051005
10. Cochelin B (1994) A path-following technique via an asymptotic-numerical method. Comput Struct 53(5):1181–1192
11. Crisfield MA (1991) Non-linear finite element analysis of solids and structures, vol 1. Wiley, Chichester
12. Giunta G, De Pietro G, Nasser H, Belouettar S, Carrera E, Petrolo M (2016) A thermal stress finite element analysis of beam structures by hierarchical modelling. Compos Part B: Eng 95:179–195
13. De Pietro G, Giunta G, Belouettar S, Carrera E (2017) A static analysis of three-dimensional sandwich beam structures by hierarchical finite elements modelling. J Sandw Struct Mater. https://doi.org/10.1177/1099636217732907
14. Hu H, Belouettar S, Potier-Ferry M, Makradi A (2009) A novel finite element for global and local buckling analysis of sandwich beams. Compos Struct 90(3):270–278
15. Park S, Hah D (2008) Pre-shaped buckled-beam actuators: theory and experiments. Sens Actuators A: Phys 148(1):186–192
16. Pontecorvo ME, Barbarino S, Murray GJ, Gandhi FS (2013) Bistable arches for morphing applications. J Intell Mater Syst Struct 24(3):274–286
17. Qiu J, Lang JH, Slocum AH (2004) A curved-beam bistable mechanism. J Microelectromech Syst 13(2):137–146
18. Reddy JN (2004) Mechanics of laminated composite plates and shells. Theory and analysis, 2nd edn. CRC Press, Boca Raton
19. Reddy JN (2014) An introduction to nonlinear finite element analysis: with applications to heat transfer, fluid mechanics, and solid mechanics. Oxford University Press, Oxford
20. Vangbo M (1998) An analytical analysis of a compressed bistable buckled beam. Sens Actuators A: Phys 69(3):212–216
21. Xu C, Liang Z, Ren B, Di W, Luo H, Wang D, Wang K, Chen Z (2013) Bi-stable energy harvesting based on a simply supported piezoelectric buckled beam. J Appl Phys 114(11):114507

Chapter 4
Multiscale Nonlinear Analysis of Beam Structures by Means of the Carrera Unified Formulation

Y. Hui, G. Giunta, S. Belouettar, H. Hu and E. Carrera

Abstract This chapter addresses a multi-scale analysis of beam structures using the Carrera Unified Formulation (CUF). Under the framework of the FE^2 method, the analysis is divided into a macroscopic/structural problem and a microscopic/material problem. At the macroscopic level, several higher-order refined beam elements can be easily implemented via CUF by deriving a fundamental nucleus that is independent of the approximation order over the thickness and the number of nodes per element (they are free parameters of the formulation). The unknown macroscopic constitutive law is obtained by numerical homogenization of a Representative Volume Element (RVE) at the microscopic level. Vice versa, the microscopic deformation gradient is calculated from the macroscopic model. Information is passed between the two scales in a FE^2 sense. The resulting nonlinear problem is solved through the Asymptotic Numerical Method (ANM) that is more reliable and less time consuming when compared to classical iterative methods. The developed models are used as a first attempt to investigate the microstructure effect on the macrostructure geometrically nonlinear response. Results are compared regarding accuracy and computational costs towards full FEM solutions demonstrating the robustness and efficiency of the proposed approach.

Y. Hui · G. Giunta (✉) · S. Belouettar
Luxembourg Institute of Science and Technology, Esch-sur-Alzette, Luxembourg
e-mail: gaetano.giunta@list.lu

Y. Hui · H. Hu
Wuhan University, Wuhan, China

Y. Hui
MUL2 Group, Department of Mechanical and Aerospace Engineering,
Politecnico di Torino, Torino, Italy

E. Carrera
Department of Mechanical and Aerospace Engineering,
MUL2 Group, Politecnico di Torino, Italy

M. Petrolo (ed.), *Advances in Predictive Models and Methodologies for Numerically Efficient Linear and Nonlinear Analysis of Composites*, PoliTO Springer Series,
https://doi.org/10.1007/978-3-030-11969-0_4

4.1 Introduction

The relationship between microstructure and macroscopic properties is an important factor for the optimization and design of lightweight, strong, tough materials. To predict the macroscopic and microscopic behavior of heterogeneous materials, there are several different information-passing/hierarchical multiscale methods. Under the framework of micromechanics methods, a classification is made based upon the solution type method used for solving Unit Cell (UC) or RVE problems: analytical, semi-analytical and numerical methods. Thanks to the development of computers, numerical methods for UC/RVE problems are easier to be solved. Therefore, these methods (which are often referred to computational upscaling methods or computationally homogenizations) are widely developed and used.

Analytical methods are firstly adopted for solving the UC/RVE problem. An effective medium approximation was established by Eshelby [9], and further developed by Mori and Tanaka [16]. Based on this approach, the self-consistent approach was developed by Hill [12], and its generalisation was presented by Dvorak and Bahei-El-Din [7].

Semi-analytical methods are developed as another group of solutions for determining global composite properties starting from the constituent materials. Fish et al. [11] developed a theory based on the transformation field analysis (see Dvorak and Benveniste [8]) and finite element method for nonlinear problems. Aboudi [1] developed the method of cells. Furthermore, the Generalized Method of Cells (GMC) was presented by Aboudi [2], where a second-order displacement field is applied instead of linear displacement field. GMC should be used on an orthogonal array of UCs for simulating the geometry of the phases. To be noticed, this method requires a relatively large number of cells to capture enough geometric features accurately. Pineda [19] provided a novel progressive damage and failure model for fiber reinforced laminated composites based on GMC. Under the same framework, a variational asymptotic method of unit cell homogenization was successfully applied for periodically heterogeneous material by Yu and Tang [21].

Various numerical methods were developed to ensure computational efficiency and accuracy. Ladevéze [15] proposed a novel multiscale computational strategy based on the so-called LATIN method. Kouznetsova et al. [14] presented a second-order computational homogenization method. In the framework of FE^2, a RVE is

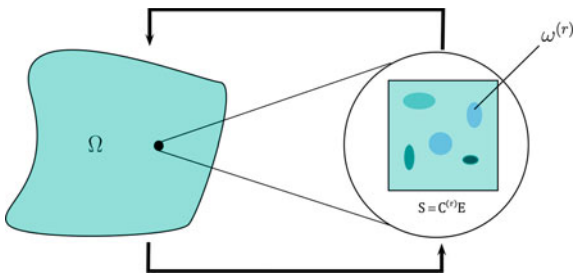

Fig. 4.1 Schematic diagram of a multiscale FE^2 approach

assigned to each integration point at the macroscopic scale as shown in Fig. 4.1. As a consequence, parallel computing can be applied to increase efficiency.

By using this approach, Feyel and Chaboche [10] presented a multiscale analysis of long fiber reinforced SiC/Ti material. Xu et al. [20] proposed a 3D generic FE^2 method for modeling the pseudo-elasticity and the shape memory effects of shape memory alloy fiber reinforced composites. Nezamabadi et al. [18] developed an approach called Multiscale-ANM based on the FE^2 and the ANM, which aimed at dealing with instability phenomena in the context of heterogeneous materials where buckling may occur at both macroscopic and microscopic scale. The governing equations were derived by the virtual work principle, and their discrete form was obtained within the framework of the finite element method. The nonlinear system was solved by the ANM, see Damil and Potier-Ferry [6] and Cochelin et al. [5]. As far as the nonlinear solver is concerned, ANM is a continuation method that associates a perturbation technique with a discretization principle. Under this framework, the computation of a solution path is achieved step-by-step, where at each step the solution is represented by a truncated power series. Many studies presented in the literature show that the ANM is more robust and efficient compared to classical nonlinear solvers (e.g., Newton-Raphson's method, modified Newton-Raphson's method and Risks' method).

Stemming from Nezamabadi et al. [18], a multiscale framework is proposed by extending CUF non-linear beam formulation to the FE^2 multiscale framework and using ANM as a non-linear solver. At macroscopic scale, the kinematic field is axiomatically assumed along the thickness through CUF, see Carrera et al. [4] and Carrera and Giunta [3]. Because the approximation order is a free parameter, several kinematic models can be directly derived. This chapter is organized as follows: in Sect. 4.2, control equations, boundary conditions, and the kinematic models for macroscopic and microscopic scales are described. In Sect. 4.3, numerical results are shown and a final section presents some conclusions.

4.2 Theoretical Background

4.2.1 Macroscopic Scale

Preliminaries. A two-dimensional beam structure is considered at macroscopic scale. Beam axial extension is l. The cross-section (Ω) is identified by intersecting the beam with planes that are orthogonal to its axis. A Cartesian reference system is adopted: y- and z-axis are two orthogonal directions laying on Ω. The x coordinate is coincident to the axis of the beam, and it is bounded such that $0 \leq x \leq l$. In order to distinguish the macroscale model from the microscale one, the quantities belonging to macroscopic scale are all addressed by an overlined symbol. The displacement field is:

$$\overline{\mathbf{u}}\,(x,z) = \left\{ \overline{u}_x\,(x,z)\ \overline{u}_z\,(x,z) \right\}^T \tag{4.1}$$

where $\overline{u}_x$ and $\overline{u}_z$ are the displacement components along x- and z-axis. Superscript 'T' stands for the transposition operator. For two-dimensional problem, the gradient of the displacement $\overline{\boldsymbol{\theta}}$ is expressed by a vector of four components:

$$\overline{\boldsymbol{\theta}}(\overline{\mathbf{u}}) = \left\{ \overline{u}_{,x} \ \overline{u}_{,z} \ \overline{w}_{,x} \ \overline{w}_{,z} \right\}^T \tag{4.2}$$

Since geometrical nonlinearity is considered, the Green-Lagrange strain tensor as a function of the displacement gradient is defined as:

$$\overline{\mathbf{E}} = \begin{bmatrix} \overline{E}_{xx} \\ \overline{E}_{xz} \\ \overline{E}_{zx} \\ \overline{E}_{zz} \end{bmatrix} = \begin{bmatrix} \overline{u}_{,x} \\ \overline{u}_{,z} + \overline{w}_{,x} \\ \overline{u}_{,z} + \overline{w}_{,x} \\ \overline{w}_{,z} \end{bmatrix} + \frac{1}{2} \begin{bmatrix} \overline{u}_{,x}^2 + \overline{w}_{,x}^2 \\ 2\overline{u}_{,x}\overline{u}_{,z} + 2\overline{w}_{,x}\overline{w}_{,z} \\ 2\overline{u}_{,x}\overline{u}_{,z} + 2\overline{w}_{,x}\overline{w}_{,z} \\ \overline{u}_{,z}^2 + \overline{w}_{,z}^2 \end{bmatrix} = \overline{\mathbf{E}}^l + \overline{\mathbf{E}}^{nl} \tag{4.3}$$

where $\mathbf{E}^l$ and $\mathbf{E}^{nl}$ account for the linear and non-linear strains, respectively. In compact matrix notation they read:

$$\overline{\mathbf{E}}^l = \mathbf{H}\overline{\boldsymbol{\theta}}(\overline{\mathbf{u}}), \quad \overline{\mathbf{E}}^{nl} = \frac{1}{2}\overline{\mathbf{A}}\left(\overline{\boldsymbol{\theta}}(\overline{\mathbf{u}})\right)\overline{\boldsymbol{\theta}}(\overline{\mathbf{u}}) \tag{4.4}$$

Matrices $\mathbf{H}$ and $\overline{\mathbf{A}}\left(\overline{\boldsymbol{\theta}}(\overline{\mathbf{u}})\right)$ are defined by the following equations:

$$\mathbf{H} = \begin{bmatrix} 1 & 0 & 0 & 0 \\ 0 & 1 & 1 & 0 \\ 0 & 1 & 1 & 0 \\ 0 & 0 & 0 & 1 \end{bmatrix} \tag{4.5}$$

$$\overline{\mathbf{A}}\left(\overline{\boldsymbol{\theta}}(\overline{\mathbf{u}})\right) = \begin{bmatrix} \overline{u}_{,x} & 0 & \overline{w}_{,x} & 0 \\ \overline{u}_{,z} & \overline{u}_{,x} & \overline{w}_{,z} & \overline{w}_{,x} \\ \overline{u}_{,z} & \overline{u}_{,x} & \overline{w}_{,z} & \overline{w}_{,x} \\ 0 & \overline{u}_{,z} & 0 & \overline{w}_{,z} \end{bmatrix} \tag{4.6}$$

A virtual variation of the Green-Lagrange strain vector $\overline{\mathbf{E}}$ is:

$$\delta\overline{\mathbf{E}} = \delta\left\{\mathbf{H}\overline{\boldsymbol{\theta}}(\overline{\mathbf{u}}) + \frac{1}{2}\overline{\mathbf{A}}\left(\overline{\boldsymbol{\theta}}(\overline{\mathbf{u}})\right)\overline{\boldsymbol{\theta}}(\mathbf{u})\right\} = \mathbf{H}\delta\overline{\boldsymbol{\theta}}(\overline{\mathbf{u}}) + \overline{\mathbf{A}}\left(\overline{\boldsymbol{\theta}}(\overline{\mathbf{u}})\right)\delta\overline{\boldsymbol{\theta}}(\overline{\mathbf{u}}) \tag{4.7}$$

where δ stands for the virtual variation operator. The vectorial form of second Piola-Kirchhoff's stress tensor $\overline{\mathbf{S}}$ can be written in the following form:

$$\overline{\mathbf{S}} = \left\{ \overline{S}_{xx} \ \overline{S}_{xz} \ \overline{S}_{zx} \ \overline{S}_{zz} \right\}^T \tag{4.8}$$

The weak form of the governing equations is derived by means of the Principle of Virtual Displacement:

$$\delta\overline{\mathscr{L}} = \delta\overline{\mathscr{L}}_{int} - \delta\overline{\mathscr{L}}_{ext} = 0 \tag{4.9}$$

where $\overline{\mathscr{L}}$ is the total work, and $\overline{\mathscr{L}}_{int}$ the internal one:

$$\delta\overline{\mathscr{L}}_{int} = \int_{V_0} \delta\overline{\mathbf{E}}^T \overline{\mathbf{S}} dV \tag{4.10}$$

V_0 is the volume of the reference undeformed configuration since a total Lagrangian formulation is considered. $\overline{\mathscr{L}}_{ext}$ is the work done by the external forces. Within the used multiscale approach, in order to obtain the constitutive relation for macroscopic scale, a tensor $\overline{\mathbf{L}}$ is introduced. Its matrix form is as follows:

$$\overline{\mathbf{L}} = \begin{bmatrix} \overline{L}_{11} & \overline{L}_{12} & \overline{L}_{13} & \overline{L}_{14} \\ \overline{L}_{21} & \overline{L}_{22} & \overline{L}_{23} & \overline{L}_{24} \\ \overline{L}_{31} & \overline{L}_{32} & \overline{L}_{33} & \overline{L}_{34} \\ \overline{L}_{41} & \overline{L}_{42} & \overline{L}_{43} & \overline{L}_{44} \end{bmatrix} \tag{4.11}$$

Tensor $\overline{\mathbf{L}}$ accounts for the geometry and constitutive relation computed at the microscopic scale, and it plays a key role in transferring information from the microscopic scale to the macroscopic one. The macroscopic constitutive relation is obtained by a numerical finite element homogenization:

$$\overline{\mathbf{L}} = \frac{1}{\omega} \int_{\omega} \mathbf{L} d\omega \tag{4.12}$$

The explicit form of the microscopic tensor $\mathbf{L}$ will be discussed in the next section. By introducing the tensor $\overline{\mathbf{L}}$, the internal virtual work of the macroscopic scale, then, can be rewritten as (the details of its derivation can be found in Nezamabadi [17]):

$$\delta\overline{\mathscr{L}}_{int} = \int_{V_0} \delta\overline{\boldsymbol{\theta}}(\mathbf{u})^T \overline{\mathbf{L}\boldsymbol{\theta}}(\overline{\mathbf{u}}) dV \tag{4.13}$$

In the case of an external load proportional to a given load parameter λ, the external virtual work takes the following form:

$$\delta\overline{\mathscr{L}}_{ext} = \lambda \delta\overline{\mathbf{u}}^T \overline{\mathbf{f}} \tag{4.14}$$

where $\lambda\overline{\mathbf{f}}$ is the external applied force. The Principle of Virtual Displacements finally becomes:

$$\delta\overline{\mathscr{L}} = \int_{V_0} \delta\overline{\boldsymbol{\theta}}(\mathbf{u})^T \overline{\mathbf{L}\boldsymbol{\theta}}(\overline{\mathbf{u}}) dV - \lambda\delta\overline{\mathbf{u}^T\mathbf{f}} \tag{4.15}$$

Hierarchical beam elements. According to CUF, the displacement field is a-priori assumed over the thickness, and it is written in the following manner:

$$\overline{\mathbf{u}}\,(x,z) = \overline{F}_{\tau}\,(z)\,\overline{\mathbf{u}}_{\tau}\,(x) \quad \text{with} \quad \tau = 1,\ 2,\ \ldots,\ N_u \tag{4.16}$$

According to Einstein's notation, a twice repeated subscript implicitly represents a summation. $F_\tau\,(z)$ is a generic expansion function over the thickness and N_u is the number of accounted terms. This kinematic formulation allows to account for several beam theories since the choice of the expansion functions $F_\tau\,(z)$ and N_u are arbitrary. In the case of MacLaurin's polynomials (as used in this work), the explicit form of a generic N-order displacement field reads:

$$\begin{aligned} \overline{u}_x &= \overline{u}_{x1} + \overline{u}_{x2} z + \cdots + \overline{u}_{x(N+1)} z^N, \\ \overline{u}_z &= \overline{u}_{z1} + \overline{u}_{z2} z + \cdots + \overline{u}_{z(N+1)} z^N. \end{aligned} \tag{4.17}$$

As far as the displacements variation along the beam axis is concerned, a one-dimensional finite element approximation is used:

$$\overline{\mathbf{u}}\,(x,z) = \overline{F}_{\tau}\,(z)\,\overline{N}_i\,(x)\,\overline{\mathbf{q}}_{\tau i} \quad \text{with} \quad \tau = 1,\ 2,\ \ldots,\ N_u \quad \text{and} \quad i = 1,\ 2,\ \ldots,\ \overline{N}_n^e \tag{4.18}$$

$N_i\,(x)$ is a C^0 shape function, $\overline{N}_n^e$ the number of nodes per element and $\mathbf{q}_{\tau i}$ the nodal displacement unknown vector. The displacements gradient vector in the framework of CUF reads:

$$\overline{\boldsymbol{\theta}} = \left\{ \overline{F}_{\tau}\overline{N}_{i,x}\overline{q}_{\tau i}^{(u)}\ \overline{F}_{\tau,z}\overline{N}_i\overline{q}_{\tau i}^{(u)}\ \overline{F}_{\tau}\overline{N}_{i,x}\overline{q}_{\tau i}^{(w)}\ \overline{F}_{\tau,z}\overline{N}_i\overline{q}_{\tau i}^{(w)} \right\} = \overline{\mathbf{G}}_{\tau i}\overline{\mathbf{q}}_{\tau i} \tag{4.19}$$

where $\overline{\mathbf{G}}_{\tau i} \in \mathbb{R}^{4\times 2}$ and $\overline{\mathbf{q}}_{\tau i} \in \mathbb{R}^{2\times 1}$ are:

$$\overline{\mathbf{G}}_{\tau i} = \begin{bmatrix} \overline{F}_{\tau}\overline{N}_{i,x} & 0 \\ \overline{F}_{\tau,z}\overline{N}_i & 0 \\ 0 & \overline{F}_{\tau}\overline{N}_{i,x} \\ 0 & \overline{F}_{\tau,z}\overline{N}_i \end{bmatrix} \tag{4.20}$$

$$\overline{\mathbf{q}}_{\tau i}^T = \left\{ \overline{q}_{\tau i}^{(u)}\ \overline{q}_{\tau i}^{(w)} \right\} \tag{4.21}$$

Element tangent stiffness matrix. According to Eq. 4.13, the virtual internal work for one element becomes:

$$\begin{aligned} \delta\overline{\mathscr{L}}_{int}^e &= \int_{V_0^e} \delta\overline{\boldsymbol{\theta}}(\overline{\mathbf{u}})^T \overline{\mathbf{L}\boldsymbol{\theta}}(\overline{\mathbf{u}}) dV \\ &= \delta\overline{\mathbf{q}}_{\tau i}^T \int_{V_0^e} \overline{\mathbf{G}}_{\tau i}^T \overline{\mathbf{L}\mathbf{G}}_{\sigma j} dV \overline{\mathbf{q}}_{\sigma j} \\ &= \delta\overline{\mathbf{q}}_{\tau i}^T \left(\overline{\mathbf{K}}_{\tau\sigma ij}^{el} \right) \overline{\mathbf{q}}_{\sigma j} \end{aligned} \tag{4.22}$$

where V_0^e is an element reference volume and $\overline{\mathbf{K}}_{\tau\sigma ij}^{el}$ is the fundamental nucleus of the element stiffness matrix. This nucleus does not depend on the approximation order over the thickness (N_u) nor the number of nodes per element along the beam

axis ($\overline{N}_n^e$), see Carrera et al. [4]. It is worth noting that the macroscopic geometric nonlinearity is accounted for within the stiffness matrix in Eq. 4.22. The components of the stiffness matrix nucleus $\overline{\mathbf{K}}_{\tau\sigma ij}^{el}$ are:

$$\begin{aligned}
\overline{K}_{\tau\sigma ij}^{elxx} &= \overline{J}_{\tau\sigma i_{,x} j_{,x}}^{11} + \overline{J}_{\tau_{,z}\sigma_{,z} ij}^{22} + \overline{J}_{\tau_{,z}\sigma ij_{,x}}^{21} + \overline{J}_{\tau\sigma_{,z} i_{,x} j}^{12} \\
\overline{K}_{\tau\sigma ij}^{elxz} &= \overline{J}_{\tau\sigma_{,z} i_{,x} j}^{14} + \overline{J}_{\tau\sigma i_{,x} j_{,x}}^{13} + \overline{J}_{\tau_{,z}\sigma_{,z} ij}^{24} + \overline{J}_{\tau_{,z}\sigma ij_{,x}}^{23} \\
\overline{K}_{\tau\sigma ij}^{elzx} &= \overline{J}_{\tau_{,z}\sigma ij_{,x}}^{41} + \overline{J}_{\tau\sigma i_{,x} j_{,x}}^{31} + \overline{J}_{\tau_{,z}\sigma_{,z} ij}^{42} + \overline{J}_{\tau\sigma_{,z} i_{,x} j}^{32} \\
\overline{K}_{\tau\sigma ij}^{elzz} &= \overline{J}_{\tau_{,z}\sigma_{,z} ij}^{44} + \overline{J}_{\tau\sigma i_{,x} j_{,x}}^{33} + \overline{J}_{\tau\sigma_{,z} i_{,x} j}^{34} + \overline{J}_{\tau_{,z}\sigma ij_{,x}}^{43}
\end{aligned} \tag{4.23}$$

The generic term $J_{\tau_{(,z)}\sigma_{(,z)}}^{gh}$ is the following volume integral:

$$\overline{J}_{\tau_{(,z)}\sigma_{(,z)} i_{(,x)} j_{(,x)}}^{gh} = \int_{\Omega_e = h_e \times b_e} \int_{l_e} \overline{L}_{gh} \overline{F}_{\tau_{(,z)}} \overline{F}_{\sigma_{(,z)}} \overline{N}_{i_{(,x)}} \overline{N}_{j_{(,x)}} \, d\Omega \, dx \tag{4.24}$$

where h_e, b_e and l_e are the element thickness, width and length, respectively. Similarly, the external work of one element can be rewritten as following form:

$$\delta \overline{\mathscr{L}}_{ext}^e = \lambda \delta \overline{\mathbf{q}}_{\tau i}^T \overline{\mathscr{P}}_{\tau i}^{el} \tag{4.25}$$

where $\overline{\mathscr{P}}_{\tau i}$ can be written as:

$$\overline{\mathscr{P}}_{\tau i} = \overline{F}_{\tau}^T \overline{N}_i^T \overline{\mathbf{F}}^{el} \tag{4.26}$$

being $\overline{\mathbf{F}}^{el}$ an external force.

Resulting nonlinear problem. The internal virtual work for the whole beam is obtained by expanding the stiffness matrix nucleus for each element and assembling the resulting matrix in a classical finite element fashion:

$$\delta \overline{\mathscr{L}}_{int} = \delta \overline{\mathbf{q}}^T \overline{\mathbf{K}} \overline{\mathbf{q}} \tag{4.27}$$

where $\overline{\mathbf{K}}$ is global stiffness matrix and $\mathbf{q}$ is the global unknown vector. The global external virtual work $\delta \mathscr{L}_{ext}$ can be obtained in a similar manner:

$$\delta \overline{\mathscr{L}}_{ext} = \lambda \overline{\mathbf{q}} \overline{\mathscr{P}} \tag{4.28}$$

4.2.2 Microscopic Scale

Preliminaries. In the framework of the FE^2 method, the microscopic solution needs as input the macroscopic strain. Hooke's law for microscopic scale reads:

$$\mathbf{S} = \mathbf{CE} = \mathbf{C}[\mathbf{H} + \frac{1}{2}\mathbf{A}\left(\boldsymbol{\theta}(\mathbf{u})\right)]\boldsymbol{\theta}(\mathbf{u}) \tag{4.29}$$

where $\mathbf{C}$ is the material stiffness tensor. As a result, the microscopic internal virtual work reads:

$$\delta\mathscr{L}_{int} = \int_{\omega} \delta\mathbf{E}^T\mathbf{S}\, d\omega = \int_{\omega} \delta\boldsymbol{\theta}(\mathbf{u})^T[\mathbf{H} + \mathbf{A}\left(\boldsymbol{\theta}(\mathbf{u})\right)]^T\mathbf{C}[\mathbf{H} + \frac{1}{2}\mathbf{A}\left(\boldsymbol{\theta}(\mathbf{u})\right)]\boldsymbol{\theta}(\mathbf{u})d\omega \tag{4.30}$$

where ω is the volume in microscopic scale. Periodic boundary conditions are considered for the homogenisation problem:

$$\widetilde{\mathbf{u}}^+ - \widetilde{\mathbf{u}}^- = \mathbf{X}^+ - \mathbf{X}^-, \text{ on } \partial\omega. \tag{4.31}$$

where $\widetilde{\mathbf{u}}$ is a constrained microscopic displacement, and $\mathbf{X}$ represents the coordinate vector at microscale, which is a two components vector in two-dimensional problems in a implicit form here. $^+$ and $^-$ stand for a positive or negative boundary, respectively. $\partial\omega$ stands for the RVE frontier.

Homogenization and localization. The microscopic tensor $\mathbf{L}$ in Eq. 4.12 provides the material constitutive behavior of the microscopic scale. It consists of the product of the two unknowns $\mathscr{H}$ and $\mathscr{A}_{,x}$:

$$\mathbf{L} = \mathscr{H}^{(r)}\mathscr{A}_{,x} \tag{4.32}$$

$\mathscr{H}^{(r)}$ is:

$$\mathscr{H}^{(r)} = \boldsymbol{\beta}^T\mathbf{C}^{(r)}\boldsymbol{\beta} \tag{4.33}$$

where $\mathbf{C}^r$ is the constitutive tensor for each material phase r in the RVE and $\boldsymbol{\beta}$ is related with the derivative of the displacement field:

$$\boldsymbol{\beta} = \mathbf{H} + \mathbf{A}\left(\boldsymbol{\theta}(\mathbf{u})\right) \tag{4.34}$$

For two-dimensional problems, the second unknown term $\mathscr{A}$ is as follows:

$$\mathscr{A} = \left[\widetilde{\mathbf{u}}^{(11)}\ \widetilde{\mathbf{u}}^{(12)}\ \widetilde{\mathbf{u}}^{(21)}\ \widetilde{\mathbf{u}}^{(22)}\right] \tag{4.35}$$

in which $\widetilde{\mathbf{u}}^{(ij)}$ $(i, j = 1, 2)$, four two components vectors, are the solutions of linear deformation condition and periodic boundary conditions. The linear deformation boundary value problem is:

$$\begin{cases} \mathscr{L}_{int}(\widetilde{\mathbf{u}}^{(ij)}, \delta\mathbf{u}) = 0, \text{ in } \omega. \\ \widetilde{\mathbf{u}}^{(ij)} = \mathbf{X}^{(ij)}, \text{ on } \partial\omega. \end{cases} \tag{4.36}$$

with

$$\begin{aligned}\mathbf{X}^{(11)} &= \begin{bmatrix}1 & 0\\ 0 & 0\end{bmatrix}\mathbf{X},\ \mathbf{X}^{(12)} = \begin{bmatrix}0 & 1\\ 0 & 0\end{bmatrix}\mathbf{X}\\ \mathbf{X}^{(21)} &= \begin{bmatrix}0 & 0\\ 1 & 0\end{bmatrix}\mathbf{X},\ \mathbf{X}^{(22)} = \begin{bmatrix}0 & 0\\ 0 & 1\end{bmatrix}\mathbf{X}\end{aligned} \tag{4.37}$$

The periodic boundary value problem is:

$$\begin{cases}\mathscr{L}_{int}(\widetilde{\mathbf{u}}^{(ij)}, \delta\mathbf{u}) = 0, \text{ in } \omega.\\ \widetilde{\mathbf{u}}^{(ij)+} - \widetilde{\mathbf{u}}^{(ij)-} = \mathbf{X}^{(ij)+} - \mathbf{X}^{(ij)-}, \text{ on } \partial\omega.\end{cases} \tag{4.38}$$

with

$$\begin{aligned}\mathbf{X}^{(11)+} - \mathbf{X}^{(11)-} &= \begin{bmatrix}1 & 0\\ 0 & 0\end{bmatrix}(\mathbf{X}^{+} - \mathbf{X}^{-}),\ \mathbf{X}^{(12)+} - \mathbf{X}^{(12)-} = \begin{bmatrix}0 & 1\\ 0 & 0\end{bmatrix}(\mathbf{X}^{+} - \mathbf{X}^{-})\\ \mathbf{X}^{(21)+} - \mathbf{X}^{(21)-} &= \begin{bmatrix}0 & 0\\ 1 & 0\end{bmatrix}(\mathbf{X}^{+} - \mathbf{X}^{-}),\ \mathbf{X}^{(22)+} - \mathbf{X}^{(22)-} = \begin{bmatrix}0 & 0\\ 0 & 1\end{bmatrix}(\mathbf{X}^{+} - \mathbf{X}^{-})\end{aligned} \tag{4.39}$$

in which the four types of boundary conditions account for the in-plane and shear deformations. The process of exchanging information from macroscopic scale to microscopic scale is performed by constructing $\mathscr{A}$. In a two-dimensional case, the linear part of displacement at microscopic scale $\mathbf{u}^l$ can be considered as the sum of four contributions:

$$\mathbf{u}^l = \overline{\boldsymbol{\theta}}^{(11)}\widetilde{\mathbf{u}}^{(11)} + \overline{\boldsymbol{\theta}}^{(12)}\widetilde{\mathbf{u}}^{(12)} + \overline{\boldsymbol{\theta}}^{(21)}\widetilde{\mathbf{u}}^{(21)} + \overline{\boldsymbol{\theta}}^{(22)}\widetilde{\mathbf{u}}^{(22)} = \mathscr{A}\overline{\boldsymbol{\theta}}(\overline{\mathbf{u}}) \tag{4.40}$$

The nonlinear displacement part $\mathbf{u}^{nl}$ results from the following problem:

$$\mathscr{L}(\widetilde{\mathbf{u}}^{(ij)}, \delta\mathbf{u}) = \mathscr{F}^{nl}, \text{ in } \omega. \tag{4.41}$$

The total displacement is obtained by combining the two contributions:

$$\mathbf{u} = \mathbf{u}^l + \mathbf{u}^{nl} \tag{4.42}$$

Finite element discretization. For one element, the displacement field $\mathbf{u}$ in the domain can be discretized as classically done:

$$\mathbf{u} = \mathbf{N}\mathbf{q}^e \tag{4.43}$$

where $\mathbf{q}^e$ is the nodal displacement vector of the element, and $\mathbf{N}$ is a matrix whose components are the considered shape functions [22]. The remaining quantities for discretization of Eq. 4.30 can be written as:

$$\begin{aligned} \delta\mathbf{u} &= \mathbf{N}\delta\mathbf{q}, \\ \boldsymbol{\theta}(\mathbf{u}) &= \mathbf{G}\mathbf{q}^e, \\ \delta\boldsymbol{\theta}(\mathbf{u}) &= \mathbf{G}\delta\mathbf{q}^e. \end{aligned} \tag{4.44}$$

in which $\mathbf{G}$ is the shape function derivatives matrix. According to Eq. 4.29, the virtual work equation for a single element can be derived as follows:

$$\int_{\omega^e} \delta\mathbf{q}^e \mathbf{G}[\mathbf{H} + \mathbf{A}\left(\boldsymbol{\theta}(\mathbf{q}^e)\right)]^T \mathbf{S} d\omega = 0 \tag{4.45}$$

The right had side of previous equation is zero since no external force is considered at microscale. Substituting Eq. 4.43 and Eq. 4.44 into Eq. 4.30, the second Piola-Kirchhoff stress tensor becomes:

$$\mathbf{S} = \mathbf{C}\mathbf{H}\mathbf{G}\mathbf{q}^e + \frac{1}{2}\mathbf{C}\mathbf{A}\left(\boldsymbol{\theta}(\mathbf{q}^e)\right)\mathbf{G}\mathbf{q}^e \tag{4.46}$$

For the sake of brevity, the following notation is introduced:

$$\begin{aligned} \mathbf{B}^l &= \mathbf{H}\mathbf{G}, \\ \mathbf{B}^{nl}(\mathbf{q}^e) &= \mathbf{A}(\boldsymbol{\theta}(\mathbf{q}^e))\mathbf{G}, \\ \mathbf{B} &= \mathbf{B}^l + \mathbf{B}^{nl}(\mathbf{q}^e). \end{aligned} \tag{4.47}$$

By replacing Eq. 4.47, Eq. 4.45 and 4.46 are rewritten as follows:

$$\int_{\omega^e} \delta\mathbf{q}^{eT}(\mathbf{B}^{lT} + \mathbf{B}^{nl}(\mathbf{q})^T)\mathbf{S} d\omega = 0 \tag{4.48}$$

$$\mathbf{S} = \mathbf{C}\mathbf{B}^l\mathbf{q}^e + \frac{1}{2}\mathbf{C}\mathbf{B}^{nl}(\mathbf{q}^e)\mathbf{q}^e \tag{4.49}$$

The problem for the whole RVE is obtained by a finite element assembly procedure similarly to what done at macroscale.

4.2.3 Asymptotic Numerical Method

ANM is used to solve the resulting nonlinear problem. The macroscale solution point $(\overline{\mathbf{u}}^{j+1}, \overline{\mathbf{S}}^{j+1}, \overline{\lambda}^{j+1})$ at step $j+1$ is determined from the point solution $(\overline{\mathbf{u}}^{j}, \overline{\mathbf{S}}^{j}, \overline{\lambda}^{j})$ of the previous step j as starting solution point. According to the perturbation technique, an approached solution path at step $j+1$ is represented by truncated power series at the highest order N_{max}:

$$\begin{aligned} \overline{\mathbf{u}}^{j+1} &= \overline{\mathbf{u}}^{j} + \overline{a}^{p}\overline{\mathbf{u}}_{p}, \\ \overline{\mathbf{S}}^{j+1} &= \overline{\mathbf{S}}^{j} + \overline{a}^{p}\overline{\mathbf{S}}_{p}, \quad \text{with} \quad p = 1,\ 2,\ \ldots,\ N_{max} \\ \overline{\lambda}^{j+1} &= \overline{\lambda}^{j} + \overline{a}^{p}\overline{\lambda}_{p}. \end{aligned} \tag{4.50}$$

p represents the number of the series expansion order. The problem presents $3N_{max} + 1$ unknowns ($\overline{\mathbf{u}}_p, \overline{\mathbf{S}}_p, \overline{\lambda}_p, \overline{a}$), but only $3N_{max}$ equations are available. Therefore, a complimentary equation needs to be introduced. The path parameter $\overline{a}$ is defined by imposing it equal to the projection of the increment on the tangent direction ($\overline{\mathbf{u}}_1, \overline{\lambda}_1$) as follows:

$$\overline{a} = \overline{\mathbf{u}}_1(\overline{\mathbf{u}} - \overline{\mathbf{u}}^{j}) + \overline{\lambda}_1(\overline{\lambda} - \overline{\lambda}^{j}) \tag{4.51}$$

The validity range of truncated series is determined by the maximum value of the path parameter $\overline{a}_{max}$:

$$\overline{a}_{max} = (\varepsilon \frac{||\overline{u}_1||}{||\overline{u}_{N_{max}}||})^{\frac{1}{N_{max}-1}} \tag{4.52}$$

in which ε is a tolerance whose value is chosen by the user and $||\cdot||$ is the vector norm. $\overline{a}_{max}$ decreases when ε decreases. Substituting the approached solution Eq. 4.50 in Eq. 4.15, by collecting terms with the same powers of a, the algebraic equations for order 1 up to order p at macroscale can be derived. At microscopic scale, solution ($\mathbf{u}^{j+1}, \mathbf{S}^{j+1}$) is also represented by a truncated power series:

$$\begin{aligned} \mathbf{u}^{j+1} &= \mathbf{u}^{j} + a^{p}\mathbf{u}_{p} \quad \text{with} \quad p = 1,\ 2,\ \ldots,\ N_{max} \\ \mathbf{S}^{j+1} &= \mathbf{S}^{j} + a^{p}\mathbf{S}_{p} \quad \text{with} \quad p = 1,\ 2,\ \ldots,\ N_{max} \end{aligned} \tag{4.53}$$

By substituting the approached solution Eq. 4.53 in Eq. 4.48, and by collecting the terms with the same expansion order of a, the algebraic equations for order 1 up to order p at microscale can be obtained.

4.3 Results

Some numerical results are here presented. First, the proposed framework is validated towards a case study presented in the literature, see Nezamabadi et al. [18]. Then, more results are provided in a second case to show the comparison between the proposed method and a full FE^2 method, where two dimensional elements are used at both macro and micro scales.

The case study consists of a heterogeneous cantilever rectangular beam under a concentrated unit vertical force at the top point as shown in Fig. 4.2. The length of the beam is 100 mm, and the thickness is 10 mm. At the microscale, the material consists of a matrix with a circular inclusion (the volume fraction of the inclusion is equal to 28%). Constituents material properties are presented in Table 4.1. Results from Nezamabadi et al. [18] and computed via Ansys are presented.

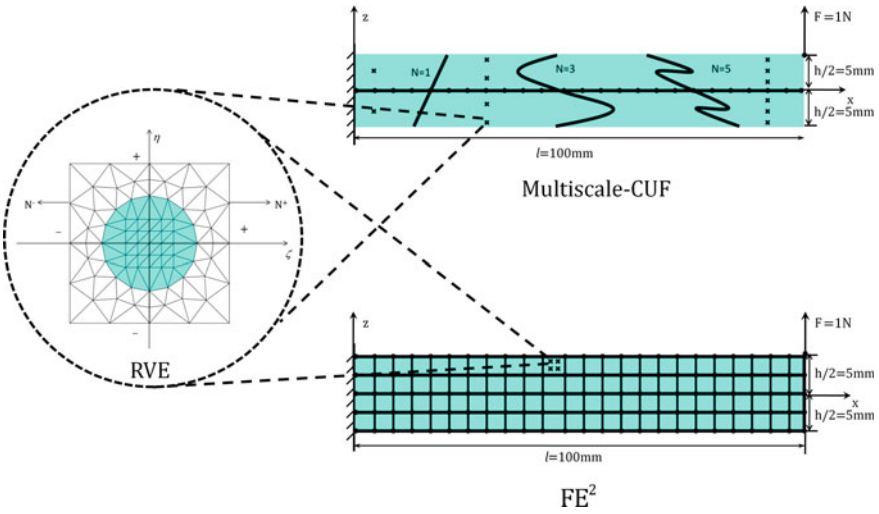

Fig. 4.2 Geometry of cantilever beam under static load with round inclusion RVE

Table 4.1 Material property of the constituents, first case

	Matrix	Inclusion
Young Modulus (MPa)	10,000	100,000
Poisson's ratio	0.3	0.3
Volume fraction	0.72	0.28

Table 4.2 Effective properties estimations

	E (GPa)	G (GPa)	v
Multiscale-CUF[a]	151.70	53.63	0.28
FE^2[b]	153.27	54.01	0.28
ANSYS[c]	153.36	54.03	0.28

[a] 144 triangular 6 nodes elements
[b] 4132 triangular 6 nodes elements
[c] 4044 PLANE 183 elements

A convergence analysis of the effective properties determination is carried out in Table 4.2. E stands for Young's modulus, G for the shear modulus and v for the Poisson ratio. The solution used here presents a mesh with 144 elements which proofs to be a good compromise between accuracy and computational costs. The comparison of degrees of freedoms between the proposed Multiscale-CUF model with different beam theories ($N = 2, 3, 4, 5$) and the FE^2 method from the reference paper is shown in Table 4.3 where a clear reduction of the DOFs number can be remarked.

Table 4.3 DOFs comparison between Multiscale-CUF and FE^2 models, where at macroscale Multiscale-CUF model uses 40 quadratic elements whereas a mesh 40×4 (length×thickness) is used for the FE^2 solution

	RVE number	DOFs (Microscale[a])	DOFs (Macroscale)
Multiscale-CUF $N = 5$	720	439′200	972
Multiscale-CUF $N = 4$	600	366′000	810
Multiscale-CUF $N = 3$	480	292′800	648
Multiscale-CUF $N = 2$	360	219′600	486
FE^2	1440	878′400	1′138

[a] DOFs (Microscale) is the number of RVEs multiplied by the DOFs of each RVE

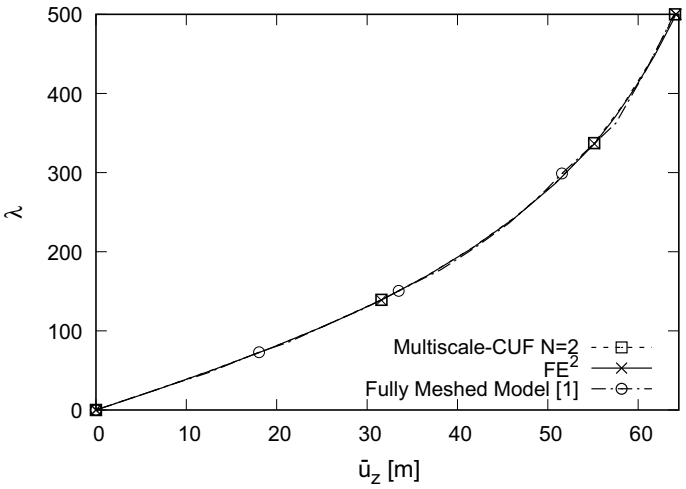

Fig. 4.3 Displacement $\overline{u}_z$ at $(l, h/2)$

It is well-known that the FE^2 method is much less computationally expensive compared with a fully meshed model. Thanks to the proposed approach, even the model with the highest order ($N = 5$) presents half of the DOFs of the FE^2 model. Furthermore, the results with $N = 2$ is already accurate as shown in Fig. 4.3, where the macroscale transverse displacement is presented.

As a second problem, at the structural level, a concentrated load is applied at the point $(l, 0)$, where the length and the width of the beam are 10 m and 1 m, respectively. At the microscopic scale, the same matrix-circular inclusion configuration as the previous case is considered where the constituent material properties are presented in Table 4.4. For this case, the load-displacement curves for $\overline{u}_x$ and $\overline{u}_z$ are presented in Fig. 4.4. $N = 2$ yields accurate results.

Moreover, as shown in Fig. 4.5, results show an excellent agreement at the microstructural level between the proposed model and the FE^2 model.

Table 4.4 Material Property of RVE constituents, second case

	Matrix	Inclusion
Young modulus (MPa)	100	1000
Poisson's ratio	0.3	0.3
Volume fraction	0.72	0.28

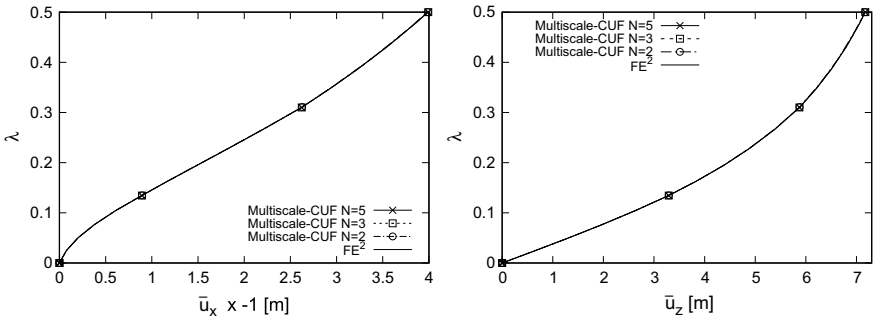

Fig. 4.4 Displacement $\overline{u}_x$ at $(l, h/2)$ and $\overline{u}_z$ at $(l, -h/2)$ of short cantilever beam

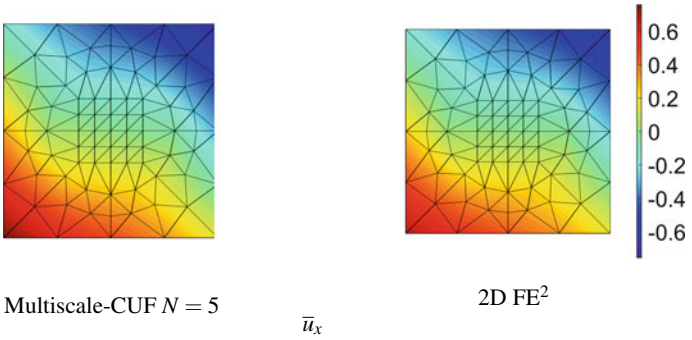

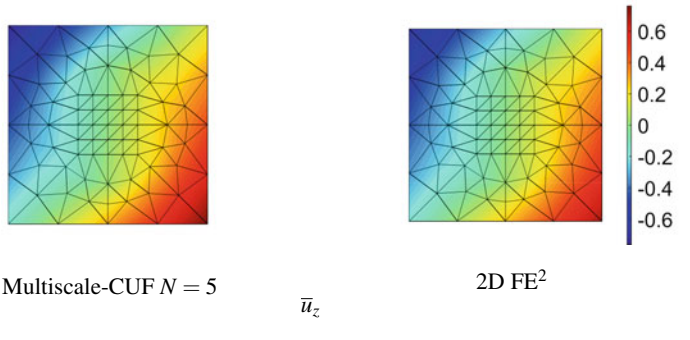

Fig. 4.5 Displacement u_x at $(l, h/2)$ and u_z at $(l, -h/2)$ of short cantilever beam at the last load step

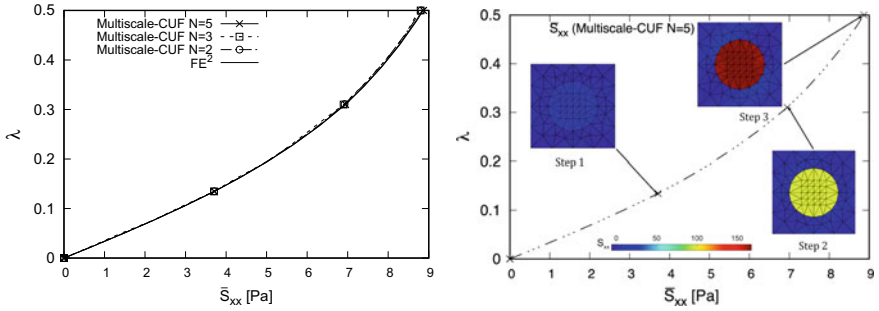

Fig. 4.6 Stress $\overline{S}_{xx}$ at $(l/4, -h/2)$ in a short cantilever beam. On the right-hand side figure, only the result for $N = 5$ is shown

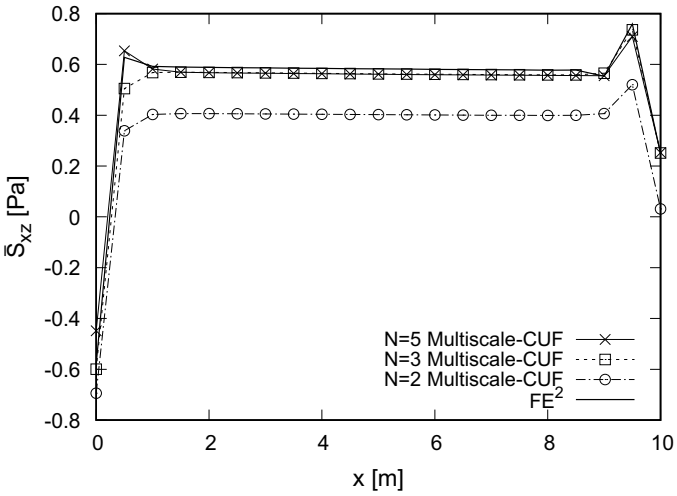

Fig. 4.7 Stress $\overline{S}_{xz}$ at $(z/l = 0)$ of short cantilever beam at last load step

From Fig. 4.6, it can be concluded that the stress components require a higher-order theory $(N = 5)$ to get an accurate result. In Fig. 4.7, the shear stress at the middle line $(z/l = 0)$ of the beam is plotted. The results with $N = 3$ and $N = 5$ compare well with the FE^2 model.

4.4 Conclusions

In this chapter, a novel multiscale model based on the FE^2 method and CUF is proposed. The robust and efficient nonlinear solver ANM is applied for the geometrically nonlinear problem. At the macroscopic scale, several higher-order beam

theories have been derived straightforwardly. Results have been validated through comparison with reference results and traditional FE^2 method.The numerical investigation shows that, for the considered cases, results via a quadratic beam theory already yield a good accuracy when displacements are sought. Besides, higher-order theories with an expansion order as high as five are mandatory for predicting an accurate shear stress field. It has been shown that the proposed approach possess the capability to simulate the nonlinear response at both the microscopic and macroscopic scale efficiently and accurately.

References

1. Aboudi J (1982) A continuum theory for fiber-reinforced elastic-viscoplastic composites. Int J Eng Sci 20(5):605–621
2. Aboudi J, Pindera MJ, Arnold SM (2003) Higher-order theory for periodic multiphase materials with inelastic phases. Int J Plast 19(6):805–847
3. Carrera E, Giunta G (2010) Refined beam theories based on a unified formulation. Int J Appl Mech 2(1):117–143
4. Carrera E, Giunta G, Petrolo M (2011) Beam structures: classical and advanced theories. Wiley-Blackwell
5. Cochelin B, Damil N, Potier-Ferry M (1994) Asymptotic-numerical methods and pade approximants for non-linear elastic structures. Int J Number Meth Eng 37(7):1187–1213
6. Damil N, Potier-Ferry M (1990) A new method to compute perturbed bifurcations: application to the buckling of imperfect elastic structures. Int J Eng Sci 28(9):943–957
7. Dvorak GJ, Bahei-El-Din YA (1979) Elastic-plastic behavior of fibrous composites. J Mech Phys Solids 27(1):51–72
8. Dvorak GJ, Benveniste Y (1992) On transformation strains and uniform fields in multiphase elastic media. Proc R Soc Lond A 437(1900):291–310
9. Eshelby JD (1959) The elastic field outside an ellipsoidal inclusion. Proc Royal Soc London Ser A 252:561–569
10. Feyel F, Chaboche JL (2000) FE^2 multiscale approach for modelling the elastoviscoplastic behaviour of long fibre sic/ti composite materials. Comput Methods Appl Mech Eng 183(3):309–330
11. Fish J, Shek K, Pandheeradi M, Shephard MS (1997) Computational plasticity for composite structures based on mathematical homogenization: Theory and practice. Comput Methods Appl Mech Eng 148(1–2):53–73
12. Hill R (1965) A self-consistent mechanics of composite materials. J Mech Phys Solids 13(4):213–222
13. Hu H, Belouettar S, Potier-Ferry M et al (2009) A novel finite element for global and local buckling analysis of sandwich beams. Compos Struct 90(3):270–278
14. Kouznetsova VG, Geers MGD, Brekelmans WAM (2004) Multi-scale second-order computational homogenization of multi-phase materials: a nested finite element solution strategy. Comput Methods Appl Mech Eng 193(48):5525–5550
15. Ladevèze P, Nouy A, Loiseau O (2002) A multiscale computational approach for contact problems. Comput Methods Appl Mech Eng 191(43):4869–4891
16. Mori T, Tanaka K (1973) Average stress in matrix and average elastic energy of materials with misfitting inclusions. Acta Mater 21(5):571–574
17. Nezamabadi S (2009) Méthode Asymptotique Numérique pour l'tude multiéchelle des instabilités dans les matériaux hétérogenes. PhD thesis, Université Paul Verlaine Metz

18. Nezamabadi S, Yvonnet J, Zahrouni H et al (2009) A multilevel computational strategy for handling microscopic and macroscopic instabilities. Comput Methods Appl Mech Eng 198(27):2099–2110
19. Pineda EJ, Waas AM, Bednarcyk BA et al (2009) Progressive damage and failure modeling in notched laminated fiber reinforced composites. Int J Fract 158(2):125–143
20. Xu R, Bouby C, Zahrouni H et al (2018) 3d modeling of shape memory alloy fiber reinforced composites by multiscale finite element method. Compos Struct 200:408–419
21. Yu W, Tang T (2007) Variational asymptotic method for unit cell homogenization of periodically heterogeneous materials. Int J Solids Struct 44(11–12):3738–3755
22. Zienkiewicz OC, Taylor RL (1977) The finite element method. McGraw-hill London

Part II
Failure Analysis, Impact and Health-Monitoring

Chapter 5
On the Effectiveness of Higher-Order One-Dimensional Models for Physically Nonlinear Problems

I. Kaleel, M. Petrolo, E. Carrera and A. M. Waas

Abstract The chapter presents numerical assessments of physically nonlinear problems through a class of refined one-dimensional theories based on the Carrera Unified Formulation (CUF). CUF is a hierarchical formulation to generate refined structural theories through a variable kinematic approach. Physical nonlinearities include von Mises plasticity and cohesive interface modeling for delamination of composites. This work aims to provide insights into the effect of kinematic enrichment on the overall nonlinear behavior of the structure. Guidelines stem from the evaluation of the accuracy and numerical efficiency of the proposed models against analytical and numerical approaches from the literature.

5.1 Introduction

The engineering practice tends to use simple analytical and finite element models for the stress analysis of structures to obtain computational efficiency and acceptable levels of accuracy. One-dimensional models (1D)—referred to as beams—fall within the scope of the analysis of slender structures such as columns, blades, and aircraft wings. Classical models such as Euler–Bernoulli (EBBT) [4, 12] and Timoshenko (TBT) [29] are common options for practical engineering analyses, but the effectiveness of such models depend on many assumptions such as geometrical dimensions, the prismatic nature of the structure, material homogeneity and isotropy. Since the accurate resolution of displacement and stress fields serves as a precursor for reliable nonlinear simulations, the validity of classical models in the nonlinear regime may be questionable and 2D, or 3D models are often mandatory with significant

I. Kaleel (✉) · M. Petrolo · E. Carrera
MUL2 Group, Department of Mechanical and Aerospace Engineering, Politecnico di Torino, Torino, Italy
e-mail: ibrahim.kaleel@polito.it

A. M. Waas
Department of Aerospace Engineering, University of Michigan Ann Arbor, Ann Arbor, MI, USA

M. Petrolo (ed.), *Advances in Predictive Models and Methodologies for Numerically Efficient Linear and Nonlinear Analysis of Composites*, PoliTO Springer Series,
https://doi.org/10.1007/978-3-030-11969-0_5

computational overheads. This chapter presents a novel approach in modeling the physical nonlinearities through higher-order 1D. Over the past few decades, significant efforts have led to the development of 1D models to solve diverse classes of physically nonlinear problems, and a brief overview follows.

Timoshenko and Gere extended the TBT to doubly-symmetric inelastic beams [30]. Abambres et al. employed the Generalized Beam Theory (GBT), originally developed by Schardt [25], for elastoplastic and post-buckling analyses of metallic thin-walled beam structures [1]. A class of 1D models stemmed from the Variational Asymptotic Beam Section Analysis (VABS), a variational asymptotic method which replaces a 3D structural model with a reduced-order model via asymptotic series [10]. The methodology also has nonlinear capabilities as shown by Pollayi et al. to model matrix cracking in helicopter rotors or wind turbine blades [23]. Jiang and Yu extended VABS to hyperelastic beams subjected to finite deformations and damage analyses of composites [16, 17]. Groh and Tessler developed a computationally efficient beam model to capture the delamination in laminated composite beams [14] via a nine degrees of freedom (DOF) and eight-DOF locking-free beam elements employing a mixed form of a refined zig-zag theory capturing the transverse stress field. Škec et al. [28] developed a 2D multilayered beam finite element for mixed-mode delamination analyses. Eijo et al. presented a method based on a refined zig-zag theory within a 1D finite element to model delamination in composite laminated beams [11].

The chapter deals with extensions of 1D CUF models for analyzing physically nonlinear problems and effectiveness concerning accuracy and computational efficiency. CUF is a hierarchical formulation that reduces 3D problems to 2D or 1D in a unified manner through a variable kinematic description [9]. The ability of 1D CUF models to recover accurate 3D stress fields efficiently can solve broad categories of physically nonlinear problems. Originally developed for plates and shells, 1D CUF models can deal with nonlinearities due to large deflections and post-buckling [22], elastoplastic and progressive damage analysis [8, 19, 20], and rotordynamics [13].

This chapter provides an overview of the nonlinear constitutive laws in Sect. 5.2, describes the structural modeling and FE framework in Sect. 5.3, highlights the most important aspects related to the solution schemes for nonlinear problems in Sect. 5.4, and shows results and comments in Sects. 5.5 and 5.6.

5.2 Nonlinear Constitutive Equations

The adopted Cartesian coordinate system has the beam axis along the y-axis and the cross-section along the $x - z$ plane. The displacement vector at any given point in the structural domain is

$$\mathbf{u}\,(x, y, z) = [u_x \quad u_y \quad u_z]^T \tag{5.1}$$

The vectorial notations for strain and stress states are

$$\boldsymbol{\varepsilon} = [\varepsilon_{xx} \quad \varepsilon_{yy} \quad \varepsilon_{zz} \quad \varepsilon_{yz} \quad \varepsilon_{xz} \quad \varepsilon_{xy}]^T; \quad \boldsymbol{\sigma} = [\sigma_{xx} \quad \sigma_{yy} \quad \sigma_{zz} \quad \sigma_{yz} \quad \sigma_{xz} \quad \sigma_{xy}]^T \tag{5.2}$$

Under the small strain assumption, geometrical and constitutive equations are

$$\boldsymbol{\varepsilon} = \mathbf{b}\,\mathbf{u}; \qquad \mathbf{b}^T = \begin{bmatrix} \partial_x & 0 & 0 & 0 & \partial_z & \partial_y \\ 0 & \partial_y & 0 & \partial_z & 0 & \partial_x \\ 0 & 0 & \partial_z & \partial_y & \partial_x & 0 \end{bmatrix}; \qquad \boldsymbol{\sigma} = \mathbf{C}\,\boldsymbol{\varepsilon} \tag{5.3}$$

where $\mathbf{b}$ is the differential operator and $\mathbf{C}$ reads a nonlinear generic constitutive material matrix with 36 constants to describe the stress-strain behavior.

5.2.1 Plasticity

The von Mises (J_2) theory hypothesizes that the material starts to yield when the J_2 invariant of the stress tensor attains a certain threshold, often referred to as the yield stress,

$$f = q(\boldsymbol{\sigma}) - \sigma_y(\bar{\varepsilon_p}) \tag{5.4}$$

where f is the von Mises yield locus, $q(\boldsymbol{\sigma})$ is the von Mises stress and σ_y is the yield stress which is a material input. A return mapping numerical scheme solves the local nonlinear problem, as detailed in Carrera et al. for CUF models [8]. In addition to metals, the nonlinear shear response exhibited by unidirectional laminates is due to inelastic deformation incurred by matrix constituents, often modeled through the von Mises based plasticity method.

5.2.2 Cohesive Modeling

Let us consider a domain Ω with a crack zone Γ_c as shown in Fig. 5.1. Essential boundary conditions act along the boundary Γ_u and prescribed tractions τ_i along Γ_n. The domain has two sub-domains, Ω_+ and Ω_-, along the crack boundary Γ_c, as depicted in Fig. 5.1. The equilibrium equations within the domain Ω are

$$\begin{aligned} \sigma_{ij,j} + \rho b_i = 0 \quad in \quad \Omega; \qquad \sigma_{ij} n_j = t_i \quad in \quad \Gamma_n \\ \sigma_{ij} n_j^+ = \tau_i^+ = -\tau_i^- = -\sigma_{ij} n_j^- n_j^- \quad in\ \Gamma_c \end{aligned} \tag{5.5}$$

where σ_{ij} is the stress field within the domain due to external loading $\mathbf{t}_i$, b_i are the body forces, ρ is the density of the material, and τ_i^+, τ_i^- are the closing tractions acting along the cohesive surface. Via the Principle of Virtual Displacements (PVD)

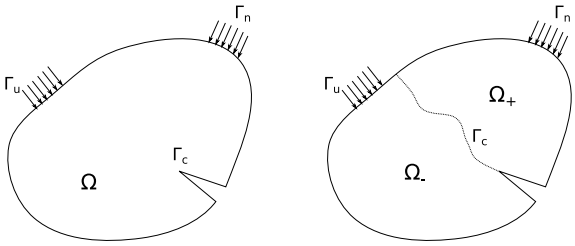

Fig. 5.1 Boundary value problem for cohesive formulation

and considering the additional contributions to work due to the cohesive crack, the weak formulation reads

$$\begin{aligned} &\delta L_{int} + \delta L_{coh} - \delta L_{ext} = 0, \quad \delta L_{int} = \int_{\Omega} \boldsymbol{\nabla}^s \delta \mathbf{u} : \boldsymbol{\sigma}\, dV \\ &\delta L_{coh} = \int_{\Gamma_c} \delta[[\mathbf{u}]] \cdot \mathbf{t}^c d\Gamma_c, \quad \delta L_{ext} = \int_{\Omega} \delta \mathbf{u} \cdot \mathbf{b} d\Omega + \int_{\Gamma_n} \delta \mathbf{u} \cdot \mathbf{t}\, d\Gamma_n \end{aligned} \tag{5.6}$$

where δ indicates the virtual variation, L_{int}, L_{coh} and L_{ext} refer to the bulk strain energy, work due to the cohesive crack, and external loading, respectively. $[[\mathbf{u}]]$ denotes the displacement jump across the cohesive surface,

$$[[u_i]] = u_i^+ - u_i^- \tag{5.7}$$

where u_i^+ and u_i^- denote the displacement of the given point i on the upper (Ω_+) and lower surface (Ω_-) of the interface.

The cohesive constitutive law describes the relationship between the cohesive traction τ_i and the displacement jump Δ_i across the interface,

$$\tau_j = D_{ji}\, \Delta_i \tag{5.8}$$

where D_{ji} is the constitutive operator and Δ_i is the displacement jump across the interface in the local coordinate system. Formulated within the context of the damage mechanics, the free energy density Ψ reads [27, 31]

$$\Psi(\Delta, d) = (1-d)\Psi^0(\Delta) - d\Psi^0(\delta_{3i}\langle -\Delta_3 \rangle) \tag{5.9}$$

where Ψ^0 is the free energy per unit surface. δ_{ij} is the Kronecker delta and d is the scalar damage parameter accounting for decohesion. The operator $< . >$ used in Eq. 5.9 is $< x >= \frac{1}{2}(x + |x|)$. By differentiating Eq. 5.9),

$$\tau_i = (1-d) D_{ij}^0 \Delta_j - d\, D_{ij}^0 \delta_{3j} \langle -\Delta_3 \rangle \tag{5.10}$$

where D_{ij}^0 is the undamaged stiffness tensor expressed in terms of the input penalty parameter. Under mixed-mode loading, the decohesion onset follows the quadratic criterion proposed by Ye [33],

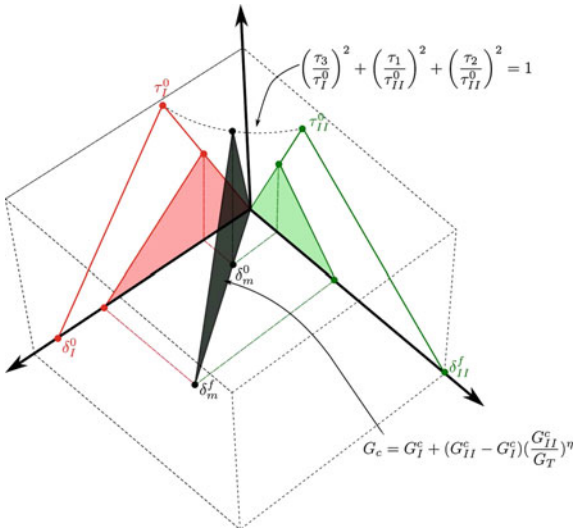

Fig. 5.2 Mixed-mode cohesive criteria

$$\left(\frac{<\tau_3>}{\tau_I^0}\right)^2+\left(\frac{\tau_1}{\tau_{II}^0}\right)^2+\left(\frac{\tau_2}{\tau_{II}^0}\right)^2=1 \tag{5.11}$$

where τ_i refers to the cohesive traction in direction i, τ_I^0 and τ_{II}^0 are the cohesive strengths under mode I and mode II, receptively. A bilinear constitutive law defines the cohesive traction and displacement jump [21]. The damage propagation criteria uses the expression for the critical energy release rate for mixed-mode proposed by Benzeggagh and Kenane [3],

$$G_c = G_I^c + (G_{II}^c - G_I^c)\left(\frac{G_I^c}{G_T}\right)^\eta; \quad G_T = \frac{G_{II}}{G_I + G_{II}} \tag{5.12}$$

where G_I^c and G_{II}^c are the critical energy release rates under mode I and mode II, respectively. η is an experimentally fitted parameter. As illustrated in Fig. 5.2, the area under the traction-displacement jump relation equals to the fraction toughness G_c.

5.3 Structural Theories and Finite Element Formulation

Within the 1D CUF formulation, $\mathbf{u}\,(x, y, z)$ becomes a generic expansion of primary unknowns as follows:

$$\mathbf{u}\,(x, y, z) = F_\tau(x, z)\,\mathbf{u}_\tau(y) \quad \forall \quad \tau = 1, 2, \ldots, M \tag{5.13}$$

where F_τ is the expansion function that defines the kinematic field on $x-z$ with M number of terms. $\mathbf{u}_\tau(y)$ is the vector of generalized displacements along the beam axis. The choice of the expansion function determines the class of 1D CUF models. This chapter deals with two classes of expansion functions, namely (a) Taylor Expansion (TE) and (b) Lagrange Expansion (LE). TE employ Maclaurin polynomials of the kind $x^i z^j$ [6], whereas LE use Lagrange polynomials [7]. Unlike TE, LE have pure displacement variables as detailed in [9]. The discretization along the y-axis follows the Finite Element Method (FEM),

$$\mathbf{u}\,(x,\,y,\,z) = N_i(y)\;F_\tau(x,\,z)\;\mathbf{u}_{\tau i}(y) \qquad \forall \quad \tau = 1,\ldots,M \quad i = 1,\ldots p+1 \tag{5.14}$$

$$\mathbf{u}_{\tau i} = [u_{x_{\tau i}}\;u_{y_{\tau i}}\;u_{z_{\tau i}}] \tag{5.15}$$

where N_i is the ith shape function of order p [2] and $\mathbf{u}_{\tau i}$ is the FE nodal vector. Numerical results employed three types of beam elements, B2 (two nodes), B3 (three nodes) and B4 (four nodes) leading to linear, quadratic and cubic approximations, respectively. The choice of shape functions used along the beam axis remains independent of the expansions employed for the cross-section.

5.3.1 Nonlinear Governing Equations

Within a nonlinear FEM context, the original problem becomes a set of incremental finite element equations solved at definite step instances,

$$\mathbf{f}_{int}(\mathbf{u}) - \mathbf{f}_{ext} = 0 \tag{5.16}$$

where $\mathbf{f}_{int}$ is the global internal force vector which is a function of global finite element displacement vector $\mathbf{u}$ and $\mathbf{f}_{ext}$ refers to the external force vector. In CUF, finite element arrays are

$$\mathbf{k}^{S}_{ij\tau s}\mathbf{u}_{\tau i} - \mathbf{p}_{sj} = 0 \tag{5.17}$$

where $\mathbf{k}_s^{ij\tau s}$ and $\mathbf{p}_{sj}$ refer to Fundamental Nuclei (FNs) of the secant stiffness matrix and the nodal loading vector, respectively. The strain vector relates to the generalized nodal unknowns via the differential operator of Eq. 5.3,

$$\boldsymbol{\varepsilon} = \mathbf{B}_{\tau i}\;\mathbf{u}_{\tau i} \qquad \mathbf{B}_{\tau i} = \mathbf{b}(N_i F_\tau) = \begin{bmatrix} N_i F_{\tau,x} & 0 & 0 \\ 0 & N_{i,y} F_\tau & 0 \\ 0 & 0 & N_i F_{\tau,z} \\ 0 & N_i F_{\tau,z} & N_{i,y} F_\tau \\ N_i F_{\tau,z} & 0 & N_i F_{\tau,x} \\ N_{i,y} F_\tau & N_i F_{\tau,x} & 0 \end{bmatrix} \tag{5.18}$$

Analogously for virtual variations,

$$\delta\boldsymbol{\varepsilon} = \mathbf{B}_{sj}\,\delta\mathbf{u}_{sj} \tag{5.19}$$

The strain energy becomes

$$\delta L_{int} = \delta\mathbf{u}_{sj}\int_V \left\{\mathbf{B}_{sj}^T C^S \mathbf{B}_{\tau i}\,dV\right\}\mathbf{u}_{\tau i} = \delta\mathbf{u}_{sj}\mathbf{k}_{ij\tau s}^S\mathbf{u}_{\tau i} \tag{5.20}$$

where C^S is the secant material matrix and the secant matrix $\mathbf{k}_{ij\tau s}^S$ is of size 3×3,

$$\mathbf{k}_{ij\tau s}^S = \begin{bmatrix} k_{ij\tau s}^{xx} & k_{ij\tau s}^{xy} & k_{ij\tau s}^{xz} \\ k_{ij\tau s}^{yx} & k_{ij\tau s}^{yy} & k_{ij\tau s}^{yz} \\ k_{ij\tau s}^{zx} & k_{ij\tau s}^{zy} & k_{ij\tau s}^{zz} \end{bmatrix} \tag{5.21}$$

Diagonal and off-diagonal terms have recurrent expressions stemming from the following:

$$\begin{aligned} k_{ij\tau s}^{xx} &= (C_{11}^S F_{s,x}N_j + C_{51}^S F_{s,z}N_j + C_{61}^S F_s N_{j,y})F_{\tau,x}N_i + (C_{15}^S F_{s,x}N_j + C_{55}^S F_{s,z}N_j + \\ &\quad C_{65}^S F_s N_{j,y})F_{\tau,z}N_i + (C_{16}^S F_{s,x}N_j + C_{56}^S F_{s,z}N_j + C_{66}^S F_s N_{j,y})F_\tau N_{i,y} \\ k_{ij\tau s}^{xy} &= (C_{12}^S F_{s,x}N_j + C_{52}^S F_{s,z}N_j + C_{62}^S F_s N_{j,y})F_\tau N_{i,y} + (C_{14}^S F_{s,x}N_j + C_{54}^S F_{s,z}N_j + \\ &\quad C_{64}^S F_s N_{j,y})F_{\tau,z}N_i + (C_{16}^S F_{s,x}N_j + C_{56}^S F_{s,z}N_j + C_{66}^S F_s N_{j,y})F_{\tau,x}N_i \end{aligned} \tag{5.22}$$

The virtual variation of external work is

$$\delta L_{ext} = \int_V \delta\mathbf{u}^T\mathbf{g}dV + \int_S \delta\mathbf{u}^T\mathbf{q}dS + \int_l \delta\mathbf{u}^T\mathbf{r}dl + \delta\mathbf{u}^T P_m \tag{5.23}$$

where $\mathbf{g}$, $\mathbf{q}$, $\mathbf{r}$ and P_m are body forces per unit volume, surface forces per unit area, line forces per unit line and concentrated forces acting at point m, respectively. Within the scheme of 1D CUF, the external load vector becomes

$$\mathbf{p}_{sj} = \int_V N_j F_s\,\mathbf{g}\,dV + \int_S N_j F_s\,\mathbf{q}\,dS + \int_l N_j F_s\,\mathbf{r}\,dl + N_j F_s P_m \tag{5.24}$$

For a generic, arbitrary higher-order beam elements of order p and expansion functions with M terms, the global assembly exploits the expanding indices of FN $\tau, s = 1, 2, \ldots M$ and $i, j = 1, 2, \ldots p+1$,

$$\mathbf{K}^S = \sum_{n=1}^{n_{elem}}\sum_{i,j=1}^{p+1}\bigcup_{\tau,s=1}^{M} k_{ij\tau s}^S \quad \mathbf{f}_{int} = \sum_{n=1}^{n_{elem}}\sum_{i=1}^{p+1}\bigcup_{\tau=1}^{M} f_{int_{\tau i}} \quad \mathbf{p} = \sum_{n=1}^{n_{elem}}\sum_{j=1}^{p+1}\bigcup_{s=1}^{M} p_{\tau i} \tag{5.25}$$

where $\sum$ is the finite element assembly operator that sum the corresponding contributions from all the elements based on the order of FE for given shared DOF.

$\bigcup$ is the CUF assembly operator which sums the corresponding contributions based on the theory of structure. $\mathbf{K}^S$, $\mathbf{f}_{int}$ and $\mathbf{p}$ are the global assembled secant stiffness matrix, global internal force vector and global external load vectors, respectively. The internal force vector derives from the multiplication of the stiffness matrix and the current displacement field. Therefore, Eq. 5.17 becomes

$$\mathbf{K}^S\mathbf{u} = \mathbf{p} \tag{5.26}$$

Readers are referred to the book by Carrera et al. [9] for detailed information on assembly procedure within CUF framework.

5.3.2 CUF Cohesive Elements

Within CUF, the displacement field on the upper and lower faces of the cohesive Lagrange element is

$$\mathbf{u}^+ = F_\tau N_i \mathbf{u}^+_{\tau i} \qquad \mathbf{u}^- = F_\tau N_i \mathbf{u}^-_{\tau i} \qquad [[\mathbf{u}]] = F_\tau N_i \, (\mathbf{u}^+_{\tau i} - \mathbf{u}^-_{\tau i}) \tag{5.27}$$

where $\mathbf{u}^+$ and $\mathbf{u}^-$ are the displacement along the upper and lower edge of the CS element, respectively. Figure 5.3 shows three classes of cohesive Lagrange cross-section element, namely, (a) four-node CS4—linear, (b) six-node CS6—quadratic, and (c) eight-node CS8—cubic. Therefore, the fundamental nuclei of cohesive forces become

$$f^+_{coh_{\tau i}} = \int_{\Gamma_c} F_\tau N_i \, \mathbf{u}^+_{\tau i} \, t^+ d\Gamma_c \quad f^-_{coh_{\tau i}} = \int_{\Gamma_c} F_\tau N_i \, \mathbf{u}^-_{\tau i} \, t^- d\Gamma_c \tag{5.28}$$

The derivation of the fundamental nuclei of the cohesive tangent nucleus makes use of a generic constitutive cohesive law in the rate form,

$$\dot{\mathbf{t}}^c = \mathbf{Q}\,\mathbf{D}\,\mathbf{Q}^T[[\dot{\mathbf{u}}]] = \mathbf{Q}\,\mathbf{D}\,\mathbf{Q}^T \; F_\tau N_i \, (\mathbf{u}^+_{\tau i} - \mathbf{u}^-_{\tau i}) \tag{5.29}$$

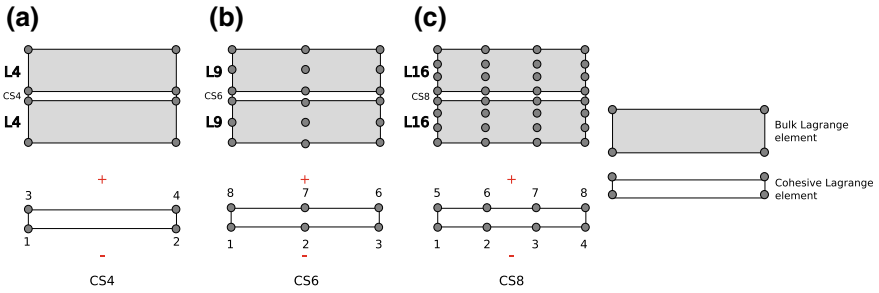

Fig. 5.3 Cohesive Lagrange cross-section elements

where $\mathbf{D}$ is the cohesive tangent material matrix along with orthogonal transformation matrix $\mathbf{Q}$. The fundamental nuclei for the cohesive tangent matrix stems from the linearization of the cohesive force vector (Eq. 5.28),

$$\mathbf{k}_{\mathbf{ij\tau s}}^{\mathbf{coh}} = \int_{\mathbf{c}} \mathbf{F}_{\tau}\mathbf{N}_{\mathbf{i}}\mathbf{Q}\,\mathbf{D}\,\mathbf{Q}^{\mathbf{T}}\mathbf{F}_{\mathbf{s}}\mathbf{N}_{\mathbf{j}}\mathbf{d}_{\mathbf{c}} \tag{5.30}$$

5.4 Nonlinear Solution Schemes

The nonlinear nature of the set of algebraic equations formulated in Eq. 5.16 necessitates iterative schemes such as the Newton-Raphson method (NR),

$$\boldsymbol{\phi}_{res} = \mathbf{K}^{S}\mathbf{u} - \mathbf{p} \tag{5.31}$$

where $\boldsymbol{\phi}_{res}$ is the unbalanced residual nodal vector. Next step requires the truncation of the Taylor series expansion to linear terms of $\boldsymbol{\phi}_{res}$ about a known solution $(\mathbf{u}, \mathbf{p})$,

$$\begin{aligned}\boldsymbol{\phi}_{res}(\mathbf{u}+\delta\mathbf{u}, \mathbf{p}+\delta\mathbf{p}) &= \boldsymbol{\phi}_{res}(\mathbf{u}, \mathbf{p}) + \frac{\partial\boldsymbol{\phi}_{res}}{\partial\mathbf{u}}\delta\mathbf{u} + \frac{\partial\boldsymbol{\phi}_{res}}{\partial\mathbf{p}}\delta\lambda\mathbf{p} = 0 \\ &= \boldsymbol{\phi}_{res}(\mathbf{u}, \mathbf{p}) + \mathbf{K}^{T}(\mathbf{u})\delta\mathbf{u} - \delta\lambda\mathbf{p} = 0\end{aligned} \tag{5.32}$$

where $\mathbf{K}^{T}(\mathbf{u})$ is the tangent stiffness matrix and λ is the load parameter ($\mathbf{p} = \lambda\mathbf{p}_{ref}$). Accounting for additional sets of constraint relationships for the load-scaling parameter λ within the global system of equation, the matrix form of Eq. 5.32 becomes

$$\begin{bmatrix}\mathbf{K}^{tan} & -\mathbf{p} \\ \mathbf{h}^{T} & s\end{bmatrix}\begin{bmatrix}\delta\mathbf{u} \\ \delta\lambda\end{bmatrix} = \begin{bmatrix}\boldsymbol{\phi}_{res} \\ -g\end{bmatrix} \tag{5.33}$$

where g is the path following constraint equation. $\mathbf{h}$ and scalar s are

$$g(\mathbf{u}_0, \lambda_0, \delta\mathbf{u}, \delta\lambda) = 0; \qquad \mathbf{h} = \frac{\partial g}{\partial\mathbf{u}}; \qquad s = \frac{\partial g}{\partial\lambda} \tag{5.34}$$

The constraint equation depends on the incremental scheme adopted. Standard incremental schemes, such as the displacement-control method, require $g(\delta\mathbf{u}, \delta\lambda) = 0$, whereas, load-controlled methods require $\delta\lambda = 0$. Based on the pioneering work of Riks, numerical strategies based on arc-length techniques are of interest to characterize complex equilibrium paths [24] and are powerful for nonlinear elastic problems [5]. Traditional arc-length techniques often fail when the analysis involves material instabilities with localized failure. Gutiérrez introduced a path-following constraint based on the energy-released rate for geometrically linear continuum damage models [15]. Based on the assumption that the unloading behavior remains elastic, the dissipation-based arc-length constraint equation is

$$g = \frac{1}{2}\mathbf{p}^T(\lambda_0 \Delta\mathbf{u} - \Delta\lambda\mathbf{u}_0) - \Delta\tau \tag{5.35}$$

where λ_0 and $\mathbf{u}_0$ are the last converged load factor and displacement vector and $\Delta\tau$ is the path parameter. The derivatives required for the construction of the global consistent tangent matrix (Eq. 5.33) read [32]

$$\mathbf{h} = \frac{\partial g}{\partial \mathbf{u}} = \frac{1}{2}\lambda_0\mathbf{p}^T, \qquad s = \frac{\partial g}{\partial \lambda} = -\frac{1}{2}\mathbf{p}^T\mathbf{u}_0 \tag{5.36}$$

The derivatives yield additional consistent tangent terms independent of the displacement and load increment, thereby making it computationally attractive.

At each NR iteration, the system of equations is

$$\begin{bmatrix} \mathbf{K}^{tan} & -\mathbf{p} \\ \mathbf{h}^T & s \end{bmatrix} \begin{bmatrix} d\mathbf{u} \\ d\lambda \end{bmatrix} = \begin{bmatrix} \boldsymbol{\phi}_{res}^k \\ -g^k \end{bmatrix}; \qquad \begin{bmatrix} d\mathbf{u} \\ d\lambda \end{bmatrix} = \begin{bmatrix} \Delta\mathbf{u} \\ \Delta\lambda \end{bmatrix}^{k+1} - \begin{bmatrix} \Delta\mathbf{u} \\ \Delta\lambda \end{bmatrix}^{k} \tag{5.37}$$

where k refers to the previous iteration and $\Delta\mathbf{u}$ and $\Delta\lambda$ are the displacement and load increments, respectively. It is evident from the Eq. 5.37 that the banded structure of the global consistent tangent matrix deteriorates due to the presence of additional terms pertaining to constraint equations. Using the Sherman-Morrison formula, the global consistent tangent (Eq. 5.37) becomes [26, 32]

$$\begin{bmatrix} d\mathbf{u} \\ d\lambda \end{bmatrix} = \begin{bmatrix} \mathbf{d}^I \\ -g^k \end{bmatrix} - \frac{1}{\mathbf{h}^T\mathbf{d}^{II} - s} \begin{bmatrix} (\mathbf{h}^T\mathbf{d}^I + g^k)\mathbf{d}^{II} \\ -\mathbf{h}^T\mathbf{d}^I - g^k(1 + \mathbf{h}^T\mathbf{d}^{II} - s) \end{bmatrix} \tag{5.38}$$

where the vectors $\mathbf{d}^I$ and $\mathbf{d}^{II}$ stem from the factorization of the structural tangent matrix $\mathbf{K}^{tan}$,

$$\mathbf{K}^{tan}\,\mathbf{d}^I = \boldsymbol{\phi}_{res} \qquad \mathbf{K}^{tan}\,\mathbf{d}^{II} = -\mathbf{p} \tag{5.39}$$

The amount of energy dissipated during a given load increment is always a monotonically increasing quantity. However, the solver can run into numerical issues at non-dissipative regions—such as pure elastic loading—on the equilibrium path as the path parameter can approach the machine precision. The addition of a robust switching algorithm based on the introduction of threshold values can alleviate this problem. The algorithm switches to displacement/force controlled loading in non-dissipative regions and switches back to dissipation-controlled according to the energy threshold. In addition, the path parameter $\Delta\tau$ needs adjustments during the course of computation to limit the number of steps. The adjustment is automatic via setting the optimal value of iterations per increment k_{opt}. The path parameter for a given increment i is [15]

$$\Delta\tau^i = \Delta\tau^{i-1}\frac{k_{opt}}{k^{i-1}} \tag{5.40}$$

where k^{i-1} refers to the number of iterations required in the last converged load step.

5.5 Numerical Applications

This section presents three numerical examples to assess the efficiency of higher-order models. The first example deals with a multilayered cantilever beam under bending with physical nonlinearities modeled through the von Mises plasticity model. The second numerical case deals with the delamination of a double cantilever beam test through the cohesive-based models. A numerical case based on the nonlinear micromechanical framework is the third numerical case.

5.5.1 Multilayered Cantilever Beam Under Bending

This example uses two configurations, (a) asymmetric two-layered and (b) symmetric three-layered, see Fig. 5.4. Classical beam models–EBBT and TBT—and the linear TE model (TE1) provide accurate responses in the linear regime whereas the lack of accurate stress resolution invalidates their effectiveness beyond the elastic limit. The results are consistent with findings by Carrera et al. for monolayered cantilever beam examples [8]. Figure 5.4 and Table 5.1 show comparisons against 3D FEM solutions

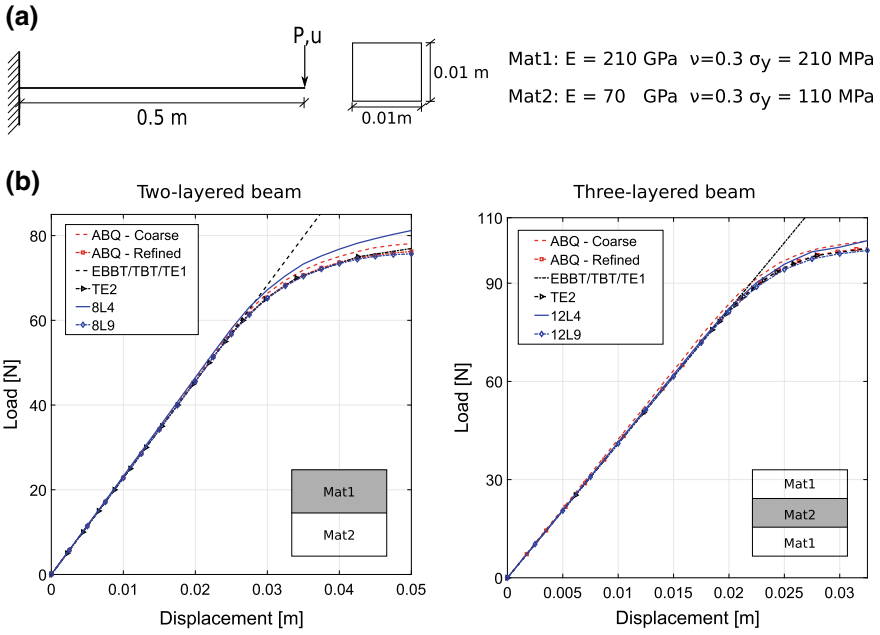

Fig. 5.4 Nonlinear response of multilayered cantilever beam under bending: **a** Geometry, boundary condition and material properties of the multilayered beam and **b** Comparison of equilibrium path for two-layered and three-layered beam configuration using various models

Table 5.1 Comparison of maximum accumulated equivalent plastic strain for different models for the multi-layered cantilever beam under bending

Model	Two layers		Three layers	
	DOF	$\bar{\varepsilon}_p^{max}[\times 10^{-3}]$	DOF	$\bar{\varepsilon}_p^{max}[\times 10^{-3}]$
3D FE models				
ABQ-Coarse	21084	7.66	42210	4.79
ABQ-Refined	64260	8.07	63210	4.89
TE models				
EBBT	363	–	363	–
TBT	605	–	605	–
TE1	1089	–	1089	–
TE2	2178	5.65	2178	3.57
LE models				
8L4[a]/12L4[b]	5445	5.35	7623	3.99
8L9[a]/12L9[b]	16335	8.56	23595	4.87

[a]Two layers
[b]Three layers

based on standard 8-node brick elements using ABAQUS with varying mesh density. Higher-order models can capture the nonlinear response with great computational efficiency without deteriorating the accuracy.

5.5.2 Double Cantilever Test

This problem highlights the necessity to capture high-stress gradients and its effects on the overall response. The geometry and boundary conditions along with material properties are in Fig. 5.5a. The beam model has a 4 L9 cross-section along with 2 CS6 cohesive elements interfaced between the layers. DOF for the CUF models are, 6290 for 180B2, 32490 for 360B2, and 16290 for 60B4. Verification makes use of an analytical solution based on a classical beam theory [21]. From Fig. 5.5c, the use of B4 proves to be effective whereas B2 tends to over-predict the results.

5.5.3 Nonlinear Response of Randomly Distributed RVE

This section deals with the inelastic pre-peak nonlinear response of a randomly distributed Representative Volume Element (RVE). Kaleel et al. investigated the pre-peak nonlinear and progressive failure analysis of fiber-reinforced composites for various classes of RVE and material systems based on a nonlinear micromechanical platform [18, 19]. The numerical examples focus on a twelve-fiber randomly distributed RVE equipped with the von Mises plasticity constitutive law to model the shear-driven nonlinear behavior of the matrix. The fiber is linear elastic. As depicted

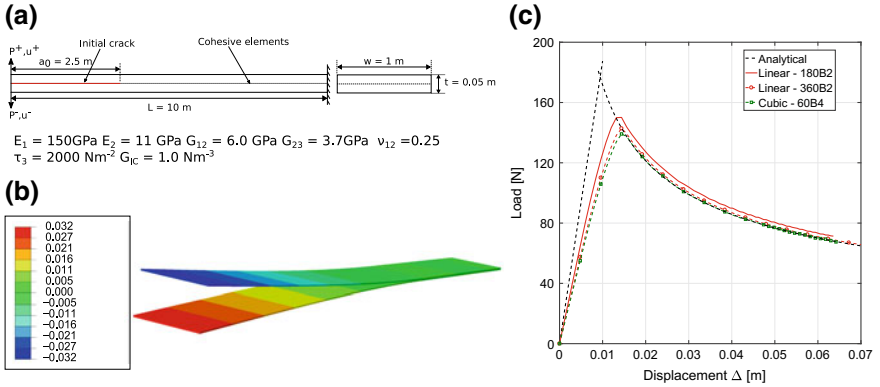

Fig. 5.5 Double cantilever beam test of a composite beam **a** Geometry and material properties of the DCB, **b** 3D deformed configuration for the 60B4 **c** Comparison of equilibrium curves along with analytical solutions

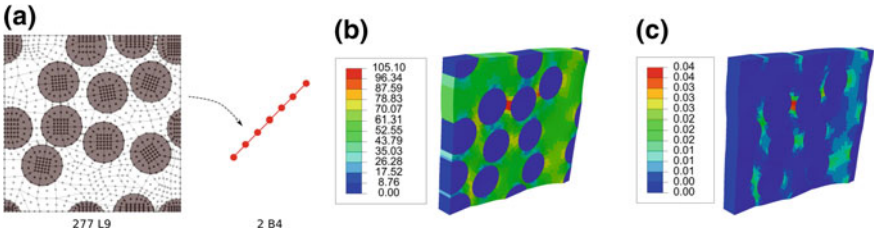

Fig. 5.6 Randomly distributed RVE under applied out-of-plane shear $\bar{\varepsilon}_{13}$ of 0.02 **a** CUF modeling, **b** von Mises stress (σ_{vm}), **c** Accumulated plastic strain

in Fig. 5.6a, the RVE has 277 L9 elements with 2 B4 elements, 24801 DOF, and subjected to an out-of-plane macro shear strain ε_{13} of 0.02 through periodic boundary conditions. The contour plots for the von Mises stress and accumulated plastic strain are in Fig. 5.6b, c, respectively. The results present severe local accumulations of stress and strain requiring higher-order kinematics along the cross-section. Kaleel et al. demonstrated that for the linear elastic homogenization CUF requires a one-order magnitude of DOF less than standard 3D brick elements and multi-fold decrease in computational time in the case of nonlinear analysis [18, 19].

5.6 Conclusion

This chapter has presented results on the nonlinear analysis of structures via refined 1D models. The physical nonlinearities consider plasticity and delamination effects. The structural modeling adopts the CUF to generate 1D models with enriched displacement field. The nonlinear structural analysis may benefit from the use of refined 1D models for two main reasons,

- The proper detection of 3D effects is fundamental to capture local effects due, for instance, to plasticity or delamination onsets. Classical models, such as Euler–Bernoulli and Timoshenko, cannot detect such effects along the cross-section of the structure and may lead to significantly wrong results.
- The need for iterative solution schemes leads to computational overheads limiting the complexity of the structural configuration. The use of 1D models can decrease such an overhead given that 10–100 times less unknown variables than 2D and 3D models are necessary.

As general guidelines, the use of Taylor expansions is recommended when the global response is of interest. The proper detection of highly 3D local effects requires the use of Lagrange expansions. The latter, moreover, have only pure displacements as DOF and can model the geometry and material characteristics of each component of the structure accurately without homogenization procedures.

References

1. Abambres M, Camotim D, Silvestre N (2014) GBT-based elastic-plastic post-buckling analysis of stainless steel thin-walled members. Thin-Walled Struct 83:85–102
2. Bathe KJ (1996) Finite element procedures. Prentice Hall, USA
3. Benzeggagh ML, Kenane M (1996) Measurement of mixed-mode delamination fracture toughness of unidirectional glass/epoxy composites with mixed-mode bending apparatus. Compos Sci Technol 56(4):439–449
4. Bernoulli D (1751) Commentarii academiae scientiarum imperialis petropolitanae, chapter De vibrationibus et sono laminarum. Petropoli
5. Carrera E (1994) A study on arc-length-type methods and their operation failures illustrated by a simple model. Comput Struct 50(2):217–229
6. Carrera E, Giunta G (2010) Refined beam theories based on a unified formulation. Int J Appl Mech 2:117–143
7. Carrera E, Petrolo M (2011) Refined beam elements with only displacement variables and plate/shell capabilities. Meccanica 47:537–556
8. Carrera E, Kaleel I, Petrolo M (2017) Elastoplastic analysis of compact and thin-walled structures using classical and refined beam finite element models. Mech Adv Mater Struct (in press)
9. Carrera E, Cinefra M, Petrolo M, Zappino E (2014) Finite element analysis of structures through unified formulation. Wiley, United Kingdom
10. Cesnik CES, Hodges DH (1997) VABS: a new concept for composite rotor blade cross-sectional modeling. J Am Helicopter Soc 42(1):27–38
11. Eijo A, Oñate E, Oller S (2013) A numerical model of delamination in composite laminated beams using the LRZ beam element based on the refined zigzag theory. Compos Struct 104:270–280
12. Euler L (1744) De curvis elasticis. Bousquet, Geneva
13. Filippi M, Carrera E (2016) Capabilities of 1D CUF-based models to analyse metallic/composite rotors. Adv Aircr Spacecr Sci 3(1):1–14
14. Groh RMJ, Tessler A (2017) Computationally efficient beam elements for accurate stresses in sandwich laminates and laminated composites with delaminations. Comput Methods Appl Mech Eng 320:369–395
15. Gutiérrez MA (2004) Energy release control for numerical simulations of failure in quasi-brittle solids. Commun Numer Methods Eng 20(1):19–29

16. Jiang F, Yu W (2016) Nonlinear variational asymptotic sectional analysis of hyperelastic beams. AIAA J 54(2):679–690
17. Jiang F, Yu W (2017) Damage analysis by physically nonlinear composite beam theory. Compos Struct 182:652–665
18. Kaleel I, Petrolo M, Waas AM, Carrera E (2017) Computationally efficient, high-fidelity micromechanics framework using refined 1D models. Compos Struct 181:358–367
19. Kaleel I, Petrolo M, Waas AM, Carrera E (2018) Micromechanical progressive failure analysis of fiber-reinforced composite using refined beam models. J Appl Mech 85(2)
20. Kaleel I, Petrolo M, Carrera E (2018) Elastoplastic and progressive failure analysis of fiber-reinforced composites via an efficient nonlinear microscale model. Aerotec Missili Spaz 97(2):103–110
21. Mi Y, Crisfield MA, Davies GAO, Hellweg HB (1998) Progressive delamination using interface elements. J Compos Mater 32(4):1246–1272
22. Pagani A, Carrera E (2017) Large-deflection and post-buckling analyses of laminated composite beams by Carrera Unified Formulation. Compos Struct 170:40–52
23. Pollayi H, Yu W (2014) Modeling matrix cracking in composite rotor blades within VABS framework. Compos Struct 110:62–76
24. Riks E (1979) An incremental approach to the solution of snapping and buckling problems. Int J Solids Struct 15(7):529–551
25. Schardt R (1994) Generalized beam theory-an adequate method for coupled stability problems. Thin-Walled Struct 19(2–4):161–180
26. Sherman J, Morrison WJ (1950) Adjustment of an inverse matrix corresponding to a change in one element of a given matrix. Ann Math Stat 21(1):124–127
27. Simo JC, Ju JW (1987) Strain- and stress-based continuum damage models—-i. formulation. Int J Solids Struct **23**(7):821–840
28. Škec L, Jelenić G, Lustig N (2015) Mixed-mode delamination in 2D layered beam finite elements. Int J Numer Methods Eng 104:767–788
29. Timoshenko SP (1921) On the correction for shear of the differential equation for transverse vibration of prismatic bars. Philos Mag Ser 41(6):744–746
30. Timoshenko SP, Gere JM (1991) Mechanics of materials. Springer-Science+Business Media, New York
31. Turon A, Camanho PP, Costa J, Davila CG (2006) A damage model for the simulation of delamination in advanced composites under variable-mode loading. NASA/Tech. Mem. 213277
32. Verhoosel CV, Remmers JJ, Gutiérrez MA (2009) A dissipation-based arc-length method for robust simulation of brittle and ductile failure. Int J Numer Methods Eng 77:1290–1321
33. Ye L (1996) Measurement of mixed-mode delamination fracture toughness of unidirectional glass/epoxy composites with mixed-mode bending apparatus. Compos Sci Technol 56(4):439–449

Chapter 6
Post-buckling Progressive Failure Analysis of Composite Panels Using a Two-Way Global-Local Coupling Approach Including Intralaminar Failure and Debonding

M. Akterskaia, E. Jansen, S. R. Hallet, P. M. Weaver and R. Rolfes

Abstract A novel two-way global-local coupling approach to model progressive separation of skin and stringer in combination with intralaminar damage in stiffened CFRP panels under compression is presented. The methodology makes it possible to examine the damage at two levels of accuracy, taking advantage of fast calculations at the global level and assessing in detail the damage propagation at the local level. The required appropriate information exchange between the global and local level in both directions has been attained. This chapter presents an overview of this efficient approach for progressive failure analysis of composite panels and illustrates the approach on the basis of a one-stringer panel, in particular for the case of skin-stringer debonding.

6.1 Introduction

Composite laminate stiffened panels are often used in aircraft design for fuselage structures by virtue of their excellent material properties such as high strength and high stiffness to weight ratio. In order to increase the failure load of these structures and to exploit possible reserves, a reliable simulation capable for capturing the post-buckling behavior of thin-walled structures is required. For this reason the accurate prediction of the failure behavior of composite structures is of high importance.

M. Akterskaia · E. Jansen (✉) · R. Rolfes
Institute of Structural Analysis, Leibniz Universität Hannover, Hannover, Germany
e-mail: e.jansen@isd.uni-hannover.de

S. R. Hallet · P. M. Weaver
Advanced Composites Centre for Innovation and Science, University of Bristol, Bristol, United Kingdom

P. M. Weaver
Bernal Institute, University of Limerick, Castletroy, Limerick, Ireland

M. Petrolo (ed.), *Advances in Predictive Models and Methodologies for Numerically Efficient Linear and Nonlinear Analysis of Composites*, PoliTO Springer Series,
https://doi.org/10.1007/978-3-030-11969-0_6

Global-local methods are attractive approaches that can reduce computational effort on the one hand and accurately explore the damage onset and propagation in localized areas on the other hand. The main characteristic of the global-local strategy presented is its ability to perform progressive failure analysis of typical panel-type composite structures. The approach demonstrated in this chapter uses achievements from the work of Hühne et al. [24]. A two-way methodology was formulated for intralaminar damage that includes matrix cracking and fiber breakage and the approach was applied to a one-stringer composite panel. This work was extended by Akterskaia et al. [2] and applied to investigate the effect of localized predamage and to examine progressive damage in a multi-stringer panel. Later on a novel global-local approach was developed by Akterskaia et al. [3] to simulate the skin-stringer debonding by using cohesive and discrete interface elements at the local and global level, respectively. The main challenge of the method was the development of a reliable method to transfer degraded properties from the local to the global level. A combination of intralaminar damage and skin-stringer debonding has been considered in subsequent work [4] including a comparison with experimental results.

The global-local method developed includes all critical failure modes observed during various experiments performed for stiffened panels under compression [16, 19, 32, 39, 49], such as intralaminar and interlaminar failure modes. Intralaminar damage distinguishes between fiber and matrix failure. Interlaminar damage in the present work is assumed to be debonding between the skin and the flange of the stringer. The main advantage of the global-local approach developed is that local models can be easily allocated based on the information from the global model, while the size of the local models can be adjusted and extended with damage evolution through the coupling steps, and additional local models can also be created and analyzed. Another important aspect of the approach is that the information about the damage state obtained from the local model is transferred to the global model in the form of corresponding degraded stiffness properties. This strategy ensures that the damage progression is accounted for at the global level and a progressive failure analysis can be executed. Due to the relatively small size of the local models together with the simple geometry and material definition at the global model level using shell elements, the saving in computational effort compared to an analysis with a full model using solid elements is potentially significant. In view of the accuracy of the damage modeling at the local level and including the resulting material nonlinearity at the global level, the approach developed thereby provides an efficient tool for progressive failure analysis.

The flowchart of the two-way global-local coupling procedure is shown in Fig. 6.1. First, the global model is analyzed with a linear material model. Afterwards, the critical areas where the damage might initiate are detected and based on this information the local models are created. Making use of the results of the local model analysis, new reduced properties are calculated and transferred back to the global model. The global analysis is repeated to ensure that no new areas with damage appear or existing ones are extended due to the stress redistribution. If no new damage has been identified, the prescribed load is increased and the next “coupling step” is started. The global-local analysis is conducted until the final failure of the structure occurs.

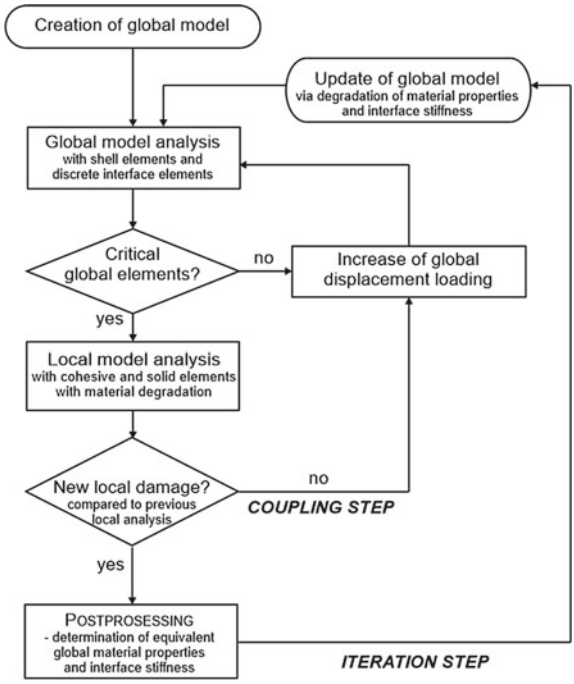

Fig. 6.1 Flowchart of two-way coupling procedure for intralaminar failure and skin-stringer debonding

The objective of the current chapter is to present an overview of the global-local approach developed and in particular to discuss the coupling procedure for intralaminar damage and skin-stringer debonding, respectively. The approach is illustrated for the specific typical case of a one-stringer panel under compression, in which skin-stringer debonding takes place.

6.2 Theory

Laminated fiber-reinforced composites consist of stacked laminae of different orientations, where each lamina represents a single layer of polymer matrix with embedded uni-directional fibers. Composite laminates may experience various failure mechanisms es a result of applied loads, boundary conditions or material properties of constituents. These failure modes could be classified into two categories: intralaminar and interlaminar failure. Intralaminar failure includes matrix cracking, fiber breakage and matrix-fiber decohesion. Interlaminar damage describes separation of adjacent layers, called delamination. Failure criteria have been extensively developed in order to determine the critical regions where the damage occurs, to identify failure types and final loads that the composite structure could sustain. Material degradation models have been suggested to account for a gradual or instant decrease of the load carrying capacity simulating real failure mechanisms.

6.2.1 Intralaminar Damage

Three main types of intralaminar failure are to be distinguished: matrix cracking, fiber breakage and debonding of the interface between matrix and fiber. Matrix cracking usually is not a catastrophic failure mode which means that it does not usually lead alone to a final collapse and the structure with matrix cracks can still bear applied loads due to fiber reinforcement. However, matrix cracks tend to grow and especially crack coalescence can provoke delamination of a composite laminate [50]. Fibers are the main constituents of the composite designed to withstand loads. Hence, fiber failure is a crucial failure mechanism that can lead to a spontaneous structural failure. Fiber-matrix interface decohesion is commonly a result of a fiber pull-out from the matrix. Failure analysis of composite structures requires determination of failure criteria in order to account for the damage initiation. Strength-based criteria comprising different stress-based and strain-based criteria are generally used. These criteria can be formulated as a global failure criteria defined by one equation or they can distinguish between failure modes as well as between tension or compressive load applied. An extensive overview and comparison of different failure criteria that have been actively developed and extended since 1950s is given in World Wide Failure Exercises (WWFE), see Hinton et al. [23], Kaddour and Hinton [27], Kaddour et al. [28] and Kaddour et al. [29].

6.2.1.1 Intralaminar Damage Onset and Propagation

Matrix cracking and fiber breakage are the principal intralaminar damage modes observed in composite panels under compression. In order to determine the initiation of damage and to examine the propagation through the structure, the Linde criterion [33] is chosen, which stems from the Puck criterion and distinguishes between fiber and matrix damage . It should be noted that the global-local approach is not restricted to any particular damage criterion. The material damage model performs a gradual degradation of material properties based on the fracture energies of the fiber and matrix material. In the following, X_T and X_C are the longitudinal tensile and compressive strength, respectively, and Y_T and Y_C denote the transverse in-plane tensile and compressive strength, respectively, while S_A is the axial shear strength and C_{ij} are the components of the stiffness matrix. The appearance of the matrix and fiber damage is detected by the following two equations:

$$f_m = \sqrt{\frac{Y_T}{Y_C}(\varepsilon_{22})^2 + \left(Y_T - \frac{Y_T^2}{Y_C}\right)\frac{\varepsilon_{22}}{C_{22}} + \left(\frac{Y_T}{S_A}\right)^2 \varepsilon_{12}^2} > \frac{Y_T}{C_{22}} \tag{6.1}$$

$$f_f = \sqrt{\frac{X_T}{X_C}(\varepsilon_{11})^2 + \left(X_T - \frac{X_T^2}{X_C}\right)\frac{\varepsilon_{11}}{C_{11}}} > \frac{X_T}{C_{11}} \tag{6.2}$$

where the strain components ε_{ij} correspond to the local material coordinates related to the orientation of the fibers, index *1* refers to the fiber direction, while index *2* (in-plane) and index *3* (out-of-plane) refer to the transverse directions.

Linde et al. introduced two different damage parameters d_m and d_f to distinguish between fiber failure and matrix failure:

$$d_m = 1 - \frac{Y_T}{f_m} e^{-\left(\frac{C_{22} Y_T (f_m - Y_T) L_c}{G_m}\right)} \tag{6.3}$$

$$d_f = 1 - \frac{X_T}{f_f} e^{-\left(\frac{C_{11} X_T (f_f - X_T) L_c}{G_f}\right)} \tag{6.4}$$

The characteristic element length L_C is applied to alleviate the mesh dependency of the degradation model. G_m and G_f denote the matrix and fiber strengths, respectively. The damage parameters d_m and d_f are used to calculate the effective elasticity tensor C_d:

$$\mathbf{C} = \begin{pmatrix} (1-d_f)C_{11} & (1-d_f)(1-d_m)C_{12} & (1-d_f)C_{13} & 0 & 0 & 0 \\ & (1-d_m)C_{22} & (1-d_m)C_{23} & 0 & 0 & 0 \\ & & C_{33} & 0 & 0 & 0 \\ & & & (1-d_f)(1-d_m)C_{44} & 0 & 0 \\ & symmetric & & & C_{55} & 0 \\ & & & & & C_{66} \end{pmatrix}. \tag{6.5}$$

6.2.1.2 Global-Local Approach for Intralaminar Damage

Within the context of global-local methods, one-way coupling and coupling methods that solve global and models simultaneously prevail. The term one-way coupling method usually refers to the global-local approaches where the information is transferred only in one direction, either from the global to local level, or, rarely, from the local to global level. The submodeling technique or so-called zooming technique was successfully used in the past for one-way global-local transition. Examples can be found in the works of Mote [36], Noor [37], Mao and Sun [35], and Whitcomb [46]. Another type of the global-local techniques consists of embedding a finer local model into the coarse global model and to solve the systems of equations concurrently. This approach does not allow for any changes to the size or the location of the local model being introduced during the calculations. Hence, it is impossible to account for the damage progression or to create new local models during analysis. For the time being only several methods have been elaborated that can treat global and local models separately. The multiscale projection method by Löhnert and Belytschko [34] uses XFEM to model fracture and crack propagation and to examine the macrocracks and microcracks interactions leading to damage. Labeas et al. [31] presented the adaptive progressive damage modeling technique to predict the damage initiation and

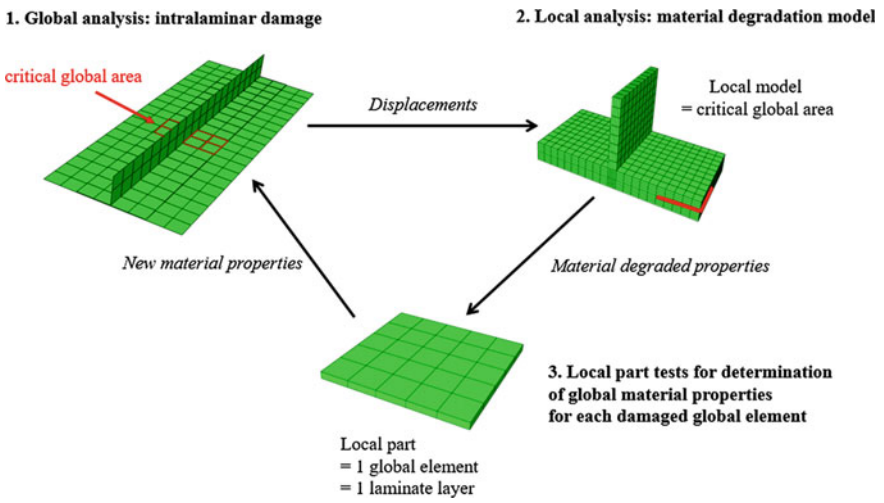

Fig. 6.2 Two-way global-local coupling procedure for intralaminar damage

evolution in composite structures based on progressive damage modeling technique and the submodeling procedure. The degraded material properties for the global model were calculated based on the mean values of the local engineering constants obtained after damage evolution. Chrupalla et al. [14] formulated the homogenization-based iterative two-way multiscale approach (HIMSA) to account for local effects on the global behavior of composite structures. The discussed above methods mainly differ in the approach used to determine how to degrade material properties and how to transfer them back from the local to the global level. The more accurate homogenization technique for matrix and fiber failure proposed by Hühne [24] was adopted by Akterskaia et al. [2] for the intralaminar damage. An extension to this method for the local-global transition is demonstrated below.

A progressive failure analysis is carried out until the global failure of the structure occurs. The skin and the stringer of the panel in the global model are represented by conventional shell elements using one element through the thickness including all laminate layers in order to reduce computational costs. The coarse model with linear elasticity at the global level is used to identify the areas where matrix or fiber failure are expected to take place by applying the Linde criterion, see Eqs. 6.1 and 6.2. Based on these critical areas at the global level, local models with a finer solid element mesh are created through the submodeling procedure with displacements from the global solution serving as boundary conditions for the local models. These local models include the discussed above material degradation model by Linde, see Eqs. 6.3–6.5. After completion of the local models' numerical analysis the degraded engineering properties are extracted. The global-local procedure is illustrated in Fig. 6.2.

It is important to note that direct application of the degraded properties from the local to global level is not possible due to the mesh size difference between two models. For this reason, the homogenization approach formulated by Hühne et al.

[24] is applied for this case to obtain the effective global degraded properties. Each global element ply obtains each new reduced material property using the following procedure: First, two tension and one shear tests are performed in order to determine the Young's modulus in longitudinal and transverse directions, E_{11} and E_{22}, respectively, Poisson's ratios ν_{12} and ν_{23}, and the shear modulus G_{12}. Then another step proposed here is employed to transform obtained properties from the principal material coordinates to the global coordinates for an orthotropic lamina [26]:

$$\frac{1}{E_x} = \frac{1}{E_1} cos^4\theta + \left(\frac{1}{G_{12}} - \frac{2\nu_{12}}{E_1}\right) sin^2\theta cos^2\theta + \frac{1}{E_2} sin^4\theta \tag{6.6}$$

$$\nu_{xy} = E_x \left(\frac{\nu_{12}}{E_1}(sin^4\theta + cos^4\theta) - \left(\frac{1}{E_1} + \frac{1}{E_2} - \frac{1}{G_{12}}\right) sin^2\theta cos^2\theta\right) \tag{6.7}$$

$$\frac{1}{E_y} = \frac{1}{E_1} sin^4\theta + \left(\frac{1}{G_{12}} - \frac{2\nu_{12}}{E_1}\right) sin^2\theta cos^2\theta + \frac{1}{E_2} cos^4\theta \tag{6.8}$$

$$\frac{1}{G_{xy}} = 2\left(\frac{2}{E_1} + \frac{2}{E_2} + \frac{4\nu_{12}}{E_1} - \frac{1}{G_{12}}\right) sin^2\theta cos^2\theta + \frac{1}{G_{12}}(sin^4\theta + cos^4\theta) \tag{6.9}$$

The main difference with a methodology employed by Hühne et al. [24] is the way these above equations transform angles, which works correctly even for $\pm 45°$ angles. Previously the material with fiber orientation of $\pm 45°$ was considered homogeneous as it has the same Young's modulus in these directions.

6.2.2 Interlaminar Damage

Laminated composite structures experience delamination and, in particular, skin-stringer debonding as one of the prime failure mechanisms in stiffened panels under compression [7, 13, 20, 40, 41, 45, 49].

Accurate modeling of the delamination of the full structure is computationally expensive. That is the reason for the development of the reliable global-local procedure that could be an efficient compromise allowing lower simulation time on the one hand, and considering the damage onset and evolution at both levels, on the other hand.

6.2.2.1 Delamination in Composite Materials

Delamination occurs under various combinations of loads leading to a significant reduction of the load-carrying capacity of the structure. Two approaches are

commonly used to numerically model delamination: Virtual Crack Closure Technique (VCCT) and cohesive interface elements.

The VCCT is based on fracture mechanics and uses Irwin's assumption to calculate the energy released rate needed for the crack extension taking it equal to the work required to close this crack back to its original length. This work is calculated from multiplication of nodal point forces and corresponding differences in nodal displacements [30]. This approach was further elaborated by Rybicki and Kanninen for application to the finite element analysis [42]. In order to determine whether the crack propagates, the calculated energy release rate has to be compared to the threshold of the critical value. The main drawback of the VCCT is that it predicts only crack propagation assuming that the crack initiation location is known in advance. Another difficulty is related to the accurate calculation of the nodal variables for the energy release rate. It either implies the requirement of a very fine three-dimensional solid element mesh, or a remeshing technique should be applied during the analysis [44].

The Cohesive Zone Model approach (CZM) assumes existence of a softening region in front of the crack tip, a cohesive damage zone. This idea originates from Dugdale [17] and Barenblatt [8]. Dugdale suggested that there is a plastic area ahead of the crack tip with constant stresses equal to the yield strength. Barenblatt in turn assumed that the stresses vary during the deformation process. Hillerborg [22] proposed a formulation based on this latter suggestion. The method of Hillerborg allows the crack to grow and, more importantly, predicts the crack initiation, which takes place when the tensile stress at the crack tip reaches the tensile strength. Interface elements based on the CZM rely on the traction-separation law that is formulated in terms of the traction versus displacement jumps at the interface of potential crack. For the pure mode loading most commonly an initially linear behavior until the tensile strength σ_{max} is reached, is followed by the softening region until the crack surfaces are completely separated which results in zero traction. Different shapes of the softening curve, such as linear, exponential or trapezoidal, have been proposed in the literature [15]. The fracture toughness G_c is equal to the area under the traction-separation curve and total crack opening takes place when this toughness is dissipated completely. The penalty stiffness has to be chosen as large as possible because physically no degradation of the cohesive elements should take place at this region and also quite low to avoid numerical issues [43].

Mixed-mode loading that could include interaction between normal and two shear modes often takes place and requires additional attention. Initiation and growth criteria should be chosen that are able to account for the interaction of complex loadings. Usually stress-based criteria are preferred. One of the commonly used criterion predicting delamination onset is quadratic stress criterion:

$$\left(\frac{<\sigma_n>}{N_{max}}\right)^2 + \left(\frac{\sigma_s}{S_{max}}\right)^2 + \left(\frac{\sigma_t}{T_{max}}\right)^2 = 1 \tag{6.10}$$

Here $< \ldots >$ represents Macauley brackets operator applied here to remind that

compression is generally not involved in interface separation. σ_n is a stress in the pure normal mode, σ_s and σ_t are nominal stresses acting in the first and second shear directions and N_{max}, S_{max}, T_{max} are the corresponding strengths.

One of the most commonly applied criterion for the delamination propagation under mixed-mode loading is Benzeggagh and Kenane criterion [9] extended to three dimensional cases.

$$G_c = G_{IC} + (G_{IIc} - G_{IC}) \left(\frac{G_{II} + G_{III}}{G_I + G_{II} + G_{III}} \right)^{\eta} \tag{6.11}$$

where G_{IC} and G_{IIC} are mode I and II fracture toughness and G_I, G_{II}, G_{III} are single mode energy release rates corresponding to fracture modes I, II and III. Their sum is the total energy release rate. The parameter η is determined empirically [44].

A scalar damage variable d is usually utilized to identify the damage state. This damage variable changes from 0 when no damage is detected to 1 when the crack is fully opened. Camanho et al. [13] suggested to determine the damage variable for the monotonic loading as following:

$$d = \frac{\delta_{fail}(\delta - \delta_{init})}{\delta(\delta_{fail} - \delta_{init})} \tag{6.12}$$

where d is a damage variable, δ is a current maximum relative displacement, δ_{init} corresponds to the displacement of the delamination beginning and δ_{fail} is a displacement of the complete failure.

The stiffness of the cohesive element in linear traction-separation law is defined as following [13]:

$$K = \begin{cases} K_0 & \delta < \delta_{init} \\ (1-d)K_0 & \delta_{init} < \delta < \delta_{fail} \\ 0 & \delta > \delta_{fail} \end{cases} \tag{6.13}$$

where K_0 is an initial penalty stiffness that is degraded after displacement δ reaches the value of δ_{init} and becomes 0 when the crack opening is equal to δ_{fail}.

For the uncoupled behavior of normal and shear components of stresses Abaqus [1] provides the following stress-strain relation for the elastic behavior:

$$\begin{pmatrix} \sigma_n \\ \sigma_s \\ \sigma_t \end{pmatrix} = \begin{pmatrix} K_n & 0 & 0 \\ 0 & K_s & 0 \\ 0 & 0 & K_t \end{pmatrix} \begin{pmatrix} \varepsilon_n \\ \varepsilon_s \\ \varepsilon_t \end{pmatrix} = \mathbf{K}\,\varepsilon \tag{6.14}$$

where σ_n is an out-of-plane stress, σ_s and σ_t are shear stresses and the same holds for the corresponding strains ε_n, ε_s and ε_t. K_n is a normal stiffness that is related to the Mode I delamination, K_t and K_s are in-plane stiffnesses responsible for the Mode II and III damage behavior respectively. Here strains are defined as separation displacements divided by initial thickness t of the cohesive element:

$$\varepsilon_n = \frac{\delta_n}{t}, \varepsilon_s = \frac{\delta_s}{t}, \varepsilon_t = \frac{\delta_t}{t} \tag{6.15}$$

The Cohesive Zone Model could be implemented by means of the continuum (CCZM) or discrete (DCZM) approaches. To apply CCZM continuum type interface elements are used to model the cohesive process zone in front of the crack tip. This technique was widely examined and extended by Allix and Ladeveze [6], Turon et al. [43], Camanho and Dávila [13] among others. One of the drawbacks of CCZM is a high number of cohesive elements required to mitigate mesh sensitivity. DCZM method consists of using point-wise discrete elements instead of continuum elements. This method was applied and developed by Borg et al. [12], Wisnom and Chang [47], Xie and Waas [48], Hallett and Wisnom [21], Jiang et al. [25]. To accurately predict the delamination onset and evolution the DCZM requires accurate calculation of forces or stresses in nodes of the elements which also involves high computational costs. Therefore, a multi-scale approach could be regarded as a desirable methodology allowing reduction of the computational time while keeping a required accuracy of the delamination modeling.

6.2.2.2 Global-Local Approach for Skin-Stringer Debonding

As for the case of the interlaminar damage mainly one-way coupling approaches exist nowadays for the modeling skin-stringer debonding in stiffened panels. Reinoso et al. [39] applied solid elements at the global level and cohesive elements at the local level to represent the interface layer. The information was transferred from the global to local levels through the submodeling procedure. Bertolini et al. [10] suggested global-local one-way coupling approach to model skin-stringer debonding in stiffened panels subjected to different loads. VCCT technique was utilized. Global-local analysis by Orifici et al. [38] employed user-defined multi-point constraint (MPC) elements controlled by Virtual Crack Closure Technique (VCCT) for the interface layer and the ply damage degradation. Local models were defined based on the stress distribution. Alesi et al. [5] presented a global-local method based on coupling with multipoint constraints. Faggiani and Falzon [18] elaborated an optimization technique based on a genetic algorithm to improve the damage resistance for the skin-stringer interface in the postbuckling regime of stiffened panels by finding an optimized stacking sequence. The authors made use of a global-local method in their optimization analysis. A substitution method by Bettinotti et al. [11] for the multi-scale analysis of delamination under high-velocity impact allows a concurrent run of global and local analyses. The main limitations of existing coupling approaches usually relate to efficient detection of critical areas at the global level and information transition from the local to the global level, thus not allowing to observe the damage evolution. That is the reason of the development of a novel global-local method by Akterskaia et al. [3] that ensures accurate exchange of information between both levels to perform an accurate progressive failure analysis.

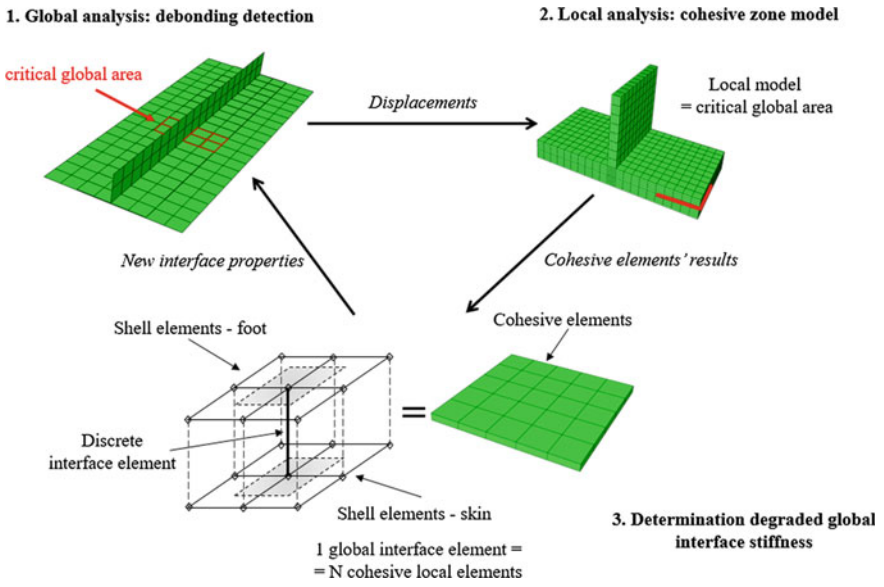

Fig. 6.3 Two-way global-local coupling procedure for skin-stringer debonding

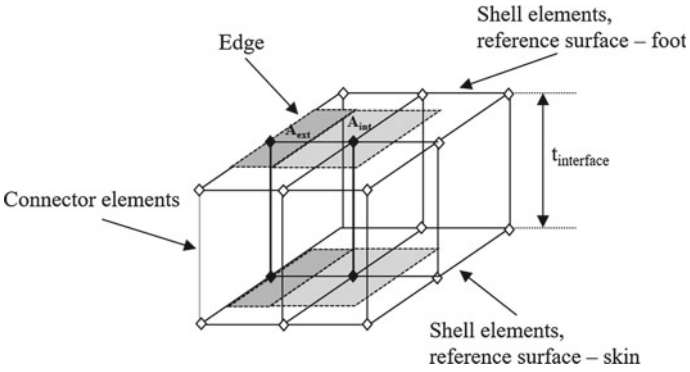

Fig. 6.4 Shell elements connected by connector elements

The global-local method formulated by Akterskaia et al. [3] is illustrated in Fig. 6.3 and it consists of several coupling loops repeated consecutively until the final collapse occurs. First, the global model is created using a coarse mesh and shell elements to model the structure. Discrete elements of the connector type in Abaqus [1] tie the corresponding nodes of shell elements as shown in Fig. 6.4. These elements enable the definition of stiffness in three directions. Following the stiffness definition, the normal and shear stiffness are calculated as:

$$K_n = \frac{EA}{t} \tag{6.16}$$

$$K_s = \frac{GA}{t} \tag{6.17}$$

where E and G are the Young's modulus and shear modulus of the adhesive zone, respectively, A is the area associated with a node and t is the interface thickness.

Normal and shear stresses at the nodes of connector elements are calculated from forces in connector elements distinguishing between free edge and internal nodal areas that are tied by connector elements:

$$\sigma_{i3} = \frac{F_i}{A_{el}}, \quad i = 1, 2, 3 \tag{6.18}$$

where F_i is a nodal force, A_{el} determines a nodal area of applied force and taken as the sum of one quarter of each element area tied to that node. Therefore, A_{el} either represents the full in-plane area of the shell element A_{int}, referring to Fig. 6.4 for interior connectors, or a half of this area denoted as A_{ext} corresponding to the case when connectors tie the edges, or a quarter if connectors tie corner elements. Index i specifies local Cartesian directions. σ_{33} corresponds to the normal stress that acts through the thickness, σ_{13} and σ_{23} are two in-plane shear stresses. In Eq. 6.16, the penalty stiffness definition includes non-material parameters, such as nodal area A and thickness t. The force F_i from Eq. 6.18 is proportional to the corresponding stiffness which means that the stresses σ_{i3} are independent from the nodal area and depend only on the thickness of the adhesive layer. Connector elements that tie four-node 2D shell elements are presented in Fig. 6.4, indicating the nodal areas A_{ext} and A_{int}.

Based on the areas detected as probable damaged regions, the local models are created with a finer mesh and solid elements are used to capture full three-dimensional stress states. The interface layer is modeled with cohesive elements with a bilinear traction-separation law to simulate delamination. Displacements as kinematic boundary conditions are transferred to the boundaries from the global to the local model through a submodeling procedure. Moreover, the stress-based criterion, see Eq. 6.10, is used to predict the initiation of delamination, while the Benzeggagh and Kenane criterion, see Eq. 6.11, is applied for modeling the delamination propagation.

In order to transfer degraded stiffness back from the local to the global level, a special procedure is required that accounts for the mesh difference between two levels. First, to calculate the degraded stiffness of each connector element, an averaged local stiffness is calculated for each area that corresponds to one connector element:

$$K_{local} = \frac{\sum_{i=1}^{N} K_{local,i}}{N} = \frac{\sum_{i=1}^{N} (1 - d_i) K_{local,0}}{N} = K_{local,0} \left(1 - \frac{\sum_{i=1}^{N} d_i}{N} \right) \tag{6.19}$$

where $K_{local,0}$ is the initial stiffness of a cohesive element at the local level, i is one of N local cohesive elements with corresponding damage variable d_i. The damage multiplication factor in brackets of Eq. 6.19 is utilized to reduce the global interface stiffness. Thus, the information about the damage state is transferred from the local to the global level. After reduction of the global interface stiffness of each damaged connector element, the global analysis is conducted again to verify if the stress redistribution provokes further skin-stringer debonding. During this global analysis, the initial interface stiffness is used until the time increment where the damage criterion was met, since that point the updated stiffness is applied.

6.3 Application of the Two-Way Coupling Procedure to a One-Stringer Composite Panel

In order to demonstrate the application of the global-local approach described above, a stiffened composite panel with one T-stringer under compression shown in Fig. 6.5 is analyzed with particular attention to a skin-stringer debonding. The results are described by Akterskaia et al. [3]. The unidirectional layups of the skin and the stringer are symmetrical $[0, 90]_s$ of a nominal thickness of 0.25 mm and the interface layer has a thickness of 0.2 mm. One of the transverse edges is fully clamped, except for the longitudinal direction, and displacement is prescribed in compression at the

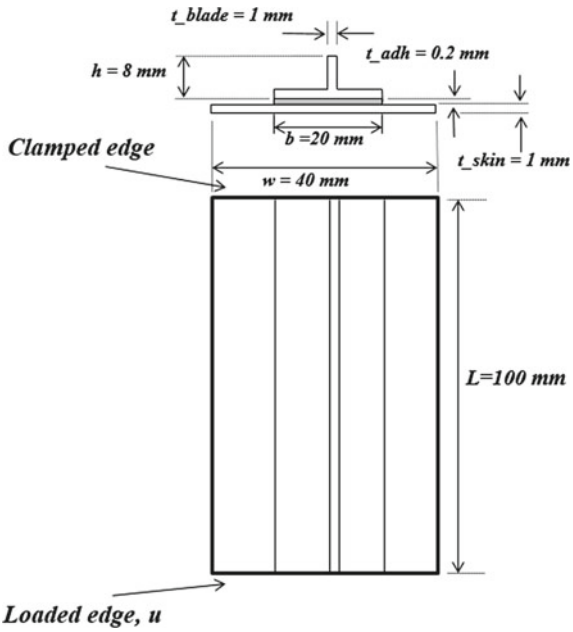

Fig. 6.5 Geometry of the tested one-stringer stiffened panel

opposite edge. The panel's length is 100 mm and the width is 40 mm, the stringer has a width of 20 mm and a height of 8 mm. Material properties of the composite layup are the following: Young's modulus in longitudinal direction $E_{11} = 146.5$ GPa, Young's modulus in transverse direction $E_{22} = 9.7$ GPa, shear modulus $G_{12} = 5.1$ GPa and Poisson's ratio $\nu_{12} = 0.28$. The interface layer is characterized by the Young's modulus $E_{int} = 3.0$ GPa and $\nu_{int} = 0.4$, similar to [24].

6.3.1 Reference Model

The reference model corresponds to a three-dimensional solid element model of the stiffened panel. Solid linear elements with an in-plane side-length of 1 mm are used to model the skin and the stringer of the panel and cohesive non-zero thickness elements for the interface layer. One element per lamina in thickness direction is used resulting in 0.25 mm size in out-of-plane. The application of the higher order solid elements does not demonstrate any improvements in accuracy while detecting the damage onset or the collapse load. A material degradation model, see Eqs. 6.3–6.5, was utilized through the UMAT procedure available in the Abaqus finite element software [1]. A bilinear traction-separation law was used for cohesive elements. Interface element stiffness was assumed to be 10^6 N/mm^3, and $\tau_I = 61$ MPa, $\tau_{II} = 61$ MPa are interfacial strength in mode I and mode II, respectively. Four cohesive elements per side of the solid element were used to decrease the size of one cohesive element to 0.25 mm which was recommended after parametric studies. The quadratic stress criterion given in Eq. 6.10 and the Benzeggagh and Kenane criterion from Eq. 6.11 were applied to determine the cohesive elements behaviour. A constraint is utilized (the *Tie constraint in Abaqus [1]) to connect cohesive elements to the solid elements of skin and stringer foot. Based on parametric studies, a viscous damping parameter has been used in this nonlinear analysis [1] to mitigate the convergence difficulties related to cohesive elements and their softening behavior. The first eigenmode of the linear buckling analysis for the stiffened panel was applied as an imperfection in the nonlinear analysis.

6.3.2 Global Model: Linear Material Model

The global model with a coarse mesh and shell elements with reduced integration was built for the skin and the stringer with a side length of 5 mm. Connector elements of Cartesian type [1] represented the connection between these panel components. In order to calculate the real distances and forces at nodes, the shell reference surfaces were offset from the middle surfaces towards the lower and upper surfaces respectively.

The quadratic stress criterion given in Eq. 6.10 was used to determine the critical regions, where the onset of skin-stringer separation may take place. Buckling

was triggered similarly as for the reference model by applying an initial geometrical imperfection as the first eigenmode of the linear buckling analysis. To avoid interpenetration of the skin and the stringer layers, a *Clearance option available in Abaqus is utilized [1]. When the local models analyses are performed, the reduced stiffnesses of connector elements are obtained following Eq. 6.19. Afterwards the global analysis is started again in order to verify if the reduction in the stiffness of interface elements would not lead to the new damaged areas. Initial stiffnesses in connector elements are used until the displacement of the debonding initiation, from that moment the updated stiffnesses are applied. If there is no new damage onset or propagation is detected, then the prescribed displacement is further increased.

6.3.3 Local Model: Skin-Stringer Debonding

Local models are created based on the information about critical areas obtained from the global model analysis. These local models include the skin and the stringer to capture the skin-stringer debonding initiation and evolution in details. With an aim of comparison, the local model mesh size and the element type were chosen the same as for the reference model. Thus, the linear solid elements are used to model the skin and the stringer, while cohesive elements with bilinear traction-separation law are employed for the interface layer. After completion of the local models analyses, the degraded damage variables d, described in Eq. 6.12, are extracted for each cohesive element during the post-processing procedure.

6.3.4 Local-Global Transition

A special averaging procedure has been proposed, see Eq. 6.19, in order to enable the transfer of the information about the skin-stringer debonding from the local to the global level. Due to the different mesh sizes in the global and local models a special mapping technique is required, see Eq. 6.19. First, by using coordinates of local and global elements the corresponding cohesive elements to one global connector element are found and then the degraded stiffnesses are recalculated.

6.3.5 Results

The final collapse was attained through six coupling steps (Fig. 6.1) with consecutive increase of the prescribed displacement: 0.56, 0.58, 0.60, 0.63, 0.67 mm and finally until 0.82 mm. With each increase of the applied load either new local critical areas were determined, or old local models were increased in size to account for the damage evolution as was discussed by Akterskaia et al. [3]. Each coupling step includes also

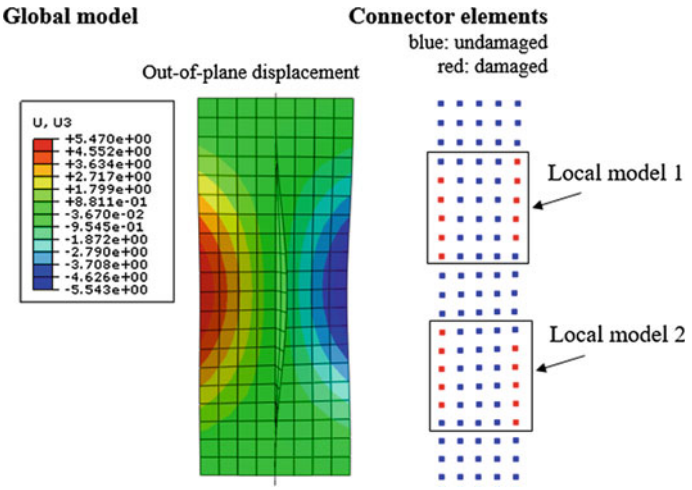

Fig. 6.6 Coupling step 1 with applied displacement of 0.56 mm. Global model (left) and connector elements with damage predicted in red (right)

several iteration analyses at the same load level in order to ensure that no new damage happens due to the stress redistribution that corresponds to the reduction of the interface stiffness properties. The onset of the skin-stringer separation at free edges on both longitudinal sides of the panel was detected through the criterion from Eq. 6.10 at a displacement level of 0.56 mm and led to the creation of two local models as demonstrated in Fig. 6.6. The comparison between the local model and solid element reference model at the same displacement level is shown in Fig. 6.7. In both the local model and the reference model the skin-stringer debonding starts at a free edge and the cohesive element degradation and deletion occur in a very similar manner.

The subsequent local analyses confirmed the onset and the evolution of debonding between the skin and the stringer. After reduction of the corresponding interface stiffness, the results were returned to the global model, in this way connecting the two different model levels. Each of the following coupling steps also resulted in the interface stiffness degradation, which in turn led to a decrease in the load-bearing capacity of the whole structure. The load-displacement curves of the global-local analysis together with the reference analysis results are shown in Fig. 6.8, where each drop of the global-local curve corresponds with the reduction of the global interface stiffness properties [3]. During the last coupling loop with the applied displacement of 0.82 mm the final failure, which is characterized by the sudden drop of the load-displacement curve, was attained.

The reference three-dimensional solid element model and the global-local approach curves demonstrate a good agreement with regard to the prediction of the structural stiffness and the maximum load reached. First buckling took place at a displacement of 0.147 mm for the global-local analysis and for the reference model

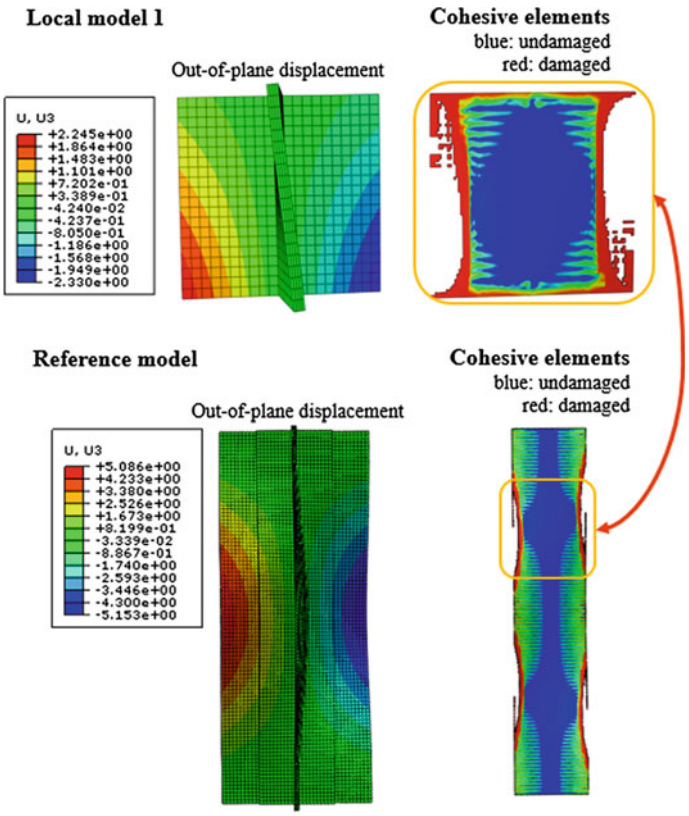

Fig. 6.7 Coupling step 1 with applied displacement of 0.56 mm. Local model 1 and reference model (left), and corresponding cohesive elements (right)

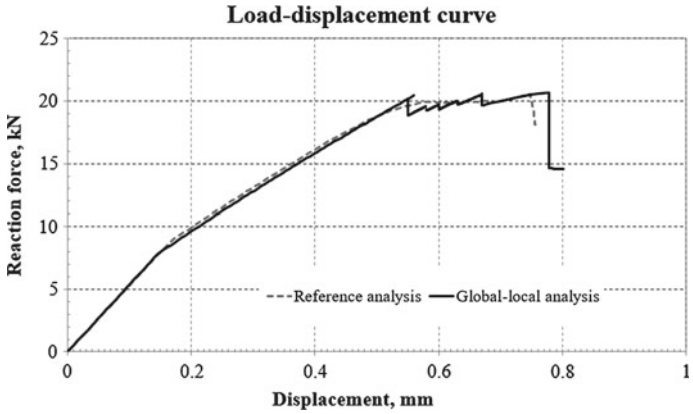

Fig. 6.8 Load-displacement curve for progressive failure analysis of stiffened panel

at 0.167 mm leading to slightly different, although parallel, curves. The maximum load level of 20.68 kN determined by the global-local procedure is relatively close to the reference solution load level of 20.54 kN. The displacements associated with total failure of the panel are also in good agreement, being 0.76 and 0.78 mm for the global-local approach and reference model solution, respectively.

6.4 Concluding Remarks

The global-local approach developed allows the modeling of the damage onset and propagation up to structural failure including two main damage mechanisms, skin-stringer separation and intralaminar damage. This method represents a reliable and efficient strategy not only to investigate the detailed damage evolution at the local level, but it ensures that damage is accounted for at the global level as well. This allows performing a progressive damage analysis up to final failure by means of this global-local approach. The full potential of the approach can be seen in the case of larger panels where localized damage will result in relatively small local models, corresponding to a significant reduction of the computational effort as compared to a three-dimensional solid element model analysis.

Acknowledgements This work was carried out using the computational facilities of the Institute of Structural Analysis at Leibniz University Hannover as well as computational facilities within the Advanced Computing Research Centre, University of Bristol - http://www.bris.ac.uk/acrc/.

References

1. Abaqus 6.14 Documentation (2017) Dassault systemes 6.14 edn (V):1–172
2. Akterskaia M, Jansen E, Hühne S, Rolfes R (2018) Efficient progressive failure analysis of multi-stringer stiffened composite panels through a two-way loose coupling global-local approach. Compos Struct 183:137–145
3. Akterskaia M, Jansen E, Hallett SR, Weaver R, Raimund R (2018) Analysis of skin-stringer debonding in composite panels through a two-way global-local method. Compos Struct 202:1280–1294
4. Akterskaia M, Jansen E, Hallett SR, Weaver R, Raimund R (2018) Progressive failure analysis of stiffened composite panels using a two-way loose coupling approach including intralaminar failure and debonding. In: AIAA/ASCE/AHS/ASC structures, structural dynamics, and materials conference, pp 1–16
5. Alesi H, Nguyen VM, Mileshkin M, Jones R (1998) Global/local postbuckling failure analysis of composite stringer/skin panels. AIAA J 36(9):1699–1705
6. Allix O, Ladevèze P (1992) Interlaminar interface modelling for the prediction of laminate delamination. Compos Struct 22:235–242
7. Balzani C, Wagner W (2010) Numerical treatment of damage propagation in axially compressed composite airframe panels. Int J Struct Stab Dyn 10(4):683–703
8. Barenblatt GI (1962) The mathematical theory of equilibrium cracks in brittle fracture. Adv Appl Mech 7(C):55–129

9. Benzeggagh ML, Kenane M (1996) Measurement of mixed-mode delamination fracture toughness of unidirectional glass/epoxy composites with mixed-mode bending apparatus. Compos Sci Technol 56:439–449
10. Bertolini J, Castanié B, Barrau JJ, Navarro JP, Petiot C (2009) Multi-level experimental and numerical analysis of composite stiffener debonding. Part 2: element and panel level. Compos Struct 90(4):392–403
11. Bettinotti O, Allix O, Perego U, Oancea V, Malherbe B (2017) Simulation of delamination under impact using a global-local method in explicit dynamics. Finite Elem Anal Des 125:1–13
12. Borg R, Nilsson L, Simonsson K (2001) Simulation of delamination in fiber composites with a discrete cohesive failure model. Compos Sci Technol 61(5):667–677
13. Camanho PP, Dávila CG (2002) Mixed-mode decohesion finite elements for the simulation of delamination in composite materials. Technical memorandum TM-2002-211737. Hampton, VI 23681-2199, NASA, Langley Research Center, USA
14. Chrupalla D, Berg S, Kärger L, Doreille M, Ludwig T, Jansen E, Rolfes R, Kling A (2011) A homogenization-based two-way multiscale approach for composite structures. In: Rolfes R, Jansen EL (eds) Proceedings of the 3rd ECCOMAS thematic conference on the mechanical response of composites, Hannover, Germany, pp 263–270
15. Dávila CG, Camanho PP, de Moura M (2001) Mixed-mode decohesion elements for analyses of proressive delamination. In: 19th AIAA applied aerodynamics conference
16. Degenhardt R, Kling A, Klein H, Hillger W, Goetting HC, Zimmermann R, Rohwer K (2007) Experiments on buckling and postbuckling of thin-walled CFRP structures using advanced measurement systems. Int J Struct Stab Dyn 7(2):337–358
17. Dugdale DS (1960) Yielding of steel sheets containing slits. J Mech Phys Solids 8:100–104
18. Faggiani A, Falzon BG (2007) Optimization strategy for minimizing damage in postbuckling stiffened panels. AIAA J 45(10):2520–2528
19. Falzon BG, Stevens KA, Davies GO (2000) Postbuckling behaviour of a blade-stiffened composite panel loaded in uniaxial compression. Compos Part A 31:459–468
20. Falzon BG, Davies GAO, Greenhalgh E (2001) Failure of thick-skinned stiffener runout sections loaded in uniaxial compression. Compos Struct 53:223–233
21. Hallett SR, Wisnom MR (2006) Numerical investigation of progressive damage and the effect of layup in notched tensile tests. J Compos Mater 40(14):1229–1245
22. Hillerborg A, Modeer M, Petersson PE (1976) Analysis of crack formation and crack growth in concrete by means of fracture mechanics and finite elements. Cement Concrete Res 6:773–782
23. Hinton MJ, Kaddour AS, Soden PD (2002) A comparison of the predictive capabilities of current failure theories for composite laminates, judged against experimental evidence. Compos Sci Technol 62:1725–1797
24. Hühne S, Reinoso J, Jansen E, Rolfes R (2016) A two-way loose coupling procedure for investigating the buckling and damage behaviour of stiffened composite panels. Compos Struct 136:513–525
25. Jiang WG, Hallett SR, Green BG, Wisnom MR (2007) A concise interface constitutive law for analysis of delamination and splitting in composite materials and its application to scaled notched tensile specimens. Int J Numer Methods Eng 69(9):1982–1995
26. Jones RM (1998) Mechanics of composite materials. CRC Press, Boca Raton
27. Kaddour AS, Hinton MJ (2013) Maturity of 3D failure criteria for fibre-reinforced composites: comparison between theories and experiments: Part B of WWFE-II. J Compos Mater 47:925–966
28. Kaddour AS, Hinton MJ, Soden PD (2004) A comparison of the predictive capabilities of current failure theories for composite laminates: additional contributions. Compos Sci Technol 64:449–476
29. Kaddour AS, Hinton MJ, Smith PA, Li S (2013) Mechanical properties and details of composite laminates for the test cases used in the third world-wide failure exercise. J Compos Mater 47(20–21):2427–2442
30. Krueger R (2015) The virtual crack closure technique for modeling interlaminar failure and delamination in advanced composite materials. Woodhead publishing series in composites science and engineering, pp 3–53

31. Labeas GN, Belesis SD, Diamantakos I, Tserpes KI (2012) Adaptative progressive damage modeling for large-scale composite structures. Int J Damage Mech 21(3):441–462
32. Lauterbach S, Orifici AC, Wagner W, Balzani C, Abramovich H, Thomson R (2010) Damage sensitivity of axially loaded stringer-stiffened curved CFRP panels. Compos Sci Technol 70(2):240–248
33. Linde P, Pleitner J, Boer H, Carmone C (2004) Modelling and simulation of fibre metal laminates. In: ABAQUS users' conference, pp 421–439
34. Loehnert S, Belytschko T (2007) A multiscale projection method for macro/microcrack simulations. Int J Numer Methods Eng 71:1466–1482
35. Mao KM, Sun CT (1991) A refined global-local finite element analysis method. Int J Numer Methods Eng 32:29–43
36. Mote CD (1971) Global-local finite element. Int J Numer Methods Eng 3:565–574
37. Noor AK (1986) Global-local methodologies and their application to nonlinear analysis. Finite Elem Anal Des 2:333–346
38. Orifici AC, Ortiz I, Alberdi DZ, Thomson RS, Bayandor J (2008) Compression and post-buckling damage growth and collapse analysis of flat composite stiffened panels. Compos Sci Technol 68(15–16):3150–3160
39. Reinoso J, Blázquez A, Estefani A, París F, Cañas J, Arévalo E, Cruz F (2012) Experimental and three-dimensional global-local finite element analysis of a composite component including degradation process at the interfaces. Compos Part B 43(4):1929–1942
40. Riccio A, Raimondo A (2016) Inter-laminar and intra-laminar damage evolution in composite panels with skin-stringer debonding under compression. Compos Part B 94:139–151
41. Riccio A, Raimondo A, Scaramuzzino F (2015) A robust numerical approach for the simulation of skin-stringer debonding growth in stiffened composite panels under compression. Compos Part B 71:131–142
42. Rybicki EF, Kanninen MF (1997) A finite element calculation of stress intensity factors by modified crack closure integral. Eng Fract Mech 9:931–938
43. Turon A, Camanho PP (2006) A damage model for the simulation of delamination in advanced composites under variable-mode loading. Mech Mater 38:1072–1089
44. Turon A, Camanho PP, Costa J (2007) An engineering solution for mesh size effects in the simulation of delamination using cohesive zone models. Eng Fract Mech 74:1665–1682
45. Wang JTS, Bigger SB (1984) Skin-stiffener interface stresses in composite stiffened panels. NASA Contractor Report 172261
46. Whitcomb JD (1991) Iterative global/local finite element analysis. Comput Struct 40(4):1027–1031
47. Wisnom MR, Chang FK (2000) Modelling of splitting and delamination in notched cross-ply laminates. Compos Sci Technol 60(15):2849–2856
48. Xie D, Waas AM (2006) Discrete cohesive zone model for mixed-mode fracture using finite element analysis. Eng Fract Mech 73(13):1783–1796
49. Yap JWH, Scott ML, Thomson RS, Hachenberg D (2002) The analysis of skin-to-stiffener debonding in composite aerospace structures. Compos Struct 57:425–435
50. Zubillaga L, Turon A, Renart J, Costa J, Linde P (2015) An experimental study on matrix crack induced delamination in composite laminates. Compos Struct 127:10–17

Chapter 7
Mesoscale Hyperelastic Model of a Single Yarn Under High Velocity Transverse Impact

P. Del Sorbo, J. Girardot, F. Dau and I. Iordanoff

Abstract In this chapter the modellisation of a single dry yarn under impact load as an homogeneous hyperelastic continuous body will be treated. In the first part, a preliminary introduction to dry fabrics mesoscopic models in impact applications will be performed. In the second part, an hyperelastic constitutive law for yarn structures continuous modeling will be presented. The proposed constitutive behaviour aims to the modellisation of the yarn transverse cross section evolution during an impact which is actually obliged in the classical linear elastic formulation. A theoretical introduction to the hyperelastic law is followed by its validation using the numerical model of transversely impacted yarn as benchmark test. The obtained results are compared with those from microscopic and classic linear elastic mesoscopic studies. A good agreement is obtained from the comparison with the different approaches. Moreover, the ability of the proposed model in representing yarn transverse behavior and formulate multiaxial failure criteria compared to the linear elastic approach universally adopted is remarked.

7.1 Introduction

High performance polymeric fibers as aramid (Kevlar and Twaron) and UHMWPE (Dyneema and Spectra) are actually employed in different ballistic applications in the form of composites panels and dry woven textile layers. These applications include flexible protective garments, armored vehicles protection and helmets. Aim of these structures is to provide the required level of protection from high velocity colliding object while limiting to the minimum their weight contribution to the global structure. The current design process of ballistic panels consist in a trial-and-error process where the design choices are validated experimentally by costly impact tests. The effectiveness of this process could be drastically increased if a predictive numerical

P. Del Sorbo (✉) · J. Girardot · F. Dau · I. Iordanoff
Institut de mécanique et d'ingénierie (I2M), dépt. DUMAS,
Arts et Métiers ParisTech, Talence, France
e-mail: pi.delsorbo@gmail.com

M. Petrolo (ed.), *Advances in Predictive Models and Methodologies for Numerically Efficient Linear and Nonlinear Analysis of Composites*, PoliTO Springer Series,
https://doi.org/10.1007/978-3-030-11969-0_7

model of these structure would be adopted. Limiting our discussion to dry fabric layers, different numerical models have been proposed for this type of structures [21]. Among them, the so called mesoscopic models resulted to be the most successful since they offer a good compromise in terms of accuracy and computational costs. Since their introduction by Duan [9, 10], this type of models remains substantially unvaried while adopted for different studies [3, 12, 17]. Here weaving geometry is explicitly represented and fabric yarns are modeled as a continuous medium whose constitutive law should make them behave as an aligned fibers bundles. The constitutive law universally adopted in mesoscopic models of dry fabrics under impact loads was proposed by Gasser [11]. It consists in a anisotropic linear elastic behavior where the Young modulus in fibers direction is determined according to physical strategies while the other parameters are numerically adapted to provide yarn flexibility and simulation stability. The ability of the Gasser model in representing the yarn longitudinal behavior has been assessed by different studies [3, 10] while the modelisation of yarn transverse behavior remains an unsolved problem. Unfortunately, this last aspect assumes a fundamental role in determining ballistic performance of multilayer textiles [6, 17]. In the current chapter an hyperelastic constitutive law for yarn structure is introduced. The proposed law can be fully characterized using experimental or numerical approach avoiding the numerical calibration typical of the linear elastic model. At the same time the following approach opens new possibilities in terms of failure modeling making possible the formulation of physical multiaxial failure criteria. In the first part of the chapter the fundamental theory behind the proposed hyperelastic constitutive law is introduced. Here the concept of hyperelasticity, physical invariants and the adopted elementary strain energy functions are presented. This first theoretical part ends with the formulation of failure criteria in terms of invariants. The second part of the chapter focus on the application of the proposed hyperelastic constitutive law to the benchmark problem of a single yarn transversely impacted by an high velocity projectile. Here the results obtained using the proposed constitutive law are compared with those by linear elastic mesoscopic and microscopic approaches. In the final part the possibility of formulating a multiaxial failure criterion are exploited.

7.2 Theory

7.2.1 General Notions of Transverse Isotropic Hyperelasticity

The total mechanical energy per unitary volume of a body is a composed by the kinetic energy K and the potential energy W. The value assumed by W is a measure of the energy stored in the material as a result of a deformation process and it is even referred as strain energy density. For an hyperelastic material, the relation between the second Piola–Kirchoff stress tensor $\mathbf{S}$ and the right Cauchy–Green tensor $\mathbf{C}$ is defined by:

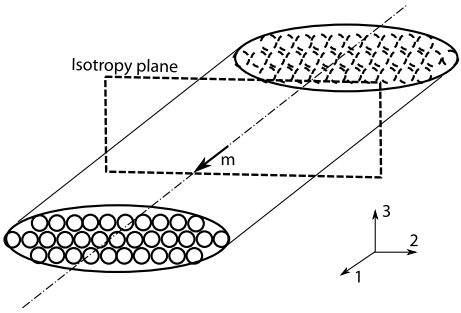

Fig. 7.1 Yarn as an transverse isotropic medium

$$\mathbf{S} = 2\frac{\delta W(\mathbf{C})}{\delta \mathbf{C}} \tag{7.1}$$

Where is assumed that the strain energy is a scalar-valued tensor function of the only deformation state. Since yarn microstructure is composed by a large number of slightly twisted fibers all oriented in a preferential direction, a transverse isotropic constitutive behavior will be considered. For a transversely isotropic hyperelastic material the general strain energy function W can be written in the following form [13]:

$$W(\mathbf{C}) = W(I_1, I_2, I_3, I_4, I_5)$$

$$I_1 = trc(\mathbf{C}) \quad I_2 = \frac{1}{2}(trc(\mathbf{C})^2 - trc(\mathbf{C}^2)) \quad I_3 = det(\mathbf{C}) \quad I_4 = \mathbf{C} : \mathbf{M} \quad I_5 = \mathbf{C}^2 : \mathbf{M} \tag{7.2}$$

Where I_1, I_2, I_3, I_4, I_5 are mathematical invariants of the tensors $\mathbf{M}$ and $\mathbf{C}$. The tensor $\mathbf{M} = \mathbf{m} \otimes \mathbf{m}$ is the structural tensor associated to the transverse isotropy symmetry group. The unitary vector $\mathbf{m}$ specifies the fiber orientation in the initial configuration and is orthogonal to the isotropy plane, Fig. 7.1.

7.2.2 The Notion of Physical Invariants

The advantage of using the mathematical invariants for the formulation of the strain energy function relies in the fact that the desired form of anisotropy is automatically obtained. On the other side, this type of entities have no direct physical counterpart for the material and are difficult to relate with results of experimental tests.

An alternative set of invariants for hyperelastic transversely isotropic material was recently proposed by Charmetant [2].

Following the previous work of Criscione et al. [5], the deformation gradient $\mathbf{F}$ in each point of an transverse isotropic deformed body can be written into a particular orthonormal basis $B = \{\mathbf{m}, \mathbf{n}_1, \mathbf{n}_2\}$ where it assumes the following form:

$$\mathbf{F} = \begin{bmatrix} f_m & f_{m1} & f_{m2} \\ 0 & f_{11} & 0 \\ 0 & 0 & f_{22} \end{bmatrix} \tag{7.3}$$

With the tensor in this form, the following multiplicative decomposition can be applied:

$$\mathbf{F} = \mathbf{F}_{el} \cdot \mathbf{F}_{tc} \cdot \mathbf{F}_{td} \cdot \mathbf{F}_{ld} \tag{7.4}$$

$$\mathbf{F}_{el} = \begin{bmatrix} f_m & 0 & 0 \\ 0 & 1 & 0 \\ 0 & 0 & 1 \end{bmatrix} \qquad \mathbf{F}_{tc} = \begin{bmatrix} 1 & 0 & 0 \\ 0 & \sqrt{f_{11} f_{22}} & 0 \\ 0 & 0 & \sqrt{f_{11} f_{22}} \end{bmatrix}$$

$$\mathbf{F}_{td} = \begin{bmatrix} 1 & 0 & 0 \\ 0 & \sqrt{\frac{f_{11}}{f_{22}}} & 0 \\ 0 & 0 & \sqrt{\frac{f_{22}}{f_{11}}} \end{bmatrix} \qquad \mathbf{F}_{ld} = \begin{bmatrix} 1 & \frac{f_{m1}}{f_m} & \frac{f_{m2}}{f_m} \\ 0 & 1 & 0 \\ 0 & 0 & 1 \end{bmatrix}$$

The important point about this representation relies in the physical meaning behind the decomposition. The global deformation is seen as a combination of four elementary deformation modes namely represented by the four tensorial terms $\mathbf{F}_{el}, \mathbf{F}_{tc}, \mathbf{F}_{td}, \mathbf{F}_{ld}$, Fig. 7.2. More specifically:

- $\mathbf{F}_{el}$ represents an elongation along the fibre direction
- $\mathbf{F}_{tc}$ represents a transverse section variation in terms of area, i.e. fiber crushing and section rearrangement
- $\mathbf{F}_{td}$ represents a transverse section variation in terms of shape, i.e. fiber crushing and section rearrangement

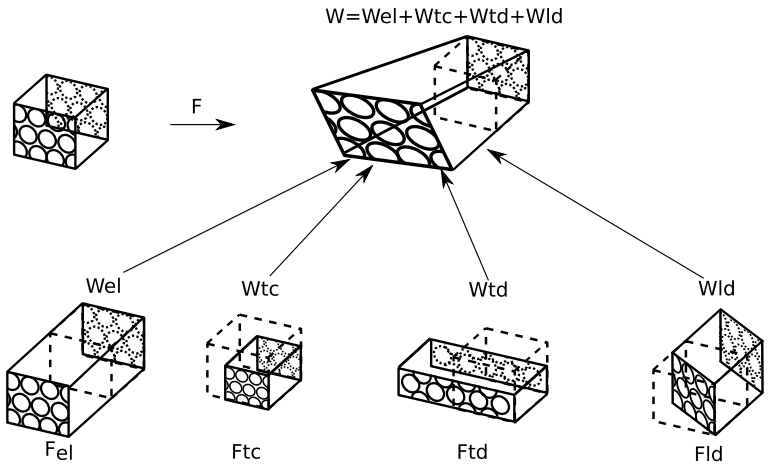

Fig. 7.2 Multiplicative decomposition and elementary deformation modes

- $\mathbf{F}_{ld}$ represents a shear deformation along the fibres direction, i.e. fiber-fiber slippage.

Each tensor of the decomposition, then each deformation mode, is represented by a single scalar with the only exception of longitudinal shear:

$$\mathbf{F}_{el} = \begin{bmatrix} \alpha_{el} & 0 & 0 \\ 0 & 1 & 0 \\ 0 & 0 & 1 \end{bmatrix} \quad \mathbf{F}_{tc} = \begin{bmatrix} 1 & 0 & 0 \\ 0 & \alpha_{tc} & 0 \\ 0 & 0 & \alpha_{tc} \end{bmatrix}$$

$$\mathbf{F}_{td} = \begin{bmatrix} 1 & 0 & 0 \\ 0 & \alpha_{td} & 0 \\ 0 & 0 & \frac{1}{\alpha_{td}} \end{bmatrix} \quad \mathbf{F}_{ld} = \begin{bmatrix} 1 & \alpha_{ld}\alpha_{el}\cos\gamma & \alpha_{ld}\alpha_{el}\sin\gamma \\ 0 & 1 & 0 \\ 0 & 0 & 1 \end{bmatrix}$$

$$\alpha_{el} = f_m \quad \alpha_{tc} = \sqrt{f_{11} f_{22}} \quad \alpha_{td} = \sqrt{\frac{f_{11}}{f_{22}}} \quad \alpha_{ld} = \sqrt{\frac{f_{m1}^2 + f_{m2}^2}{f_m}} \quad \tan\gamma = f_{m1}/f_{m2}$$

The idea at this point is to build a strain energy function taking advantage of this decomposition.

Firstly the longitudinal elongation and longitudinal shear are considered to be uncoupled, in this way α_{ld} is assumed to be fully representative of the longitudinal shear mode. Then a normalization is applied to the scalars in order to make them all zeros in rigid body motions:

$$I_{el} = \ln(\alpha_{el}) \quad I_{tc} = \ln(\alpha_{tc}) \quad I_{td} = \ln(\alpha_{td}) \quad I_{ld} = \alpha_{ld}$$

These new parameters are usually called physical invariants [2, 5].

Their values are a quantitative description of the contribution of a singular mode to the global deformation of the material and can be directly related to the mathematical invariants with some algebra.

$$I_{el} = \frac{1}{2}\ln I_4 \quad I_{tc} = \frac{1}{4}\ln\frac{I_3}{I_4}$$

$$I_{td} = \frac{1}{2}\ln\left(\frac{I_1 I_4 - I_5}{2\sqrt{I_3 I_4}} + \sqrt{\left(\frac{I_1 I_4 - I_5}{2\sqrt{I_3 I_4}}\right)^2 - 1}\right) \quad I_{ld} = \sqrt{\frac{I_5}{I_4^2} - 1} \tag{7.5}$$

Finally the global strain energy function is assumed as a linear combination of singular strain energy functions individually associated to each deformation mode:

$$W = W_{el}(I_{el}(I_4)) + W_{tc}(I_{tc}(I_3, I_4)) + W_{td}(I_{td}(I_1, I_3, I_4, I_5)) + W_{ld}(I_{ld}(I_4, I_5)) \tag{7.6}$$

From the physical point of view the strain energy stored within the material is assumed to be a composition of that stored by fiber elongation, W_{el}, by transverse deformation, $W_{tc} + W_{td}$, and by fiber-fiber slipping, W_{ld}.

Finally, the resultant second Piola–Kirchoff stress tensor can be written as:

$$\mathbf{S} = \mathbf{S}_{el} + \mathbf{S}_{tc} + \mathbf{S}_{td} + \mathbf{S}_{ld}$$

$$\mathbf{S}_{el} = 2\frac{\delta W_{el}}{\delta I_{el}}\frac{\delta I_{el}}{\delta \mathbf{C}}$$

$$\mathbf{S}_{tc} = 2\frac{\delta W_{tc}}{\delta I_{tc}}\frac{\delta I_{tc}}{\delta \mathbf{C}}$$

$$\mathbf{S}_{td} = 2\frac{\delta W_{td}}{\delta I_{td}}\frac{\delta I_{td}}{\delta \mathbf{C}}$$

$$\mathbf{S}_{ld} = 2\frac{\delta W_{ld}}{\delta I_{ld}}\frac{\delta I_{ld}}{\delta \mathbf{C}}$$

Where $\mathbf{S}_{el}, \mathbf{S}_{tc}, \mathbf{S}_{td}, \mathbf{S}_{ld}$ are the contribution of the different elementary energies.

7.2.3 The Material Model

In the current part, the form assumed for the elementary strain energy function $W_{el}, W_{tc}, W_{td}, W_{ld}$ and their relative material parameters will be presented.

7.2.3.1 Longitudinal Elongation

According to the results available in bibliography, a linear relation among stress and strain is sufficient to accurately describe the yarn longitudinal behavior under uniaxial tension [3, 10]. This linear relation results in a quadratic form of the energy for the universally adopted linear elastic model:

$$W = \frac{1}{2}E\varepsilon^2 \tag{7.7}$$

where E is the yarn longitudinal modulus and ε is the deformation in the longitudinal direction. In the same way W_{el} is assumed as a quadratic function of I_{el}:

$$W_{el} = \frac{1}{2}k_{el}I_{el}^2 \quad for \quad I_{el} > 0$$
$$W_{el} = 0 \quad for \quad I_{el} < 0$$

Where k_{el} is a material parameter to determine.

The contribution of this deformation mode to the tensor S is indicated with S_{el} and is equal to:

$$\mathbf{S}_{el} = \frac{1}{I_4}\mathbf{M}k_{el}I_{el} \quad for \quad I_{el} > 0 \quad else \quad 0$$

7.2.3.2 Transverse Compaction

The strain energy function for transverse compaction is presented as the a power based function [2]:

$$W_{tc} = k_{tc} \| I_{tc} \|^p \quad for \quad I_{tc} < 0$$
$$W_{tc} = 0 \quad for \quad I_{tc} > 0$$

For this specific mode two parameter have to be identified, k_{tc} and p.

It is worth to notice that zero energy is assumed when the associated invariant I_{tc} is greater then zero. From the physical point of view this is representative of the fact that no energy is stored in the yarn when fibers are separated from each other. The contribution of transverse compaction to the second Piola–Kirchoff stress tensor is indicated with S_{tc} and is equal to:

$$\mathbf{S}_{tc} = \frac{-p}{2} k_{tc} \| I_{tc} \|^{p-1} \left(\mathbf{C}^{-1} - \frac{\mathbf{M}}{I_4} \right) \quad for \quad I_{tc} < 0 \quad else \quad 0 \tag{7.8}$$

7.2.3.3 Transverse Distortion

For the transverse distortion strain energy is assumed the same form proposed by Charmetant for static applications [2]:

$$W_{td} = \frac{1}{2} k_{td} I_{td}^2$$

where k_{td} is a material parameter which have to be identified.

The contribution of this mode to the second Piola–Kirchoff stress tensor is indicated with S_{td} and is equal to:

$$\mathbf{S}_{td} = 2k_{td} I_{td} \frac{2I_4 \mathbf{I} - (I_1 I_4 - I_5)\mathbf{C}^{-1} + \left(I_1 + \frac{I_5}{I_4} \right) \mathbf{M} - 2(\mathbf{C} \cdot \mathbf{M} + \mathbf{M} \cdot \mathbf{C})}{4\sqrt{(I_1 I_4 - I_5)^2 - 4I_3 I_4}} \tag{7.9}$$

Where $\mathbf{I}$ is the identity tensor.

7.2.3.4 Longitudinal Shear

This form of energy is physically representative of the internal energy stored in the yarn while it is sheared in those plane which include its longitudinal axis. It is mostly related to fiber-fiber sliding and is assumed to be negligible compared to the others

modes. Due to this assumption, its contribution to the global energy absorption will be neglected:

$$W_{ld} = 0 \tag{7.10}$$

7.2.4 *Failure Modelling Using Physical Invariants*

In this part an invariant based failure criteria equivalent to the maximum longitudinal elastic stress/strain usually adopted [3, 12, 17] will be presented. The proposed criterion will be successively enriched with the longitudinal properties degradation effect related to transverse deformation.

7.2.4.1 Longitudinal Elongation Failure Criterion Using Physical Invariants

The length of the unitary vector $\mathbf{m}$ after the deformation is indicated by λ_m and is equal to:

$$\lambda_m = \sqrt{\mathbf{Cm} \cdot \mathbf{m}} = \sqrt{\mathbf{C} : \mathbf{M}} = \sqrt{I_4} \tag{7.11}$$

While the longitudinal strain in the fiber direction is defined as:

$$\varepsilon_m = \frac{\lambda_m - ||\mathbf{m}||}{||\mathbf{m}||} = \frac{\lambda_m - 1}{1} = \lambda_m - 1 \tag{7.12}$$

Using the definition of I_{el} we obtain:

$$I_{el} = ln(\varepsilon_m + 1) \tag{7.13}$$

It gives the physical interpretation of the longitudinal elongation invariant which is equal to true strain in the fiber direction.

Writing the previous relation in terms of maximum elongation strain ε_{el}^{lim} it becomes:

$$I_{el}^{lim} = ln(\varepsilon_m^{lim} + 1) \tag{7.14}$$

And the relative purely longitudinal failure criteria is written as:

$$I_{el} < I_{el}^{lim} \tag{7.15}$$

According to this criterion, the material will fail if the invariants associated to the longitudinal elongation will be greater than the limit true strain along fibers recorded during a uniaxial traction test.

This type of criterion is the invariant counterpart of that normally used in the linear elastic orthotropic model, usually formulated in terms of stress.

7.2.4.2 Inclusion of Transverse Effects

Different questions have been posed concerning the necessity of a multiaxial failure criterion for yarn structure. Thanks to the current approach is it possible to include the effect of transverse modes on the material failure [14, 22].

In this case the following failure criterion is proposed to take into account the damage induced by fibers transverse deformation:

$$I_{el} < I_{el}^{lim}(1 - \alpha \|I_{tc}\| - \beta I_{td}) \quad for \quad I_{tc} < 0$$
$$I_{el} < I_{el}^{lim}(1 - \beta I_{td}) \quad for \quad I_{tc} > 0$$

Where I_{el}^{lim} is the limit longitudinal elongation invariant adopted for the uniaxial criterion and α, β are material parameters.

This criterion is equivalent to the uniaxial one if the yarn cross section remains undeformed or expanded, however a reduction of the axial failure properties is considered when yarn transverse compaction and distortion is recorded. This reduction can be physically attributed to fiber damage due to permanent transverse deformations. The parameters α and β regulate the decrease of axial strain limit and have to be identified using experimental or numerical approaches.

7.3 Case of Study: Single Yarn Transverse Impact

The current section is dedicated to the study of the transverse impact on a single yarn using a mesoscopic numerical model.

This type of impact scenario has been successfully modeled using linear elastic mesoscopic and microscopic approaches [3, 8, 10, 16]. Both of them have proved their abilities in modelling the inertial and longitudinal properties of the yarn, however the representation of the transverse section evolution of the structure remains confined to the seconds. For the previously mentioned reasons, this study can be used as a benchmark which assesses the correct representation of the yarn longitudinal, transverse and inertial properties.

The proposed hyperelastic constitutive law here is adopted. In the first part, the impact scenario and the relative finite element model will be presented. Then classical results universally attributed to the yarn longitudinal and inertial properties as projectile speed trend or yarn kinematic will be validated using those obtained by linear elastic mesoscopic and microscopic approach. To validate the response of the material, no failure criteria will be implemented in the first part of this study.

Finally, failure criteria will be included in the model. Yarn penetration and projectile residual speed will be compared for the three approaches while the new opportunities offered by the proposed constitutive law in terms of failure modeling will be presented.

7.3.1 Impact Scenario

In order to validate the hyperelastic constitutive law, the same impact scenario assumed in previous microscopic studies will be considered [8, 16].

It consist of a straight 25.4 mm length Kevlar KM2 600 yarn clamped at the extremities and impacted transversely in the centre by a cylindrical projectile, Fig. 7.3.

This type of yarn is composed of 400 circular fibers with a diameter of 12μm. The 9.91mg projectile has an height h of 2 mm, a diameter ϕ of 2.2 mm and an initial velocity V of 120 ms^{-1}.

The finite element model has been implemented in the commercial software LS-DYNA. The symmetry of the problem has been exploited, then just half of the yarn has been modeled.

The yarn cross section is elliptical with major and minor axis respectively equal to 0.5337 and 0.115 mm which results into a yarn volume fraction ν of 0.93848.

Twelve elements have been used to discretize the whole cross section which results in 1200 eight-nodes reduced integration hexahedral solid elements for the whole yarn.

Symmetry boundary condition has been imposed to the nodes at the yarn center while those on the extremity have been perfectly clamped.

The proposed transverse isotropic hyperelastic material model has been adopted for the yarn. The material parameters identification is presented in Appendix 7.5 and its results are resumed in Table 7.1.

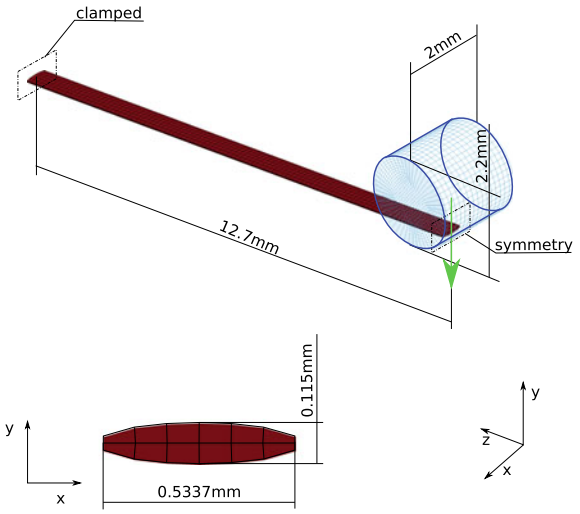

Fig. 7.3 Finite element model

Table 7.1 Properties of hyperelastic Kevlar KM2 yarn model

k_{el} (GPa)	k_{tc} (GPa)	p	k_{td} (GPa)
82.341	1.055	2.2	0.649

The density ρ of the yarn is obtained multiplying the density of a fiber ρ_f 1.440 g/cm^3 for the yarn volume fraction and is equal to 1.351 g/cm^3.

In order to avoid contact problem between the two parts, the whole projectile has been modeled. Since symmetry conditions are applied, projectile mass has been divided by two and its displacement have been limited to the impact direction. As in the microscopic case, the projectile is assumed to be a rigid.

An automatic surface-to-surface contact has been chosen for the projectile-yarn interaction with a friction coefficient of 0.18.

7.3.2 Results

7.3.2.1 Yarn Kinematic, Projectile Speed and Energy Balance: Model Validation

Here results of the proposed model are compared with those obtained by a microscopic model and a mesoscopic linear elastic approach.

For the linear elastic mesoscopic study the same numerical model has been used, but a linear elastic anisotropic material has been adopted for the yarn. Material properties adopted for the yarn in the linear elastic case are reported in Table 7.2:

Table 7.2 Properties of linear elastic Kevlar KM2 yarn model

E_1 (GPa)	$E_2 = E_3$ (GPa)	$\nu_{23} = \nu_{12} = \nu_{13}$	$G_{23} = G_{13} = G_{12}$ (GPa)
79.414	0.794	0	0.126

The longitudinal elastic modulus has been obtained multiplying the fiber modulus 84.62 GPa for the yarn volume fraction, the transverse moduli have been assumed to order of magnitude lower the longitudinal one and shear moduli have been set according to the work of Duan [9].

Figure 7.4 reports the yarn kinematic in the impact plane for the hyperelastic mesoscopic model.

The propagation of the transverse wave is observed. This particular wave is directly related to the yarn longitudinal behaviour, inertial properties and strain state along the fiber direction. The transverse wave travels from the impact point toward the extremities of the yarn, 0–18 μs, it is reflected and then come back to the impact zone, 18–30 μs.

The same kinematic has been obtained by the microscopic and the linear elastic model.

The coherence of the linear elastic model with the microscopic simulation is not a surprise [3, 9]. On the other side, the observation of this same kinematic in the hyperelastic model is a validation of the good representation of the yarn longitudinal and inertial properties, which is the minimum requirement for a correct representation of an impact phenomenon at the fabric level.

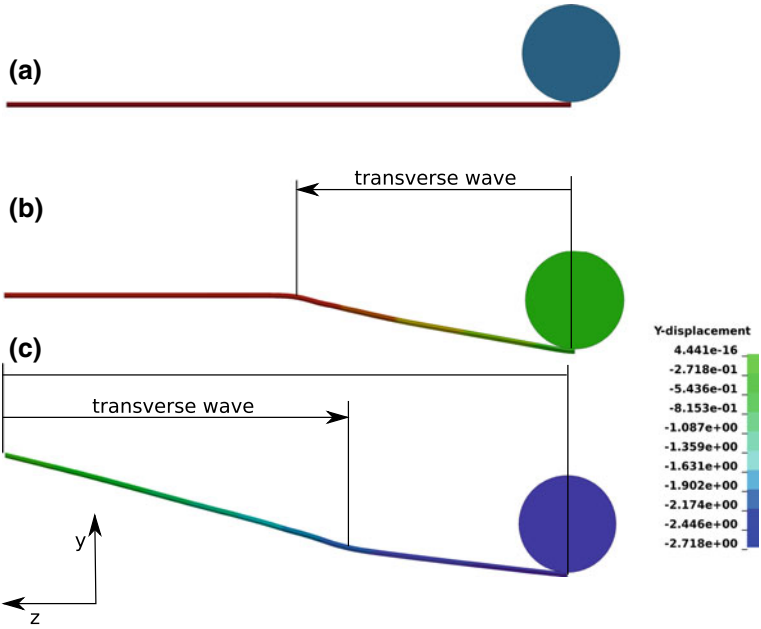

Fig. 7.4 Y displacement [mm] and transverse wave propagation in hyperelastic mesoscopic model at 0 μs (**a**), 10 μs (**b**), 25 μs (**c**)

Concerning the behavior in the x-z plane, the three models are not equivalent. Figure 7.5 reports the yarn configuration in this specific plane during the impact.

The hyperelastic model as the microscopic one presents the propagation of a spreading wave which is not observed in the linear elastic one. It represents the reorganization of the yarn fibers within the cross section which travels outside the impact zone, then its related to yarn transverse mechanical behavior.

Up to know, this wave was typical of the microscopic approaches and has never been observed in any other yarn continuum model.

The last step of the validation is the analysis of the internal and kinetic energy stored during the impact. These energies are presented in Fig. 7.6.

Even in this case a good agreement among the models is obtained. The coherence of these trends gives an explicit indication about the correct representation of the mass and the mechanical properties of the system.

Another validation of the global kinematic is given by the time in which the trends of the energies are inverted. Those instant correspond to transverse wave reflection, then they mark the time required by the wave to travel form one side of the yarn to the other. Since those instant are the same for the three models, the wave speed will be equal in all the three cases, which is another prove of the good representation of the yarn kinematic.

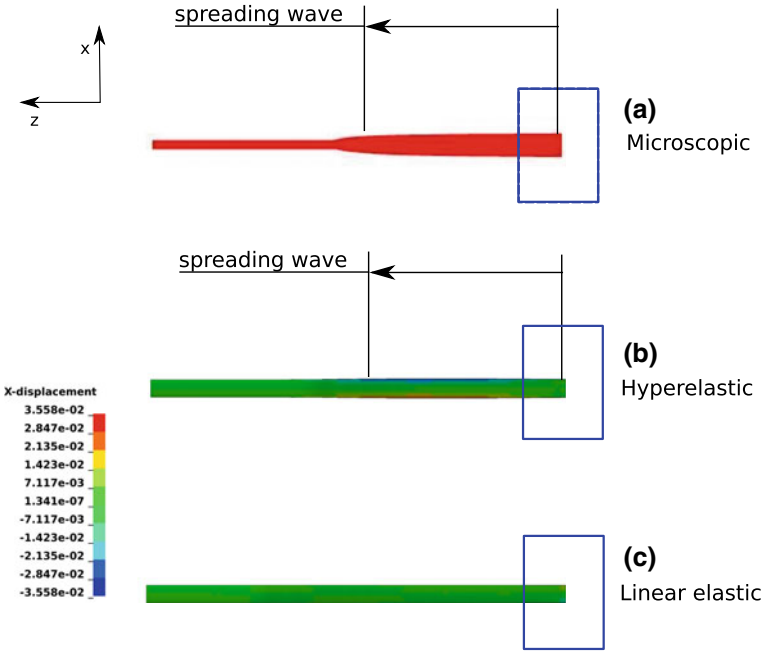

Fig. 7.5 X displacements and spreading wave propagation in microscopic [8] and mesoscopic models at 10 µs

Fig. 7.6 Internal and kinetic energies

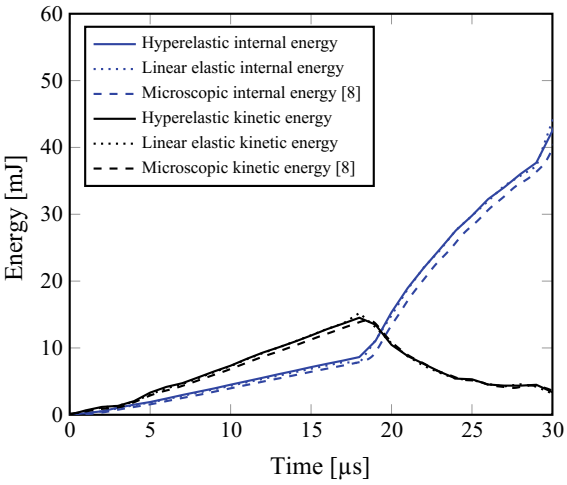

7.3.2.2 Failure Parameters Identification

In this final part the choice of the failure criterion for the proposed hyperelastic model is treated.

In the frame of the previously presented impact scenario both the criteria presented in Sect. 7.2.4 have been tested and compared with the results obtained using linear elastic mesoscopic and microscopic approach.

A the maximum longitudinal strain criterion has been assumed as basic failure criterion for the two mesoscopic models. Maximum strain value ε_{el}^{lim} has been assumed equal to those of the Kevlar fibers, 4.58%, which is equivalent to a maximum longitudinal elongation invariant I_{el}^{lim} of 0.044782.

This criterion has been implemented in the linear elastic model as the classical maximum stress failure criterion. Here the maximum stress σ_{lim} is equal to 3.637 GPa and has been obtain multiplying the yarn longitudinal modulus for the maximum strain in the fiber direction.

Concerning the multiaxial failure criteria, this is obviously implemented just for the hyperelastic case and the parameters α and β have been optimized in order to minimize the discrepancy among the proposed model and the microscopic simulation.

Table 7.3 reports the ballistic limit study for the three different failure criteria, maximum longitudinal strain (mesoscopic hyperelastic, microscopic), maximum stresses (mesoscopic linear elastic), multiaxial (mesoscopic hyperelastic). The cases for which no penetration occurs are indicated by "NP" while no performed cases are indicated by "–".

According to microscopic results, projectile residual velocity for an impact speeds over $120\,\mathrm{ms}^{-1}$ is $64\,\mathrm{ms}^{-1}$, while for lower velocities yarn failure doesn't appear. As it possible to see, classical mesoscopic approach predicts yarn failure for an impact speed of $100\,\mathrm{ms}^{-1}$ which is inconsistent with results obtained at the microscale where no failure occurs. The proposed model overestimate the yarn resistance if the purely longitudinal criterion is adopted. No penetration is observed for an impact speed of $120\,\mathrm{ms}^{-1}$ but penetration occurred for $140\,\mathrm{ms}^{-1}$ with a residual speed of $18\,\mathrm{ms}^{-1}$. It is interesting to observe how a real uniaxial failure criterion, adopted by the hyperelastic model, differs in the results from a principal stress based criterion.

On the other side, it is possible to get a very good coherence among the microscopic and mesoscopic response if the multiaxial failure criterion is adopted.

Table 7.3 Projectile Residual Speed for different models and failure criteria (ms^1)

In. Velocity (ms^{-1})	Micro [8, 16]	Meso Lin. El.	Meso Hyp. UF	Meso Hyp. MF $\alpha = 1.8\ \beta = 0.0$
80	NP	NP	NP	NP
100	NP	40	NP	NP
120	64	74	NP	64
140	–	–	18	–

7.4 Conclusions

In the present chapter a novel hyperelastic constitutive law for yarn mesoscopic models has been presented. Aim of the proposed model is to take into account the yarn transverse behavior during mesoscopic simulations and opens new possibilities in terms of yarn failure modeling. Firstly, a theoretical introduction to the model and the adopted failure criteria has been presented. Secondly, the benchmark test of a yarn transversely impacted by an high velocity projectile has been used to validate the proposed law. The obtained results have been compared to those of microscopic and linear elastic mesoscopic models. Results shown how the mesoscopic hyperelastic model is in very good agreement with microscopic and linear elastic mesoscopic ones. The energy absorption process and transverse wave propagation are equivalent for the two mesoscopic models, however they differ for the kinematic of the yarn cross section and projectile residual speed. Compared to the linear elastic approach, the proposed hyperelastic model is able to represent the propagation of the spreading wave and is much closer to microscopic projectile residual speed when a proper multiaxial failure criterion is adopted.

7.5 Appendix: Constitutive Law Parameters Identification

The identification of material parameters which characterize an hyperelastic constitutive behavior is usually formulated as an inverse problem. This problem consists in the identification of the optimal set of parameters which minimize a defined error among the experimental data curves and the analytical material response.

This problems can be formulated in term of stresses [18, 19], load-displacement curves [1, 15] or energy [7]. In this work the latest approach will be adopted.

For the proposed constitutive model, the strain energy function is a combination of three independent parts respectively related to three deformation modes. Following this idea, it is ideally possible to identify separately the parameters related to W_{el}, W_{tc} and W_{td}. In order to do this, three set of data which express the elementary strain energy as a function of its relative invariants are required.

In the present appendix the strategy adopted for the identification of these data sets is explained and the parameters identified by curve fitting are presented.

Longitudinal Elongation Mode

The effectiveness of the linear elastic orthotropic model in describing the yarn longitudinal behaviour has been largely assessed, then it is possible to use this model to get the data for the determination of the parameter k_{el}.

Let's induce into a mesoscopic hyperelastic yarn material block a pure homogeneous longitudinal strain state imposing the following boundary condition on the external faces, Fig. 7.7:

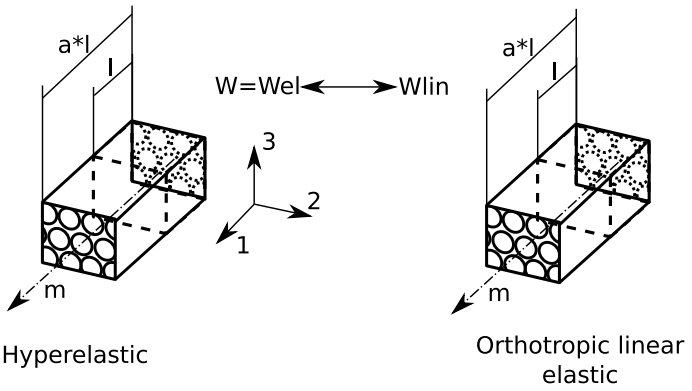

Fig. 7.7 Energetic equivalence for the identification of k_{el}

$$\mathbf{u} = \mathbf{F}\mathbf{x}$$

$$F = \begin{bmatrix} \lambda & 0 & 0 \\ 0 & 1 & 0 \\ 0 & 0 & 1 \end{bmatrix}$$

Where **u** is the displacement vector of the point on the faces, **x** is their position vector in the proposed reference system and **F** is the homogeneous deformation gradient induced written in the proposed reference system.

Under this condition all the physical invariants are equal to zero with the exception of I_{el}, then the strain energy stored within the block is reduced to the contribution of the longitudinal elongation mode:

$$I_{el} \neq 0 \quad I_{tc} = I_{td} = 0$$
$$\tilde{W} = \tilde{W}_{el}$$

For this strain state, the infinitesimal strain tensor ε and the longitudinal elongation invariants are written:

$$\varepsilon = \frac{1}{2}(\mathbf{F}^T + \mathbf{F}) - I = \begin{bmatrix} \varepsilon_f & 0 & 0 \\ 0 & 0 & 0 \\ 0 & 0 & 0 \end{bmatrix}$$

$$I_{el} = ln(\varepsilon_f + 1)$$

Where $\varepsilon_f = \lambda - 1$ is the infinitesimal strain in the fiber direction.

If the Gasser constitutive model would be adopted for the same block under the same boundary conditions, the strain energy function will have the following form:

$$W_{lin} = \frac{1}{2} E_f v_f \varepsilon_f^2 \tag{7.16}$$

Where E_f is the young modulus of the fiber in the longitudinal direction and v_f is the fiber volume fraction of the yarn. These parameters are usually known, then the strain energy associated to a generic ε_f can be easily evaluated.

The previous relation can be written as a function of the physical invariant I_{el}:

$$W_{lin} = \frac{1}{2} E_f v_f (e^{I_{el}} - 1)^2 \tag{7.17}$$

At this point the energetic equivalence among the two models is assumed:

$$\tilde{W}_{el} = W_{lin} = \frac{1}{2} E_f v_f (e^{I_{el}} - 1)^2 \tag{7.18}$$

This relation is obviously different from the quadratic form previously assumed, however a good approximation of this function can be obtained with the optimum choice of the parameter k_{el}.

The relation (7.18) has been used to generate a sufficiently large number of couples to provide a good fitting of the hyperelastic model to the linear elastic orthotropic one under pure longitudinal strain condition. Figure 7.8 reports the results of the curve fitting for a Kevlar KM2 yarn whose properties are listed in Table 7.4 which led to $k_{el} = 82.341\,\text{GPa}$.

The strain energy $\tilde{W}_{el}$ has been evaluated up to the invariant value for which failure is expected.

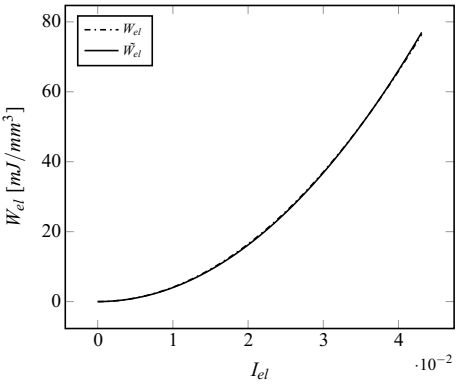

Fig. 7.8 Identification of the parameter k_{el}

Table 7.4 Longitudinal Properties of Kevlar KM2 yarn

E_{long} fiber (GPa)	Yarn volume fraction	ε_{max}
84.62	0.9385	4.58%

Transverse Compaction Mode

For the parameters identification of transverse compaction and transverse distortion the procedure is similar to that adopted for the longitudinal elongation, however here the energetic equivalence is assumed with a numerical yarn RVE.

If a pure transverse compaction mode would be induced within the continuum material block, the following boundary condition should be applied on the six faces:

$$\mathbf{u} = \mathbf{F}\mathbf{x}$$

$$\mathbf{F} = \begin{bmatrix} 1 & 0 & 0 \\ 0 & \lambda & 0 \\ 0 & 0 & \lambda \end{bmatrix}$$

and:

$$I_{tc} = ln(\lambda) \quad I_{el} = I_{td} = 0 \tag{7.19}$$

Under this condition the strain energy stored within the block is reduced to the contribution of the transverse compaction mode, Fig. 7.9a:

$$\tilde{W} = \tilde{W}_{tc} \tag{7.20}$$

From a numerical point of view, the same homogeneous strain state is obtained for a bidimensional plain strain problem where the displacement are applied by four rigid walls in contact with the mesoscopic material, Fig. 7.9b,

The relation among the displacement δ of the wall i and the scalar λ, representative of the strain state, is given by:

$$L_i - \delta_i = \lambda L_i \tag{7.21}$$

Where L_i is the length of the relative side.

At this point the energetic equivalent model is introduced.

A group of fibers arranged into an hexagonal close packing configuration has been chosen as the energetic counterpart of the mesoscopic model [16, 20]. A plain strain finite element model of 115 fibres arranged into an HCP configuration subjected to the wall load previously described have been developed.

According to previous results [20], each fiber has been modeled using 108 plain strain four nodes bi-dimensional elements. This mesh density assures a correct representation of the fiber transverse behaviour.

For the specific case of Kevlar fibers, a linear elastic transversely isotropic behavior has been used, Table 7.5. No friction is considered for contact among fibres and walls while a friction coefficient of 0.2 has been assumed for fiber-fiber contact. The model has been implemented in the finite element software LS-Dyna while an implicit integration scheme has been adopted to solve the non-linear static analysis. Figure 7.9c reports the Von Mises stresses during the simulation. Boundary condition effects are clearly in those fibers directly in contact with the rigid plates. Those

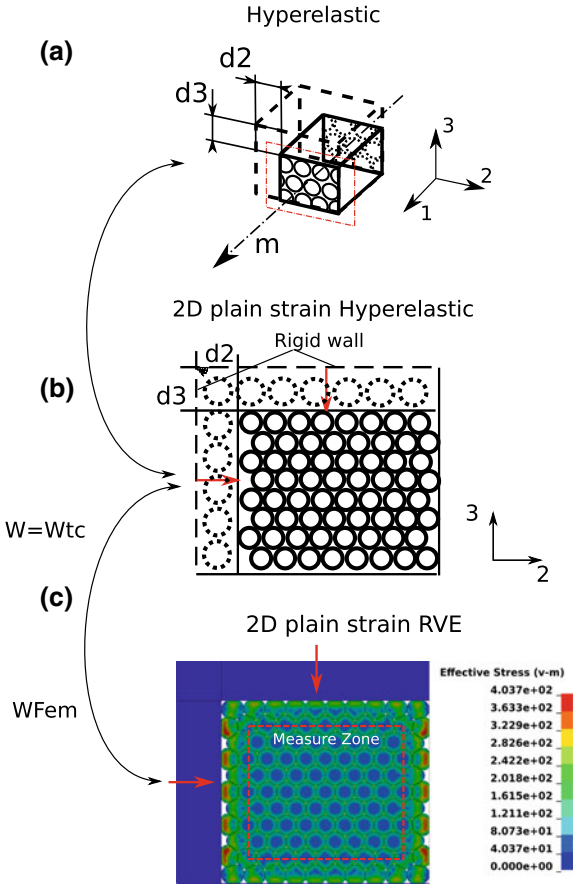

Fig. 7.9 Energetic equivalence for the identification of k_{tc} and p

Table 7.5 Properties of Kevlar KM2 fiber

Density (kg/m^3)	E_1 (GPa)	$E_2 = E_3$ (GPa)	ν_{23}	$\nu_{12} = \nu_{13}$	G_{23} (GPa)	$G_{13} = G_{12}$ (GPa)
1440	84.62	1.34	0.24	0.6	0.540	24.4

present the highest values of stresses while a periodic solution is obtained at the RVE center.

The strain energy has been recorded in the central zone of the numerical specimen where the solution appears to be periodic while the associated invariant has been computed using relations (7.21)–(7.19).

Figure 7.10 reports the evolution of the strain energy density stored within the RVE as a function of the transverse compaction invariant and the fitting results from which k_{tc} and p resulted equal to 1.055 GPa and 2.2 respectively.

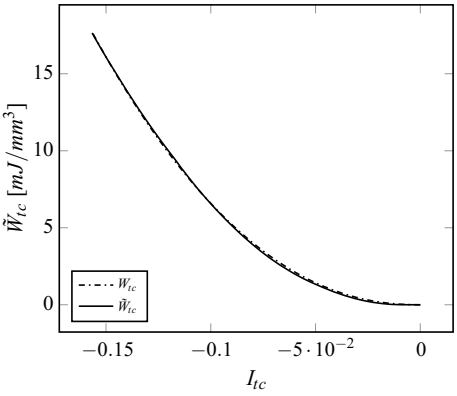

Fig. 7.10 Identification of the parameter k_{tc}, p

Transverse Distortion Mode

The strategy adopted for the parameters identification of transverse distortion is based on the same procedure and the same FE model adopted for transverse compaction. The only difference relies in the boundary conditions.

In this specific case a uniaxial compression is applied using wall displacement which induce the following strain state:

$$\mathbf{F} = \begin{bmatrix} 1 & 0 & 0 \\ 0 & 1 & 0 \\ 0 & 0 & \lambda \end{bmatrix} \tag{7.22}$$

where the relation among the λ and the wall displacement δ is always given by Eq. 7.21. For this strain state two physical invariants are different from zeros:

$$I_{tc} = \sqrt{\lambda} I_{td} = \sqrt{\frac{1}{\lambda}} \tag{7.23}$$

and the strain energy function W is given by the combination of two different components W_{tc} and W_{td} (Fig. 7.11).

The values of strain energy associated to the transverse distortion mode can be obtained subtracting the transverse compaction strain energy, evaluated using the parameters previously identified, to the global strain energy density measured in the FE analysis.:

$$\tilde{W}_{td} = \tilde{W} - \tilde{W}_{tc} \tag{7.24}$$

Figure 7.12 reports the results of the curve fitting for a Kevlar yarn and the energies recorded during the test. From this procedure k_{td} resulted equal to 0.64974 GPa.

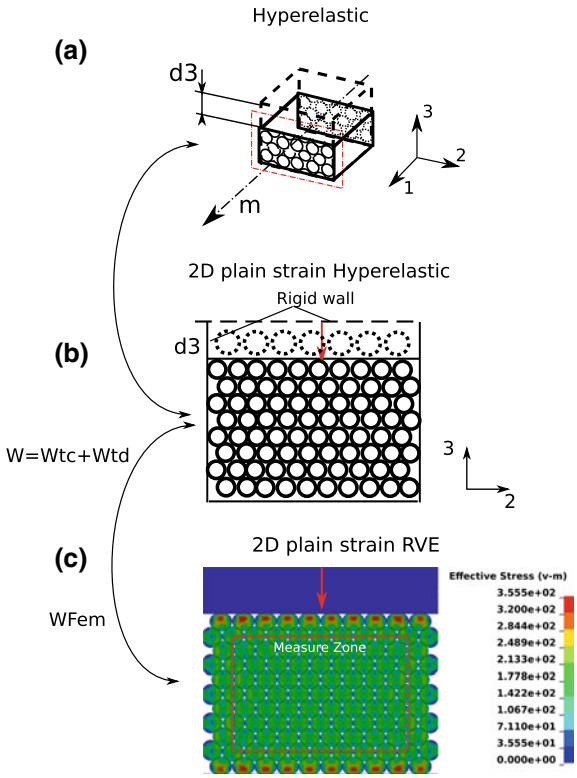

Fig. 7.11 Energetic equivalence for the identification of k_{ld}

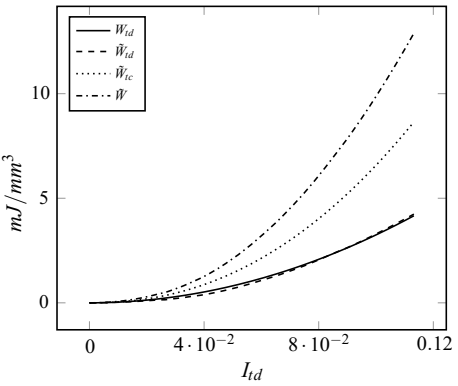

Fig. 7.12 Identification of the parameter k_{td}

References

1. Aimène Y, Vidal-Sallé E, Hagège B, Sidoroff F, Boisse P (2009) Hyperelastic approach for composite reinforcement large deformation analysis. J Compos Mater 44(1):5–26
2. Charmetant A, Vidal-Sallé E, Boisse P (2011) Hyperelastic modelling for mesoscopic analyses of composite reinforcements. Compos Sci Technol 71(14):1623–1631
3. Chocron S, Figueroa E, King N, Kirchdoerfer T, Nicholls A, Sagebiel E, Weiss C, Freitas CJ (2010) Modeling and validation of full fabric targets under ballistic impact. Compos Sci Technol 70(13):2012–2022
4. Chocron S, Kirchdoerfer T, King N, Freitas CJ (2011) Modeling of fabric impact with high speed imaging and Nickel-Chromium wires validation. J Appl Mech 78(5)
5. Criscione JC, Douglas SA, Hunter WC (2001) Physically based strain invariant set for materials exhibiting transversely isotropic behavior. J Mech Phys Solids 49(4):871–897
6. Cunniff P (1999) Decoupled response of textile body armor. Decoupled response of textile body armor. In: Proceedings of the 18th international symposium on ballistics
7. Darijani H, Naghdabadi R (2010) Hyperelastic materials behavior modeling using consistent strain energy density functions. Acta Mech 213(3–4):235–254
8. del Sorbo P, Girardot G, Dau F, Iordanoff I (2018) Numerical investigations on a yarn structure at the microscale towards scale transition. Compos Struct 183:489–498
9. Duan Y, Keefe M, Bogetti TA, Cheeseman BA, Powers B (2006) A numerical investigation of the influence of friction on energy absorption by a high-strength fabric subjected to ballistic impact. Int J Impact Eng 32(8):1299–1312
10. Duan Y, Keefe M, Bogetti TA, Powers B (2006) Finite element modeling of transverse impact on a ballistic fabric. Int J Mech Sci 48(1):33–43
11. Gasser A, Boisse P, Hanklar S (2000) Mechanical behaviour of dry fabric reinforcements. 3D simulations versus biaxial tests. Comput Mater Sci 17(1):7–20
12. Ha-Minh C, Imad A, Kanit T, Boussu F (2013) Numerical analysis of a ballistic impact on textile fabric. Int J Mech Sci 69:32–39
13. Holzapfel GA (2000) Nonlinear solid mechanics: a continuum approach for engineers. Wiley, New York
14. Hudspeth M, Chu M, Jewell E, Lim B, Ytuarte E, Tsutsui W, Horner S, Zheng J, Chen W (2016) Effect of projectile nose geometry on the critical velocity and failure of yarn subjected to transverse impact. Text Res J 87(8):953–972
15. Isvilanonda V, Iaquinto JM, Pai S, Mackenzie-Helnwein P, Ledoux WR (2016) Hyperelastic compressive mechanical properties of the subcalcaneal soft tissue: an inverse finite element analysis. J Biomech 49(7):1186–1191
16. Nilakantan G (2013) Filament-level modeling of Kevlar KM2 yarns for ballistic impact studies. Compos Struct 104:1–13
17. Nilakantan G (2018) Experimentally validated predictive finite element modeling of the V0-V100 probabilistic penetration response of a Kevlar fabric against a spherical projectile. Int J Prot Struct (In Press)
18. Ogden RW, Saccomandi G, Sgura I (2004) Fitting hyperelastic models to experimental data. Comput Mech 34(6):484–502
19. Rashid B, Destrade M, Gilchrist MD (2013) Mechanical characterization of brain tissue in simple shear at dynamic strain rates. J Mech Behav Biomed Mater 28:71–85
20. Sockalingam S, Gillespie JW, Keefe M (2014) On the transverse compression response of Kevlar KM2 using fiber-level finite element model. Int J Solids Struct 51(13):2504–2517
21. Sockalingam S, Chowdhury SC, Gillespie JW, Keefe M (2016) Recent advances in modeling and experiments of Kevlar ballistic fibrils, fibers, yarns and flexible woven textile fabrics - a review. Text Res J 87(8):984–1010
22. Sockalingam S, Gillespie JW, Keefe M (2016) Influence of multiaxial loading on the failure of Kevlar KM2 single fiber. Text Res J 88(5):483–498
23. Tabiei A, Nilakantan G (2008) Ballistic impact of dry woven fabric composites: a review. Appl Mech Rev 61(1)

Chapter 8
Structural Health Monitoring: Numerical Simulation of Lamb Waves Via Higher-Order Models

A. G. de Miguel, A. Pagani and E. Carrera

Abstract This chapter proposes a numerically efficient method to simulate Lamb waves in laminated structures in the framework of structural health monitoring (SHM). Due to the high frequencies involved in Lamb wave problems, time-domain analyses call for very fine spatial and temporal discretizations of the numerical model. As a consequence, standard models based on the finite element method (FEM) might become extremely large, and new efficient simulation tools must be introduced. A series of multi-layered plate elements for the wave propagation problem are proposed. Equivalent single layer (ESL) and layer wise (LW) kinematics based on hierarchical assumptions are tested. Exploiting their superior convergence rates, higher-order polynomials are used as shape functions of the finite elements. Numerical examples of composite plates are included to show the advantages of each model proposed.

8.1 Lamb Wave-Based Damage Detection Systems

The use of guided ultrasonic waves (GUW) to detect structural defects is receiving vast attention among the research community [7]. Unlike off-line non-destructive tests (NDT), the main advantage of this technique is that the structure can be continuously and autonomously monitored on-line, ensuring its integrity during service. In aeronautics for instance, this capability would allow the airliners to optimize the inspection and repair works, which could have a major impact in the maintenance costs. Indeed, it is expected that this kind of structural health monitoring (SHM) systems will be introduced in a large scale in the latest composite aircrafts, for which there is less failure experience than in conventional metallic ones.

The deployment of robust SHM systems in composite structures requires a good knowledge of the mechanics of elastic waves. Therefore, the fundamental characteris-

A. G. de Miguel (✉) · A. Pagani · E. Carrera
MUL2 Group, Department of Mechanical and Aerospace Engineering, Politecnico di Torino, Torino, Italy
e-mail: alberto.garcia@polito.it

M. Petrolo (ed.), *Advances in Predictive Models and Methodologies for Numerically Efficient Linear and Nonlinear Analysis of Composites*, PoliTO Springer Series,
https://doi.org/10.1007/978-3-030-11969-0_8

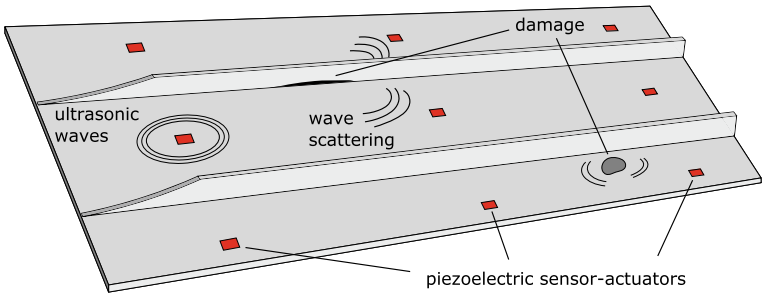

Fig. 8.1 SHM methodology

tics of the propagation of guided waves in thin-walled media must be fully understood as an initial step in the design [11]. Figure 8.1 illustrates the basic methodology of GUW-based damage detection, where one can get an idea of the complex physical phenomena that are involved in the problem, such as the propagation and reflection of the waves in reinforced structures and their scattering under the presence of defects. All this information must be acquired and transfer into on-board computers for the evaluation of the location and severity of the damage.

Lamb waves, first described by Lamb [10], are a class of GUW propagating in plates with free surface conditions that produce an elliptical motion of the material particles. This type of waves appears due to the reflections of longitudinal and transversal waves in the stress-free boundaries of the plate. As a consequence of the combination of these two waves, various modes might appear which can be classified into symmetric (S_0, S_1, ...) and antisymmetric (A_0, A_1, ...). The convenience of Lamb waves for on-line damage detection is twofold: first, they are able to travel long distances with low attenuation, therefore large areas can be inspected; and second, they feature very short wavelengths, making it possible to detect small defects of different nature, such as impacts, debonds, delaminations, etc. When dealing with the GUW in anisotropic media and layered structures, the dynamic response of the thin-walled structure becomes more cumbersome. In addition to the out-of-plane symmetric and antisymmetric modes of Lamb waves, in-plane shear horizontal waves (SH) might be excited as well. Figure 8.2 illustrates the displacement profiles of the fundamental modes of GUW in anisotropic media. Moreover, due to the directionality of the mechanical properties in anisotropic materials, the phase and group velocities are not constant over the plane of propagation and, as a result, the excited modes travel faster in certain directions. In laminates, the heterogeneities of the multiphase materials and the interaction between layers have substantial effects on the resulting modes, which might be coupled and exhibit continuous conversion along the wave paths.

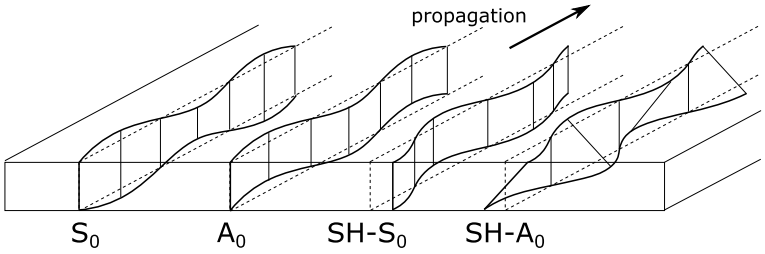

Fig. 8.2 Representation of the fundamental modes of guided waves in an anisotropic layer, from left to right: Lamb symmetric (S_0), Lamb antisymmetric (A_0), shear horizontal symmetric (SH-S_0) and shear horizontal antisymmetric (SH-A_0)

8.2 Numerical Modeling of Lamb Waves

The basic methodology of Lamb wave-based SHM is based on the processing of the time of flight of the wave packets along different paths over the structure. Eventual variations in the time signals are evaluated to infer the existence and severity of the damage. In this matter, the development of simulation techniques is necessary to obtain fundamental characteristics of the wave propagation in different media, such as the wavelength, the wavenumber or the phase and group velocities. In the last years, researchers have introduced a family efficient models to solve the wave problem in the frequency domain and provide the dispersion curves for generic composite materials. Some of these methods are the transfer matrix method [13], the global matrix method [15], the local interaction simulation approach (LISA) [5] and the semi-analytical finite element (SAFE) [4].

The analysis of the transient phenomena and the scattering of Lamb waves usually calls for time-domain numerical models, which are able to provide the time signals at any point of the structure. The finite element method (FEM) and similar techniques can be used to support direct measurements and to extract essential information about the response of the structure under different kinds of defects [8]. Nevertheless, the implementation of weak-form solutions for the analysis of ultrasonic waves is highly challenging. The high frequencies involved in the dynamic problem require fine spatial and temporal resolutions. Indeed, for standard FEM solutions, values as low as $\frac{1}{20}$ were suggested for ratio between the element size and the minimum wavelength [14]. Also, due to the high dispersion of Lamb waves, large spatial domains have to be accounted in the analysis, making the model extremely expensive in terms of computational cost.

Example 8.1 Let's consider the propagation of Lamb waves in an aluminum strip, see Table 8.1. In the case of elastic isotropic materials, the wavenumber of the symmetric and antisymmetric modes can be obtained analytically [7] from the Rayleigh–Lamb equations:

$$\frac{tan\left(b\frac{h}{2}\right)}{tan\left(a\frac{h}{2}\right)} = -\left[\frac{4abk^2}{(k^2-b^2)^2}\right]^{\pm 1}, \tag{8.1}$$

Table 8.1 Mechanical characteristics of the Aluminum plate in Example 8.1

Thickness, h	4 mm
Young's modulus, E	70×10^9 Pa
Poisson ratio, ν	0.33
Density, ρ	2700 kg/m^3
Longitudinal speed, c_1	6197 m/s
Transversal speed, c_2	3121 m/s

a and b being

$$a^2 = \omega^2/c_1^2 - k^2, \qquad b^2 = \omega^2/c_2^2 - k^2, \tag{8.2}$$

where ω is the angular frequency and k the wavenumber. The sign of the power of the right-hand term of Eq. 8.1 denotes whether the solution is symmetric (+) or antisymmetric (−). Once we have the relation between k and ω, it is possible to obtain the dispersion curve of the phase velocity, c_p, and the group velocity, c_g, as follows:

$$c_p = \omega/k, \qquad c_g = c_p^2 \left(c_p - \omega \frac{\partial c_p}{\partial \omega} \right). \tag{8.3}$$

Considering an excitation of central frequency, $f = 2\pi/\omega$, equal to 0.5 MHz, the analytical phase and group velocities result:

$$c_{p_{S0}} \simeq 4757, \qquad c_{g_{S0}} \simeq 3062, \tag{8.4}$$

$$c_{p_{A0}} \simeq 2674, \qquad c_{g_{A0}} \simeq 3126, \tag{8.5}$$

units in m/s. The wavelengths, $\lambda = 2\pi/k$, of the two modes are then:

$$\lambda_{S0} \simeq 9.51 \text{ mm}, \qquad \lambda_{A0} \simeq 5.34 \text{ mm}, \tag{8.6}$$

From these values, it is possible to infer that the most critical mode for a FEM model is the antisymmetric. To provide some figures: to accurately simulate the A_0-wave in a plate of 1 m × 1 m, accounting for 20 elements per wavelength, the total number of elements along each direction raises up to 3746. Furthermore, regarding the time step size, the Courant–Friedrich–Levy condition [3] states:

$$\Delta t \leq \frac{l_e}{c_g}, \tag{8.7}$$

where Δt is the time increment and l_e is the size of the finite element. Accordingly, for the present example we obtain $\Delta t \leq 2 \times 10^{-7}$ s.

As a consequence of these numerical requirements, the simulation of SHM systems in real structures become an extremely demanding task, and therefore, more efficient tools are needed. In this line, many research works have been directed towards the implementation of higher-order models for wave propagation. It is well-

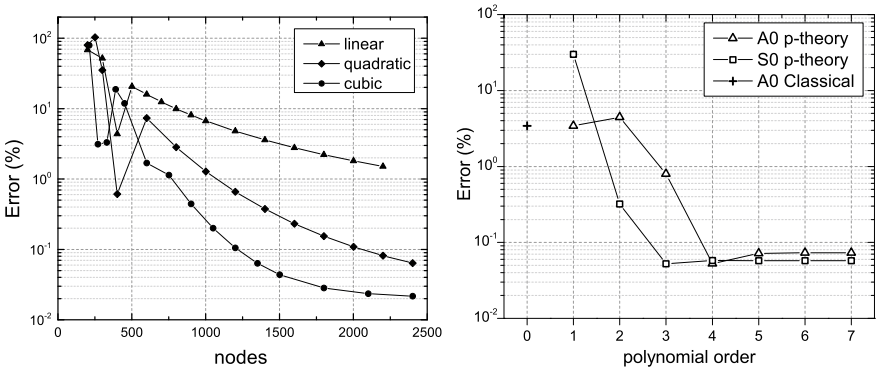

(a) In-plane mesh (b) Transverse order

Fig. 8.3 Convergence rates of the solutions for increasing polynomial orders of **a** the longitudinal mesh and **b** the transverse assumptions

known that higher-order methods including p-refinement schemes exhibit better convergence properties compared to standard h-methods. Figure 8.3a shows the convergence rate of linear, quadratic and cubic order for a metallic strip similar to that of Example 8.1. One can observe how the numerical error, calculated as the ratio between the computed c_g and the analytical one, diminishes substantially faster when higher-order shape functions are employed. Based on this concept, several advanced weak-form solutions can be found in the literature, such as the spectral element method (SEM) [9], the finite cell method [6] and the p-version of FEM [17].

To bring the computational cost down, the geometrical features of thin-walled structures are usually exploited to derive dimensionally reduced models, such as plates and shells. This approach allows one to substitute the discretization along the thickness direction by certain kinematic assumptions, thus reducing the size of the numerical problem and making it possible to extend the aforementioned methods to larger problems [16]. However, one must be aware of the fact that the classical theories describing the kinematics of the plate elements have inherent limitations when simulating Lamb waves. First, they do not account for the stretching effects, therefore the symmetric modes are neglected. Also, by removing the FEM approximation in the transverse direction, the displacement fields of the antisymmetric modes cannot be accurately simulated, introducing a numerical error in the analysis. Figure 8.3b shows the numerical error of Mindlin-based elements (A0 Classical) and higher-order theories (p-theory). Higher-order structural theories are able to overcome the limitations of the linear assumptions of classical theories and to compute a 3D-like resolution in the displacement solutions.

8.3 Multi-layered Elements for Wave Propagation

The main goal of the present chapter is to propose advanced multi-layered elements for the efficient GUW analysis. To this end, the two possible FEM-based solutions for the Lamb wave propagation in laminated structures are: (1) large scale 3D models that account for the stack of plies using a mesh of solid elements over the volume; and (2) plate elements based on first shear deformation theories (FSDT), which reduce the size of the numerical problem. The goal of this research is to extend the latter approach to account for 3D effects, keeping the computational costs in a low range without compromising the level of detail in the analysis.

In this section, we consider a Cartesian reference system in which the mid-surface of the laminate lies on the xy-plane, being z the thickness coordinate. First we introduce two types of kinematics for the multi-layered structure, namely equivalent single layer (ESL) and layer wise (LW). Then, a class of higher-order plate elements is proposed and the fundamental matrices are depicted. Finally, the choice of the time integration scheme is discussed.

8.3.1 Multi-layered Theories

The structural theories for multi-layered materials can be classified in equivalent single layer (ESL), in which the kinematic assumptions are independent of the number of layers, and layer wise (LW), in which the number of degrees of freedom (DOF) is proportional to the number of layers.

8.3.1.1 Equivalent Single Layer

One of the simplest plate models for multi-layered structures is the FSDT, which is based in the Mindlin kinematics:

$$u_x(x, y, z, t) = u_{x_0}(x, y, t) + z\,\phi_y(x, y, t), \tag{8.8}$$

$$u_y(x, y, z, t) = u_{y_0}(x, y, t) - z\,\phi_x(x, y, t), \tag{8.9}$$

$$u_z(x, y, z, t) = u_{z_0}(x, y, t). \tag{8.10}$$

The FSDT accounts for 5 DOF (3 displacements and 2 rotations) and it is implemented in most standard FEM codes. In order to overcome the aforementioned issues of classical theories, the Carrera's unified formulation (CUF) [1] is employed to generate arbitrary expansions of the thickness coordinate, expressing the kinematics of the plate as:

$$\boldsymbol{u}(x, y, z, t) = F_\tau(z)\,\boldsymbol{u}_\tau(x, y, t), \qquad \tau = 1, \ldots, M, \tag{8.11}$$

where F_τ are arbitrary functions of the z-coordinate, and M is the total number of expansion terms in the kinematic field. A Taylor-class theory is implemented in this work to build higher-order ESL models. In this manner, the expansion functions take the form of $F_\tau = z^p$, being p the polynomial order. If a second order model is chosen, the displacement field can be described as

$$u_x(x, y, z, t) = u_{x_0}(x, y, t) + z\, u_{x_1}(x, y, t) + z^2\, u_{x_2}(x, y, t), \tag{8.12}$$
$$u_y(x, y, z, t) = u_{y_0}(x, y, t) + z\, u_{y_1}(x, y, t) + z^2\, u_{y_2}(x, y, t), \tag{8.13}$$
$$u_z(x, y, z, t) = u_{z_0}(x, y, t) + z\, u_{z_1}(x, y, t) + z^2\, u_{z_2}(x, y, t), \tag{8.14}$$

which accounts for 9 DOF in total among constant, linear and quadratic terms. Note that Taylor-class expansions include stretching terms in the kinematics (Eq. 8.14), therefore the symmetric modes can be captured. Also, by increasing the order of the expansion, the distribution of the displacements across the laminate can be better approximated.

8.3.1.2 Layer Wise

On the other hand, LW models make use of independent expansions for each layer, allowing it to capture the intralaminar deformations with higher resolution. The price comes in the form of the extra DOF associated to each layer. Non-local hierarchical expansions are chose here as F_τ. These can be obtained from the 1D set of Legendre polynomials:

$$L_0 = 1, \tag{8.15}$$
$$L_1 = s, \tag{8.16}$$
$$L_p = \frac{2p-1}{p} s L_{p-1}(s) - \frac{p-1}{p} L_{p-2}(s), \quad p = 2, 3, 4, \ldots \tag{8.17}$$

Subsequently, a set of 1D thickness functions can be defined as:

$$F_1(r) = \frac{1}{2}(1 - r), \tag{8.18}$$
$$F_2(r) = \frac{1}{2}(1 + r), \tag{8.19}$$
$$F_p(r) = \sqrt{\frac{2p-1}{p}} \int_{-1}^{r} L_{p-1}(r)\, dr, \quad p = 2, 3, 4, \ldots, \tag{8.20}$$

where the first two functions correspond to the top and bottom nodal expansions, and the rest are obtained from the normalized integrals of the Legendre polynomials. Note that the variable r is defined in the natural domain $[-1, 1]$, therefore a Jacobian transformation is needed to compute the integrals of the energies in the global domain. The C^0 continuity of the displacements is imposed via assembly in the element matrices.

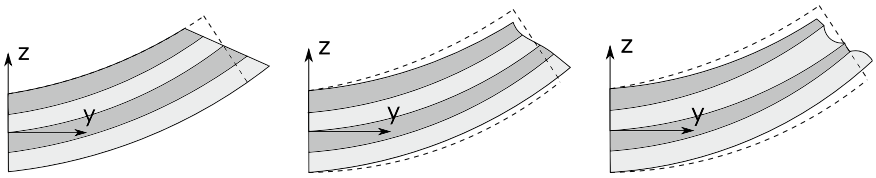

(a) FSDT (b) Refined ESL (c) LW

Fig. 8.4 Possible deformations of FSDT, ESL and LW models

Figure 8.4 illustrates the mechanical response that can be expected from each of the studied models. From left to right in the figure, it is clear that more physical effects are added to the model at the expense of extra DOF. One additional advantage of LW modes lies in the fact that displacement unknowns are placed at the top and bottom of the layers. This property is convenient for the simulation of the excitation forces generated by piezoelectric transducers, and also for the simulation of interlaminar defects such as delaminations.

8.3.2 Higher-Order Plate Elements

The weak-form of the dynamic problem can be derived from the principle of virtual displacements, which reads:

$$\int_V \delta \boldsymbol{u}^T \rho \, \ddot{\boldsymbol{u}} \, dV + \int_V \delta \boldsymbol{\varepsilon}^T \boldsymbol{\sigma} \, dV = \int_S \delta \boldsymbol{u}^T P_S \, dS + \int_V \delta \boldsymbol{u}^T P_V \, dV, \tag{8.21}$$

where the first two terms correspond to the virtual inertial work and the elastic energy, and the last two to the virtual work done by the surface, P_S, and volume, P_V, forces. In this expression, it is common to write the strain and stress tensors in vectorial form as:

$$\begin{aligned} \boldsymbol{\varepsilon}^T &= \left\{ \varepsilon_{xx} \ \varepsilon_{yy} \ \varepsilon_{zz} \ \varepsilon_{xz} \ \varepsilon_{yz} \ \varepsilon_{xy} \right\}, \\ \boldsymbol{\sigma}^T &= \left\{ \sigma_{xx} \ \sigma_{yy} \ \sigma_{zz} \ \sigma_{xz} \ \sigma_{yz} \ \sigma_{xy} \right\}. \end{aligned} \tag{8.22}$$

For the present implementation, both physical and geometrical linear theories are used. Therefore, for the relation between strains and displacements, we have:

$$\boldsymbol{\varepsilon} = \mathbf{D} \, \boldsymbol{u}, \tag{8.23}$$

where $\mathbf{D}$ is the following differential operator, defined as:

$$\mathbf{D}^T = \begin{bmatrix} \frac{\partial}{\partial x} & 0 & 0 & \frac{\partial}{\partial z} & 0 & \frac{\partial}{\partial y} \\ 0 & \frac{\partial}{\partial y} & 0 & 0 & \frac{\partial}{\partial z} & \frac{\partial}{\partial x} \\ 0 & 0 & \frac{\partial}{\partial z} & \frac{\partial}{\partial x} & \frac{\partial}{\partial y} & 0 \end{bmatrix}. \tag{8.24}$$

The constitutive relations are obtained from the Hooke's law, which reads:

$$\boldsymbol{\sigma} = \mathbf{C}\,\boldsymbol{\varepsilon}, \tag{8.25}$$

where $\mathbf{C}$ is the 6×6 stiffness matrix of the material. In the generic case of anisotropic materials, $\mathbf{C}$ is full and should be written in the global framework.

In FEM applications, the domain of the analysis is divided into smaller subdomains, where the displacement unknowns are approximated by sets of shape functions. In the present formulation, the generalized unknowns of the plate problem, $\boldsymbol{u}_\tau$ (Eq. (8.11)), are interpolated over the 2D domain as follows:

$$\boldsymbol{u}_\tau(x, y, t) = N_i(x, y)\,\boldsymbol{u}_{\tau i}(t), \qquad i = 1, \ldots, N, \tag{8.26}$$

where N is the number of nodes in the element and $\boldsymbol{u}_{\tau i}$ are the generalized unknowns of the dynamic problem. For the wave propagation problem, 2D Lagrange-class polynomials of higher-order are chosen as the shape functions of the plate element. This set is constructed as the product of the 1D Lagrange polynomials:

$$N_i(\xi, \eta) = \phi_m(\xi)\,\phi_n(\eta), \qquad \xi, \eta \in [-1, 1], \tag{8.27}$$

where

$$\phi_m(\xi) = \prod_{m=1, m\neq n}^{p_{FE}} \frac{\xi - \xi_m}{\xi_n - \xi_m}, \qquad m, n = 1, \ldots, p_{FE} + 1, \tag{8.28}$$

with p_{FE} being the order of the plate element. The roots ξ_m of the Lagrange polynomials are chosen to be equidistant. Now, making use of Eqs. (8.11) and (8.26), one can write:

$$\boldsymbol{u} = F_\tau N_i \boldsymbol{u}_{\tau i}, \tag{8.29}$$

$$\delta\boldsymbol{u} = F_s N_j \boldsymbol{u}_{sj}. \tag{8.30}$$

Introducing these expressions into Eqs. (8.23), (8.25) and (8.21), the equation of motion can be written as:

$$\delta\boldsymbol{u}_{sj}^T\,\mathbf{M}^{ij\tau s}\,\ddot{\boldsymbol{u}}_{\tau i} + \delta\boldsymbol{u}_{sj}^T\,\mathbf{K}^{ij\tau s}\,\boldsymbol{u}_{\tau i} = \delta\boldsymbol{u}_{sj}^T\,\mathbf{P}^{i\tau}, \tag{8.31}$$

where $\mathbf{K}^{ij\tau s}$ and $\mathbf{M}^{ij\tau s}$ are 3×3 building blocks of the stiffness and mass matrices, respectively, and $\mathbf{P}^{i\tau}$ is the 3×1 force vector. Only surfaces loads are accounted at this point. These so-called fundamental nuclei are defined as:

$$\mathbf{M}^{ij\tau s} = \int_h \int_\Omega F_s\,N_j\,\rho\,F_\tau\,N_i\,d\Omega\,dz, \tag{8.32}$$

$$\mathbf{K}^{ij\tau s} = \int_h \int_\Omega (\mathbf{D}\,F_s\,N_j)^T\,\mathbf{C}\,\mathbf{D}\,F_\tau\,N_i\,d\Omega\,dz, \tag{8.33}$$

$$\mathbf{P}^{i\tau} = \int_{\Omega} F_{\tau}\ N_i\ P_S\ d\Omega. \tag{8.34}$$

Note that the integrals of the components of these matrices can be split into the in-plane and the thickness domains, respectively:

$$I_{i_{(,x)(,y)}j_{(,x)(,y)}} = \int_{\Omega} N_{i_{(,\xi)(,\eta)}} N_{j_{(,\xi)(,\eta)}} |\boldsymbol{J}_{\Omega}| d\xi d\eta, \tag{8.35}$$

$$E_{\tau_{(,z)}s_{(,z)}} = \int_{h} F_{\tau_{(,z)}} F_{s_{(,z)}} dz, \tag{8.36}$$

where $\boldsymbol{J}_{\Omega}$ is the Jacobian matrix of the finite element and the subindices $(,x)$, $(,y)$ and $(,z)$ refer to the eventual derivatives of the shape functions and the expansion polynomials. Standard Gaussian quadrature is used to compute all the integrals. It is worth noting that the integrals of the expansion functions, $E_{\tau_{(,z)}s_{(,z)}}$, vary depending on the multi-layered theory selected:

- ESL, over the laminate thickness:

$$\int_{h} \dots\ dz = \sum_{l=1}^{n_l} \int_{z_l^b}^{z_l^t} \dots\ dz, \tag{8.37}$$

  where z_l^b and z_l^t are the bottom and top coordinates, respectively, of layer l and n_l is the total number of layers.
- LW, for each layer:

$$\int_{h} \dots\ dz = \int_{-1}^{+1} \dots\ |\boldsymbol{J}_z|\, dr, \tag{8.38}$$

  where $\boldsymbol{J}_z$ is the Jacobian of the transformation between r and z.

Finally, by expanding the fundamental nuclei over τ, s, i and j, the system of equations reads:

$$\mathbf{M}\ddot{\mathbf{U}} + \mathbf{K}\mathbf{U} = \mathbf{P}, \tag{8.39}$$

where $\mathbf{M}$, $\mathbf{K}$ and $\mathbf{P}$ are the global arrays of the dynamic problem and $\mathbf{U}$ and $\ddot{\mathbf{U}}$ are the vectors of the displacement and acceleration unknowns, respectively. For more information about the derivation of the finite element matrices in the framework of CUF, the reader is referred to [2].

8.3.3 Time Integration Scheme

In time-domain analyses, the equation of motion has to be discretized in time as well. Due to the high frequency regimes involve in GUW problems, the time steps

are usually small (see Example 8.1). For this reason, explicit time schemes are preferred along with an appropriate mass lumping method which allow it to obtain the solution of the system at each time step using only matrix multiplications. This capability is advantageous for GUW problems in which the number of steps increases considerably. However, since explicit solvers are conditionally stable one must be careful when defining the time step size.

Since in the present research we compare different higher-order plate theories, it is not always possible to diagonalize the mass matrix, therefore explicit solvers do not present any advantage. For this reason, an efficient implicit solver based on the Newmark method is implemented. Using the Newmark time scheme, the displacements and velocities at a certain time step are defined as:

$$\begin{aligned}\dot{\mathbf{U}}_{t+\Delta t} &= \dot{\mathbf{U}}_t + [(1-\gamma)\ddot{\mathbf{U}}_t + \gamma\ddot{\mathbf{U}}_{t+\Delta t}],\\ \mathbf{U}_{t+\Delta t} &= \mathbf{U}_t + \dot{\mathbf{U}}_t\Delta t + [(1/2-\beta)\ddot{\mathbf{U}}_t + \beta\ddot{\mathbf{U}}_{t+\Delta t}]\Delta t^2,\end{aligned} \tag{8.40}$$

where γ and β are the parameters controlling the stability and accuracy of the solver. An unconditionally stable solver is obtained for $\gamma = 1/2$ and $\beta = 1/4$. The linear assumptions of the formulation imply that the stiffness and mass matrices do not vary along the time, which can be exploited to devise an efficient integration scheme as follows:

1. Assembly of the mass matrix $\mathbf{M}$ and stiffness $\mathbf{K}$ (the damping is neglected)
2. Assignation of the time step Δt and computation of the dynamic stiffness matrix

$$\bar{\mathbf{K}} = \mathbf{K} + \frac{1}{\Delta t^2\beta}\mathbf{M} \tag{8.41}$$

3. Initialization of $\mathbf{U}_0$, $\dot{\mathbf{U}}_0$ and $\ddot{\mathbf{U}}_0$ for $t = t_0$.
4. Factorization of the dynamic stiffness matrix $\bar{\mathbf{K}} = \mathbf{L}\,\mathbf{D}\,\mathbf{L}^T$
5. Start the loop on the time steps
6. Computation of the dynamic force vector at $t + \Delta t$:

$$\bar{\mathbf{P}}_{t+\Delta t} = \mathbf{P}_{t+\Delta t} + \mathbf{M}\left(\frac{1}{\Delta t^2\beta}\mathbf{U}_t + \frac{1}{\Delta t\beta}\dot{\mathbf{U}}_t + \left(1-\frac{1}{2\beta}\right)\ddot{\mathbf{U}}_t\right) \tag{8.42}$$

7. Solution at current time step $\mathbf{U}_{t+\Delta t} = \bar{\mathbf{K}}^{-1}\,\bar{\mathbf{P}}_{t+\Delta t}$
8. Computation of $\dot{\mathbf{U}}$ and $\ddot{\mathbf{U}}$ at current step:

$$\dot{\mathbf{U}}_{t+\Delta t} = \frac{\gamma}{\Delta t\beta}(\mathbf{U}_{t+\Delta t} - \mathbf{U}_t) + \left(1-\frac{\gamma}{\beta}\right)\dot{\mathbf{U}}_t + \left(1-\frac{\gamma}{2\beta}\right)\Delta t\,\ddot{\mathbf{U}}_t \tag{8.43}$$

$$\ddot{\mathbf{U}}_{t+\Delta t} = \frac{1}{\Delta t^2\beta}(\mathbf{U}_{t+\Delta t} - \mathbf{U}_t) - \frac{1}{\Delta t\beta}\dot{\mathbf{U}}_t + \left(\frac{1}{2\beta}-1\right)\ddot{\mathbf{U}}_t \tag{8.44}$$

In this manner, the solution travels in time making only multiplications, therefore reducing the computational effort massively. Lumping methods such as row summing

or Gauss–Lobatto–Legendre nodal grids (characteristic of SEM) could be implemented in the current framework for Lagrange-based polynomial expansions. In that case, explicit schemes such as the central difference method could be employed.

8.4 Laminate Examples

This section shows some numerical applications of the proposed formulation for the simulation of Lamb waves in laminated structures. A squared composite plate made of T300/F593 material is studied. The material properties are taken from [12], being: $E_1 = 128.1\,\text{GPa}$, $E_2 = E_3 = 8.2\,\text{GPa}$, $G_{12} = G_{13} = 4.7\,\text{GPa}$, $G_{23} = 3.44\,\text{GPa}$, $\nu_{12} = \nu_{13} = 0.27\,\text{GPa}$, $\nu_{23} = 0.2$ and density $\rho = 1570\,\text{kg/m}^3$. The overall dimensions are $500 \times 500 \times 1.72$, in mm. Three different lay-ups are considered: (1) an unidirectional ply, (2) a $[0_2/90_2]_S$ cross-ply and (3) a $[45/-45/0/90]_S$ quasi-isotropic laminate. A wave packet is excited in all cases by means of a Hanning window of 100 kHz and 5 cycles. The fundamental modes are generated by means of two unitary forces applied at top and bottom in the center of the plate. The forces applied in-phase excite the antisymmetric modes, whereas when applied out-of-phase, the symmetric modes appear.

Since the purpose of this study is to test and compare the different multi-layered theories here proposed, a refined mesh of 6400 cubic plate elements is employed, ensuring a minimal numerical error from the FE discretization. The quality of the numerical results produced by the FSDT and higher-order theories is evaluated in laminate (1) through the computed value for the group velocity, c_g, of the A_0 mode in the x-direction. This value is obtained from the peak of the envelope of the time signal evaluated at $x = 150\,\text{mm}$ on the central axis. Table 8.2 includes the results compared to those of a 3D SEM model of the same case [12]. It can be noticed that the symmetric terms in the thickness expansion (HL2, HL4) do not have an effect in the solution when only antisymmetric responses are present in the solution. The contour plots of the waves propagating over the plate are shown in Figs. 8.5 and 8.6. Note that in the latter, for a symmetric excitation both S_0 and SH_0 are visible.

Multi-layered structures represent a much bigger challenge for the numerical model. LW models can be used to provide 3D solutions but the computational costs rise up considerably as the number of layers increases. Figure 8.7 shows the computed A_0-waves in laminates (2) and (3). It is possible to observe that the existence of ± 45

Table 8.2 Computed group velocities of the A_0-wave propagating in the unidirectional laminate

Model	Group velocity (A_0) (m/s)	Error (%)
SEM 3D [12]	1794	–
FSDT	1884	5.04
HL1	1884	5.04
HL2	1884	5.04
HL3	1773	1.17
HL4	1773	1.17

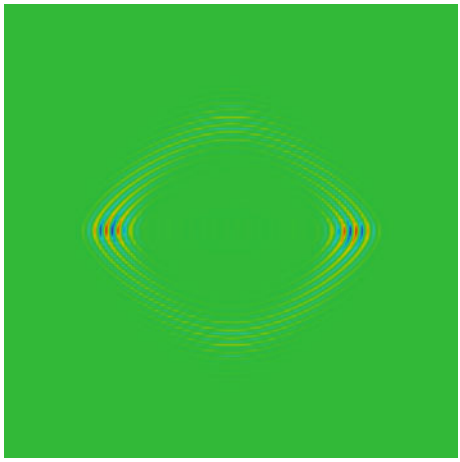

Fig. 8.5 Displacements (u_z) at $t = 7.5 \times 10^{-5}$ s showing the A_0-wave propagating over the T300 ply. Model HL3

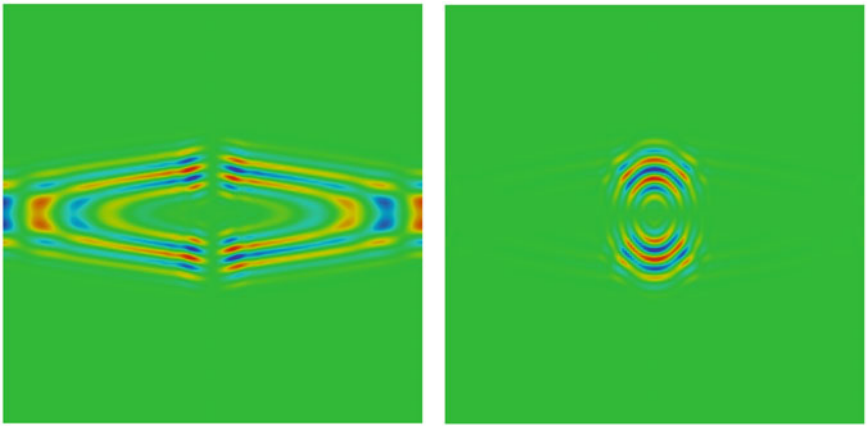

(a) u_x (b) u_y

Fig. 8.6 Displacement fields at $t = 5 \times 10^{-5}$ s showing **a** the S_0-wave and **b** the SH_0-wave. Model HL3

plies at top and bottom in laminate (3) has a notable effect on the shape of the wavefront. More efficient ESL models are tested and compared LW solutions to evaluate under what circumstances they can provide satisfactory results. It is found that for the two multi-layered plates considered, the FSDT models differ from the LW solutions in 14.7% for the $[0_2/90_2]_S$ and in 10.6% for the $[45/-45/0/90]_S$. If a third-order ESL model is employed, these errors go down to 5.7% for the cross-ply and 0.5% for the quasi-isotropic laminate. These results show that higher-order ESL elements outperform FSDT elements in GUW problems, showing high levels of accuracy as the number of plies increases.

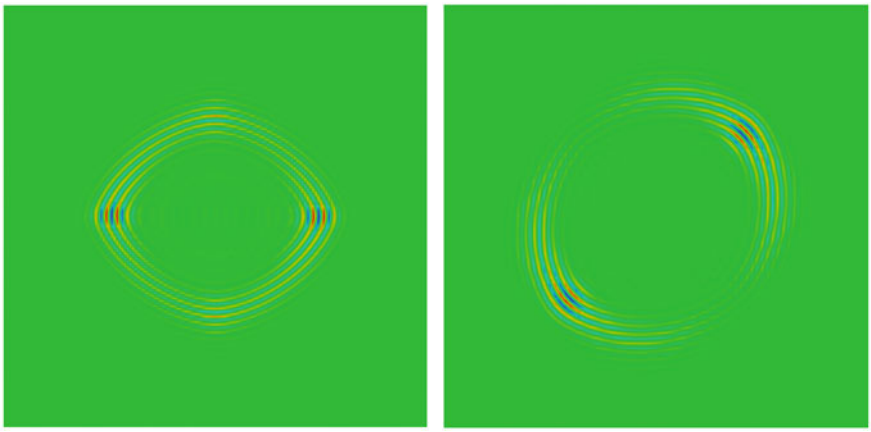

(a) Cross-ply (b) Quasi-isotropic

Fig. 8.7 Screenshots of the A_0-wave in **a** the $[0_2/90_2]_S$ cross-ply at $t = 7.5 \times 10^{-5}$ s and **b** $[45/-45/0/90]_S$ laminate at $t = 1.125 \times 10^{-4}$ s

8.4.1 Damage Detection

The capabilities of the proposed multi-layered elements for the modeling of composite damage is also addressed. For that, a defect is simulated in the quasi-isotropic laminate by removing the uppermost ± 45 plies in a sector of dimensions 37 mm $\times$ 37 mm. Using a LW approach based on Legendre expansions, the modeling of this defect can be done straightforwardly, as only two expansion domains are removed in the correspondent elements. A screenshot of the traveling as it propagates over the damaged area is included in Fig. 8.8. It is possible to observe the distortion of the

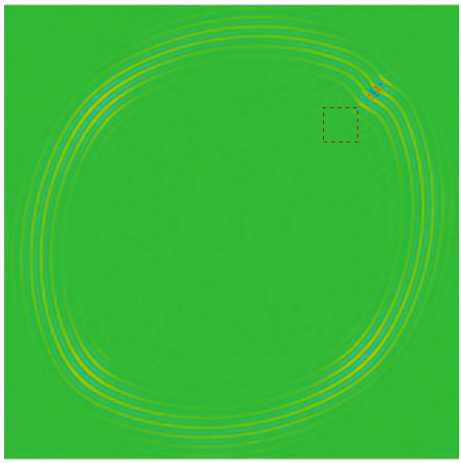

Fig. 8.8 Scattering of the A_0-wave in the quasi-isotropic laminate with a defect (uppermost ± 45 missing in the sector marked with the dashed line)

wavefront, which is slowed down at the damaged region. LW solutions like the one included here are necessary to acquire knowledge of the scattering of Lamb waves under different types of defects.

8.5 Conclusions

This chapter has shown the implementation of multi-layered structural theories for the analysis of ultrasonic waves in composites with applications to structural health monitoring (SHM). Two classes of plate kinematics are confronted, namely equivalent single layer (ESL) and layer wise (LW). Widely used first shear deformation theories (FSDT) can be generated as a particular case of the former one. Higher-order polynomials are used as interpolation functions. The purpose of this dissemination is to propose solutions for the time-domain analyses of Lamb waves which can fill the gap between standard FSDT plates and solid models. It is demonstrated that LW solutions are able to provide a 3D resolution in the computation of wave propagation. Higher-order ESL solutions are able to show LW-like levels of accuracy as the number of plies increases.

References

1. Carrera E (2002) Theories and finite elements for multilayered, anisotropic, composite plates and shells. Arch Comput Methods Eng 9(2):87–140
2. Carrera E, Cinefra M, Zappino E, Petrolo M (2014) Finite element analysis of structures through unified formulation. Wiley, United Kingdom
3. Courant R, Friedrichs K, Lewy H (1928) Über die partiellen Differenzengleichungen der mathematischen Physik. Math Ann 100:32–74
4. Datta SK, Shah AH, Bratton RL, Chakraborty T (1988) Wave propagation in laminated composite plates. J Acous Soc Am 83(6):2020–2026
5. Delsanto PP, Whitcombe T, Chaskelis HH, Mignogna RB (1992) Connection machine simulation of ultrasonic wave propagation in materials. I: the one-dimensional case. Wave Motion 16(1):65–80
6. Duczek S, Joulaian M, Düster A, Gabbert U (2014) Numerical analysis of lamb waves using the finite and spectral cell methods. Int J Numer Methods Eng 99(1):26–53
7. Giurgiutiu V (2014) Structural health monitoring with piezoelectric wafer active sensors, 2nd edn. Academic Press, Oxford
8. Ke W, Castaings M, Bacon C (2009) 3D finite element simulations of an air-coupled ultrasonic NDT system. NDT & E Int 42(6):524–533
9. Komatitsch D, Tromp J (2002) Spectral-element simulations of global seismic wave propagation — I. validation. Geophys J Int 149(2):390–412
10. Lamb H (1917) On waves in an elastic plate. R Soc Lond Proc Ser A 93:114–128
11. Lammering R, Gabbert U, Sinapius M, Schuster T, Wierach P (eds) (2018) Lamb-wave based structural health monitoring in polymer composites. Springer, Cham
12. Li F, Peng H, Sun X, Wang J, Meng G (2012) Wave propagation analysis in composite laminates containing a delamination using a three-dimensional spectral element method. Math Probl Eng 2012(659849)

13. Lowe MJS (1995) Matrix techniques for modeling ultrasonic waves in multilayered media. IEEE Trans Ultrason Ferroelectr Freq Control 42(4):525–542
14. Moser F, Jacobs LJ, Qu J (1999) Modeling elastic wave propagation in waveguides with the finite element method. NDT & E Int 32(4):225–234
15. Obenchain MB, Cesnik CES (2013) Producing accurate wave propagation time histories using the global matrix method. Smart Mater Struct 22(125024)
16. Schulte RT, Fritzen CP (2011) Simulation of wave propagation in damped composite structures with piezoelectric coupling. J Theor Appl Mech 49(3)
17. Willberg C, Duczek S, Vivar Perez JM, Schmicker D, Gabbert U (2012) Comparison of different higher order finite element schemes for the simulation of Lamb waves. Comput Methods Appl Mech Eng 241–244:246–261

Part III
Virtual Characterization, Manufacturing Effects and Uncertainty Quantification

Chapter 9
Improving the Static Structural Performance of Panels with Spatially Varying Material Properties Using Correlations

S. van den Broek, S. Minera, E. Jansen, A. Pirrera, P. M. Weaver and R. Rolfes

Abstract This chapter introduces an approach to systematically analyze stochastic distributions of spatially varying material properties in structures. The approach gives insight into how spatial variations of material properties affect the mechanical response of a structure. If sufficient knowledge of the production processes is available, this allows designers to analyze the probability that a certain design criterion (e.g. a certain buckling load level) is met. Stochastic structural analyses can be used to analyze how variations are correlated to a structural measure. This gives information on the sensitivity of the structure with respect to variations. In the present work, this is used to improve the structural performance by distributing a material pattern according to a pattern based on the sensitivity topology. This approach is illustrated by redistributing the material properties of an axially loaded panel on the basis of the correlation of the spatially varying Young's modulus with the linear buckling load of the panel.

9.1 Introduction

9.1.1 Background and Motivation

Spatial variations of structural and material properties are important aspects which should be included in the design of structures. Mainstream structural engineering practice is for geometric imperfections of a structure to be taken into account by

S. van den Broek · E. Jansen (✉) · R. Rolfes
Institute of Structural Analysis, Leibniz Universität Hannover, Hannover, Germany
e-mail: e.jansen@isd.uni-hannover.de

S. Minera · A. Pirrera · P. M. Weaver
Advanced Composites Centre for Innovation and Science, University of Bristol, Bristol, UK

P. M. Weaver
Bernal Institute, University of Limerick, Castletroy, Limerick, Ireland

M. Petrolo (ed.), *Advances in Predictive Models and Methodologies for Numerically Efficient Linear and Nonlinear Analysis of Composites*, PoliTO Springer Series,
https://doi.org/10.1007/978-3-030-11969-0_9

using buckling mode shape imperfections within stability analyses. Structures are usually analyzed with the assumption of homogeneity of material properties. This chapter focuses on the effect of spatially varying material properties with respect to thin-walled structures. There are a variety of phenomena that can affect the material properties of a composite structure. Differences in the chemical composition of materials and processes such as curing, introducing air voids [18], can affect the mechanical properties of materials. Misalignments in the fiber angle also exist within a lamina [40]. The effects of these variations are studied in the field of reliability [5]. Quantifying these variations in real structures is not trivial. Many of these variations are highly dependent on the materials used, as well as the production processes utilized [10]. There has been recent work related to finding properties to characterize the shape of these distributions [25, 33] and statistical properties of FRP composite panels [15, 32].

Getting a better understanding of the variations of material properties makes it possible to quantify the probability of mechanical response characteristics. This quantification can directly lead to more robust structures, which are reliable within an expected range of parameter variation. The information generated in these analyses also has the potential to identify the sensitivity of a structural response characteristic with respect to spatial variations. These sensitivities can be used to determine points which may be critical for inspection, or be used to selectively reinforce sensitive areas and thereby increase the overall performance of the structure.

9.1.2 Previous Work

Imperfections can have a significant effect on the post-buckling response of structures. This is particularly prominent in buckling of imperfection-sensitive structures, the cylindrical shell being a well-known example. A lot of work has been done to analyze the effect of geometric imperfections on the buckling behavior of thin-walled structures.

Stochastic analysis and optimization of structures prone to buckling have been carried out by making use of buckling modes and by alternative ways to describe spatially random geometric imperfection patterns, [3, 4, 12, 13, 17, 26, 27, 37].

The geometric imperfections of a structure are not the only factor affecting the post-buckling response. Variations in thickness, material properties, boundary conditions and loads can also have a significant effect [2, 7, 13, 22, 23]. All of these factors play a role in actual structures, due to manufacturing processes and approximations made in the design processes. The analysis of these variations is not trivial, and difficult to achieve in most commercial finite element software.

Systematic analysis of these variations is done within the Stochastic Finite Element Method (SFEM) [5, 6]. The main issue with approaching stochastic structural problems is the necessity of accurate statistical and stochastic data of structures. There is only a limited amount of experimental data available which analyzes the material variations [25, 33]. Having full statistical and correlation data of material

data, force imperfections, boundary imperfections, thickness variation and geometric variation of a structure requires extensive experimental research.

Many authors instead focus on analyzing different distributions, in an effort to find a critical, worst case distribution [22, 24, 28]. This approach can give engineers information on which distributions to avoid if possible, and can be used for design guidelines. It does not, however, lead to quantitative results which can be used to estimate the reliability of a structural performance measure.

9.1.3 Current Work

The approaches discussed thus far have focused on quantifying the structural response given certain input parameters. An alternative approach presented in this chapter is to gain a better understanding of how sensitive a structure is to spatial variations. This approach looks at the effect of a spatially varying parameter on the structural response, and finds the correlation of this parameter with a structural performance measure on the topology of the structure. The analysis shown in this chapter shows how correlations of Young's modulus variations can be used to improve the linear buckling load.

This approach can help engineers in identifying areas of a structure sensitive to spatial variations. This information can be used to make product inspection more effective. Another use for this sensitivity information is to enhance the performance of the structure. The sensitivities obtained, when properly normalized, can be seen as a performance gradient and can be used to improve the correlated structural performance measure. When these sensitivities are used to change the nominal design it is possible to enhance the structure to make it more effective with respect to the corresponding design criterion.

9.2 Applying Material Property Variations to a Structure

The approach used in the current chapter is to apply material property imperfections using random fields. Random fields are fields in n-dimensional space which distribute a parameter in space with a distribution (usually Gaussian). These points are not completely random, but are correlated with each other. There is a large variety of methods which can be used to generate random fields [31]. These methods have their own advantages and disadvantages. This section gives a brief overview of the basics of random fields and describes the method used to generate the fields in this chapter.

9.2.1 Basics

The values of a random field are usually generated as a (log)normal distribution with an associated mean (μ) value and standard deviation (σ). These points are correlated in space, thereby giving a relationship to a point's value and those in its vicinity. The mathematical definition of correlation is

$$\rho_{X,Y} = \frac{\text{cov}(X,Y)}{\sigma_X \sigma_Y} = \frac{\text{E}[(X-\mu_X)(Y-\mu_Y)]}{\sigma_X \sigma_Y} \tag{9.1}$$

which is bound between $-1 \leq \rho \leq 1$ where -1 would represent perfect inverse correlation ($y = -x$ for example) and 1 perfect correlation (x = y for instance). For the generation of fields it is useful to switch to a more convenient definition of correlation which can be used as an input of a function. The two most common definitions of correlation functions found in literature are

$$\rho_{exp} = e^{-\frac{\Delta L}{L_c}} \tag{9.2}$$

$$\rho_{sexp} = e^{-\left(\frac{\Delta L}{L_c}\right)^2}, \tag{9.3}$$

which are known as the exponential and squared exponential definitions. The exponential type has a sharper initial decrease in the correlation moving away from a point. The squared type has a comparatively smoother correlation moving away from a point. The squared however does reduce correlation faster than the exponential type after the correlation length has been reached. They have the same value for correlation at the correlation length (e^{-1}). A graph comparing the value of correlation ρ over distance for both functions a value of $L_c = 5$ and $L_c = 10$ can be found in Fig. 9.1.

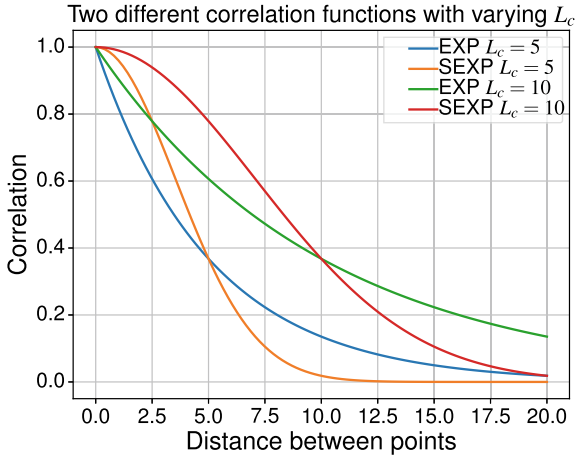

Fig. 9.1 Comparison between correlation functions

9.2.2 Generating Fields

There are numerous approaches to generate random fields, which can be continuous or discretized. Continuous methods are usually based on a series expansion, such as the Karhunen-Loève (KL) expansion [14, 30]. A limitation to these approaches is that they usually have numerical problems at boundaries [1, 16].

The approach taken in this approach uses discretized fields. There are many discrete approaches, such as Fourier Transformation approaches[1] [29] or local average subdivision [9]. The approach taken in this work is one based on covariance matrix decomposition (CMD). This done due to the simplicity to change the correlation function, flexibility in discretization, potential to easily implement geodesic length and fewer numerical difficulties than FFT-type approaches [8, Chap. 2].

9.2.2.1 Discretized Spatially Correlated Random Values

Discretized approaches use spatial grids which are usually constantly spaced. The space between nodes should be in the range of $\frac{L_c}{10}$ to $\frac{L_c}{5}$ for the exponential definition (Eq. (9.2)) and between $\frac{L_c}{4}$ to $\frac{L_c}{2}$ for other definitions [16].

A field can be defined as

$$\mathbf{z}_c = z_c(\mathbf{x}_i) = \begin{bmatrix} z_c(\mathbf{x}_1) \\ \vdots \\ z_c(\mathbf{x}_n) \end{bmatrix}. \tag{9.4}$$

in which $\mathbf{x}$ has the dimension $\Re^m$, $m = 1, 2, 3$ and n the number of points in the field. This means that a 2D field can be represented through a matrix of scalar elements. The approach used in this section generates fields with a zero mean, unit standard deviation ($\mathbf{X}$). These fields can be transformed to the desired field using

$$\mathbf{Y} = \mu + \sigma\mathbf{X} \tag{9.5}$$

where $\mathbf{Y}$ is the correctly scaled random field. The fields used in this work are generated using the covariance matrix decomposition method.

9.2.2.2 Covariance Matrix Decomposition

Covariance matrix decomposition makes it possible to generate a field using explicit correlation values of points relative to other points. This done by first assembling a correlation matrix, a symmetric positive definite matrix in which the correlation of

[1] These are classified as discrete approaches as they are evaluated at discrete points, and do not result in a continuous function.

points within field are defined

$$R_{ij} = \frac{\text{cov}(y_i, y_j)}{\sqrt{\sigma_{y_i}\sigma_{y_j}}} \rightarrow \mathbf{R} = \begin{bmatrix} 1 & \rho(y_1, y_2) & \dots & \rho(y_1, y_n) \\ \rho(y_2, y_1) & 1 & \dots & \rho(y_2, y_n) \\ \vdots & & \ddots & \vdots \\ \rho(y_n, y_1) & \rho(y_2, y_n) & \dots & \rho(y_n, y_n) \end{bmatrix}, \tag{9.6}$$

in which $\rho(y_i, y_j) = \rho(y_j, y_i)$. Note that the correlation here can be calculated using Eqs. (9.2) or (9.3).

The covariance matrix decomposition method (CMD) generates random fields using

$$z_c(\mathbf{x}_i) = \mathbf{L}\chi, \tag{9.7}$$

in which $\mathbf{L}$ is a decomposed version of the $\mathbf{R}$ matrix, and χ a vector with zero mean and unit variance. Taking the definition of covariance in Eq. (9.2), it is possible to show that $\mathbf{R}$ can be decomposed into two matrices

$$\begin{aligned} \mathbf{R} &= \text{cov}[\mathbf{x}, \mathbf{x}] = \text{E}(\mathbf{x}, \mathbf{x}^T) - 0 \cdot 0 \\ &= \text{E}(\mathbf{L}\chi\mathbf{L}\chi^T) = \mathbf{L}\text{E}(\chi\chi^T)\mathbf{L}^T = \mathbf{L}\mathbf{I}\mathbf{L}^T = \mathbf{L}\mathbf{L}^T. \end{aligned} \tag{9.8}$$

This decomposition operation can be done using different methods, the most common methods are Cholesky factorization and eigenmode factorization. Cholesky decomposition is found in many books on linear algebra and computational methods, e.g. [38, Ch. 7]. Eigenmode decomposition can be done as

$$\mathbf{R} = \mathbf{Q}\boldsymbol{\Lambda}\mathbf{Q}, \tag{9.9}$$

in which Λ is a diagonal matrix with the eigenvalues of $\mathbf{R}$ on the diagonal, and $\mathbf{Q}$ contains the eigenvectors of the matrix. The matrix $\mathbf{L}$ can be extracted from

$$\mathbf{R} = \mathbf{Q}\hat{\boldsymbol{\Lambda}}\hat{\boldsymbol{\Lambda}}\mathbf{Q} = \mathbf{L}\mathbf{L}^T \rightarrow L = Q\hat{\boldsymbol{\Lambda}}, \tag{9.10}$$

in which $\hat{\boldsymbol{\Lambda}} = \text{diag}(\sqrt{\lambda})$. As the correlation matrix grows, it can become ill-conditioned, becoming very close to being singular, causing numerical problems. In such cases, the Cholesky decomposition may fail, as eigenvalues which are (close to) 0 might show up as negative values in the algorithm. This results in imaginary eigenvalues, which are not realistic. This can be partially resolved by setting eigenvalues which are below a certain threshold to zero. A comparative study showed that that eigenmode decomposition is slightly more accurate in generating the random fields [11, Sect. 4.2]. A further advantage is that random fields can be generated by only calculating the dominating eigenvectors [31, 36]. Though it is necessary to first analyze the error relative to the field size to make sure that the field is not unduly constrained.

In general the decomposing of the matrix is the most time consuming computation within this method. Once the matrix has been decomposed, it is fairly straightforward and fast to compute new random fields. All that is required is a new random unit variance vector to be multiplied with the decomposed matrix (Eq. 9.7). It is also possible to sample these random fields in a more clever way, using spectral or Latin Hypercube Sampling (LHS) related methods [39].

9.2.3 *Random Field Discretization and Mapping of Variations to Structure*

The fields from Sect. 9.2.2.1 are generally not discretized in the same points as the random field mesh. There are a variety of methods to calculate the value at an element or integration point found within a field. A random field is ideally located in such a way to have the finite element/integration point between random field nodes (mapping techniques can be used if this is not the case). These techniques are not very easy to combine with complex structures, and in the case of integration points requires a random field mesh much finer than the structural mesh.

Other methods are less dependent on the positioning of the meshes with respect to each other. The shape function (SF) method for instance, uses a shape function in the form of

$$\hat{H}(\mathbf{x}) \sum_{i=1}^{q} N_i(\mathbf{x}) z_c(\mathbf{x}_i) \qquad x \in \Omega_e,$$

where N_i is the shape function (usually polynomial), Ω_e is the domain of an element and $\mathbf{x}_i$ are the coordinates of the i^{th} node [35]. An extension of this is the Optimal Linear Estimation (OLE) method, in which a continuous surface is made of the random field by minimizing the variance of the approximation error at each point [16].

Another approach is taken by the Spatial Average method (SE). In this method the field over an element is described by the spatial average of a field over the element

$$\hat{H}(\mathbf{x}) = \frac{\int_{\Omega_e} H(\mathbf{x}) d\Omega_e}{\int_{\Omega_e} d\Omega} = \bar{z}_c(\mathbf{x}_c). \tag{9.11}$$

This creates step-wise discontinuities along the boundaries of the elements [35]. There are a few limitations to this method, its nature makes it very hard to be used for anything other than Gaussian distributions [20]. The averaging process also reduces the variance in the spatially averaged field [6, 34, Sect. 7.6].

It should finally be noted that not all discretization methods can be combined with all random field generation methods. The CMD method is easy to combine with the OLE and SA methods. The OLE uses an eigendecomposed covariance matrix to find the optimal shape functions, which is also used in the CMD method. Similarly,

the SA method can be easy to implement in the CMD, as it can use the covariance between two local averages.

9.2.4 Post-processing Results

The results generated using the previous methods have to be post-processed in order to find interesting patterns or variations in the structure. This section discusses how these can be recovered from stochastic runs, and how these can be applied to improve a structural performance measure.

9.2.4.1 Analyzing Structural Measures

Results of structural analyses can be recovered through various structural measures, including both input parameters and response measures. These measures can for example correspond to input parameters such as material properties, and to structural response measures such as stress, strain, displacement and linear buckling load or an expression combining these. Analyzing one of these properties at a certain coordinate will result in a list of n values. These values will give a statistical mean and standard deviation, and can also be used to generate an estimation of the probability density function of the response.

It is often of interest to find relationships between these properties, for instance how material property variations affect the linear buckling load. In these cases it is possible to analyze the correlation of two parameters. In some cases it is more relevant to analyze the average of a measure throughout a structure. When analyzing the linear buckling load the structure's average Young's modulus may be of interest, as well as the local effect of these variations.

9.2.4.2 Finding Patterns of Correlation

As mentioned in the introduction, stochastic variations can also be used to identify areas which affect a structural measure. To do this, fields should be applied to vary a chosen parameter. It is then possible to calculate the correlation of every point related to a measure. The resulting pattern forms a sensitivity topology, showing the relative sensitivity of the structure to local variations.

An example would be to find the distribution of correlation of the Young's modulus to the linear buckling load. This would give a topology of a non-dimensional sensitivity of the effect of perturbations.

9.2.5 Perturbing Structure to Improve Performance

The patterns generated using the structural correlation analyses of the previous section represent a sensitivity of a structural measure to parameter redistribution. These patterns are non-physical, and can be interpreted to a sensitivity field to redistribution. Negative values in the field indicate that the measure will increase by moving e.g. material from there to an area which has a positive value.

One approach to apply these non-dimensional fields F_{pt} is by renormalizing the fields to $F_{pt,n} \in \Re | 0 \leq F_{pt,n} \leq 1$, where the mean has an expected value of 0.5. The actual mean will vary depending on the minima and maxima of the field. These fields can then be applied to a structure to vary a parameter using as

$$a_{pt} = a_{min} + (a_{max} - a_{min}) F_{pt,n}, \tag{9.12}$$

where a_{min} and a_{max} are the minimum and maximum value of the parameter.

In certain cases it may be of interest to scale the fields to localize variations, smoothen them or affect to mean value of the field. This can be achieved by raising the field to an exponent

$$a_{pt} = a_{min} + (a_{max} - a_{min}) F_{pt,n}^{m}, \tag{9.13}$$

where m is a scaling parameter. The mean value, range and scaling parameter are all linked. To find a specific mean value for a certain range a unique m value has to be computed numerically. Due to the nature of the fields it is not trivial to apply these patterns onto a structure.

9.3 Numerical Example

The approach of the previous section is demonstrated through a numerical example. This example is analyzed to find the mechanical response, the linear buckling load is then increased by using a redistributed Young's modulus.

This example is run using the covariance matrix decomposition method described in Sect. 9.2.2.2. The fields are generated on a shell mesh within a 3D mesh, and used to map to the integration points of a 3D mesh using shape functions. The 3D structural solver is based on a Serendipity Lagrange Unified Formulation developed at the University of Bristol [21]. This mapping procedure is illustrated in Fig. 9.2. The random field is used to evaluate values which are part of the structural mesh. Shape functions are used during matrix assembly to assign the correct material properties to each integration point in the structure.

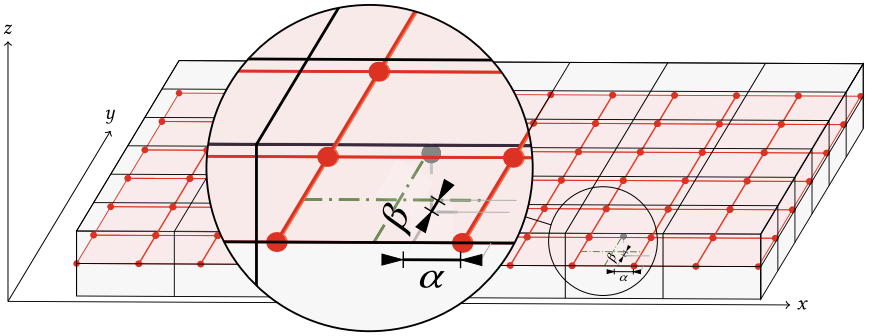

Fig. 9.2 Mapping between random field and 3D structural mesh

9.3.1 Description of the Structure

The analyses used as an example are performed on a curved panel with the geometry shown in Fig. 9.3. The structure is isotropic, and has a Young's modulus of 181 GPa and $\nu = 0.3$. The panel is restricted to load-direction displacement at the loaded edges. Rigid body modes in the load direction are removed by applying two point constraints in the center of the panel along the straight edges (at $L = 0.075$). The baseline linear buckling load, without material variations is 178 930 N, which was verified using a commercial FE solver.

9.3.2 Linear Buckling Analysis

The linear buckling analysis was run 2000 times with a correlation length $L_c = 0.01$ m and a standard deviation of the Young's modulus of $E_\sigma = 9.05$ GPa, which is equivalent to a 5% coefficient of variation. The results show a spread of the linear buckling load of $\sigma = 897.6$ N with a mean of $\mu = 178\,731$ N. This is a lower mean

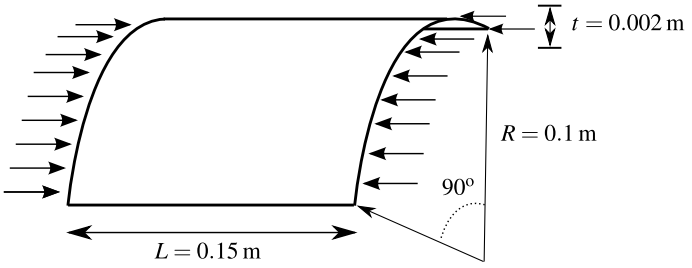

Fig. 9.3 Geometry of curved panel

than in the baseline homogeneous results, meaning that most variations result in a lower linear buckling load. A significant amount of results have a linear buckling load that is higher than the baseline result. The probability density and cumulative density functions can be found in Fig. 9.4.

The results shown make it possible to determine a probability that a certain linear buckling load is achieved. This does however require that the field characteristics, both in the form of statistical distribution and correlation function are well defined, which is not the case for most structures. Using the approach described in Sect. 9.2.4.2 a pattern of sensitivities can be found. The pattern associated with the first buckling load is shown in Fig. 9.5.

When comparing the pattern of correlation of Young's modulus to the first buckling mode, shown in Fig. 9.6, it is clear that there is some relationship between the correlation pattern and the buckling mode. The locations associated with a higher sensitivity to the buckling load correspond to the areas in which buckles are formed. Areas in which buckling mode deformations are limited are relatively unaffected by the material property variations.

9.3.3 *Enhancement of Linear Buckling Behavior*

Using the pattern of sensitivities of the previous section it is possible to redistribute material properties as described in Sect. 9.2.5. In this hypothetical scenario the objective is to increase the buckling load of a structure using functionally graded materials (FGM), without increasing the mean Young's modulus of the structure. FGM are materials that have varying material properties throughout the structure, through the thickness, in-plane, or selectively within additive manufacturing. In this example the Young's modulus will be varied between 108 and 254 GPa. This is an estimated

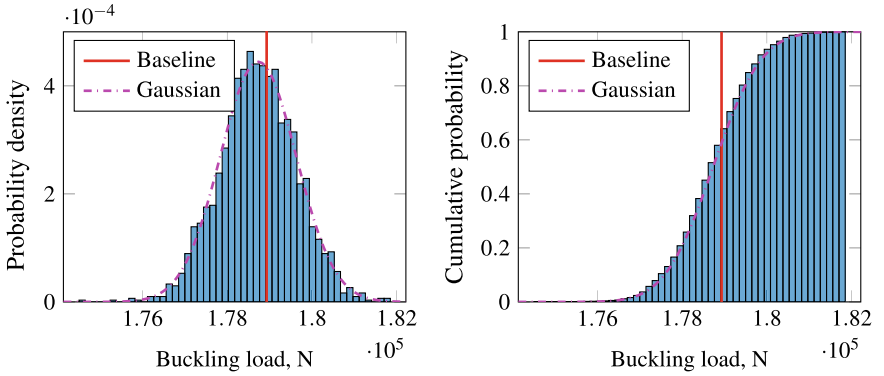

(a) Probability density function (b) Cumulative distribution function

Fig. 9.4 Probability functions of the buckling load of the curved panel under compression

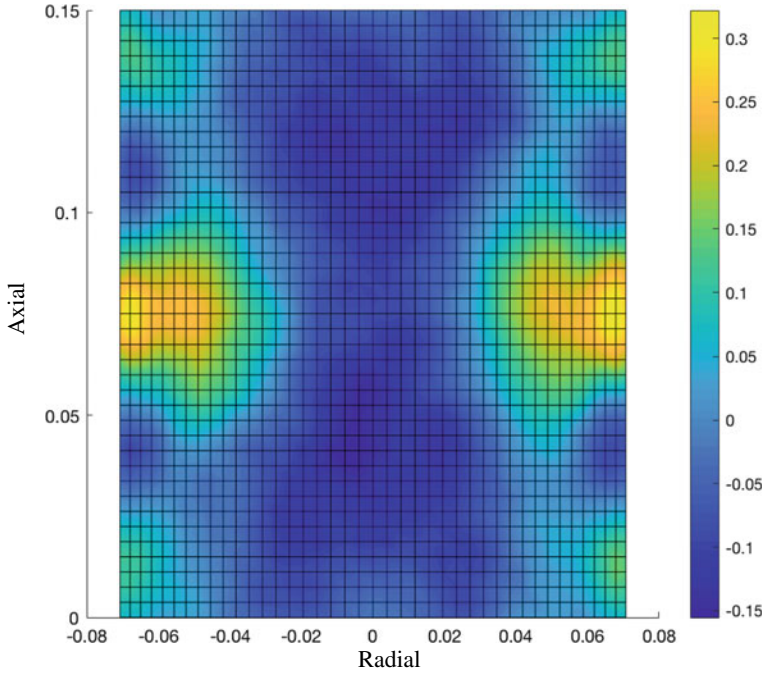

Fig. 9.5 Correlation of E with first linear buckling load

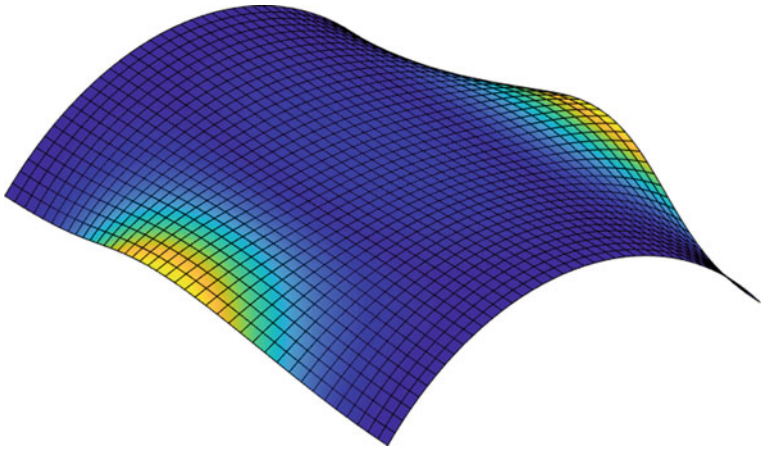

Fig. 9.6 First linear eigenmode

range of the Young's modulus from the Ti64Al4V/TiC functionally graded materials described in [19]. These are materials that can be printed, allowing for tuned levels of material stiffness throughout the structure. To retain the mean stiffness and make

it a reasonable study, an additional boundary condition is added for the mean value of the Young's modulus, forcing it to remain the same as the baseline study (181 GPa).

Using Eq. (9.13) to apply material properties an exponent of $m = 0.56$ is used in order to fully utilize the range, and maintain the original mean. The resulting Young's modulus distribution is found in Fig. 9.7. This distribution leads to an increase in linear buckling load of 10.2%.

Additional studies have been done in which, while retaining the average Young's modulus the range was varied by either increasing the minimum or decreasing the maximum Young's modulus. The results from this analysis can be found in Table 9.1. The results indicate that decreasing the maximum Young's modulus has a more significant effect than increasing the minimum. This seems plausible as this limits the stiffness locally, while varying the minimum has the effect of limiting the area in which stiffening can take place, while maintaining the mean stiffness constraint.

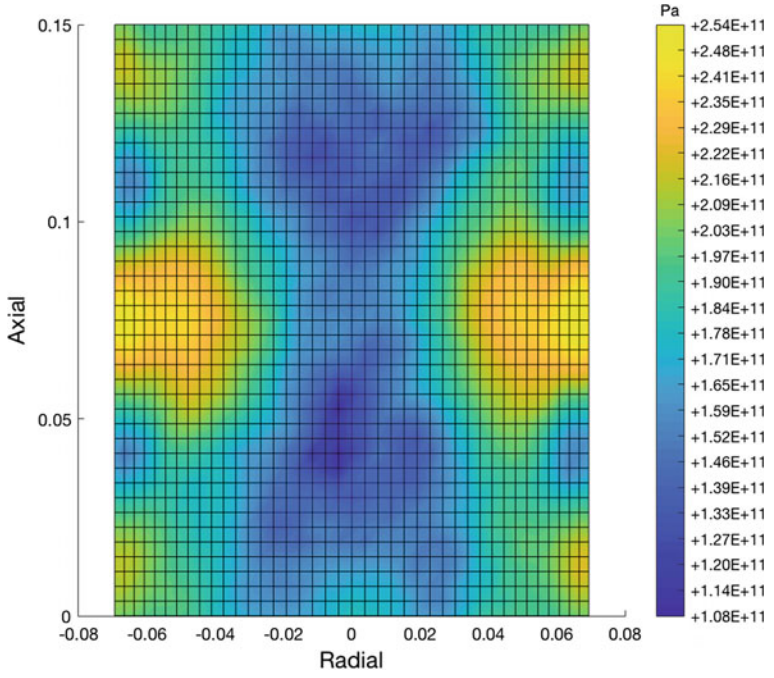

Fig. 9.7 Young's modulus distribution

Table 9.1 Improvement range by varying the range of Young's modulus within the $E_{min} = 108$ GPa and $E_{max} = 254$ GPa range

Variation of minimum Young's modulus			Variation of maximum Young's modulus		
E_{min}, GPa	m	F_{crit} increase (%)	E_{max}, GPa	m	F_{crit} increase (%)
108	0.56	10.2	190	0.08	1.8
120	0.64	9.8	200	0.17	3.5
130	0.75	9.4	210	0.25	4.9
140	0.98	8.8	220	0.33	6.3
150	1.08	8	230	0.40	7.6
160	1.43	6.9	240	0.47	8.9
170	2.19	5	250	0.56	10.2

9.4 Concluding Remarks

Using the techniques presented in this chapter it is possible to analyze the properties of structures affected by spatially varying material properties. This does however require the input of accurate statistical and correlation properties of these parameters, which are often not directly available for real structures. What can be recovered is a mapping of the structure's sensitivity to variations. These variations can be used to redistribute material properties or to change the geometry of the structure. This can lead to enhanced structural performance.

The current results in the example of the curved panel were generated using a linear pre-buckling assumption. In certain cases non-linear effects can influence the pre-buckling state and buckling load and consequently influence the pattern of correlation. In these cases correlation patterns can be generated using a bifurcation buckling analysis on the nonlinear pre-buckling state or for the limit-point buckling load. In non-linear analyses it would also be possible to use other structural performance parameters, such as the slope of the load-displacement curve, to optimize the structure to be stiffer or more compliant. This is of particular interest in the tailoring of post-buckling responses of structures.

Acknowledgements This work was carried out using the computational facilities of the Advanced Computing Research Centre, University of Bristol—http://www.bris.ac.uk/acrc/ as well as computational facilities within the Institute of Structural Analysis at Leibniz University Hannover.

References

1. Allaix DL, Carbone VI (2009) Discretization of 2D random fields: a genetic algorithm approach. Eng Struct 31(5):1111–1119
2. Arbocz J, Starnes JH (2002) Future directions and challenges in shell stability analysis. Thin-Walled Struct 40(9):729–754

3. Bielewicz E, Górski J (2002) Shells with random geometric imperfections simulation—based approach. Int J Non-Linear Mech 37(4–5):777–784
4. Chen G, Zhang H, Rasmussen KJ, Fan F (2016) Modeling geometric imperfections for reticulated shell structures using random field theory. Eng Struct 126:481–489
5. Chiachio M, Chiachio J, Rus G (2012) Reliability in composites—a selective review and survey of current development. Compos Part B: Eng 43(3):902–913
6. Der Kiureghian A, Ke JB (1988) The stochastic finite element method in structural reliability. Probabilistic Eng Mech 3(2):83–91
7. Elishakoff I (2000) Uncertain buckling: its past, present and future. Int J Solids Struct 37(46):6869–6889
8. Fenton GA (1990) Simulation and analysis of random fields. PhD thesis
9. Fenton GA, Vanmarcke EH (1990) Simulation of random fields via local average subdivision. J Eng Mech 116(8):1733–1749
10. Gutowski TG, Morigaki T, Cai Z (1987) The consolidation of laminate composites. J Compos Mater 21(February):172–188
11. Have RVD (2015) Random fields for non-linear finite element analysis of reinforced concrete (November)
12. Kriegesmann B, Jansen EL, Rolfes R (2012a) Semi-analytic probabilistic analysis of axially compressed stiffened composite panels. Compos Struct 94(2):654–663
13. Kriegesmann B, Rolfes R, Jansen EL, Elishakoff I, Hühne C, Kling A (2012b) Design optimization of composite cylindrical shells under uncertainty. Comput Mater Continua 32(3):177–200
14. Lawrence MA (1987) Basis random variables in finite element analysis. Int J Numer Meth Engng 24(December 1986):1849–1863
15. Lekou DJ, Philippidis TP (2008) Mechanical property variability in FRP laminates and its effect on failure prediction. Compos Part B: Eng 39(7–8):1247–1256
16. Li CC, Der Kiureghian A (1993) Optimal discretization of random fields. J Eng Mech 119(6):1136–1154
17. Lindgaard E, Lund E, Rasmussen KJ (2010) Nonlinear buckling optimization of composite structures considering "worst" shape imperfections. Int J Solids Struct 47(22–23):3186–3202
18. Liu L, Zhang BM, Wang DF, Wu ZJ (2006) Effects of cure cycles on void content and mechanical properties of composite laminates. Compos Struct 73(3):303–309
19. Mahamood RM, Akinlabi ET (2015) Laser metal deposition of functionally graded Ti6Al4V/TiC. Mater Des 84:402–410
20. Matthies HG, Brenner CE, Bucher CG, Guedes Soares C (1997) Uncertainties in probabilistic numerical analysis of structures and solids-Stochastic finite elements. Struct Saf 19(3):283–336
21. Minera S, Patni M, Carrera E, Petrolo M, Weaver PM, Pirrera A (2018) Three-dimensional stress analysis for beam-like structures using Serendipity Lagrange shape functions. Int J Solids Struct 141–142:279–296
22. Papadopoulos V, Papadrakakis M (2005) The effect of material and thickness variability on the buckling load of shells with random initial imperfections. Comput Methods Appl Mech Eng 194(12–16):1405–1426
23. Papadopoulos V, Stefanou G, Papadrakakis M (2009) Buckling analysis of imperfect shells with stochastic non-Gaussian material and thickness properties. Int J Solids Struct 46(14–15):2800–2808
24. Papadopoulos V, Soimiris G, Papadrakakis M (2013) Buckling analysis of I-section portal frames with stochastic imperfections. Eng Struct 47:54–66
25. Sasikumar P, Suresh R, Vijayaghosh PK, Gupta S (2015) Experimental characterisation of random field models for CFRP composite panels. Compos Struct 120:451–471
26. Schafer BW, Graham-Brady L (2006) Stochastic post-buckling of frames using Koiter's method. Int J Struct Stab Dyn 6(3):333–358
27. Schenk CA, Schuëller GI (2007) Buckling analysis of cylindrical shells with cutouts including random boundary and geometric imperfections. Comput Methods Appl Mech Eng 196(35–36):3424–3434

28. Shang S, Yun GJ (2013) Stochastic finite element with material uncertainties: implementation in a general purpose simulation program. Finite Elem Anal Des 64:65–78
29. Shinozuka M, Deodatis G (1991) Simulation of stochastic pricesses by spectral representation. Appl Mech Rev 44(4):191–204
30. Spanos PD, Ghanem RG (1989) Stochastic finite element expansion for random media. J Eng Mech 115(5):1035–1053
31. Spanos PD, Zeldin BA (1998) Monte carlo treatment of random fields: a broad perspective. Appl Mech Rev 51(3):219
32. Sriramula S, Chryssanthopoulos MK (2009) Quantification of uncertainty modelling in stochastic analysis of FRP composites. Compos Part A: Appl Sci Manuf 40(11):1673–1684
33. Sriramula S, Chryssanthopoulos MK (2013) An experimental characterisation of spatial variability in GFRP composite panels. Struct Saf 42:1–11
34. Vanmarcke EH (1983) Random fields: analysis and synthesis. World Scientific
35. Vanmarcke EH, Grigoriu M (1983) Stochastic finite element analysis of simple beams. J Eng Mech 109(5):1203–1214
36. Vořechovský M, Novák D (2005) Simulation of random fields for stochastic finite element analysis. ICOSSAR 2545–2552
37. Vryzidis I, Stefanou G, Papadopoulos V (2013) Stochastic stability analysis of steel tubes with random initial imperfections. Finite Elem Anal Des 77:31–39
38. Willoughby RA (1981) Compact numerical methods for computers: linear algebra and function minimization (J. C. Nash). SIAM Rev 23(1):124–125
39. Yamazaki F, Shinozuka M (1990) Simulation of stochastic fields by statistical preconditioning. J Eng Mech 116(2):268–287
40. Yurgartis SW (1987) Measurement of small angle fiber misalignments in continuous fiber composites. Compos Sci Technol 30(4):279–293

Chapter 10
Multiscale Identification of Material Properties for Anisotropic Media: A General Inverse Approach

L. Cappelli, M. Montemurro, F. Dau and L. Guillaumat

Abstract This work deals with the problem of characterizing the material properties of a composite plate, made of unidirectional fiber-reinforced laminae, at each pertinent scale (microscopic and mesoscopic ones). The characterization is achieved through a single non-destructive harmonic test performed at the macroscopic scale of the specimen. A general multi-scale identification strategy (MSIS) is proposed to accomplish this goal. The multi-scale identification problem is split into two interdependent sub-problems which are stated, at both levels, as constrained minimization problems. At the first level the lamina properties are retrieved by minimizing the distance between the numerical and the reference harmonic responses of the multilayer plate. Conversely, the second-level problem aims at characterizing fiber and matrix elastic properties by exploiting the results of the first step. The whole procedure is based on a special global hybrid optimization algorithm and on the strain energy homogenization method of periodic media as well. The effectiveness of the approach is illustrated through a meaningful numerical benchmark.

10.1 Introduction

Nowadays, composite materials are widely used in several fields, from automotive applications to aerospace ones, and engineers are continuously looking for strategies that allow increasing performances, designing complex geometry and providing stiffness and strength where needed.

In order to properly conceive optimized solutions, the characterization of the composite material properties at each pertinent scale is a mandatory task. One of the

L. Cappelli · M. Montemurro (✉) · F. Dau
Arts et Métiers ParisTech, Institut de Mécanique et d'Ingénierie (I2M)
de Bordeaux CNRS UMR 5295, Talence, France
e-mail: marco.montemurro@ensam.eu; marco.montemurro@u-bordeaux.fr

L. Guillaumat
Laboratoire angevin de mécanique, procédés et innovation (LAMPA),
Arts et Métiers ParisTech, Angers, France

M. Petrolo (ed.), *Advances in Predictive Models and Methodologies for Numerically Efficient Linear and Nonlinear Analysis of Composites*, PoliTO Springer Series,
https://doi.org/10.1007/978-3-030-11969-0_10

main issues of composite materials is related to the difficulty of characterizing the full set of elastic properties at the lower scales, i.e. microscopic (that of the constitutive phases) and mesoscopic (the lamina level) ones.

From an industrial point of view, it is interesting to investigate about the cost reduction of experimental characterization tests, which are usually destructive procedures that must be carried out on a significant number of samples in order to get reliable results [1]. Moreover, as far as concerns the characterization of the elastic properties of the constitutive phases, a large data dispersion is obtained during micro-scale experimental tests, due to the difficulty to properly set the experiment and to handle the microscopic constituents [10].

Concerning the experimental (destructive) tests, they can be divided into meso and micro-scale characterization tests. The most important meso-scale tests are the ASTM tests (e.g. tension test for flat specimens, three/four points bending test etc.).

Nevertheless, ASTM standard tests conducted at the lamina level are not able to provide the full set of 3D elastic properties: only the in-plane material properties together with an approximated value of the out-of-plane shear moduli can be retrieved through these tests.

Conversely, only few standard tests can be carried out at the microscopic scale: single fiber test to obtain the Young's modulus along the fiber longitudinal direction (ASTM D3379) and the matrix tensile test (ASTM D638). In order to characterize the rest of the constitutive phases properties only non-standard tests are available in literature: pull-out [19], micro-indentation [10], fragmentation tests [7], etc. It is noteworthy that unconventional destructive tests present some major shortcomings: the experimental set-up is quite complex and the obtained results show a significant dispersion, see [24].

In order to go beyond the main restrictions imposed by destructive tests, the research activity here presented focuses on the development of a multi-scale identification strategy (MSIS), based on a non-destructive test, able to characterize the elastic properties of the composite at each relevant scale.

The main idea behind this approach is quite simple: the proposed MSIS aims at identifying the whole set of elastic properties at both lamina-level and constitutive phases-level starting from the analysis of the *macroscopic* dynamic response of a multilayer plate. In particular, the macroscopic dynamic behavior can be easily obtained by means of non-destructive modal tests: the information restrained in the harmonic spectrum response of the specimen can be then exploited to carry out the multi-scale characterization process.

It is noteworthy that the utilization of identification strategies exploiting the information restrained in a macroscopic modal analysis is not new. Such an approach has already been applied in literature [8, 25] for characterizing the elastic properties of the constitutive lamina. An assessment of these approaches is available in [20]. Usually these techniques, make use of an optimization algorithm in order to minimize the difference between the measured dynamic response (typically a given set of natural frequencies) and the numerical one calculated via a finite element model of the structure [18].

However, to the best of the authors' knowledge, this approach has never been generalized to characterize the material and geometrical features of the microstructure of composite materials. Indeed, in the context of the MSIS, the material characterization problem is split into two distinct (but related) sub-problems. The first level of the procedure focuses on the transition from macroscopic scale to mesoscopic one and aims at minimizing the distance between the *reference* harmonic response of the structure and its numerical counterpart: the goal is to search for the elastic properties of the constitutive ply minimizing this distance. The second step focuses on the transition from mesoscopic scale to microscopic one: the goal is the determination of both geometrical and elastic properties of the constitutive phases meeting the lamina elastic properties resulting from the first-level inverse problem.

The MSIS is characterized by several original features. On the one hand, it relies on a special hybrid optimization tool to perform the solution search, i.e. an in-house code made by the union of a special genetic algorithm (GA) (able to deal with problems characterized by a *variable number of design variables* [11]) and of a classical gradient-based one. On the other hand the link between the two identification problems is ensured by a general numerical homogenization scheme: the one utilizing volume-averaged stresses determined on a suitable representative volume element (RVE) of the material in the framework of the strain energy method of periodic media [2].

The Chapter is structured as follows: the problem and the MSIS are introduced in Sect. 10.1. The mathematical formulation of the first-level inverse problem and the related numerical aspects are discussed in Sect. 10.2.3, while the micro-scale characterization problem as well as the numerical homogenization scheme (and the related FE model) are presented in Sect. 10.2.4. The numerical results of the MSIS are illustrated and discussed in Sect. 10.3. Finally, Sect. 10.4 ends the Chapter with some conclusions and perspectives.

10.2 Multi-scale Identification of Composite Elastic Properties

10.2.1 Problem Description

The multi-scale inverse approach presented in this study is applied to a reference multilayer composite plate made of unidirectional laminae whose geometry is illustrated in Fig. 10.1.

The constitutive ply is made of carbon-epoxy fiber Hexcel $T650/F584$ pre-impregnated tapes, with a fiber volume fraction $V_f = 0.555$: the material properties of the constitutive phases composing the ply (taken from [21]) are listed in Table 10.1. As it can be noticed, the fiber has a transverse isotropic behavior, while the matrix is isotropic.

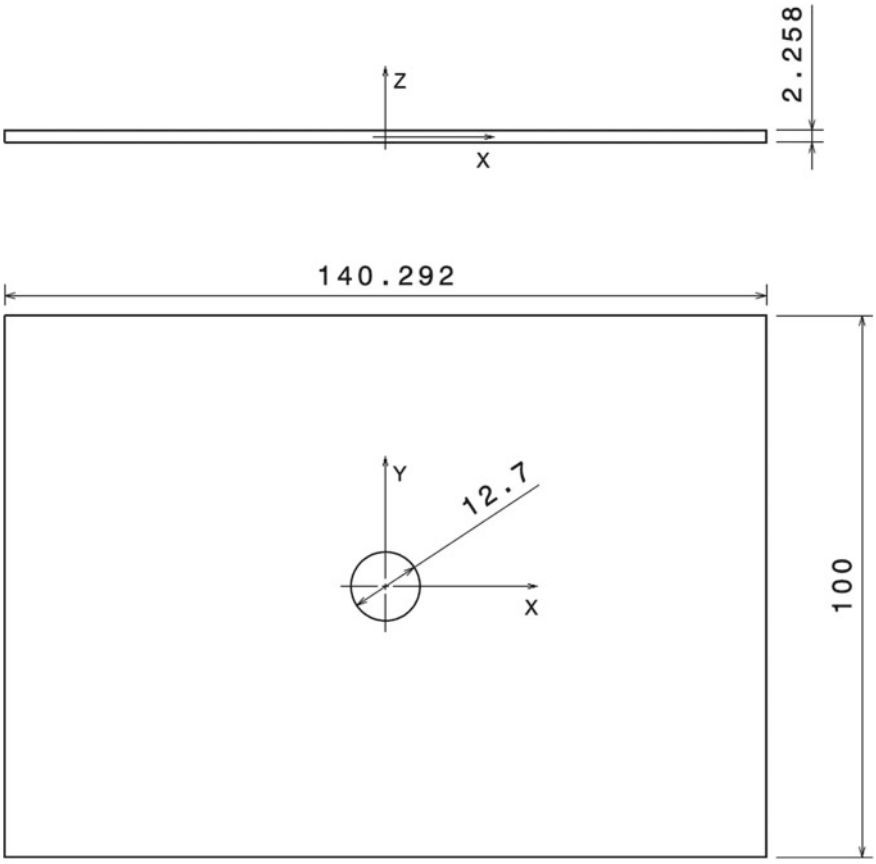

Fig. 10.1 Geometry of the multilayer composite plate (sizes in (mm))

Table 10.1 Micro-scale reference material properties for the fiber $T650/35-3K$ and the matrix $F584$ (taken from [21])

Fibre properties					Matrix properties	
E_1^f (MPa)	E_2^f (MPa)	ν_{12}^f	ν_{23}^f	G_{12}^f (MPa)	E_m (MPa)	ν_m
276000.0	17300.0	0.250	0.428	11240.0	4140.0	0.350

The reference laminate is constituted of eight identical plies (i.e. same material and thickness) arranged according to the following stack $[0°/-45°/45°/90°]_S$. The thickness of the lamina is $t_{ply} = 0.28225$ mm. The orientation angle of the generic ply is positive according to counter-clockwise rotation around the z-axis: x-axis indicates the 0° orientation.

The analysis presented in this work constitutes a numerical validation of the MSIS: the *reference response* of the structure (at each scale) is determined by means of a multi-scale numerical analysis on the reference configuration of the laminate described above.

In particular, as described in Sect. 10.3, the reference material properties of the constitutive phases are used in order to calculate, on the one hand, the *reference effective elastic properties* of the lamina at the mesoscopic scale and, on the other hand, the *reference harmonic response* and the *reference natural frequencies* of the multilayer plate.

Concerning the microscopic scale the following hypotheses apply: (a) the material of both constitutive phases has a linear elastic behavior, (b) perfect bonding condition at the fiber-matrix interface is considered, (c) the damping capability of both phases is disregarded.

As far as mesoscopic and macroscopic scales are concerned, the following assumptions are made: (a) the constitutive lamina has an elastic orthotropic behavior, (b) perfect bonding condition at the interface between two consecutive plies is considered, (c) the damping behavior of the ply is neglected, (d) the laminate kinematic is described in the framework of the first-order shear deformation theory (FSDT).

10.2.2 Description of the MSIS

The main goal of the MSIS is to find the material properties of the considered structure at each relevant scale by exploiting the information restrained in the macroscopic dynamical response of the composite. This reference response can be provided either by a non-destructive harmonic test or by a numerical harmonic analysis conducted on a reference structure. This latter is the case considered in the present study: the reference configuration of the multilayer plate as well as the reference dynamical results are presented in Sect. 10.3.

In this background, the problem of characterizing the elastic properties of the composite at different scales can be split into two distinct (but related) *inverse problems*.

- **First-level inverse problem**. This phase involves the transition from macroscopic scale (laminate-level) to mesoscopic one (ply-level): the goal is to characterize the ply elastic properties (the design variables of this phase) minimizing the distance between the numerical harmonic response of the multilayer plate and the reference one.
- **Second-level inverse problem**. This step focuses on the transition from mesoscopic scale to microscopic one (that of the constitutive phases): the goal is to find the optimum value of elastic properties of both fiber and matrix (the optimization variables of this phase) meeting the set of the lamina elastic properties provided by the first-level problem. In this second phase, the link between the two scales is ensured by means of a homogenization analysis performed on the numerical model of the RVE of the material in order to compute the effective elastic properties of the ply.

10.2.3 Mathematical Formulation of the First-Level Inverse Problem

10.2.3.1 Optimization Variables, Objective Function and Constraints

The aim of the first-level inverse problem is the characterization of the elastic properties of the constitutive lamina. In this background, the identification problem is formalized as a classical inverse problem. The goal is to find the set of elastic properties of the ply (3D case) minimizing the distance between the reference dynamic response of the structure and that provided by the numerical model of the structure.

All the ply material parameters can be collected into the vector of design variables $\mathbf{x}^{\mathrm{I}}$ as follows:

$$\mathbf{x}^{\mathrm{I}} = \left\{ E_1, E_2, G_{12}, G_{23}, \nu_{12}, \nu_{23} \right\}. \tag{10.1}$$

Six parameters have to be identified, according to the general hypotheses recalled in Sect. 10.2 and by considering the five planes of orthogonal symmetry of the RVE illustrated in Fig. 10.3. In particular, the following equalities hold $E_2 = E_3$, $G_{12} = G_{13}$ and $\nu_{12} = \nu_{13}$.

It is noteworthy that the ply elastic properties cannot get arbitrary values, rather they have to satisfy a set of existence constraints in order to ensure the positive definiteness of the lamina stiffness tensor:

$$\begin{aligned}
g_1^{\mathrm{I}}(\mathbf{x}^{\mathrm{I}}) &= |\nu_{12}| - \sqrt{\frac{E_1}{E_2}} < 0, \\
g_2^{\mathrm{I}}(\mathbf{x}^{\mathrm{I}}) &= |\nu_{23}| - \sqrt{\frac{E_2}{E_3}} < 0, \\
g_3^{\mathrm{I}}(\mathbf{x}^{\mathrm{I}}) &= 2 \cdot \nu_{12} \cdot \nu_{13} \cdot \nu_{23} \cdot \frac{E_3}{E_1} + \nu_{12}^2 \cdot \frac{E_2}{E_1} + \nu_{23}^2 \cdot \frac{E_3}{E_2} + \nu_{13}^2 \cdot \frac{E_3}{E_1} - 1 < 0.
\end{aligned} \tag{10.2}$$

Moreover, the lamina elastic constants vary within the design space defined in Table 10.2, i.e. by introducing suitable lower and upper bounds for each design variable. The lower and upper bounds are chosen equal to 80 and 120% of the reference material properties of the lamina, respectively (which are given in Table 10.4). The only exception is ν_{23} whose lower and upper bounds are set equal to 85 and 115% of the reference counterpart.

Table 10.2 First-level inverse problem: design variables lower and upper bounds

Ply elastic properties	E_1 (MPa)	E_2 (MPa)	ν_{12}	ν_{23}	G_{12}	G_{23}
Lower bound	124022.7	6558.3	0.232	0.433	3069.7	2626.2
Upper bound	186034.1	9837.4	0.348	0.586	4604.5	3939.3

Concerning the expression of the first-level objective function, an error estimator of the least-square type has been chosen:

$$\Phi^{\mathrm{I}}(\mathbf{x}^{\mathrm{I}}) = \frac{1}{N_p \cdot N_s} \sum_{q=1}^{N_p} \sum_{r=1}^{N_s} \left(\frac{f_r - f_r^{\mathrm{ref}}}{f_r^{\mathrm{ref}}} \right)^2 + \left(\frac{H_{r,q}(\mathbf{x}^{\mathrm{I}}) - H_{r,q}^{\mathrm{ref}}}{H_{r,q}^{\mathrm{ref}}} \right)^2. \tag{10.3}$$

In the previous equation, f_r is the r-th sampled frequency, while $H_{r,q}$ is the fast Fourier transform (FFT) of the frequency response function (FRF) determined at the q-th sample point of the multilayer plate and evaluated at the r-th sampled frequency. Of course, f_r^{ref}, $H_{r,q}^{\mathrm{ref}}$ are the same quantities evaluated on the reference configuration of the laminate.

N_s and N_p are the number of sampled frequencies and of sample points over the laminate (where the FRF is computed/measured), respectively.

In order to get a numerical harmonic spectrum really close to the reference one (and also to match the reference natural frequencies) a set of constraints on the laminate eigenfrequencies is considered:

$$g_{3+j}^{\mathrm{I}}\left(\mathbf{x}^{\mathrm{I}}\right) = \left| \frac{f_{jn} - f_{jn}{}^{\mathrm{ref}}}{f_{jn}{}^{\mathrm{ref}}} \right| - \varepsilon_j \leq 0, \quad j = 1, ..., n_f. \tag{10.4}$$

In Eq. (10.4) n_f is the overall number of natural frequencies involved in the analysis (i.e. in the frequency range used for the determination of the FRF), whilst f_{jn} and $f_{jn}{}^{\mathrm{ref}}$ are the j-th numerical and reference eigenfrequency, respectively. ε_j is a user-defined tolerance on the relative error for each natural frequency: in this study a maximum relative error equal to 0.005 has been considered.

Finally, the first-level inverse problem can be stated as a classical constrained non-linear programming problem (CNLPP):

$$\begin{gathered} \min_{\mathbf{x}^{\mathrm{I}}} \ \Phi^{\mathrm{I}}\left(\mathbf{x}^{\mathrm{I}}\right), \\ \text{subject to :} \\ g_j^{\mathrm{I}}\left(\mathbf{x}^{\mathrm{I}}\right) \leq 0, \quad j = 1, ..., n_f + 3. \end{gathered} \tag{10.5}$$

10.2.3.2 Macroscopic Finite Element Model

A picture of the FE model of the multilayer plate at the macroscopic scale together with the applied loads and boundary conditions (BCs) is illustrated in Fig. 10.2. Such a FE model (developed within ANSYS®environment) is built by using ANSYS®SHELL281 layered shell elements with eight nodes and six degrees of freedom (DOFs) per node. The kinematic model is that of the FSDT.

During the optimization process of the first step of the MSIS, two FE analyses are invoked for each point in the design space: firstly, a modal analysis to extract the first n_f natural frequencies and, secondly, a linear harmonic analysis in order to

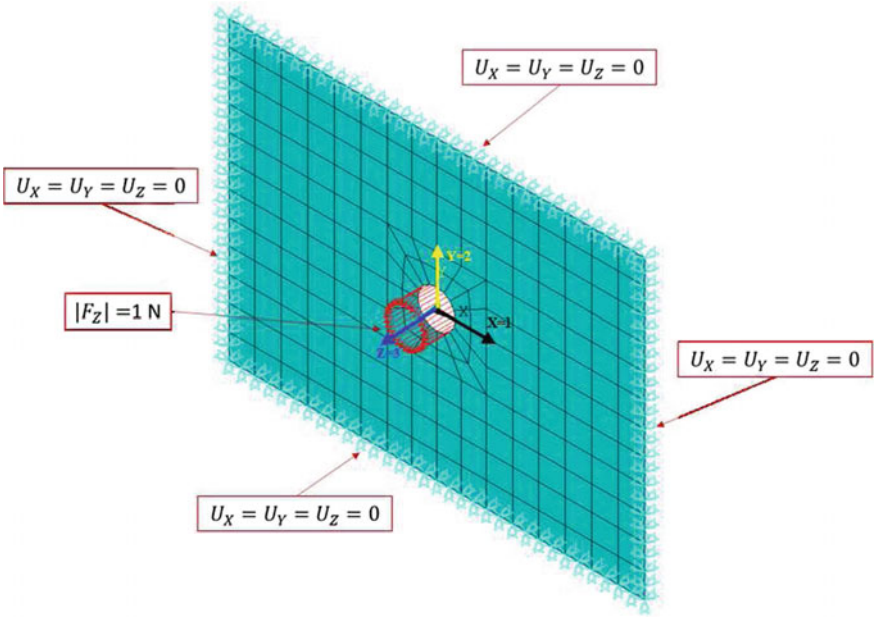

Fig. 10.2 FE model of the multilayer plate and the related BCs

determine the harmonic response of the laminate. This latter is obtained by measuring the displacement u_z in each one of the q sample nodes of the mesh, at every sampled frequency f_r.

Subsequently, the FRF for each sample point is obtained by evaluating the ratio between the FFT of the displacement $u_{zq}(f_r)$ and that of the applied force $F_z(f_r)$, namely $H_{r,q} = u_{zq}(f_r)/F_z(f_r)$.

Before starting the optimization process, a sensitivity analysis has been performed, to investigate the influence of the number of sample points N_p on the overall FRF of the multilayer plate. It has been observed that an overall number of $N_p = 62$ sample points is sufficient to properly evaluate the global FRF of the structure, also in terms of computational effort.

Finally, as far as the linear harmonic analysis is concerned, the FFT of the structure in each sample point has been evaluated in the frequency range $[500, 6000]$ Hz wherein $N_s = 82$ sampled spectrum frequencies have been considered, according to the strategy detailed in Sect. 10.3.

10.2.3.3 The Numerical Strategy

Problem (10.5) is highly non linear and non-convex in terms of both objective and constraint functions, see Eqs. (10.2)–(10.4).

For inverse problems, the uniqueness of the solution is not *a priori* guaranteed: the set of parameters matching a given *observed state* may not be unique. Nevertheless,

no proved theoretical rules exist in literature [22, 23] to define the number of data points N_p for a given number of unknowns (n) to be identified. Generally, the inverse problem is stated as a CNLPP and it can be viewed as an *over-determined system of equations* [22, 23]. Since more observation points than parameters exist ($N_p \gg n$) there are more equations than unknowns. If an optimal point exists it may be not unique, thus implying the existence of many combinations of parameters that result to be equivalent solutions for the CNLPP at hand.

Considering all these aspects and according to the practice always employed in literature, in this work a number of observed states (i.e. sample points N_p) greater than two times the number of design variables n has been considered. As previously stated, the number of sample points has been inferred by means of a numerical sensitivity analysis of the FRF of the plate with respect to parameter N_p: as a results $N_p = 62$ has been chosen to properly perform the optimization calculations.

Taking into account the previous aspects, a hybrid optimization tool composed of the GA ERASMUS (EvolutionaRy Algorithm for optimiSation of ModUlar Systems) [5, 6, 12], interfaced with the MATLAB *fmincon* algorithm, has been used. The GA ERASMUS has already been successfully applied to solve different kinds of real-world engineering problems, e.g [6, 13–15].

The optimization procedure for problem (10.5) is split in two phases. During the first phase, solely the GA ERASMUS is used to perform the solution search. Due to the strong non-linearity of problem (10.5), the aim of the genetic calculation is to provide a potential sub-optimal point in the design space, which constitutes the initial guess for the subsequent phase, i.e. the local optimization, where the MATLAB *fmincon* tool is employed to finalize the solution search. The optimization algorithm is the *active-set* which is a Quasi-Newton method making use of an approximation of the Hessian matrix to estimate the descent direction.

For the resolution of the first-level inverse problem, both optimization algorithms have been interfaced with the FE model of the multilayer plate. For each individual at each generation, the optimization tool performs two FE analyses: a modal analysis to extract the n_f natural frequencies followed by a linear harmonic analysis for the evaluation of the FRF of the laminate. Then, the GA elaborates the results provided by the two FE analyses in order to execute the genetic operations on the basis of the current values of both objective and constraint functions. These operations are repeated until the GA meets the user-defined convergence criterion.

The number of design variables and that of constraint functions is six and $n_f + 3$, respectively. The generic individual of the GA ERASMUS represents a potential solution for the problem at hand. The genotype of the individual for problem (10.5) is characterized by only one chromosome composed of six genes, each one coding a component of the vector of design variables, see Eq. (10.1).

10.2.4 Mathematical Formulation of the Second-Level Inverse Problem

10.2.4.1 Optimization Variables, Objective Function and Constraints

As stated previously, the purpose of the second-level inverse problem is the characterization of the elastic properties of fiber and matrix, by minimizing the distance between the effective elastic properties of the constitutive lamina (determined numerically) and the optimum values provided by the first-level inverse problem, which represent the *reference response* for this phase.

Of course, the effective elastic properties of the lamina must be evaluated by means of a suitable homogenization procedure. To this purpose a FE model of the RVE of the composite is built in order to carry out the numerical homogenization calculations which allow determining the equivalent ply properties as a function of those of the constitutive phases. Both geometrical and material parameters of the constitutive phases affect the equivalent material properties at meso-scale. Nevertheless, the fiber volume fraction is set *a priori*, because it is always provided by the supplier in the specification sheet.

Considering the general hypotheses described in Sect. 10.2.1, the fiber has a linear elastic transverse isotropic behavior, while the matrix has a linear elastic isotropic behavior: only seven material parameters need to be identified. Therefore, these quantities are collected into the vector $\mathbf{x}^{\mathrm{II}}$ as follows:

$$\mathbf{x}^{\mathrm{II}} = \left\{ E_1^f, E_2^f, G_{12}^f, \nu_{12}^f, \nu_{23}^f, E_m, \nu_m \right\}. \tag{10.6}$$

Similarly to the first-level inverse problem, the constitutive elastic properties cannot assume arbitrary values, but they have to fulfill a set of existence constraints to guarantee the positive definiteness of the fiber and matrix stiffness tensors:

$$\begin{aligned}
g_1^{\mathrm{II}}(\mathbf{x}^{\mathrm{II}}) &= |\nu_{12}^f| - \sqrt{\frac{E_1^f}{E_2^f}} < 0, \\
g_2^{II}(\mathbf{x}^{II}) &= |\nu_{23}^f| - 1 < 0, \\
g_3^{\mathrm{II}}(\mathbf{x}^{\mathrm{II}}) &= \frac{E_1^f}{E_2^f} \cdot \left(2 \cdot \nu_{23}^f \cdot {\nu_{12}^f}^2 + 2 \cdot {\nu_{12}^f}^2 \right) - 1 < 0, \\
g_4^{\mathrm{II}}(\mathbf{x}^{\mathrm{II}}) &= -E_m < 0, \\
g_5^{\mathrm{II}}(\mathbf{x}^{\mathrm{II}}) &= \nu_m - \frac{1}{2} < 0, \\
g_6^{\mathrm{II}}(\mathbf{x}^{\mathrm{II}}) &= -\nu_m - 1 < 0.
\end{aligned} \tag{10.7}$$

Table 10.3 Second-level inverse problem: design variables lower and upper bounds

Micro-scale elastic properties	E_1^f (MPa)	E_2^f (MPa)	ν_{12}^f	ν_{23}^f	G_{12}^f	E_m (MPa)	ν_m^f
Lower bound	220800.0	13840.0	0.200	0.343	8992.0	3312.0	0.280
Upper bound	331200.0	20760.0	0.300	0.514	13488.0	4968.0	0.420

Furthermore, the components of the design variables vector vary in a design space defined in Table 10.3, in which appropriate lower and upper bounds for each design variable are assigned. The lower and upper bounds are chosen equal to the 80 and 120% of the reference material properties of the constitutive phases (listed in Table 10.1).

Moreover, regarding the objective function expression, an error estimator of the least-square type has been chosen:

$$\Phi^{\mathrm{II}}(\mathbf{x}^{\mathrm{II}}) = \frac{1}{6}\left[\left(\frac{E_1 - E_1^{\mathrm{I}}}{E_1^{\mathrm{I}}}\right)^2 + \left(\frac{E_2 - E_2^{\mathrm{I}}}{E_2^{\mathrm{I}}}\right)^2 + \left(\frac{G_{12} - G_{12}^{\mathrm{I}}}{G_{12}^{\mathrm{I}}}\right)^2 + \cdots \right. \tag{10.8}$$

$$\left. + \left(\frac{G_{23} - G_{23}^{\mathrm{I}}}{G_{23}^{\mathrm{I}}}\right)^2 + \left(\frac{\nu_{12} - \nu_{12}^{\mathrm{I}}}{\nu_{12}^{\mathrm{I}}}\right)^2 + \left(\frac{\nu_{23} - \nu_{23}^{\mathrm{I}}}{\nu_{23}^{\mathrm{I}}}\right)^2\right]. \tag{10.9}$$

In the previous equation, superscript "I" indicates the optimum value of the ply elastic properties provided by the first-level inverse problem. Also in this case the second-level inverse problem can be formalized as a classical CNLPP:

$$\begin{gathered} \min_{\mathbf{x}^{\mathrm{II}}} \ \Phi^{\mathrm{II}}\left(\mathbf{x}^{\mathrm{II}}\right), \\ \text{subject to :} \\ g_j^{\mathrm{II}}\left(\mathbf{x}^{\mathrm{II}}\right) \leq 0, \quad j = 1, ..., 6. \end{gathered} \tag{10.10}$$

10.2.4.2 Microscopic Finite Element Model

The link between microscopic and mesoscopic scales is represented by a homogenization phase, performed on the RVE of Fig. 10.3. The lamina effective elastic properties are computed, by means of the well-known strain energy homogenization technique of periodic media described in [2]. This homogenization scheme has proven to be an efficient numerical homogenisation procedure able to determine the equivalent material properties of different heterogeneous materials characterized by complex RVE topologies. The strain energy homogenization technique of periodic media based on volume averaged stresses has already been used in other works, see [4, 13, 16].

The main hypothesis of this technique is that the repetitive unit of the periodic structure and the corresponding volume of the homogeneous solid undergo the same deformation having, hence, the same strain energy. At the mesoscopic scale (i.e. at the ply level) the heterogeneous medium is then replaced by an equivalent homogeneous

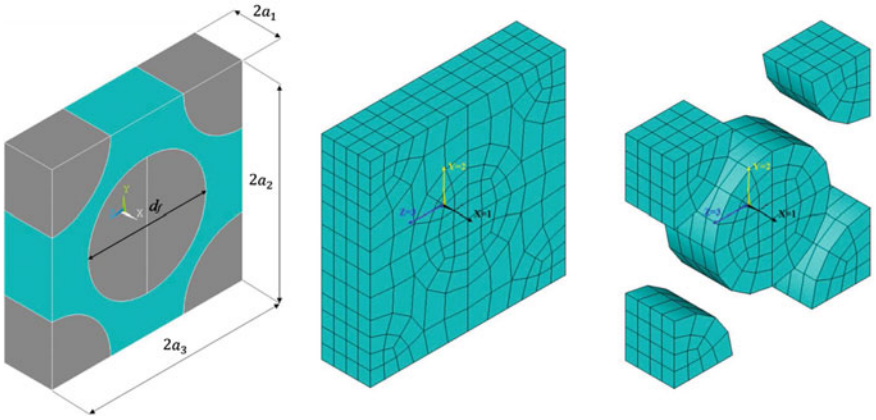

Fig. 10.3 The reference RVE with its FE model

anisotropic virtual material characterized by the elastic properties determined during the homogenization phase and which will depend upon the geometrical and material parameters of the RVE. In this study, the real random micro-structure of the lamina (which is usually characterized by misalignments of the fibers, porosity, damaged zones, etc.) is not taken into account and the topology of the RVE is described by a perfect hexagonal array, see Fig. 10.3.

The FE model of the RVE has been realized within the commercial FE code ANSYS®. A 20-nodes solid element (SOLID186) with three DOFs per node has been used. The model together with its structured mesh is illustrated in Fig. 10.3.

In order to evaluate the components of the stiffness matrix [C] of the lamina, the RVE is submitted to an average strain field ε_{ij}^0 (tensor notation). The six components of the average strain are applied by considering the classical periodic boundary conditions (PBCs) on the RVE. For more details on the application of the PBCs in the framework of the second-level inverse problem, the reader is addressed to [2, 3]. The engineering moduli of the constitutive lamina at the mesoscopic scale can be calculated starting from the components of the compliance matrix $[S] = [C]^{-1}$.

10.2.4.3 The Numerical Strategy

Problem (10.10) is a non-convex CNLPP in terms of both constraint and objective functions, see Eqs. (10.7) and (10.8). The number of variables is equal to *seven*. The existence of the optimum solution may not be unique because the number of *observed states* is lower than that of design variables to be identified. Therefore, the transition from mesoscopic to microscopic scale is governed by non-bijective relationships which can give rise to a significant amount of equivalent optimum solutions for the problem at hand. In order to find a solution for the second-level inverse problem, the two-step optimization is adapted to the transition from mesoscopic scale to microscopic one.

For the resolution of the second-level inverse problem, the optimization algorithm has been interfaced with the FE model of the RVE at micro-scale, to perform the numerical homogenization, in which six static analyses are performed: these analyses allow determining the components of the ply stiffness tensor, for each individual at each generation. Then, the optimization tool elaborates the results provided by the FE analyses in order to execute the optimization operations on the basis of the current values of both objective and constraint functions (both for the GA and the deterministic algorithm). These operations are repeated until the user-defined convergence criterion is satisfied. Concerning the GA, the genotype of the individual for problem (10.10) is characterized by only *one* chromosome composed of *seven* genes, each one coding a component of the vector of design variables of Eq. (10.6).

10.3 Numerical Results: Characterization of Elastic Properties by MSIS

10.3.1 Determination of the Harmonic Response for the Reference Configuration

Before launching the optimization process, the reference harmonic response must be determined. The geometry as well as the material properties of the reference configuration have been introduced in Sect. 10.2.1. The reference harmonic response is calculated by performing two successive analyses (modal analysis followed by a linear harmonic one) on the macroscopic FE model of the multilayer plate discussed in Sect. 10.2.3. Of course, at the macroscopic scale both the reference FRF of the laminate and the set of reference natural frequencies have been calculated by using the geometrical properties of the reference structure and by considering the ply elastic properties listed in Table 10.4. These material parameters are obtained by means of a preliminary homogenization analysis through the FE model of the RVE of the composite (see Sect. 10.2.4) in which the reference values of Table 10.1 for the elastic properties of both fiber and matrix are used.

The frequency samples used for the determination of the structure FRF vary between $f_{LB} = 500$ Hz and $f_{UB} = 6000$ Hz: $n_f = 8$ natural frequencies falls in this interval which are extracted to evaluate the optimization constraints of Eq. (10.4). Their reference values are listed in Table 10.5. The FRF of the multilayer plate is sampled ten times between two consecutive natural frequencies; only the first and the last interval are sampled six times. It must be noticed that the sampling intervals

Table 10.4 Reference values of the lamina material properties

Ply properties						
E_1 (MPa)	E_2 (MPa)	ν_{12}	ν_{23}	G_{12} (MPa)	G_{23} (MPa)	ρ (kg/m^3)
155028.4	8197.9	0.290	0.510	3837.1	3282.8	1770.0

Table 10.5 Reference natural frequencies

Nat. freq.	f_{1n}^{ref}	f_{2n}^{ref}	f_{3n}^{ref}	f_{4n}^{ref}	f_{5n}^{ref}	f_{6n}^{ref}	f_{7n}^{ref}	f_{8n}^{ref}
Value $[Hz]$	760.98	1847.19	1997.35	2966.36	3770.59	3856.76	4605.93	5061.77

Table 10.6 Optimization parameters for first and second-level inverse problem

(a) Genetic algorithm parameters (for both first-level and second-level inverse problems)

Parameters	First-level	Second-level
N. of individuals	120	140
N. of populations	2	2
N. of iterations	130	130
Crossover probability	0.85	0.85
Mutation probability	0.06	0.07
Isolation time	10	10

(b) Gradient-based algorithm parameters (for both first-level and second-level inverse problems)

Parameters	Value	
Solver algorithm	Active-set	
Max function evaluation	10,000	
Tolerance on the objective function	10^{-15}	
Tolerance on the gradient norm	10^{-15}	

used for the definition of the FRF and, hence, of the objective function of the first-level inverse problem of Eq. (10.3), have been properly parametrized in terms of the current value of the structure natural frequencies f_{jn}, $j = 1, ..., n_f$. Moreover, since damping is neglected, a small range of frequencies in the neighborhood of each natural frequency f_{jn} has been excluded from the sampling sequence (by considering a "small" interval of length $\delta = 1$ Hz centered at each natural frequency). The exciting nodal force has a value $F_z = 1\ N$.

Finally, as discussed in Sect. 10.2.3, the FRF is calculated at each one of the 62 reference points defined over the laminate.

10.3.2 Results of the First-Level Inverse Problem (Meso-Scale)

In this section, the results of the first-level inverse problem are shown and discussed. After carrying out a statistic analysis in order to evaluate the effect of the optimization parameters on the optimum solutions, according to [16], the main parameters tuning the behavior of both the GA and the active-set algorithm (used to carry out global and local optimization, respectively) are set as listed in Table 10.6.

Table 10.7 Optimum solution of the first-level inverse problem provided by the GA and the gradient-based algorithm; the percentage difference between the solution and the ply reference data are given in parentheses

Meso-scale elastic properties	Reference data	GA results	Gradient-based results
E_1 (MPa)	155028.4	153846.0 (−0.762)	155027.5 (-6.45×10^{-04})
E_2 (MPa)	8197.9	8103.3 (−1.15)	8197.7 (-1.95×10^{-03})
ν_{12}	0.290	0.284 (−1.94)	0.290 (3.45×10^{-03})
ν_{23}	0.510	0.480 (−5.76)	0.480 (−5.78)
G_{12} (MPa)	3837.1	3906.9 (1.82)	3837.1 (0)
G_{23} (MPa)	3282.8	3291.1 (0.254)	3282.5 (-7.62×10^{-03})

Table 10.8 First eight natural frequencies for the optimum solution of the first-level inverse problem; for each value, the percentage difference with respect to the reference counterpart is indicated in parentheses

Nat. freq.	f_{in}^{ref} (Hz)	f_{in} (Hz)
f_{1n}	760.98	760.97 (3.51×10^{-04})
f_{2n}	1847.19	1847.18 (3.82×10^{-04})
f_{3n}	1997.35	1997.34 (3.83×10^{-04})
f_{4n}	2966.36	2966.34 (3.99×10^{-04})
f_{5n}	3770.59	3770.57 (4.20×10^{-04})
f_{6n}	3856.76	3856.74 (4.23×10^{-04})
f_{7n}	4605.93	4605.91 (4.27×10^{-04})
f_{8n}	5061.77	5061.74 (4.58×10^{-04})

For this first case, the GA perform the exchange of information among populations through a ring-type operator every 10 generations, with a probability which is automatically evaluated by the GA itself. Moreover, concerning the constraint-handling technique for the first-level inverse problem, the Automatic Dynamic Penalisation (ADP) method has been considered, see [17].

The choice of using multiple populations of small size, i.e. with a small number of individuals, is motivated by the fact that here the goal is to find the global minimum (for the objective function of the problem at hand) without increasing too much the computational effort. Indeed, the exchange of information between best individuals belonging to different populations (through the use of the ring-type operator), and hence the possibility of crossing them, allows the GA for exploring the feasible design domain and for handling the genetic information in the best way. More details about the use of multiple populations can be found in [11].

The optimum solutions found at the end of both the genetic calculation and the local gradient-based optimization are summarized in Table 10.7, whilst the value of the eigenfrequencies for the optimum solution at the end of the optimization process are listed in Table 10.8. As it can be easily inferred from the analysis of these results, the ply elastic properties of the optimum solution are in good agreement with the

reference data: the absolute percentage difference ranges from 0% for G_{12} to 5.78% for ν_{23}. This is a quite expected result because, due to the kinematic model at the basis of the first-order shear deformation theory, the effect of ν_{23} on both the displacement field and the natural frequencies is negligible. The plate is not thick enough to observe a significant influence of ν_{23} on its dynamic response.

Nevertheless, both the eigenfrequencies and the FRF, in all sample points, are very well estimated. The numerical results found at the end of the optimization perfectly match the reference data with an absolute percentage difference ranging from 3.51×10^{-4}% (for the 1-st mode) to 4.58×10^{-4}% (for the 8-th mode).

10.3.3 Results of the Second-Level Inverse Problem (Micro-scale)

The second-level inverse problem is solved by considering a fibre volume fraction $V_F = 0.555$ [21] and a fibre diameter equal to $d_f = 6.8$ μm.

The parameters tuning the behavior of both the GA and the active-set algorithm for the second-level inverse problem are listed in Table 10.6. As in the case of the first-level inverse problem, the Automatic Dynamic Penalisation (ADP) method has been considered for handling constraints [17].

The optimum solutions of the second-level problem found at the end of both the genetic calculation and the local gradient-based optimization are summarized in Tables 10.9 and 10.10.

As it can be easily inferred from the analysis of these results, the elastic properties of the constitutive phases for the optimum solution are in agreement with the reference data. In particular, Young's and shear moduli for both fiber and matrix are estimated with a very good accuracy: the absolute percentage difference ranges from 0.254% for E_1^f to 5.56% for E_2^f.

Table 10.9 Optimum solution of the second-level inverse problem provided by both the GA and the active-set algorithm; the percentage difference between the solution and the reference material properties are given in parentheses

Micro-scale elastic properties	Reference data	GA results	Gradient-based results
E_1^f (MPa)	276000.0	276701.0 (0.254)	276701.0 (0.254)
E_2^f (MPa)	17300.0	18277.5 (5.65)	18262.1 (5.56)
ν_{12}^f	0.250	0.274 (9.76)	0.275 (9.83)
ν_{23}^f	0.428	0.487 (13.6)	0.486 (13.4)
G_{12}^f (MPa)	11240.0	10807.1 (−3.85)	10780.7 (−4.09)
E_m (MPa)	4140.0	4108.4 (−0.763)	4108.4 (−0.763)
ν_m	0.350	0.315 (−9.99)	0.315 (−9.99)

Table 10.10 Ply material properties at the end of the first-level inverse problem (used as target values) and those related to the optimum solution resulting from the second-level inverse problem; the percentage differences are indicated in parentheses

Ply elastic properties	First-level problem results	Optimum results
E_1 (MPa)	155027.5	155392.0 (0.235)
E_2 (MPa)	8197.7	8170.8 (−0.328)
ν_{12}	0.290	0.290 (0.0)
ν_{23}	0.480	0.480 (0.0)
G_{12} (MPa)	3837.1	3837.2 (2.87×10^{-3})
G_{23} (MPa)	3282.5	3289.0 (0.196)

Conversely, the estimation of the Poisson's ratio (for both phases) is characterized by a higher discrepancy: the maximum absolute percentage difference is 13.4% on ν_{23}^f. However, this is a quite expected result because, as stated above, the Poisson's ratio ν_{23} of the lamina has a negligible influence on the laminate dynamic response. Indeed, the related sensitivity of both objective and constraint functions of the first-level problem to the variable ν_{23} is not significant at all. Therefore, the relatively small absolute percentage error on ν_{23} at the end of the first-level inverse problem (5.78%) is amplified when looking for the optimum solution of the second-level inverse problem in terms of Poisson's ratios of both fiber and matrix (the associated optimization problem is non-linear).

Finally, the quality of the optimum solution of the second-level inverse problem is very good: the objective function value is 2.0519×10^{-5} at the end of the local gradient-based optimization.

10.4 Conclusions and Perspectives

In this work a multi-scale identification strategy able to characterize the elastic properties of composite materials, at each characteristic scale, is presented. The MSIS is characterized by several original features that make it a very general methodology for characterizing the elastic properties of anisotropic media.

In the context of the MSIS, the problem of characterizing the elastic properties of the composite at different scales is split into two distinct (but related) *inverse problems*. The first-level inverse problem involves the transition from macroscopic scale (laminate-level) to mesoscopic one (ply-level): the goal is to characterize the ply elastic properties minimizing the distance between the numerical harmonic response of the multilayer plate and the reference one. Conversely, the second-level inverse problem focuses on the transition from mesoscopic scale to microscopic one (that of the constitutive phases): the goal is to find the optimum value of elastic properties of both fiber and matrix matching the set of the lamina elastic properties provided by the first-level problem.

The overall identification process relies on a single non-destructive harmonic test performed at the macroscopic scale. The MSIS makes use of the strain energy homogenization technique of periodic media to carry out the scale transition as well as of a hybrid optimization tool to perform the solution search for both first-level and second-level inverse problems. The effectiveness of the MSIS is evaluated through a numerical benchmark: a multilayer plate made of unidirectional carbon/epoxy pre-preg plies $T650/F584$, whose elastic properties are taken from literature, is considered as a reference structure and its numerical harmonic response has been taken as a reference one.

At the mesoscopic scale the results of the identification process are very good: the maximum absolute percentage error is observed on the ply transverse Poisson's ratio ν_{23} and is about 5.78%. At the microscopic scale all elastic properties are identified with a good level of accuracy, except the fiber and matrix Poisson's ratios: those of the fiber, i.e. ν_{12}^f and ν_{23}^f, are affected by a absolute percentage error of about 10% and 14%, respectively, whilst that of the matrix, ν^m, is characterized by a percentage error of about 10%. The relatively small error on the transverse Poisson's ratio of the lamina is due to the very low sensitivity of the objective function to this material property. Moreover, this error propagates at the lower scale and affects the Poisson's ratios of both fiber and matrix.

Nevertheless, thanks to the MSIS, it is possible to retrieve both longitudinal and transversal elastic properties of the constitutive phases of the RVE and this task cannot be easily performed by means of standard ASTM tests. Moreover, such a result has been obtained by using a unique macroscopic non-destructive harmonic test. Of course, the proposed methodology must be generalized and improved in order to catch the true behavior of the material of the constitutive phases at the microscopic scale. To this purpose, research is ongoing in order to include into the MSIS the viscoelastic behavior of matrix, the variability effects and the geometrical features of the RVE of the composite material (e.g. parameters of the inclusions shapes).

References

1. Adams FD, Carlsson AL, Pipes RB (2003) Experimental characterization of advanced composite materials, 3rd edn. CRC Press LLC, New York
2. Barbero E (2007) Finite element analysis of composite materials. CRC Press, Taylor and Francis Group, New York
3. Cappelli L, Montemurro M, Dau F, Guillaumat L (2018) Characterisation of composite elastic properties by means of a multi-scale two-level inverse approach. Compos Struct 204:767–777
4. Catapano A, Montemurro M (2014) A multi-scale approach for the optimum design of sandwich plates with honeycomb core. Part II: the optimisation strategy. Compos Struct 118:677–690
5. Costa G (2018) Design and optimisation methods for structures produced by means of additive manufacturing. PhD thesis, Arts et Metiers ParisTech, France
6. Costa G, Montemurro M, Pailhès J (2018) A general hybrid optimization strategy for curve fitting in the non-uniform rational basis spline framework. J Optim Theory Appl 176(1):225–251

7. Feih S, Wonsyld K, Minzari D, Westermann P, Lilholt H (2004) Testing procedure for the single fiber fragmentation test. Denmark. Forskningscenter Risoe. Risoe-R No 1483(EN)
8. Furtado SCR, Araujo A, Silva A (2018) Inverse characterization of vegetable fibre-reinforced composites exposed to environmental degradation. Compos. Struct. 189:529–544
9. Jones RM (1975) Mechanics of composite materials. McGraw-Hill, Tokyo
10. Maurin R, Davies P, Baral N, Baley C (2018) Transverse properties of carbon fibres by nano-indentation and micro-mechanics. Appl Compos Mater 15:61
11. Montemurro M (2012) Optimal design of advanced engineering modular systems through a new genetic approach. PhD thesis, UPMC, Paris VI, France. http://tel.archives-ouvertes.fr/tel-00955533
12. Montemurro M (2018) A contribution to the development of design strategies for the optimisation of lightweight structures. HDR thesis, Université de Bordeaux, France
13. Montemurro M, Catapano A, Doroszewski D (2016) A multi-scale approach for the simultaneous shape and material optimisation of sandwich panels with cellular core. Compos Part B: Eng 91:458–472
14. Montemurro M, Catapano A (2017) On the effective integration of manufacturability constraints within the multi-scale methodology for designing variable angle-tow laminates. Compos Struct 161:145–159
15. Montemurro M, Catapano A (2019) A general B-Spline surfaces theoretical framework for optimisation of variable angle-tow laminates. Compos Struct 209:561–578
16. Montemurro M, Nasser H, Koutsawa Y, Belouettar S, Vincenti A, Vannucci P (2012) Identification of electromechanical properties of piezoelectric structures through evolutionary optimisation techniques. Int J Solids Struct 49(13):1884–1892
17. Montemurro M, Vincenti A, Vannucci P (2013) The automatic dynamic penalisation method (ADP) for handling constraints with genetic algorithms. Comput Methods Appl Mech Eng 256:70–87
18. Mota Soares CM, Moreira de Freitas M, Arújo AL, Pedersen P (1993) Identification of material properties of composite plate specimens. Compos Struct 25(1–4):277–285
19. Nairn JA (2000) Analytical fracture mechanics analysis of the pull-out test including the effects of friction and thermal stresses. Adv Compos Lett 9(6):373–383
20. Pedersen P, Frederiksen PS (1992) Identification of orthotropic material modul by a combined experimental/numerical method. Measurement 10(3):113–118
21. Soutis C, Beaumont PWR (eds) (2005) Multi-scale modelling of composite material systems. The art of predictive damage modelling. Woodhead publishing series in composites science and engineering. Elsevier, New York
22. Sun A (1999) Inverse problems in groundwater modelling. Kluwer Academic Publishers, Boston
23. Tarantola NZ (1988) Inverse problem theory: methods for data fitting and model parameter estimation. Elsevier, New York
24. Young TJ (2012) Characterisation of interfaces in micro- and nano-composites. PhD thesis, University of Surrey
25. Zhou XY, Gosling PD, Ullah Z, Kaczmarczyk L, Pearce C (2016) Exploiting the benefits of multi-scale analysis in reliability analysis for composite structures. Compos Struct 155:197–212

Chapter 11
Metamodel-Based Uncertainty Quantification for the Mechanical Behavior of Braided Composites

G. Balokas, B. Kriegesmann, S. Czichon, A. Böttcher and R. Rolfes

Abstract This chapter presents an uncertainty quantification framework for triaxially braided composites simulation, dealing with the stochastic stiffness prediction via numerical multiscale analysis. Efficiency is achieved by using various metamodeling techniques, such as neural networks, polynomial chaos expansion and Kriging modeling. Uncertainties accounting for material and geometric randomness are propagating through the scales to the final scatter of the mechanical properties of the macroscale. Information about the stochastic input and the dominating uncertain parameters is offered via application of a variance-based global sensitivity analysis. All methods employed in this work are non-intrusive, hence the framework can be used for all sorts of composite materials and numerical models. The need for realistic uncertainty quantification is highlighted.

11.1 Introduction

The considerable influence of inherent uncertainties on the behavior of a physical system has led the scientific community to recognize the importance of a stochastic approach to engineering problems. The rational treatment of those uncertainties, achieved by means of probability theory and statistics, cannot be addressed rigorously when following the traditional deterministic approach. Especially for composite structures, the use of deterministic approaches for design and analysis may

G. Balokas (✉) · A. Böttcher
Structure Development Department, ELAN-AUSY GmbH, Hamburg, Germany
e-mail: georgios.balokas@tuhh.de

B. Kriegesmann
Structural Optimization for Lightweight Design, Hamburg University of Technology (TUHH), Hamburg, Germany

S. Czichon
Fraunhofer Institute for Wind Energy Systems, IWES, Bremerhaven, Germany

R. Rolfes
Institute of Structural Analysis, Leibniz Universität Hannover, Hannover, Germany

M. Petrolo (ed.), *Advances in Predictive Models and Methodologies for Numerically Efficient Linear and Nonlinear Analysis of Composites*, PoliTO Springer Series,
https://doi.org/10.1007/978-3-030-11969-0_11

undermine their utilization and optimization potential and result in higher safety factors. Therefore, even though relative research work is rather limited for composite materials and especially textiles, a probabilistic framework allowing for uncertainty propagation and uncertainty quantification (UQ) is essential [12].

One of the first probabilistic approaches [4] introduced a Weibull model for the fiber strength in composite materials, which is still used in progressive damage studies. Simulation of the random fiber distribution in unidirectional composites [7] has always attracted stochastic methods as opposed to typical fibre-packing arrangements for micromechanics. The direction drawn by Chamis [3] was crucial as the uncertainties of the constituents from lower scales were taken into account, leading to variability assessment of the composite behavior and to reliability of composite structures. A classic review paper on uncertainty quantification [11] sets the basis for the stochastic perspective of composites by distinguishing epistemic and aleatoric uncertainty, classifying multiscale approaches and reporting studies in reliability assessment of macro-structures.

More recently, composite material studies of probabilistic nature evolved and covered topics like random inclusions in lower scales [13], geometric and material randomness in the microscale [5] and effects on the probability of failure for macroscale problems [8] and simulation of the random waviness of the fiber reinforcement from experimental data [15, 16]. However, a major topic is the statistical information of the random input. Whether the uncertainty concerns material or geometry information, in most cases groundless assumptions are made about the variance, type of distribution or even the number of uncertain parameters to be taken into account. Therefore, the way forward for the probabilistic analysis of composites should be the endeavor for quantification of uncertainties regarding material input, geometry or even manufacturing parameters.

As a first step towards the quantification of uncertainties for braided composite materials, the current study presents a methodology for identifying the most significant parameters in terms of variability regarding the elastic behavior. A probabilistic framework for a 3D triaxially braided model is described based on a multiscale scheme, able to predict the stiffness tensor of the macroscale starting form the properties of each constituent. A variance-based global sensitivity analysis (VBGSA) technique is described and applied, which makes use of the normalized Sobol indices to determine the contribution of each input parameter to the output scatter. The obstacles set by the numerical burden of the high-fidelity finite element model and the repetitive procedure of Monte Carlo analysis coupled with the VBGSA, are bypassed by applying metamodels/surrogate models. Three different models are presented (artificial neural networks, Kriging and polynomial chaos expansion) and compared in terms of accuracy and efficiency. Furthermore, several comments are made throughout the chapter emphasizing on the importance of realistic UQ and the advantages non-intrusive metamodeling techniques can offer to engineering sciences.

11.2 Formulation and Methodology

11.2.1 Homogenization-Based Multiscale Model

For composites and generally for heterogeneous materials, the mechanical properties of the individual components along with other lower-scale parameters defining their spatial and size distribution (e.g. volume fractions etc.), govern in fact the overall mechanical behavior. Hence, attributes of the micro and the mesoscale are extremely important for a better understanding of the elemental properties of those materials. Due to their nature, textile composites exhibit a greater level of inhomogeneity than conventional engineering materials and composite laminates. So for an accurate prediction of the mechanical behavior, multiscale schemes accounting for both the fiber and the yarn level are necessary.

In this work, a hybrid two-step homogenization method is applied in order to predict the elastic properties of a single 3D triaxially braided layer. The first step consists of homogenizing the properties of the yarns at the level of individual fibers ($\approx 10^{-6}$m). On that account, the Chamis micromechanical model is employed, assuming of course that each yarn locally behaves as a unidirectional continuous fiber reinforced composite. The elastic properties can be obtained from the properties of each phase as follows:

$$E_{11} = YV_f E_{f_{11}} + \left(1 - YV_f\right) E_m \tag{11.1}$$

$$E_{22} = E_{33} = \frac{E_m}{1-\sqrt{YV_f}\left(1-\frac{E_m}{E_{f_{22}}}\right)} \tag{11.2}$$

$$G_{13} = G_{12} = \frac{G_m}{1-\sqrt{YV_f}\left(1-\frac{G_m}{G_{f_{12}}}\right)} \tag{11.3}$$

$$G_{23} = \frac{G_m}{1-YV_f\left(1-\frac{G_m}{G_{f_{23}}}\right)} \tag{11.4}$$

$$\nu_{12} = \nu_{13} = \nu_m + YV_f\left(\nu_{f_{12}} - \nu_m\right) \tag{11.5}$$

$$\nu_{23} = \frac{E_{22}}{2G_{23}} - 1 \tag{11.6}$$

where $E_{f_{11}}$, $E_{f_{22}}$, $G_{f_{12}}$, $G_{f_{23}}$, $\nu_{f_{12}}$ and $\nu_{f_{23}}$ are the transversely isotropic material properties of the fibers, E_m, G_m and ν_m are the isotropic material properties of the polymer matrix and YV_f is the yarn volume fraction (percentage of the volume of fibers inside the volume of the yarn). The accuracy of this analytical model against the classical FE homogenization of a representative volume element (RVE) is shown in Fig.11.1 for the cases of E_{11} and $E_{22,33}$ and for various levels of the yarn volume fraction.

For the second step, a numerical homogenization is performed with a mesoscale RVE generated by TexGen [6]. This software allows easy modeling of the yarns as solid volumes representing the approximate bounds of the fibers contained within

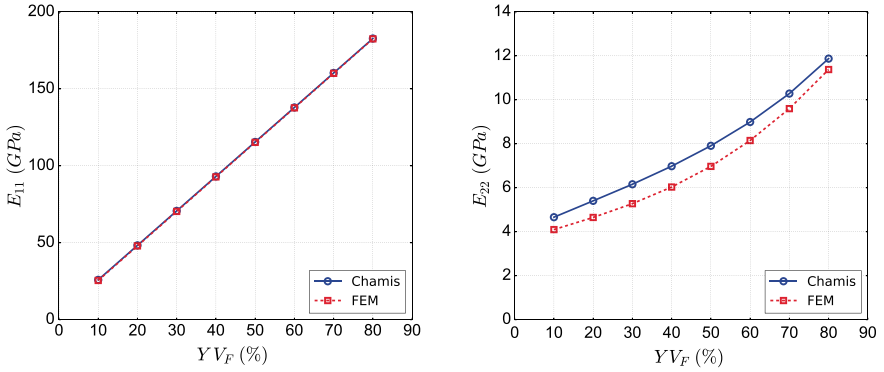

(a) Longitudinal modulus (b) Transverse modulus

Fig. 11.1 Comparison of Chamis criterion against numerical homogenization via FEM

them. The properties calculated at the first step are provided to the yarns and a voxel mesh is created with ABAQUS for the numerical solution of the six load cases corresponding to the orthotropic stiffness tensor of the macroscale. Appropriate periodic boundary conditions are applied to the RVE so that Hill's energy averaging theorem is valid at all times:

$$\boldsymbol{\sigma}^* \cdot \boldsymbol{\varepsilon}^* = \frac{1}{|V|} \int_V \boldsymbol{\sigma} \cdot \boldsymbol{\varepsilon} \, dV \tag{11.7}$$

The above equation describes that the strain energy of the homogenized continuum with stress and strain tensors $\boldsymbol{\sigma}^*$ and $\boldsymbol{\varepsilon}^*$ respectively, has to be equal to that of the RVE, with $\boldsymbol{\sigma}$ and $\boldsymbol{\varepsilon}$ being the corresponding quantities of the lower scale.

The model subjected to the aforementioned scheme is a typical 3D triaxially braided layer consisting of axial and weft yarns interlaced according to the pattern shown in Fig. 11.2a. The RVE is presented in Fig. 11.2b. The fibers forming the yarns are AS4 carbon while an EPON 9504 matrix is used. The material properties of each

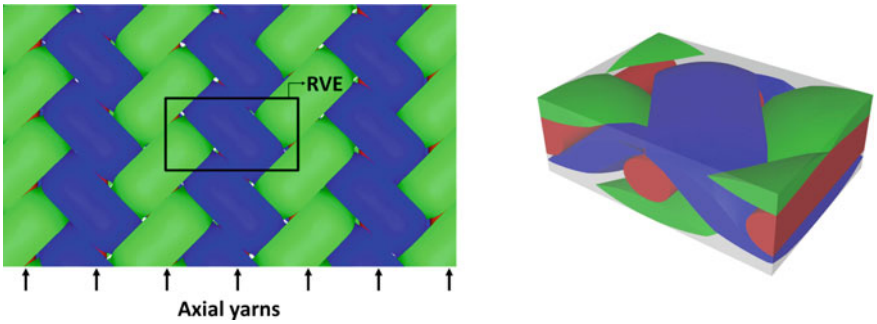

(a) Braiding pattern and RVE (b) RVE mesoscale model

Fig. 11.2 Triaxial braiding pattern: **a** Top view, **b** TexGen RVE mesoscale model

Table 11.1 Material properties of braided model

Property	Symbol	Value
Longitudinal fiber modulus	E_{f_1}	227.53 GPa
Transverse fiber modulus	E_{f_2}	16.55 GPa
In-plane shear fiber modulus	$G_{f_{12}}$	24.82 GPa
Out-of-plane shear fiber modulus	$G_{f_{23}}$	6.89 GPa
In-plane fiber Poisson's ratio	$\nu_{f_{12}}$	0.2
Out-of-plane fiber Poisson's ratio	$\nu_{f_{23}}$	0.25
Matrix Young's modulus	E_m	3.5 GPa
Matrix Poisson's ratio	ν_m	0.38
Yarn volume fraction	YV_f	80%
Braid angle	BA	45°
Undulation angle	UA	57°

phase are reported in Table 11.1. With those properties as an input and by using the described multiscale methodology, the macroscale stiffness properties extracted are the following: $E_{11} = 30.09$ GPa, $E_{22} = 10.72$ GPa, $E_{33} = 6.92$ GPa, $G_{12} = 6.46$ GPa, $G_{13} = 2.87$ GPa, $G_{23} = 3.28$ GPa, $\nu_{12} = 0.54$, $\nu_{13} = 0.07$ and $\nu_{23} = 0.54$. For further information on the multiscale scheme and the model, the reader is referred to [1].

All codes developed herein are parametric and account for uncertainties for the following input parameters: E_{f_1}, E_{f_2}, $G_{f_{12}}$, for material uncertainty and YV_f, BA and UA for geometric uncertainty. All uncertain input parameters are considered to follow a Gaussian distribution with 10% coefficient of variation (COV). The final scatter of the output will be discretized and linked to each input parameter via the VBGSA, which is described in the next section.

11.2.2 Variance-Based Global Sensitivity Analysis

This technique offers a classification of importance among the input parameters in terms of variance. The output variance of the probabilistic model is fully decomposed into terms corresponding to the input parameters and their interactions. Consider a model $y = f(x_1, x_2, \ldots x_k)$ with y a scalar. Given that f is a square integrable function over the k-dimensional unit hypercube Ω^k, the model may be decomposed as [10]:

$$f = f_0 + \sum_i f_i + \sum_{j>i} f_{ij} + \cdots + f_{12\ldots k} \tag{11.8}$$

where $f_i = f_i(x_i)$, $f_{ij} = f_{ij}(x_i, x_j)$ etc. Since all the terms are orthogonal, they can be calculated using the conditional expectations of y as:

$$f_0 = E(y) \tag{11.9}$$
$$f_i = E(y|x_i) - E(y) \tag{11.10}$$
$$f_{ij} = E(y|x_i, x_j) - f_i - f_j - E(y) \tag{11.11}$$

If each term in Eq. 11.8 is squared and integrated (due to the orthogonality of the function, integrals of mixed terms vanish):

$$\int f^2 d\mathbf{x} - f_0^2 = \sum_i \int f_i^2 dx_i + \sum_{j>i} \int f_{ij}^2 dx_i dx_j + \cdots + \int f_{12\ldots k}^2 dx_1 dx_2 \ldots dx_k \tag{11.12}$$

where the left part is the total variance of y and the terms on the right are decomposed variances with respect to the input x_i. With the aid of Eqs. 11.9–11.11 the final expression for the variance decomposition is reached:

$$Var(y) = \sum_{i=1}^{k} V_i + \sum_{j>i}^{k} V_{ij} + \cdots + V_{12\ldots k} \tag{11.13}$$
$$where \quad V_i = Var_{x_i}(E_{x_{\sim i}}(y|x_i)) \tag{11.14}$$
$$V_{ij} = Var_{x_{ij}}(E_{x_{\sim ij}}(y|x_i, x_j)) - V_i - V_j \quad etc. \tag{11.15}$$

The $x_{\sim i}$ notation indicates the set of all variables except x_i. By dividing the term of interest by the unconditional variance $Var(y)$ the first-order sensitivity index or first order Sobol index is obtained as a fractional contribution:

$$S_i = \frac{V_i}{Var(y)} \tag{11.16}$$

In practice, most models cannot be solved analytically, thus estimators have to be applied within a sapling procedure. The following estimator is used herein for the first order index:

$$V_i = Var_{x_i}(E_{x_{\sim i}}(y|x_i)) \approx \frac{1}{N} \sum_{j=1}^{N} f(B)_j (f(A_B^i)_j - f(A)_j) \tag{11.17}$$

In the above equation, A and B are two (N, k) matrices with random samples from the input space, where k is the input dimension and N is the number of evaluations. Matrix A_B^i is identical with A, except that its ith column is substituted with the ith column of B $(i = 1, ..., k)$. Estimators of this sort require excessive realizations in order to converge, so surrogate modeling is inevitable for high-fidelity FE models.

11.2.3 Surrogate Modeling Techniques

Metamodels or surrogate models are mathematical models able to perform rapid mapping between given input and output quantities, when trained appropriately via several samples. Once trained, they can produce extreme amounts of approximative results with trivial computational effort. In this study, the surrogate models are used to map the uncertain parameters reported in Sect. 11.2.1 with the stiffness properties of the braided material in the macroscale. In the following subsections, the formulation behind neural networks, Kriging and polynomial chaos will be presented. In this context, the random input vector will be denoted as $\mathbf{x} = \{x_i,\ i = 1, ..., M\}$ where M is the total amount of input random variables, which are assumed to be independent. Let the model to be bypassed denoted by Ω. By propagating the uncertainty in $\mathbf{x}$ multiple times (random realizations), the random variable of the output Y is obtained:

$$Y = \Omega(\mathbf{x}) \tag{11.18}$$

All techniques reported are non-intrusive, meaning that they can be applied to every model regardless the knowledge about its inner structure. To that end, the training of the surrogate is based on repeatedly evaluating the model Ω over a set of input realizations $\mathbf{X} = \{\mathbf{x}^{(i)} \in \mathbb{R}^M,\ i = 1, ..., N\}$. This set is essentially the training dataset and is called experimental design (ED).

11.2.3.1 Artificial Neural Networks

Artificial neural networks (ANN) are being used as a Machine Learning method for many applications. Their massively parallel structure makes them a very fast information-processing system, so they can eliminate the limitations set by high dimensional or high-fidelity models.

An ANN consists of at least three layers: the input, the output and one (or more) hidden layer. The nodes inside every layer are called neurons while the links between them are called synapses. The most common type of ANN in engineering is the multilayer feed-forward network. Such a configuration with a single hidden layer is presented in Fig. 11.3a. The input neurons (squares) do not process information and only connect the network to the external environment. The neurons of the hidden layer (circles) process information coming from a previous layer and feed their output to the next layer. Information is propagated only in a single direction (feed-forward).

For every synapse there is a weight parameter w_{ij} corresponding to the importance of the preceding neuron. The neuron then processes the information for every input x_i according to the following formula:

$$z_j = \sum_{i=1}^{M} x_i w_{ij} + b \tag{11.19}$$

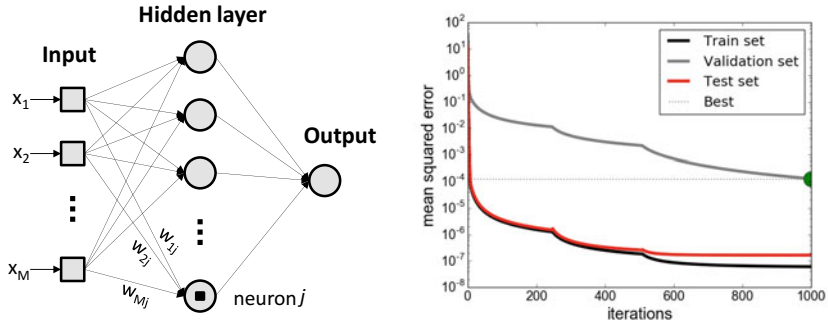

(a) Architecture of a single layer feed-forward neural network

(b) Training monitoring of a neural network

Fig. 11.3 Artificial neural networks architecture and training

where b is a bias term allowing the neuron to cover a wider range. Each result is going through an activation function where the nonlinearity of the decision boundary is introduced (usually of sigmoid type).

The learning procedure is based on a general function optimization problem, where the objective function is the sum squared error between the predicted output $t(\mathbf{w})$ and the target output y_0:

$$E(w_{ij}) = \frac{1}{2}\sum[t(w_{ij}) - y_0]^2 \tag{11.20}$$

In the minimization process, the weights of all the synapses are modified until the desired error level is achieved or the maximum number of cycles is reached. The weights are updated through an iterative procedure:

$$w_{ij}^{(t+1)} = w_{ij}^{(t)} + \Delta w_{ij} \tag{11.21}$$

where Δw_{ij} is the correction of the weight at the tth learning step, which is calculated by the following formula:

$$\Delta w_{ij} = -n\frac{\partial E}{\partial w_{ij}} \tag{11.22}$$

where n is a small parameter adjusting the correction each time, called learning rate. Since the error is spread back to the neurons and the weights are adjusted, the above algorithm is known as the back-propagation algorithm [14]. In order to avoid overfitting, a fraction of the sample data is used as a validation dataset and the error is monitored over the iterations to stop the training early enough.

For the purpose of this study, an ANN is trained for each component of the stiffness response of the macroscale, in order to make use of the costly estimator of Eq. 11.17 for the VBGSA. The neural network tool of Matlab is used and a graph with a satisfactory training procedure is presented in Fig. 11.3b.

11.2.3.2 Kriging

The basic assumption of Kriging (a.k.a. Gaussian process modeling) is that the output Y can be approximated by a single realization of a Gaussian random field [9]:

$$Y \approx \Omega(\mathbf{x}) = \boldsymbol{\beta}^T \mathbf{f}(\mathbf{x}) + \sigma^2 Z(\mathbf{x}) \tag{11.23}$$

The first term $\boldsymbol{\beta}^T \mathbf{f}(\mathbf{x})$ characterizes the trend of the field, with $\boldsymbol{\beta}$ being the first vector of hyper parameters to be computed and $\mathbf{f}$ the set of P-order regression functions. The second term includes the Kriging variance σ^2 (second hyper parameter) and a zero-mean, unit variance Gaussian random field $Z(\mathbf{x})$.

Parameters $\boldsymbol{\beta}$ and σ^2 are calibrated via the generalized least-squares method, for a specific value of the correlation length parameter of the Gaussian field $\hat{\boldsymbol{\theta}}$, as:

$$\boldsymbol{\beta}(\hat{\boldsymbol{\theta}}) = (\mathbf{F}^T \mathbf{R}^{-1} \mathbf{F})^{-1} \mathbf{F} \mathbf{R}^{-1} Y \tag{11.24}$$

$$\sigma_y^2(\hat{\boldsymbol{\theta}}) = \tfrac{1}{N} (Y - \mathbf{F}\boldsymbol{\beta})^T \mathbf{R}^{-1} (Y - \mathbf{F}\boldsymbol{\beta}) \tag{11.25}$$

where $\mathbf{F}$ is the regression matrix and $\mathbf{R}$ is the correlation matrix at the input ED points of size N. For the calculation of the optimum correlation length $\hat{\boldsymbol{\theta}}$, a minimization procedure is applied in either of the formulas:

$$\hat{\boldsymbol{\theta}}_{ML} = \arg min \left[\tfrac{1}{N} (Y - \mathbf{F}\boldsymbol{\beta})^T \mathbf{R}^{-1} (Y - \mathbf{F}\boldsymbol{\beta}) (det \mathbf{R})^{\frac{1}{N}} \right] \tag{11.26}$$

$$\hat{\boldsymbol{\theta}}_{CV} = \arg min \left[Y^T \mathbf{R}^{-1} diag(\mathbf{R}^{-1})^{-2} \mathbf{R}^{-1} Y \right] \tag{11.27}$$

where ML stands for Maximum Likelihood and CV for Cross-Validation. Predicting the mean and variance of a new point $\mathbf{x_0} \notin \mathbf{X} = \{\mathbf{x}^{(i)} \in \mathbb{R}^M,\ i = 1, ..., N\}$ of the input space, is done via the following equations:

$$\mu(\mathbf{x_0}) = \mathbf{f}(\mathbf{x_0})^T \boldsymbol{\beta} + \mathbf{r}(\mathbf{x_0})^T \mathbf{R}^{-1} (Y - \mathbf{F}\boldsymbol{\beta}) \tag{11.28}$$

$$\sigma_{\hat{y}}^2(\mathbf{x_0}) = \sigma_y^2 \left(1 - \left\langle \mathbf{f}(\mathbf{x_0})^T \mathbf{r}(\mathbf{x_0})^T \right\rangle \begin{vmatrix} 0 & \mathbf{F}^T \\ \mathbf{F} & \mathbf{R} \end{vmatrix} \begin{vmatrix} \mathbf{f}(\mathbf{x_0}) \\ \mathbf{r}(\mathbf{x_0}) \end{vmatrix} \right) \tag{11.29}$$

where $\mathbf{r}(\mathbf{x_0}) = R(|\mathbf{x_0} - \mathbf{x_i}|; \hat{\boldsymbol{\theta}})$ is the correlation between the unknown point $\mathbf{x_0}$ and the ED $\mathbf{X}$, while $\mathbf{f}(\mathbf{x_0})$ is the set of regression functions evaluated at $\mathbf{x_0}$. It is noted that Kriging is an exact interpolator:

$$\mu(\mathbf{x}^{(i)}) = \Omega(\mathbf{x}^{(i)}), \quad \sigma_{\hat{y}}^2(\mathbf{x}^{(i)}) = 0, \qquad \forall \mathbf{x}^{(i)} \in \mathbf{X} \tag{11.30}$$

The use of Kriging as a surrogate relies on using the predictor μ for points outside the ED. Parameters to be tuned for a good training are the ED size and the order of $\mathbf{f}$. The coefficient of determination Q^2 (1−error percentage) is presented in Fig. 11.4

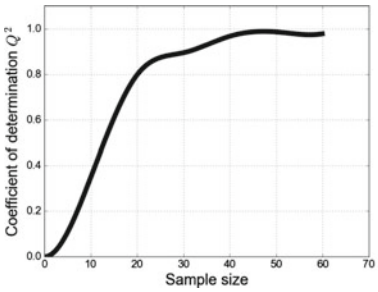

(a) Coefficient of determination against experimental design size

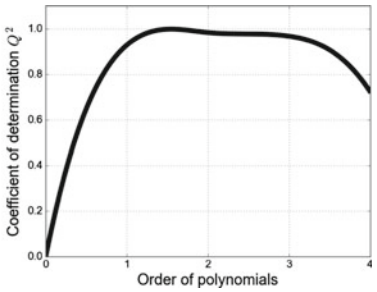

(b) Coefficient of determination against order of regression polynomials

Fig. 11.4 Training of Kriging

against both these parameters, so that the user can decide the optimum solution. By using μ the necessary realizations for the costly VBGSA estimator of Eq. 11.17 can be performed.

11.2.3.3 Polynomial Chaos Expansions

Assuming that the output variable Y has a finite variance and that the input parameters in $\mathbf{x} = \{x_i,\ i = 1, ..., M\}$ are independent, the polynomial chaos expansion (PCE) of Y expresses the model Ω as an infinite series of orthonormal polynomials in $\mathbf{X}$:

$$Y \approx \Omega(\mathbf{x}) = \sum_{\boldsymbol{\alpha} \in \mathbb{N}^M} y_{\boldsymbol{\alpha}} \Psi_{\boldsymbol{\alpha}}(\mathbf{X}) \tag{11.31}$$

where M is the size of the input vector $\mathbf{X}$, y_α are coefficients to be computed, $\boldsymbol{\alpha}$ is a M-dimensional multi-index (M-tuple) and $\Psi_{\boldsymbol{\alpha}}(\mathbf{X})$ are multivariate orthonormal polynomials. The orthonormal basis of the expansion is constructed as a product of univariate orthogonal polynomials P:

$$\Psi_{\boldsymbol{\alpha}}(\mathbf{X}) = \prod_{i=1}^{M} P_{\alpha_i}^{(i)}(x_i) \tag{11.32}$$

There is a direct correspondence between known probability distributions and polynomial families (e.g. Legendre for Uniform, Hermite for Gaussian etc.)

The challenging part is to choose a finite subset of multi-indices which can approximate the model output sufficiently within certain error measures. The simplest truncation scheme consists of limiting the total degree of polynomials with an upper bound:

$$A^{M,p} = \{\boldsymbol{\alpha} \in \mathbb{N}^M : |\boldsymbol{\alpha}| \leq p\} \tag{11.33}$$

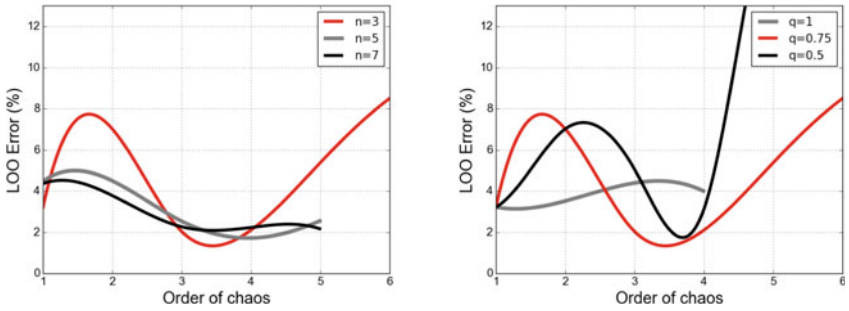

(a) Error against experimental design size and polynomial order

(b) Error against reduced q-norm scheme and polynomial order

Fig. 11.5 Training of polynomial chaos expansion

where $|\alpha| = \sum_{i=1}^{M} \alpha_i$ is the total degree of polynomials and p is the maximum degree. The cardinality of this subset is given by:

$$card A^{M,p} \equiv P = \frac{(M+p)!}{M!p!} \tag{11.34}$$

which means that the set size grows polynomially both in M and p (e.g. for $M = 6$ and $p = 5$, $P = 210$). The ED size needs to be n times the $card A^{M,p}$, hence this scheme can be expensive for problems with high stochastic dimension. A sort of order reduction may be achieved with the use of hyperbolic index sets based on q-norms [2]:

$$A_q^{M,p} = \{\boldsymbol{\alpha} \in \mathbb{N}^M : \left(\sum_{i=1}^{M} \alpha_i^q \right)^{\frac{1}{q}} \leq p\} \tag{11.35}$$

where $0 < q < 1$. This technique is suitable for problems with low interactions between the stochastic input. Parametric studies should always be performed for the optimal tuning of the polynomial order p, coefficient n (ED size) and the q-norm, as in Fig. 11.5.

The unknown PCE coefficients are gathered into a vector $\hat{Y}$ and computed by minimizing the mean square error between the prediction and the model response for each sample of the ED:

$$\hat{Y} = argmin E\left\{ \left[\sum_{j=0}^{P-1} y_j \Psi_j(\mathbf{X}) - \Omega(\mathbf{X}) \right]^2 \right\} \tag{11.36}$$

The problem can be solved analytically by least-square minimization:

$$\hat{Y} = (\mathbf{A}^T \mathbf{A})^{-1} \mathbf{A}^T \Omega \tag{11.37}$$

where $\mathbf{A} = A_{ij} = \Psi_j(x^{(i)})$ for $\{i = 1, ..., M;\ j = 0, ..., P-1\}$ is the experimental matrix and Ω is the vector of true responses within the ED.

An essential difference of PCE compared to ANN and Kriging is that the Sobol indices can be derived immediately after training, without using the expensive formula of Eq. 11.17, simply by post-processing the computed coefficients:

$$S_i = \frac{\sum_{a \in A_i} y_a^2}{Var(Y)} \tag{11.38}$$

where $A_i = \{a \in \mathbb{N}^M :\ a_i > 0,\ a_{j \neq i} = 0\}$ and $Var(Y) = \sum_{a \in \mathbb{N}^M,\ a \neq 0} y_a^2$.

11.3 Results

When sufficiently trained, all three surrogate models presented are able to emulate the stochastic elastic response of the braided composite model of Sect. 11.2.1. A practical way to verify these models and examine the stochastic accuracy is to extract estimations for the probability density function (PDF) of the response and correlate with a histogram of a brute force Monte Carlo simulation for a fair amount of realizations. The PDF contains fully the probabilistic information of a response. Such a comparison is given in Fig. 11.6 for the uniaxial stiffness moduli E_1, E_2 and E_3. It can be seen that all models can capture the true stochastic response with high accuracy. For this problem, 1000 realizations were found adequate for a smooth histogram and PDF description.

In terms of efficiency, metamodels are judged mostly by the number of model evaluations necessary for a good training, hence the size of the ED. Herein, the ANN needed around 30–50 samples, the Kriging 20–40 samples and the PCE 150–200 samples. However this is surely not the sole criterion. As mentioned in the Sect. 11.2.3.3, although PCE models need more evaluations due to the stochastic input and polynomial order dependency, the Sobol indices can be calculated immediately after training. So depending on the model, this option could still be faster than a cheap metamodel (ANN, Kriging) which uses the very expensive estimator for the VBGSA (Eq. 11.17).

The Sobol indices were calculated with all available metamodels and the comparative results are presented in Fig. 11.7, for the same components of the elastic macroscale response (E_1, E_2, E_3). Convergence between the metamodels is satisfactory for most cases, while the discrepancies can be explained by the summation

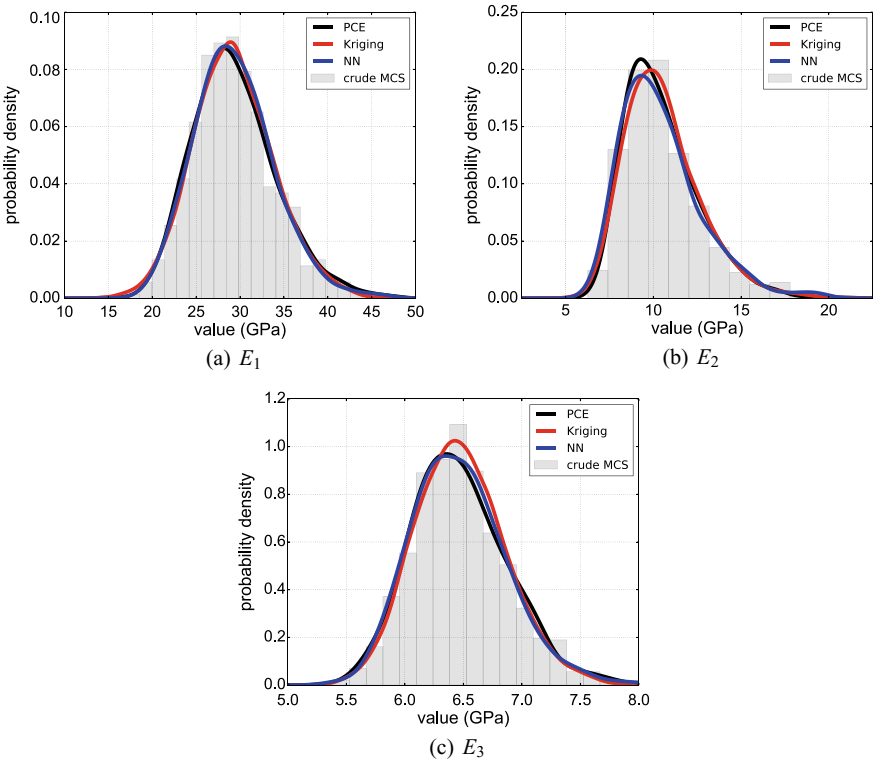

Fig. 11.6 Prediction for probability distribution of Young's moduli E_1, E_2 and E_3

of approximations of the models and the Sobol estimator of Eq. 11.17. Regarding the physical interpretation of the uncertainty quantification results, it is evident that for all cases the sum of the Sobol indices reaches unity, which means there are not any interactions among the stochastic input parameters chosen. The behavior of the longitudinal direction is partitioned between the longitudinal fiber modulus, the yarn volume fraction and the braiding angle. The transverse response of E_2 is governed by the geometrical variability of the braiding angle, while E_3 is dominated by the yarn volume fraction. Hence, the fiber architecture has more impact on the variability of the homogenized stiffness than the material stiffness properties of the fibers. However, this finding is based on the assumption that the coefficient of variation is 10% for all random parameters. The actual variability, especially of fiber architecture parameters (YVf, BA, UA), still needs to be determined experimentally. Furthermore, it should be once again highlighted, that such sensitivity analysis results would not be available without the use of surrogate modeling, since the Sobol estimator requires hundreds of thousands samples in order to converge.

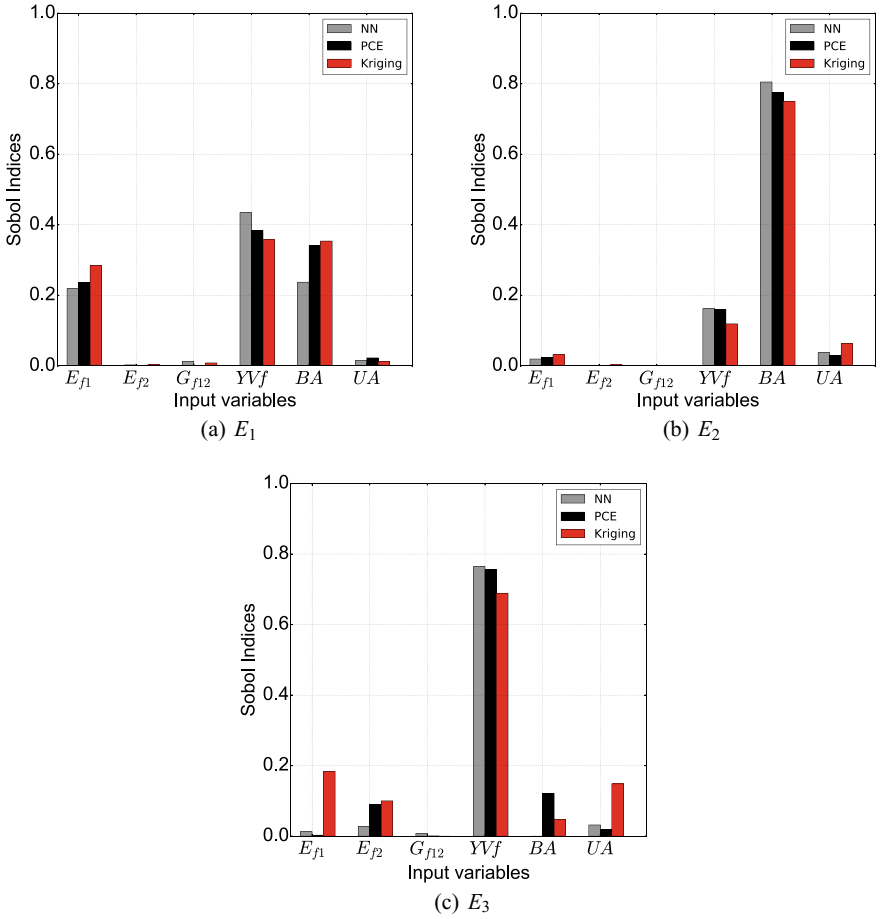

Fig. 11.7 Sobol indices for Young's moduli E_1, E_2 and E_3

11.4 Conclusions

An uncertainty quantification framework applied on a triaxially braided composite model was presented in this chapter. The effects of various aleatory uncertainties were studied and the fiber longitudinal modulus, braiding angle and yarn volume fraction were identified as the most important variable parameters via a variance-based global sensitivity analysis. Three popular metamodeling techniques were described, applied and compared to overcome the computational burden of the procedure. Attention should be aimed to the training process and the parameters to be tuned (number of neurons for ANN, order of polynomials for Kriging and PCE), since efficient

and reliable monitoring offers room for order reduction efforts, however there is not a universal answer for the ”best” metamodel, as the choice is always problem dependent.

References

1. Balokas G, Czichon S, Rolfes R (2018) Neural network assisted multiscale analysis for the elastic properties prediction of 3D braided composites under uncertainty. Compos Struct 183:550–562
2. Blatman G, Sudret B (2011) Adaptive sparse polynomial chaos expansion based on least angle regression. J Comput Phys 230(6):2345–2367
3. Chamis CC (2004) Probabilistic simulation of multi-scale composite behavior. Theor Appl Fract Mec 41(1–3):51–61
4. Curtin WA (1998) Stochastic damage evolution and failure in fiber-reinforced composites. Adv Appl Mech 36:163–253
5. Kaminski M, Pawlak A (2015) Various approaches in probabilistic homogenization of the CFRP composites. Compos Struct 133:425–437
6. Lin H, Brown LP, Long AC (2011) Modelling and simulating textile structures using TexGen. Adv Mater Res 331:44–47
7. Melro AR, Camanho PP, Pinho ST (2008) Generation of random distribution of fibres in long-fibre reinforced composites. Compos Sci Technol 68(9):2092–2102
8. Omairey SL, Dunning PD, Sriramula S (2018) Influence of micro-scale uncertainties on the reliability of fibre-matrix composites. Compos Struct 203:204–216
9. Sacks J, Welch WJ, Mitchell TJ (1989) Design and analysis of computer experiments. Stat Sci 4(4):409–423
10. Sobol IM (2001) Global sensitivity indices for nonlinear mathematical models and their Monte Carlo estimates. Math Comput Simul 55(1–3):271–280
11. Sriramula S, Chryssanthopoulos MK (2009) Quantification of uncertainty modelling in stochastic analysis of FRP composites. Compos Part A-Appl S 40(11):1673–1684
12. Stefanou G (2009) The stochastic finite element method: Past, present and future. Comput Method Appl M 198(9–12):1031–1051
13. Stefanou G, Savvas D, Papadrakakis M (2015) Stochastic finite element analysis of composite structures based on material microstructure. Compos Struct 132:384–392
14. Swingler K (1996) Applying neural networks: a practical guide. Morgan Kaufman Publishers Inc., California
15. Vanaerschot A, Cox BN, Lomov SV, Vandepitte D (2013) Stochastic multi-scale modelling of textile composites based on internal geometry variability. Compos Struct 122:55–64
16. Vanaerschot A, Cox BN, Lomov SV, Vandepitte D (2016) Multi-scale modelling strategy for textile composites based on stochastic reinforcement geometry. Comput Method Appl M 310:906–934